

FUNDAMENTAL SURFACE PROPERTIES AND GAS-SURFACE INTERACTIONS OF
TWO-DIMENSIONAL MATERIALS

A Dissertation
Submitted to the Graduate Faculty
of the
North Dakota State University
of Agriculture and Applied Science

By

Mindika Tilan Abeyrathna Nayakasinghe Mudiyan

In Partial Fulfillment of the Requirements
for the Degree of
DOCTOR OF PHILOSOPHY

Major Department:
Chemistry and Biochemistry

November 2018

Fargo, North Dakota

North Dakota State University
Graduate School

Title

FUNDAMENTAL SURFACE PROPERTIES AND GAS-SURFACE
INTERACTIONS OF TWO-DIMENSIONAL MATERIALS

By

Mindika Tilan Abeyrathna Nayakasinghe Mudiyan

The Supervisory Committee certifies that this *disquisition* complies with North Dakota
State University's regulations and meets the accepted standards for the degree of

DOCTOR OF PHILOSOPHY

SUPERVISORY COMMITTEE:

Dr. Uwe Burghaus

Chair

Dr. John Hershberger

Dr. Wenfang Sun

Dr. Wei Lin

Approved:

11/29/2018

Date

Dr. Gregory Cook

Department Chair

ABSTRACT

Heterogeneous model catalysis with supported nanomaterials on ultra-thin two-dimensional films has contributed significantly to improve the existing industrial catalytic processes, as well as to discover novel ways to enhance selectivity, specificity, and stability of the catalysts. Silica and zeolites are of particular interest, which has been widely utilized as catalysts and catalytic supports in several industrial processes. However, there are a limited number of surface science studies with zeolites due to the lack of surface analogs. Understanding the fundamental surface properties of silica and zeolites, involving the synthesis of surface analogs of silica and zeolites, characterization, surface modification, and screening for chemical and physical properties connected to the heterogeneous catalysis related applications utilizing advanced ultra-high vacuum-based surface science techniques is the main focus of this dissertation.

Catalyst particles should be finely distributed on high surface area supports, in order to have high selectivity and specificity. Particle agglomeration during extreme catalyst operation (reaction) conditions decreases the efficiency of the catalysts over time. One common strategy to address the issue of particle agglomeration is to promote strong catalyst-support interactions. In this study, chemical reactivity of the inert silica was improved by doping with aluminum, which enhanced the polarity of silica (2D-zeolites) and hence the catalyst-support interactions compared to inert silica.

Organohalide perovskite thin films are a fascinating class of material, which attract much attention in the recent past as the light harvesting materials in solar cells due to excellent power conversion efficiencies. However, poor thermal, chemical, and long-term stability limit the industrial applications of these organohalide perovskites. Gas-surface interactions on methylammonium lead iodide perovskite thin films were investigated in order to understand the

thermal and the chemical degradation mechanisms utilizing UHV-based surface analytical techniques combined with computational calculations. Thermal stability improvement of the perovskite thin films by surface passivation using a protective chemical inhibition layer was successfully investigated experimentally.

ACKNOWLEDGMENTS

Continuous and knowledgeable support provided by my advisor, Uwe Burghaus is greatly appreciated. His encouragement, availability for discussions, and guidance enabled me to grow as a successful researcher. Provided stress-free environment, flexibility, and understanding helped me to maintain a good work-life balance. The freedom given in the lab to design, test, and modify new experimental methods makes me a strong researcher.

Timely feedback provided by my committee members, John Hershberger, Wenfang Sun, and Wei Lin is greatly appreciated as well. Flexibility in arranging annual committee meetings, provided valuable feedback, and fruitful discussions were really helpful to move forward in my Ph.D. carrier and research.

I greatly appreciate the initial laboratory training given by Ashish Chakradhar, helping me to learn experimental techniques, data analysis methods, equipment maintenance, and troubleshooting. His guidance was really helpful to start as a surface chemistry researcher in the Burghaus laboratory. My thanks also go to the former lab mate, Nilushni Sivapragasm for working with me on several collaborative research projects.

I would like to acknowledge our research collaborators, Dimitri Kilin and Yulun Han for the theoretical calculations and timely group discussions, which helped us to complete a successful project. Support by Kenneth Anderson, Gregory Strommen, and Chunju Gu are acknowledged for their assistance with SEM, EDX, XRD, and surface profiling. Initial help provided by Kenneth Anderson for the fabrication of perovskite thin films is greatly appreciated.

The financial support provided by ACS-PRF, NDSU-RCA, and NDSU Department of Chemistry and Biochemistry are deeply appreciated.

Finally, I would like to thank my parents, N.M.K. Abeyrathna and B.G. Nandhawathi for encouraging me to pursue this Ph.D. and being devoted mentors of my life in every possible way. The love and the unconditional support provided by my wife, Anomy Rathnayaka is deeply appreciated.

DEDICATION

This dissertation is dedicated to my parents N.M.K. Abeyrathna, B.G. Nandhawathi, and my wife Anomy Rathnayaka for their infinite love and moral support.

TABLE OF CONTENTS

ABSTRACT.....	iii
ACKNOWLEDGMENTS.....	v
DEDICATION.....	vii
LIST OF TABLES.....	xiii
LIST OF FIGURES.....	xiv
LIST OF ABBREVIATIONS.....	xx
LIST OF SYMBOLS.....	xxii
1. INTRODUCTION.....	1
1.1. Model catalysis.....	2
1.2. Surface structures.....	6
1.3. Surface deformations.....	9
1.4. Gas-surface interactions.....	10
2. EXPERIMENTAL TECHNIQUES.....	14
2.1. Ultra-high vacuum.....	14
2.1.1. Introduction.....	14
2.1.2. Generation of ultra-high vacuum.....	16
2.1.3. UHV experimental setup.....	18
2.2. Auger electron spectroscopy.....	19
2.2.1. Historical background.....	19
2.2.2. Principles of AES.....	20
2.2.3. Instrumentation.....	21
2.3. Low energy electron diffraction.....	23
2.3.1. Historical background.....	23
2.3.2. Principles of LEED.....	24

2.3.3. Instrumentation.....	27
2.4. Thermal desorption spectroscopy.....	29
2.4.1. Introduction.....	29
2.4.2. Experimental setup.....	30
2.4.3. TDS theory.....	31
2.4.3.1. Redhead analysis.....	34
2.4.3.2. Inversion optimization analysis.....	34
2.5. Molecular beam scattering.....	36
2.5.1. Introduction.....	36
2.5.2. Experimental setup.....	37
2.5.3. Molecular beam scattering theory.....	38
2.5.3.1. Supersonic molecular beams.....	38
2.5.3.2. Molecular beam energy.....	40
2.5.3.3. Adsorption probability measurements.....	40
2.5.3.4. Activated and non-activated adsorption.....	42
2.6. X-ray photoelectron spectroscopy.....	45
2.6.1. Historical background.....	45
2.6.2. Principles of XPS.....	45
2.6.3. Instrumentation.....	46
2.7. Ultraviolet-visible spectroscopy.....	49
2.7.1. Introduction.....	49
2.7.2. Theory.....	49
2.7.3. Instrumentation.....	51
2.8. Scanning electron microscopy.....	52
2.9. X-ray diffraction.....	53

3. FUNDAMENTAL SURFACE PROPERTIES OF TWO-DIMENSIONAL SILICA AND ZEOLITES.....	55
3.1. Introduction.....	56
3.1.1. Silicatene and zeolites.....	56
3.1.2. Hydrodesulphurization.....	59
3.2. Project structure.....	61
3.3. Synthesis and characterization of silica thin films.....	62
3.3.1. Introduction.....	62
3.3.1.1. Choice of the substrate.....	63
3.3.1.2. Silica film characterization.....	64
3.3.1.3. Structure of silica thin films on Mo(112).....	67
3.3.2. Results and discussion.....	68
3.3.2.1. Substrate preparation and characterization.....	69
3.3.2.2. Silica thin film synthesis.....	71
3.3.3. Summary: Synthesis and characterization of silica thin films.....	74
3.4. Water adsorption on silica thin films.....	74
3.4.1. Introduction.....	74
3.4.2. Results and discussion.....	77
3.4.2.1. Water adsorption on Mo(112) and Mo(112)-p-(1x3)-O.....	79
3.4.2.2. Water adsorption on silica thin films.....	81
3.4.3. Summary: Water adsorption on silica thin films.....	87
3.5. Desulphurization related surface chemistry on 2D-silica films.....	88
3.5.1. Experimental procedures.....	88
3.5.2. Sample characterization.....	90
3.5.3. Thiophene adsorption kinetics.....	91
3.5.3.1. Introduction.....	91

3.5.3.2.	Results and discussion.....	92
3.5.3.3.	Summary: Thiophane adsorption on silicatene.....	97
3.5.4.	Alkane adsorption kinetics and dynamics.....	97
3.5.4.1.	Introduction.....	97
3.5.4.2.	Results and discussion.....	98
3.5.4.2.1.	Alkane adsorption kinetics.....	98
3.5.4.2.2.	Alkane adsorption dynamics.....	106
3.5.4.3.	Summary: Alkane adsorption kinetics and dynamics.....	109
3.6.	Benzene adsorption on silicatene.....	109
3.6.1.	Introduction.....	110
3.6.2.	Experimental procedures.....	111
3.6.3.	Results and discussion.....	111
3.6.3.1.	Benzene adsorption kinetics on silicatene.....	111
3.6.3.2.	Support effects of benzene adsorption.....	114
3.6.4.	Summary: Benzene adsorption on silicatene.....	119
3.7.	Alcohol adsorption on silicatene.....	119
3.7.1.	Introduction.....	119
3.7.2.	Experimental procedures.....	120
3.7.3.	Results and discussion.....	120
3.7.4.	Summary: Alcohol adsorption on silicatene.....	125
3.8.	Two-dimensional zeolite synthesis.....	126
3.8.1.	Introduction.....	126
3.8.2.	Experimental methods.....	129
3.8.3.	Results and discussion.....	129
3.8.4.	Future directions.....	135

3.8.5. Summary: 2D-Zeolites.....	135
4. GAS-SURFACE INTERACTIONS ON METHYLAMMONIUM LEAD IODIDE PEROVSKITES.....	136
4.1. Introduction.....	136
4.1.1. Advantages.....	137
4.1.2. Limitations.....	137
4.1.3. Perovskite structure.....	139
4.1.4. Degradation mechanisms of MAPbI ₃	142
4.1.5. Synthesis of MAPbX ₃ perovskite thin films.....	143
4.1.6. Carbon dioxide adsorption studies.....	146
4.1.7. Formic acid adsorption studies.....	149
4.2. Experimental procedures.....	151
4.2.1. Materials.....	151
4.2.2. UHV experimental setup.....	151
4.2.3. Ambient pressure experiments.....	152
4.2.4. Perovskite synthesis.....	152
4.3. Results and discussion.....	153
4.3.1. Characterization of MAPbI ₃ perovskite thin films.....	153
4.3.2. Thermal stability of MAPbI ₃ perovskite thin films.....	161
4.3.3. Carbon dioxide adsorption on MAPbI ₃ perovskite thin films.....	166
4.3.4. Formic acid adsorption on MaPbI ₃ perovskite thin films.....	171
4.4. Summary and conclusions.....	179
REFERENCES.....	181

LIST OF TABLES

<u>Table</u>	<u>Page</u>
3.1. Surface science studies of water adsorption on hydrophilic and hydrophobic surfaces.....	76
3.2. Thermocouple calibration by in-situ TDS.....	89
3.3. Binding energies for alkanes on defect-free silicatene and silica wafer adsorption sites.....	102
3.4. Parameterization of $E_d(\theta)$ vs θ curves obtained from inversion optimization analysis according to the function $E_d = E_0 + Y\theta + E_{\text{def}}e^{(-\theta/\theta(\text{def}))}$ (energies are in kJ/mol).....	106
3.5. Zero coverage limit ($\theta < 0.02$) of the binding energies calculated using the Redhead approximations for alcohol adsorption on silicatene and CNTs.....	125
4.1. Experimental and theoretical CO_2 binding energies on MAPbI_3 perovskite thin films.....	169

LIST OF FIGURES

<u>Figure</u>	<u>Page</u>
1.1. Commonly encountered basic unit cell structures (subcategories of cubic and hexagonal unit cell structures)	6
1.2. Different surface structures obtained by cutting through various planes in the simple cubic structure.....	7
1.3. 2D surface lattice structures (top) and corresponding LEED patterns simulated using LEEDpat version 1.0.....	8
1.4. Simple adsorbate overlayer structures on fcc(100) surface.....	8
1.5. Variation of the potential energy of an adsorbate as a function of the distance from a surface, as the adsorbate approaches the surface.....	10
2.1. Variation of the pressure in a typical vacuum chamber with time, during the initiation of the vacuum.....	17
2.2. Schematic diagram of the UHV experimental setup utilized in this research.....	18
2.3. Auger emission process.....	20
2.4. Schematic representation of the AES experimental setup in the Burghaus laboratory....	22
2.5. Electron diffraction by a one-dimensional array of atoms.....	25
2.6. LEED patterns obtained for clean Mo(112) single crystal at 60 eV (left) and at 130 eV (right).....	26
2.7. Schematic representation of the real space and the corresponding reciprocal space lattices.....	26
2.8. (a) Schematic representation of the ErLEED 150 optics, (b) Main components of a typical LEED system.....	27
2.9. TDS experimental setup in the Burghaus laboratory.....	30
2.10. Schematic representation of a typical TPD spectra.....	31
2.11. Schematic representation of TDS patterns for different desorption orders.....	32
2.12. Schematic diagram of the molecular beam scattering experimental setup in the Burghaus laboratory.....	37
2.13. Schematic representation of the theoretical axial velocity distributions for a monoatomic gas with different Mach numbers.....	39

2.14.	Seeded n-butane (3% n-butane in He) molecular beam characterization (left: n-butane molecular beam in an empty vacuum chamber, right: n-butane molecular beam interacting with a crystalline silica thin film on Mo(112)).....	41
2.15.	Lennard-Jones potential energy diagrams for activated and non-activated adsorption of a molecule as a function of the distance from the surface (adsorbent).....	43
2.16.	Schematic representations of the variation of initial adsorption probability as a function of impact energy for (a) molecular and (b) dissociative adsorption.....	44
2.17.	Photoemission process.....	46
2.18.	Schematic diagram of the XPS experimental setup in the Burghaus laboratory.....	48
2.19.	Possible electronic transitions in UV-Visible spectroscopy.....	50
3.1.	Schematic representation of the HYD and DDS pathways in catalytic HDS.....	61
3.2.	Simulated surface structures and LEED patterns of Mo(112) single crystalline surface and crystalline silica thin film on Mo(112) surface.....	65
3.3.	Schematic representation of the Goodman's cluster model of silica thin films on Mo(112), representing Mo(112)-c(2×2)-[SiO ₄] structure.....	66
3.4.	Schematic representation of the Mo (112) single crystal (left) and the Freund's structural model of the silica films on Mo(112) with a 2D network of corner-sharing [SiO ₄] tetrahedra superlattice (right).....	67
3.5.	Characterization of the Mo(112) substrate (a- AES of contaminated and clean Mo(112), b-Simulated LEED pattern of Mo(112) surface, c-The LEED pattern obtained for clean Mo(112) at 58 eV).....	69
3.6.	Characterization of the oxidic precursor of Mo(112) substrate (a- AES of clean and oxidized Mo(112), b- XPS of oxidized Mo(112), c- Mo(112)-p(1×3)-O simulated superlattice, simulated LEED pattern, and LEED pattern obtained at 58 eV from left to right).....	70
3.7.	Schematic diagram of the home-made silicon doser.....	71
3.8.	(a) to (d)-AES of silica thin films on Mo (112) after each Si dosing and oxidation cycle (In (a), dotted line indicates the clean Mo (112) support), e, f- Characteristic XPS photoelectron lines for silicon (Si2p, Si2s) and oxygen (O1s) for a silica thin film.....	72
3.9.	Simulated (left) and experimental (right, at 58 eV) LEED patterns obtained for silica thin films on Mo(112).....	73
3.10.	LEED patterns obtained after preparation of the silica film on Mo (112) using method III as described above ((a) After water TDS, (b) after flashing to 800 K, (c) after flashing to 860 K.....	74

3.11.	Schematic molecular orbital representation of the partial π bond character of Si-O bonds in silica.....	78
3.12.	Water TDS for Mo(112) (at lower (a) and larger (b) exposures) and Mo(112)-p(1 \times 3)-O (at lower (c) and larger (d) exposures). Exposure is given in Langmuir (1L \sim 1s exposure at 1 \times 10 ⁻⁶ torr).....	80
3.13.	(a), (b): LEED patterns of Mo(112)-c(2 \times 2)-[SiO ₄] obtained from method I and II, (c)-(f): water TDS curves obtained for the same surfaces ((c) and (e)- Lower and larger exposer of water adsorbed on silica films from method I, (d) and (f)- Lower and larger exposer of water adsorbed on silica films from method II).....	83
3.14.	(a), (b): LEED patterns of Mo(112)-c(2 \times 2)-[SiO ₄] obtained from method III after annealing to 860K and 910 K, (c)-(f): water TDS curves obtained for the same surfaces ((c) and (e)- Lower and larger exposer of water adsorbed on the surface annealed to 860 K, (d) and (f)- Lower and larger exposer of water adsorbed on the surface annealed to 910 K)	84
3.15.	LEED characterization of (a) Mo(112), (b) Mo(112)-p-(1 \times 3)-O, (c) Mo(112)-c(2 \times 2)-[SiO ₄]; (d) Water TDS curves on silicatene as a function of temperature; (e) AES of Mo(112), Mo(112)-p(1 \times 3)-O, and silicatene film on Mo(112).....	90
3.16.	(a) TDS curves obtained for thiophene desorption from silicatene as a function of exposure (m/z=58 amu was detected, which is the most intense fragmentation mass of thiophene), (b) Binding energies for thiophene adsorbed on silicatene (α -peak) and silica wafer as function of exposure calculated with Redhead analysis using the pre-exponential 1 \times 10 ¹³ s ⁻¹	93
3.17.	(a) Multi-mass TDS fragments of gaseous thiophene desorbed from silicatene, (b) Mass spectra of gaseous thiophene, (c) &(d) Difference spectra (Normalized multi-mass TDS intensity minus corresponding gas-phase mass fragment intensity) Positive and negative values of the difference in panels (c) and (d) respectively.....	95
3.18.	TDS curves for (a) Isobutane (C ₄ H ₁₀), (b) n-pentane (C ₅ H ₁₂), (c) n-heptane (C ₇ H ₁₆) adsorption on silicatene as a function of exposure of each alkane (data for small exposures are given in insets).....	99
3.19.	Coverage-dependent binding energies (E _d) for alkanes adsorbed on silicatene and silica wafer. E _d for silicatene was determined using the Redhead analysis with assumed pre-exponential 1 \times 10 ¹³ s ⁻¹	100
3.20.	Application of the inversion optimization analysis technique to simulate TDS data for n-pentane adsorption on silicatene (experimental TDS curve corresponding to 0.7 ML n-pentane exposure was used as an example).....	103

3.21.	(a) Experimental n-pentane TDS curves for silicatene, (b) corresponding $E(\theta)$ vs θ curves obtained for each TDS curve by applying the inverted Polanyi–Wigner equation.....	104
3.22.	Left panel- Experimental (symbols) and simulated (solid lines) TDS of isobutane, n-pentane, and n-heptane (top to bottom), with best-fitted pre-exponentials (A). Right panel- Effect of the pre-exponential to the shape and the position of the simulated (solid lines) TDS curves (for isobutane TDS).....	105
3.23.	Coverage dependent binding energies obtained from best-fitted pre-exponentials for isobutane, n-pentane, and n-heptane. Binding energy curves obtained from inversion optimization analysis and Redhead analysis are compared (with the same pre-factors).....	106
3.24.	(a) Initial adsorption probability as a function of surface temperature for n-butane adsorption on silicatene at a constant impact energy of 0.7 eV, (b) n-butane TDS curves for silicatene as a function of exposure time.....	107
3.25.	Initial adsorption probability as a function of impact energy for n-butane adsorption on silicatene at a constant surface temperature ($T_s=110$ K).....	108
3.26.	(a) TDS curves obtained for benzene adsorbed on silicatene as a function of benzene exposure, (b) coverage dependent binding energies for benzene adsorption on silicatene (different data points refer to different TDS datasets).....	112
3.27.	Sets of benzene TDS curves as a function of benzene exposure on, (a) Mo(112) and (b) Mo(112)-p-(1×3)-O. AES data comparing the elemental composition of, (a) Mo(112) and (b) Mo(112)-p(1×3)-O before and after the benzene adsorption experiments.....	115
3.28.	Coverage-dependent binding energies for benzene adsorption on silicatene, silica wafer, Mo(112), and Mo(112)-p(1×3)-O obtained by Redhead analysis using a 1 st order pre-exponential of $1 \times 10^{13} \text{ s}^{-1}$	117
3.29.	Methanol, ethanol, 1-propanol, and 1-butanol TDS as a function of exposure (left-smaller exposures, right-larger exposures, insets- AES before and after alcohol adsorption).....	122
3.30.	1-pentanol TDS curves on silicatene as a function of exposure (inset- AES characterization before and after TDS).....	123
3.31.	Coverage-dependent binding energies of methanol, ethanol, 1-propanol, and 1-butanol on silicatene calculate using Redhead analysis (a first order pre-exponential of $1 \times 10^{13} \text{ s}^{-1}$ was used).....	124
3.32.	Some example zeolite framework structures with corresponding 3D zeolites.....	127
3.33.	Proposed models of the top view and the side view (top and bottom respectively) of the Al doped silicatene films.....	128

3.34.	(a) Characterization of a silicatene film grown on Mo(112), (b) Sequential growth of an Al ₂ O ₃ thin film on clean Mo(112).....	130
3.35.	AES characterization of a silicatene film (solid blue line) and a SiO ₂ / Al ₂ O ₃ mixed oxide thin film on Mo(112) substrate.....	131
3.36.	(a) Water TDS on a silicatene film, (b) desorption profiles of D ₂ O and D ₂ after ~ 1.0 Langmuir of D ₂ O adsorption on SiO ₂ / Al ₂ O ₃ mixed oxides, (c) water TDS on mixed oxide thin films, (d) D ₂ O TDS on mixed oxide thin films.....	132
4.1.	Schematic representation of the ideal cubic perovskite structure ABX ₃ with a three-dimensional network of [BX ₆] corner-sharing octahedra, forming 12-fold cavities containing cationic A.....	140
4.2.	(a) Symmetric cubic phase and (b) less symmetric orthorhombic phase of the perovskite crystal structure.....	141
4.3.	Molecular orbital diagram of the gas-phase carbon dioxide.....	148
4.4.	(a) A photo of decomposed MAPbI ₃ forming PbI ₂ as a result of overheating (~200 ⁰ C) during the synthesis, (b) A photo of a good MAPbI ₃ perovskite thin film (photos were taken using a digital camera).....	153
4.5.	(a) UV-visible absorption spectra of a typical MAPbI ₃ perovskite thin film synthesized in the study (using the UV-Vis transmittance mode (top panel) and the diffuse reflectance mode (bottom panel)), (b) Absorption spectra of perovskite thin films employed in each step of the study, (c) comparison of absorption spectra of MAPbI ₃ perovskites and PbI ₂ thin films (which was obtained by high temperature annealing the perovskite thin films), (d) Absorption spectra of a MAPbI ₃ perovskite thin film kept at ambient conditions for 48 hours.....	155
4.6.	(a)-(c) SEM microstructures of MAPbI ₃ perovskite thin films with different magnifications, (d) EDX spectra of the same sample illustrating the elemental composition.....	156
4.7.	X-ray diffraction pattern obtained for a MAPbI ₃ perovskite thin film synthesized in this study. Phase (tetragonal) and the substrate peaks were identified by comparison with the literature reports.....	157
4.8.	AES spectra obtained for (a) MAPbI ₃ perovskite thin films, (b) PbI ₂ thin films (obtained by UHV annealing the MAPbI ₃ perovskite thin film), (c) ITO substrate (obtained by removing the PbI ₂ film by Ar ⁺ sputtering).....	158
4.9.	Schematic representation of the cross-sections of ideal structure (a) and the real structure (b) of the perovskite thin films grown on ITO coated glass slides.....	160

4.10.	(a) Thermal desorption profiles of detected mass fragments as a function of surface temperature during a linear thermal ramp (1.6 K/s) of pristine MAPbI ₃ perovskite thin films at UHV, (b) AES before and after the thermal degradation of the perovskite thin films.....	162
4.11.	(a) TDS traces of 2.0 L of CO ₂ adsorbed MAPbI ₃ perovskite thin films (dotted lines are the desorption profiles from sample holder/ background), (b) AES of perovskite thin film before and after CO ₂ adsorption experiments.....	167
4.12.	Computational models of MAPbI ₃ perovskites forming (a) H ₂ CO ₃ -H ₂ O van der Waals complex, (b) the defect structure with embedded HCO ₃ ⁻ and H ₃ O ⁺ (models were prepared by Yulun Han).....	168
4.13.	Carbon dioxide adsorption on the substrate ((a) CO ₂ TDS on PbI ₂ , (b) CO ₂ TDS on ITO, (c) AES of PbI ₂ thin film before and after CO ₂ adsorption, (d) AES of the ITO substrate before and after CO ₂ adsorption).....	170
4.14.	(a) Desorption profiles of formic acid fragments adsorbed (χ =20.0 L of formic acid) on perovskite thin films (solid lines) and silica thin films (dotted lines) as a function of surface temperature, (b) desorption profiles of formic acid fragments for a second dose of 20.0 L of formic acid after the 1 st TDS experiment, (c) comparison of the gas phase mass scan (only four selected masses were compared) of formic acid (bottom panel) with the integrated TDS peak intensities of collected mass fragments of desorbed formic acid fragments from perovskite thin film (top panel), (d) comparison of the AES spectra of perovskite thin films before and after thermal stability test (top panel) with the AES spectra of perovskites before and after formic acid TDS (bottom panel).....	172
4.15.	Formic acid TDS curves as a function of exposure on (a) PbI ₂ thin films, (b) ITO substrates.....	173
4.16.	Possible adsorption/ desorption pathways of formic acid on MAPbI ₃ perovskite thin films proposed based on the detected desorption fragments (detected fragments are highlighted in blue color).....	178

LIST OF ABBREVIATIONS

AACVD.....	Aerosol-assisted chemical vapor deposition.
AES.....	Auger electron spectroscopy.
AO.....	Atomic orbitals.
CMA.....	Cylindrical mirror analyzer.
CVD.....	Chemical vapor deposition.
DDS.....	Direct desulphurization.
DFT.....	Density functional theory.
DMF.....	Dimethylformamide.
DRS.....	Diffuse reflection spectroscopy.
EDX.....	Energy dispersive x-ray spectroscopy.
ELS.....	Energy loss spectroscopy.
ER.....	Eley-Rideal.
ESCA.....	Electron spectroscopy for chemical analysis.
FC.....	Faraday cup.
HDS.....	Hydrodesulphurization.
HREELS.....	High-resolution electron energy loss spectroscopy.
HYD.....	Hydrogenation followed by desulphurization.
IRAS.....	Infrared reflection absorption spectroscopy.
ITO.....	Indium-doped tin oxide.
LASER.....	Light amplification by stimulated emission of radiation.
LEED.....	Low energy electron diffraction.
LH.....	Langmuir-Hinshelwood.
MAPbI ₃	Methylammonium lead iodide.
MO.....	Molecular orbitals.
NIR.....	Near-infrared.
QMS.....	Quadrupole mass spectrometer.
RGA.....	Residual gas analyzer.

SAC.....Single-atom catalysis.
SEM.....Scanning electron microscopy.
STM.....Scanning tunneling microscopy.
TDS.....Thermal desorption spectroscopy.
TOF.....Time of flight.
TPD.....Temperature programmed desorption.
UHV.....Ultra-high vacuum.
UV-Vis.....Ultraviolet-visible spectroscopy.
XPS.....X-ray photoelectron spectroscopy.
XRD.....X-ray diffraction.
SBU.....Secondary building unit.
ZSM-5.....Zeolite socony mobile-5.

LIST OF SYMBOLS

aLattice constant.
a_1, a_2Real space lattice parameters.
a_1^*, a_2^*Reciprocal space lattice parameters.
dPath difference/ collision cross-section/ nozzle diameter.
eElectronic charge.
E_0Defect free desorption energy of the adsorbate.
E_FFermi level.
E_aActivation energy.
E_{che}/E_cActivation energy for chemisorption.
E_d/EDesorption energy.
E_{def}Difference between the calculated binding energy (E_d) and E_0 .
E_iImpact energy.
E_kKinetic energy of electrons.
E_{phy}/E_pActivation energy for physisorption.
E_vVacuum level.
G_{hk}Reciprocal lattice vectors.
hPlanck's constant.
kScattered wavevector.
k_0Incident wavevector.
k_dDesorption rate constant.
$K, L_1, L_{2,3}$Electronic energy levels.
LLangmuir.
MMach number.
m_eMass of the electron.

nOrder of diffraction/ kinetic order of the desorption reaction.
 N_AAvogadro's constant.
 $N(E)$Electron count.
 pNozzle pressure.
 PTransmitted radiation intensity/ pressure.
 P_0Initial pressure/ incident radiation intensity.
 P_{sat}Saturation pressure.
 RUniversal gas constant.
 $r(\theta, T)$Desorption/ reaction rate.
 S_0Initial adsorption probability.
 tTime.
 TAbsolute temperature/ transmittance.
 T_PTDS peak temperature.
 T_SSurface temperature.
 VAcceleration voltage.
 ΔEAbsolute energy resolution.
 βHeating rate.
 λ_eDe-Broglie wavelength of electrons.
 θAngle of diffraction/ surface coverage.
 λMean free path/ wavelength.
 νFrequency/ Arrhenius pre-exponential factor.
 χGas exposure.
 YAdsorbate-adsorbate interaction factor/ heat capacity ratio.

1. INTRODUCTION

Understanding the fundamental surface properties of two-dimensional materials such as silica, zeolites, and lead halide perovskites is the focus of this dissertation, which involves synthesis and characterization of the model surfaces, surface modification, and screening for chemical and physical properties utilizing advanced surface analytical techniques under ultra-high vacuum conditions for a variety of applications such as heterogeneous catalysis, semiconductor technology, solar cells, biosensors etc.

Surface science is a broad research field ranging from biological membranes to the semiconductor industry and heterogeneous catalysis, that studies chemical and physical processes occurring at the interfaces, such as solid-gas, liquid-gas, solid-liquid etc. Generally, a surface can be identified as the uppermost layer of a physical object or space, which is also defined as an existing interface in a system with a sudden and unexpected change in the materials properties such as crystalline structure, the orientation of the crystals, chemical composition, density etc. These properties can be varied depending on the preparation method of the surface. One way to visualize a surface is to cut through a bulk crystal, along a crystallographic plane. As a result, surface atoms will exhibit unsaturated valences due to uncoordinated sites, and hence show different electronic structures and chemical properties compared to the bulk. Generally, there is a tendency of such a surface to lowering their energy by reacting with species in contact with the surface by chemical bond formation. In order to study the intrinsic properties of that kind of reactive surfaces, contamination free high vacuum conditions are necessary. Surface science deals with both chemical and physical properties of the surfaces including electronic structures, geometry, chemical reactivity, vibrational properties etc.¹⁻²

Heterogeneous catalysis is one of the main aspects of surface science studies, where gas-surface interactions and chemical reactions on the surfaces are studied extensively. The term heterogeneous catalysis refers to catalytic processes where the reactants and the catalysts are in different phases. The majority of industrial heterogeneous catalysts are in the solids phase while the reactants are in the gas or liquid phase. Typically, reactive metal particles supported on porous solid materials with a large surface area are used as catalysts in many industrial processes and day-to-day applications such as The Haber process for ammonia synthesis, catalytic oil refining, catalytic converters in car exhausts for controlled emission of toxic gases, fuel cell related applications etc. In most of the heterogeneous catalytic processes, in which the catalyst is in the solid phase and reactants in the gas/ liquid phase, reactions occur on the surface of the catalyst. The catalytic surface is not only lowering the activation energy of the reaction by providing low energy pathways but also acts as a medium, bringing the reactants together. Therefore, understanding the physical and chemical properties of these catalytic surfaces are vitally important.

1.1. Model catalysis

Metal particles supported on porous supports have been successfully used as heterogeneous catalysts in the past few decades. Noble metals such as Pt, Au, Pd, and Ru are the most widely used catalysts. These actual catalytic systems are extremely complicated due to several reasons. It is difficult to obtain uniform particle size distributions with identical active sites in the real-world catalytic systems. There can be defects, dangling bonds, and several types of deformations in the catalyst and the catalytic support compared to the ideal catalytic system which catalyzes the desired reaction. Therefore, studying the industrial catalytic systems to understand the mechanistic insights of the catalytic processes are somewhat difficult. On the other hand, it is essential to understand how actually a catalyst works, what are the active sites for the reactions, effects of the support and

also the catalytic mechanisms, in order to improve the efficiency of the process. The concept of model catalysis is widely used to observe these key features of heterogeneous catalysis with fewer complexities.

Model catalysts are somewhat simpler versions of the actual catalytic systems, which are typically supported metal nanoparticles/ clusters on metal/ metal oxide/ semiconductor single crystalline surfaces, mimicking the actual catalytic systems. This enables the molecular level understanding of the catalytic surfaces, how the reactants interact with the catalyst (adsorbate-adsorbent interactions), adsorbate-adsorbate interactions on the catalytic support and even the catalytic mechanisms. With the development of ultra-high vacuum-based surface spectroscopic techniques such as AES, LEED, XPS, HREELS etc., in the past few decades, and the development of surface imaging techniques like STM, SEM etc., the ability of molecular-level understanding of surfaces improved progressively. With the understanding of the catalytic systems, activity, selectivity, specificity, and stability of the actual catalytic systems were improved significantly.

At the early stages of model catalysis research, metal single crystals were studied largely due to simplicities. Fundamentally important reactions such as carbon monoxide oxidation³⁻⁴ on precious metals (Pt, Pd, Ru) to improve the 3-way catalytic converter systems in automobile exhaust, carbon monoxide reduction to methane by Ni,⁵ which is an important step in Fischer-Tropsch synthesis, ammonia synthesis on single crystalline Fe,⁶ are some example systems. As the advancement of the spectroscopic and available synthetic methods such as molecular beam epitaxy, supported metal clusters on single crystalline metal oxide surfaces initially, and synthesized metal/ semiconductor oxide surfaces in the recent past were utilized as model catalysts. Supported metal catalysts on planar metal oxide surfaces are closer to the real catalytic systems compared to the single-crystalline metal catalysts, which enables the study of particle size

effects, stability of the catalyst etc. Cleaving the bulk oxide single crystal and synthesis of the desired oxide thin film on another substrate are the common techniques for the substrate preparation.³ Former is a more straightforward method with a limited number of choices while the latter is the most common method to form the model catalytic supports with available methods such as chemical vapor deposition and molecular beam epitaxy, enabling a variety of systems. At the early stages of the thin film growth, amorphous thin films and polycrystalline thin films were more common. Currently, several number of single crystalline metal/ semiconductor oxide thin film synthetic methods are known, which enables the study of more uniform and well-defined catalytic systems, leading to a more accurate understanding of reaction mechanisms. Oxide thin films such as SiO₂, Al₂O₃, TiO_x, MgO, NiO etc.,^{3, 7-9} were extensively studied as the catalytic supports.

When relating the model catalytic studies to the actual catalytic systems, surface scientists should overcome two major barriers called pressure gap and materials gap. The former is related to the difference between the experimental conditions and the actual catalytic operating conditions. When dealing with a model catalyst employing surface science analytical tools, UHV conditions are necessary (see section 2.1 for more details). On the other hand, industrial catalysts are operating at elevated pressures, typically higher than 1 atm. To overcome the pressure gap related to UHV-based model studies, there are attempts that utilize high-pressure reactors connected to UHV systems, which enables the study of model catalytic systems under real operation conditions. Also, industrial catalysts have highly porous catalytic supports and different sizes of metal clusters with large surface areas. Therefore, studying the support effects towards the catalytic reaction and the particle size effects are very important. Early model studies with single crystalline surfaces do not allow the investigation of the above effects. Therefore, materials gap between the real-world

catalysts and the model systems were high. With the planer oxide thin films as the catalytic supports mimicking the real supports, and with the development of the deposition/fabrication technique which allow the control over the particle size distributions such as electron beam lithography, scanning probe lithography, mass selected soft-landing techniques¹⁰ etc., the material gap between the real systems and the model catalytic systems have been reduced significantly. One of the supplementary focuses of this dissertation is to study the support effects of single crystalline silica thin films towards thiophene hydrodesulfurization.

With the advancements in the field of model catalysis, new concepts have been introduced to obtain more homogenized heterogeneous catalysts, which provides more activity and selectivity, closer to the homogeneous catalysis. One of the new frontiers of heterogeneous catalysis is to reduce the size of the nanoparticles to its extreme limit, single atom size to obtain high activity, selectivity, and specificity, known as single atom catalysis (SAC).¹⁰⁻¹¹ Reduction of the particle size directly related to the improvement of the catalytic performance. For instance, chemically inert gold exhibits exceptional catalytic activity when the particle size is reduced to the nanometer range. Also, recent studies show that sub-nanometer size particles are more catalytically active than their nanometer size counterparts. Even sub-nanometer size particles may have multiple active centers which lead to heterogeneity of the catalyst. Multiple active centers may catalyze undesired side reactions, which reduces selectivity. Therefore, catalysts with well-defined single active centers are necessary to improve the performance of the catalyst with a proper understanding of the catalytic mechanisms. SAC enables the maximum use of expensive metal atoms such as Pt, Au, Pd, Ru which are the most widely used active catalysts in heterogeneous catalysis. One of the main goals of this dissertation work is to synthesize a uniform catalytic support, providing well-defined binding sites to the catalyst particles to form a more homogenized heterogeneous catalyst.

1.2. Surface structures

In order to go forward with the model catalytic systems, a well-ordered surface is an essential requirement and therefore, understanding the different structures of the surfaces are vitally important. With the development of the low energy electron diffraction (LEED) as a surface crystallographic technique (see Section 2.3), different types of structural models and notations have been introduced to understand the different periodic patterns of the surfaces. The periodicity of a crystalline surface is defined by the lattice, which is the simplest periodic arrangement of the points (unit cells) in the space. The simplest repeat unit of the periodic structure is known as the unit cell.¹²

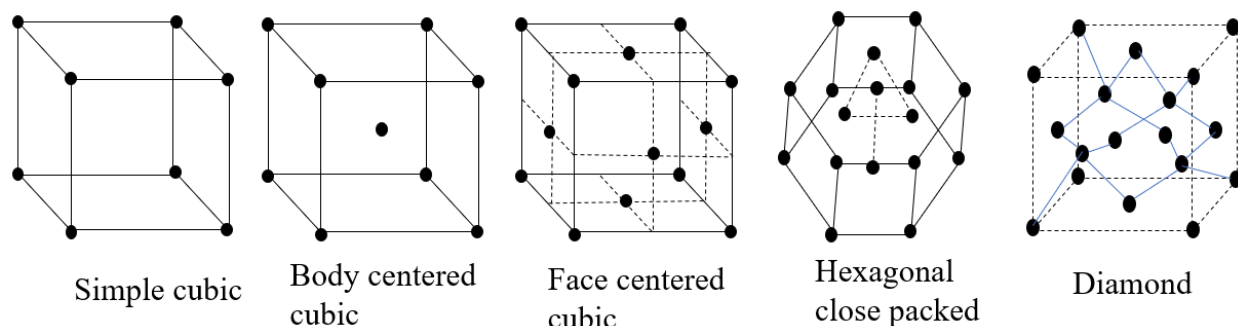


Figure 1.1. Commonly encountered basic unit cell structures (subcategories of cubic and hexagonal unit cell structures)¹²

There are 32 different possible crystal structures according to the unit cell symmetry, in which, eleven types can be distinguishable employing X-ray crystallography. Among that, seven basic unit cell types can be identified, which are cubic, tetragonal, hexagonal, trigonal, orthorhombic, monoclinic and triclinic.¹² Cubic and hexagonal structures are the most commonly encountered, which are highly symmetric and relatively simple to study. Cubic and hexagonal structures can be further categorized into simple cubic, body-centered cubic, face-centered cubic, hexagonal close-packed, and diamond.¹² Typically, the two-dimensional surface structures can be

obtained by cutting through the bulk three-dimensional crystal along a crystal plane. By changing the cutting angle, different surface structures can be obtained with the same bulk crystal, as depicted in Figure 1.2.

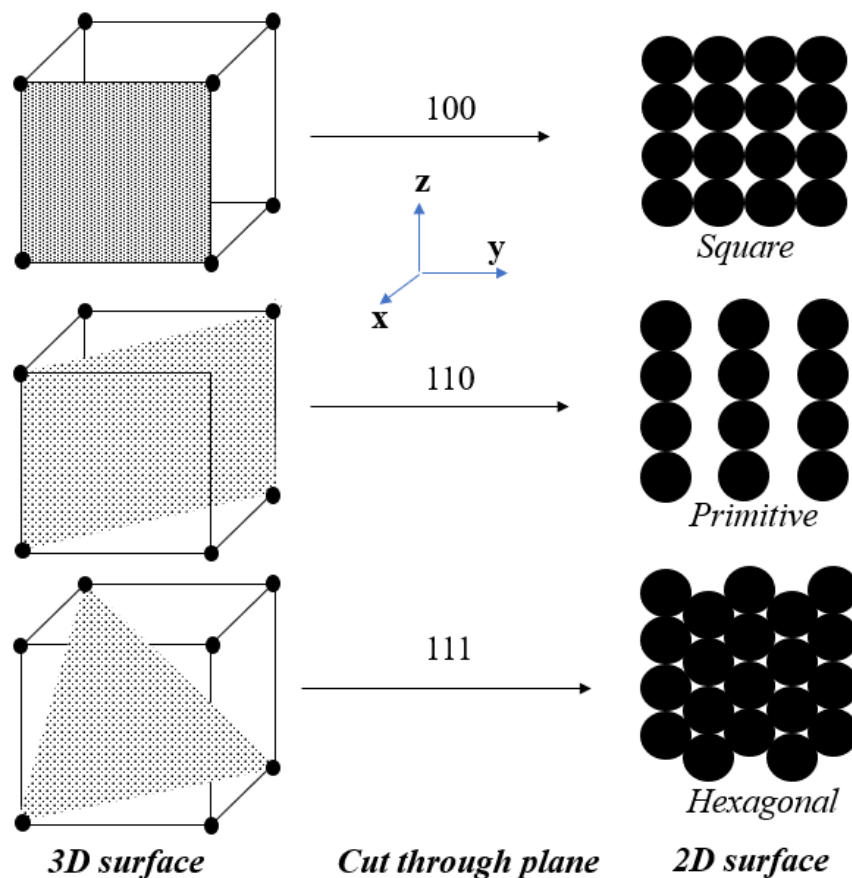


Figure 1.2. Different surface structures obtained by cutting through various planes in the simple cubic structure

When it comes to the surfaces with two-dimensional periodicity, there are five types of major surface structures which are square, primitive, central rectangular, hexagonal and oblique (see Figure 1.3). By looking at the surface unit cell structures, some general structure-activity relationships can be obtained. For instance, as depicted in Figure 1.3, the coordination numbers for the 100 and 111 surfaces are 4 and 6 respectively along the surface. Typically, the higher the coordination number, lower the reactivity of the surface and vice-versa.

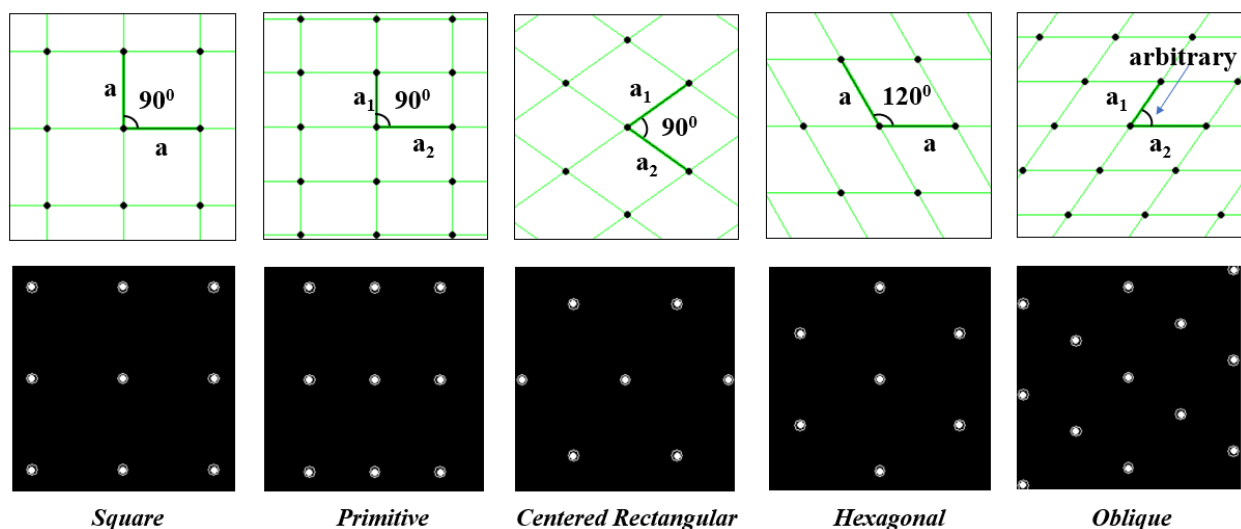


Figure 1.3. 2D surface lattice structures (top) and corresponding LEED patterns simulated using LEEDpat version 1.0 (bottom)¹³

In the surface crystallography, adsorbed species on single-crystal surfaces with the long-range order are commonly encountered, which are known as crystalline overlayer structures. Supported ultra-thin oxide films, reconstructed surfaces with adsorbates are some examples, which are typically observed in model catalysis related applications. Therefore, understanding the symmetry properties and unit cell arrangements of these overlayer structures are essential.

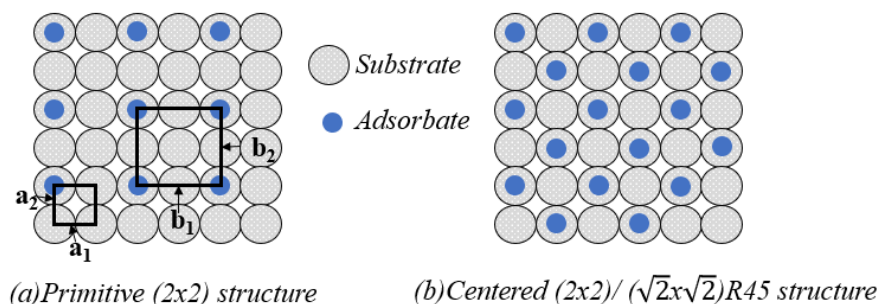


Figure 1.4. Simple adsorbate overlayer structures on fcc(100) surface

There are two commonly used notation types to explain the overlayer structures that describes the order of the adsorbate layer relating its translational lattice vectors to the underlying substrate lattice vectors. The simplest method is known as Wood's notation,¹⁴ which is only

applicable when the symmetries of the substrate and the adsorbate are closely related. If the substrate and the adsorbate layer are explained by the translational vectors a_1 , a_2 and b_1 , b_2 respectively, the overlayer is given by $(|b_1|/|a_1| \times |b_2|/|a_2|)$, where $b_1=2a_1$ and $b_2=2a_2$ for a (2×2) structure (see Figure 1.4). For instance, $p(1 \times 3)$ oxygen reconstructed surfaces and $c(2 \times 2)$ overlayers of silica thin films on Mo(112) substrates are commonly encountered in this research project (see section 3.3 for more details).

In the second notation type, overlayer lattice vectors are independently represented by linear combinations of underlying lattice vectors, in matrix form. $b_1 = G_{11}a_1 + G_{12}a_2$ and $b_2 = G_{21}a_1 + G_{22}a_2$ when a_1 , a_2 and b_1 , b_2 are translational lattice vectors of the substrate and the adsorbate respectively. G_{11} , G_{12} , G_{21} and G_{22} are coefficients of a matrix G , $G = \begin{bmatrix} G_{11} & G_{12} \\ G_{21} & G_{22} \end{bmatrix}$ when the substrate and the adsorbate lattices are related by $\begin{pmatrix} b_1 \\ b_2 \end{pmatrix} = G \begin{pmatrix} a_1 \\ a_2 \end{pmatrix}$.¹⁵

1.3. Surface deformations

Typical single crystalline surfaces are obtained by cleaving the respective 3D crystal along a 2D plane under vacuum conditions. The surface atoms have unsaturated valences and hence higher energy compared to the bulk crystal. Therefore, adatoms (adsorbed atoms) on the surfaces is a common type of defect even for single crystals at high vacuum conditions. Even at UHV, there can be trace amounts of gases such as H_2O , CO_2 etc., and these impurity gases may be adsorbed on reactive surfaces dissociatively to form adatoms.

When it comes to poly-crystalline surfaces, there can be different types of surface deformations such as steps, kinks, terraces, holes etc. In model catalysis, poly-crystalline surfaces such as graphite are commonly used as a substrate for the growth of metal/ metal oxide thin films and metal cluster deposition. These defects are highly reactive and act as nucleation centers for the

growth of the metal clusters (catalyst), which sometimes beneficial in model catalysis related applications. Even the deposited metal clusters can have different types of defects such as kinks, tilt boundaries, grain boundaries etc., which are responsible for the high reactivity of these deposited metal clusters.

1.4. Gas-surface interactions

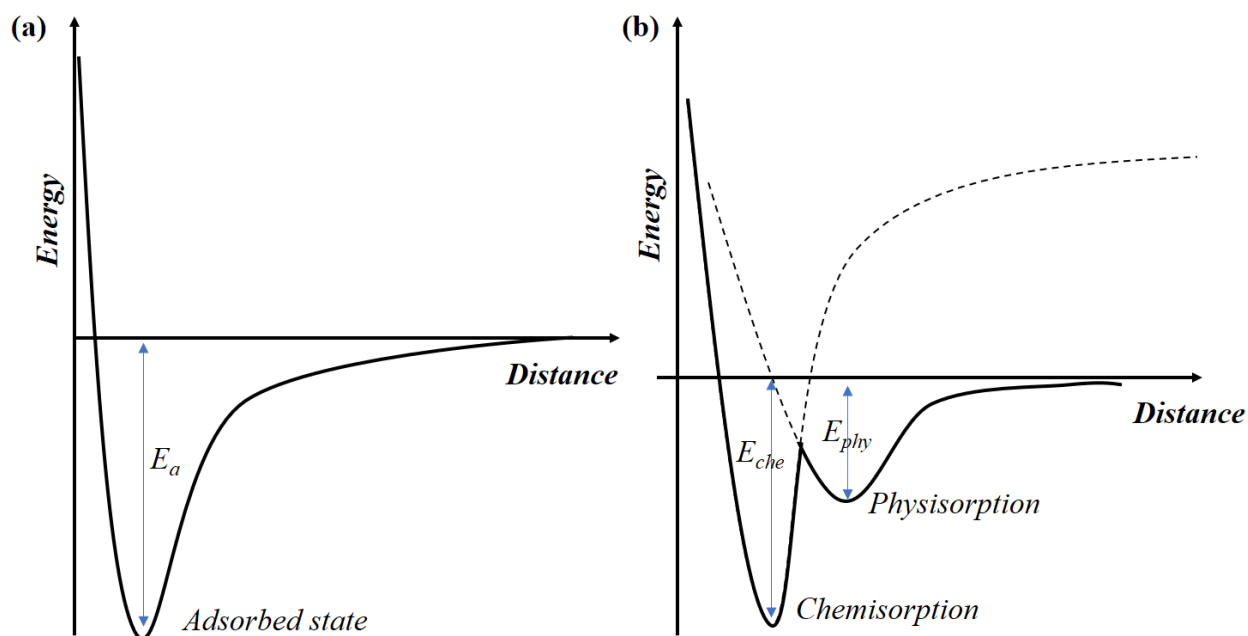


Figure 1.5. Variation of the potential energy of an adsorbate as a function of the distance from a surface, as the adsorbate approaches the surface.

In any kind of gas-surface reaction, adsorption is the initial process, which can be defined as the adhesion of the gaseous atoms/ ions/ molecules on a surface. When the adsorbate is approaching the surface (adsorbent), initially it will experience an attractive interaction. As the adsorbate approaches, the attractive interaction will be increasing with the distance first and go through a maximum. Then it will experience a repulsive interaction as it getting closer to the surface. This phenomenon is depicted in the Lenard-Jones potential energy diagram in Figure 1.5 (a).

As indicated in the potential energy surface, there is no potential barrier for the adsorption process in this example and therefore, as the adsorbate approaches, it will reach the minimum potential energy and trapped in there, which can be defined as adsorption. The depth of the potential well (E_a) depends on the types of interactions between the adsorbate and the adsorbent.¹ Depending on the strength of the adsorption (depth of the potential well) the process can be further categorized into physisorption and chemisorption.

Physisorption refers to the van der Waals interactions between the adsorbate and adsorbent in which the electronic structures of the involved species are barely perturbed. Any species can be physisorbed on a surface depending on suitable experimental conditions such as suitable temperature, pressure etc. No activation energy is necessary for physisorption and small heat of adsorption, large adsorbate-adsorbent bond distances are characteristic features of physisorption.¹⁶

Chemisorption refers to a chemical bond formation between adsorbate and the adsorbent during the adsorption process. Perturbation of the electron clouds of the involved species due to the strong covalent bond formation and hence large heat of adsorption, short bond distances are characteristic features.¹⁷ Different types of chemisorption such as activated/ non-activated chemisorption and dissociative/ molecular chemisorption are discussed in section 2, under the section 'Molecular beam scattering'.

There are different types of catalytic (surface involved) reaction mechanisms observed by the surface scientists depending on the initial state of the reactants involved. Understanding the reaction mechanisms are vitally important to improve the heterogeneous catalytic processes. For unimolecular decomposition reactions, the reactant gases are simply adsorbed on a specific adsorption site followed by decomposition to form the desired product. Typically, these type of decomposition reactions follows Michaelis-Menton kinetics as of in the enzyme-catalyzed

biological reactions. For bimolecular reactions on the surfaces, there are two major types of mechanisms observed, which are named as Langmuir-Hinshelwood (LH) and Eley-Rideal (ER) mechanisms. Most of the bimolecular surface reactions found to be following the former type, in which the reactants adsorbed on the neighboring sites of the surface undergo the reaction to form the product or adsorbed species diffused on the surface and react to form the products.^{1, 17-18} In ER type reactions, one species is adsorbed on the surface and the product is formed by the collision between the adsorbed species with a gas phase species, which somewhat resembles a gas-phase reaction.^{1, 18-19}

Distinguish the type of surface reaction mechanism is a complex process, which involves a lot of data acquisition. In the case of LH mechanisms, the reactants are fully thermalized before the product formation. Therefore, the energy distribution of the desorption products follows a Boltzmann distribution typically. The impact angle of the reactants and the desorption angle of the products with respect to the surface normal are not correlated in LH type reactions. Also, the reaction times are in the range of micro to milliseconds, that can be measured easily by simple kinetic experiments. ER type reactions are much faster than LH reactions, which occur in nano to femtosecond time scales. The angular distributions and the energy distributions of the ER reactants and products are correlated, contrast to LH mechanisms. Therefore, by measuring the reactant-product energy distributions, angular distributions, and reaction rates, the type of reaction mechanism can be distinguished.¹

Understanding the surface reaction kinetics and dynamics is essential to figure out the reaction mechanisms. Reaction kinetics is generally defined as the study of the rates of the chemical reactions, whereas the study of the energy transfer processes is referred to as reaction dynamics. In this dissertation, thermal desorption spectroscopy (TDS) and molecular beam

scattering techniques are utilized to understand the kinetics and dynamics of several surface processes. More details on reaction kinetics and dynamics and specific methods employed in this dissertation are discussed in section 2, under the sections ‘Thermal desorption spectroscopy’ and ‘Molecular beam scattering’.

2. EXPERIMENTAL TECHNIQUES

Majority of the experimental techniques utilized in this research are ultra-high vacuum surface analytical techniques. This section introduces the experimental techniques following the general outline, introduction and historical background, principles of the technique, specific experimental setup employed in this study, and specific analysis methods etc.

The elemental and chemical composition of the samples were identified employing Auger electron spectroscopy (AES) and X-ray photoelectron spectroscopy (XPS) mainly. Crystallographic structures of the sample surfaces were characterized mainly by low energy electron diffraction (LEED). Temperature programmed desorption (TPD) and molecular beam scattering techniques were extensively used to study gas-surface adsorption/ reaction kinetics and dynamics of several surface processes. All above-mentioned techniques are housed in two UHV chambers in the Burghaus laboratory, North Dakota State University.

Other than above techniques, UV-Visible absorption spectroscopy, scanning electron microscopy (SEM), energy dispersive X-ray spectroscopy (EDX), X-ray diffraction (XRD) were utilized as the supplementary surface characterization techniques, which are available in the Department of Chemistry and Biochemistry, and Research and Technology Park, North Dakota State University.

2.1. Ultra-high vacuum

2.1.1. Introduction

The SI unit of pressure is “Pascal”, which is defined as Newtons of force acting on a square meter of surface area ($1 \text{ Pa} = 1 \text{ Nm}^{-2}$). Normal atmospheric pressure is 101325 Pa, which can also be represented in different types of units such as ‘bars’ and ‘torr’ (1013 millibars (mbar) or 760 torr). Millibars and torr units are the most commonly used units in surface science to express

pressure. 'Vacuum' is a term used to describe a space or region that has a significantly low pressure compared to the atmosphere. Rough (low) vacuum ($1\text{-}10^{-3}$ mbar), medium vacuum ($10^{-3}\text{-}10^{-5}$ mbar), high vacuum ($10^{-5}\text{-}10^{-8}$ mbar) and ultra-high vacuum (pressure $<10^{-9}$ mbar) are few major categories of vacuum defined according to the range of pressure. The normal atmosphere has wet air including water vapor, N_2 , O_2 and other residual gases such as CO_2 , CO , H_2 etc. Roughing remove about 15-25% of the wet air from the original atmosphere, but still, the distances between the gaseous particles are very small and hence the viscous flow of particles is typical. When it comes to high vacuum, random motion or molecular flow of particles is evident due to the higher mean free path of particles as the pressure decreases. Gases originate from the walls of the vacuum chamber (adsorbed species) and the gas composition is generally 80% of H_2O and 20% of other residual gases. At ultra-high vacuum (UHV) conditions, primary gas source is H_2 ($>99\%$) and trace amounts of other residual gases such as H_2O , CO_2 , CO , and N_2 may be observed depending on the cleanliness of the vacuum chambers and the types and pumping speeds of pumps that are utilized to maintain the vacuum.²⁰

Majority of surface science model studies require UHV conditions to maintain atomically clean environments. According to the definition of Langmuir (L), which is the unit used in the surface science to measure the gas exposure, only one second of gas exposure at the pressure of $\sim 1 \times 10^{-6}$ torr is adequate for a particular surface to entirely covered with a monolayer of a gas. In order to have atomically clean environments and also to maintain a contamination-free environment throughout the course of the experiments, UHV conditions are necessary. Also, most of the surface analytical techniques utilize low energy electron or ion beams as probes. After bombarding the surfaces with those low energy electron/ ion beams, backscattered electrons, emitted secondary electrons, scattered ions, etc., are typically detected. In order to avoid any

inelastic collisions or gas phase scatterings of this probe or detected particles, UHV conditions are essential. This is because of the reciprocal correlation between the mean free path and the respective pressure of particles. According to the kinetic theory of gases, mean free path (λ) is defined as the average distance traveled by a particle between successive collisions, which is given by, $\lambda = \frac{RT}{\sqrt{2}\pi d^2 N_A P}$ (R- gas constant, T- temperature, N_A - Avogadro's constant, d- collisional cross-section, P- pressure).²¹ According to the equation, mean free path increases as the pressure decreases. For instance, at room temperature, mean free path of air in normal atmospheric pressure is about 68 nm, which increases up to 1-10⁵ km at UHV,²² which is larger than few orders of magnitude of a typical vacuum chamber used in surface science experiments. Furthermore, UHV is a necessary condition to maintain high voltages without breakdown or glow discharges in surface analysis experiments.

2.1.2. Generation of ultra-high vacuum

A combination of different types of pumps can be used to achieve and maintain UHV conditions. Type and the size of the pump, pumping speed, the number of pumps etc., are determined by the size of the vacuum chamber and the type of the experiments. Initially, roughing pumps (mechanical pumps) are used to rough out the vacuum chambers and achieve low vacuum conditions prior to start the turbomolecular pumps or diffusion pumps. Turbomolecular pumps can be safely started when the pressure reached below 10⁻² mbar. Most of the modern vacuum systems are equipped with oil-free turbomolecular pumps that can achieve pressure up to 10⁻¹¹ mbar with large pumping speeds. Turbomolecular pumps have high-speed rotating turbine blades, that can transfer momentum to the colliding residual gases and eventually pump them out. These pumps are most suitable for heavy gases and do not work well with lighter gases such as hydrogen. The requirement of the backup pumps (rotary pumps), vibration effects and high cost are some other

disadvantages of turbomolecular pumps. To reduce hydrogen background in the vacuum chamber, getter pumps such as Titanium sublimation pump can be used. Ion getter pump is also a type of sublimation pump, which is commonly utilized to maintain UHV conditions with the vibration-free environment. These type of getter pumps do not require backup pumps, but the lower pumping speeds and bulky designs limit the applications.

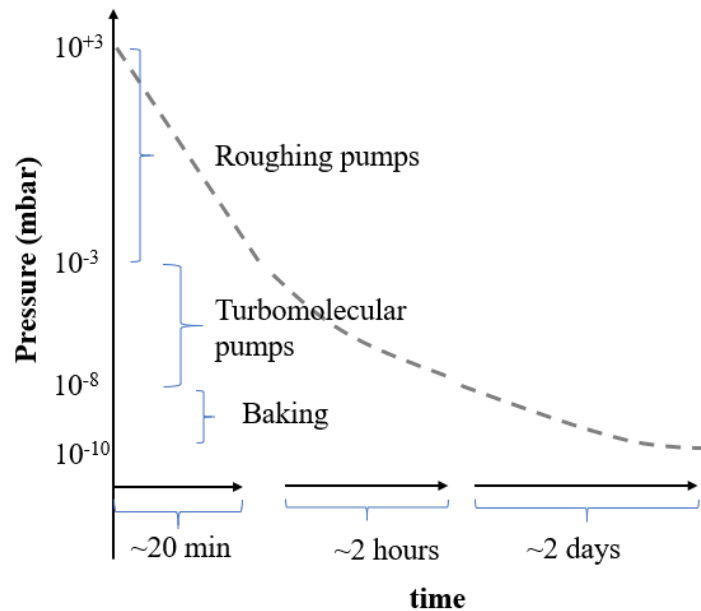


Figure 2.1. Variation of the pressure in a typical vacuum chamber with time, during the initiation of the vacuum.

As depicted in Figure 2.1, within ~ 2 hours of pumping, $\sim 10^{-8}$ mbar pressure can be achieved with a proper combination of turbomolecular and roughing pumps. But, this type of vacuum is not good enough for surface science model studies. To achieve UHV conditions, a process called baking is applied to the vacuum chambers typically. In this process, the surface temperature of the vacuum chamber is increased up to $150\text{-}200$ °C using heating tapes wrapped around the vacuum chamber or using a heating tent. At high temperatures, adsorbed residual gases on the inner surface walls of the vacuum chamber tend to desorb faster and hence they will be

pumped out. Therefore, by baking the chamber, necessary UHV conditions can be achieved eventually.

2.1.3. UHV experimental setup

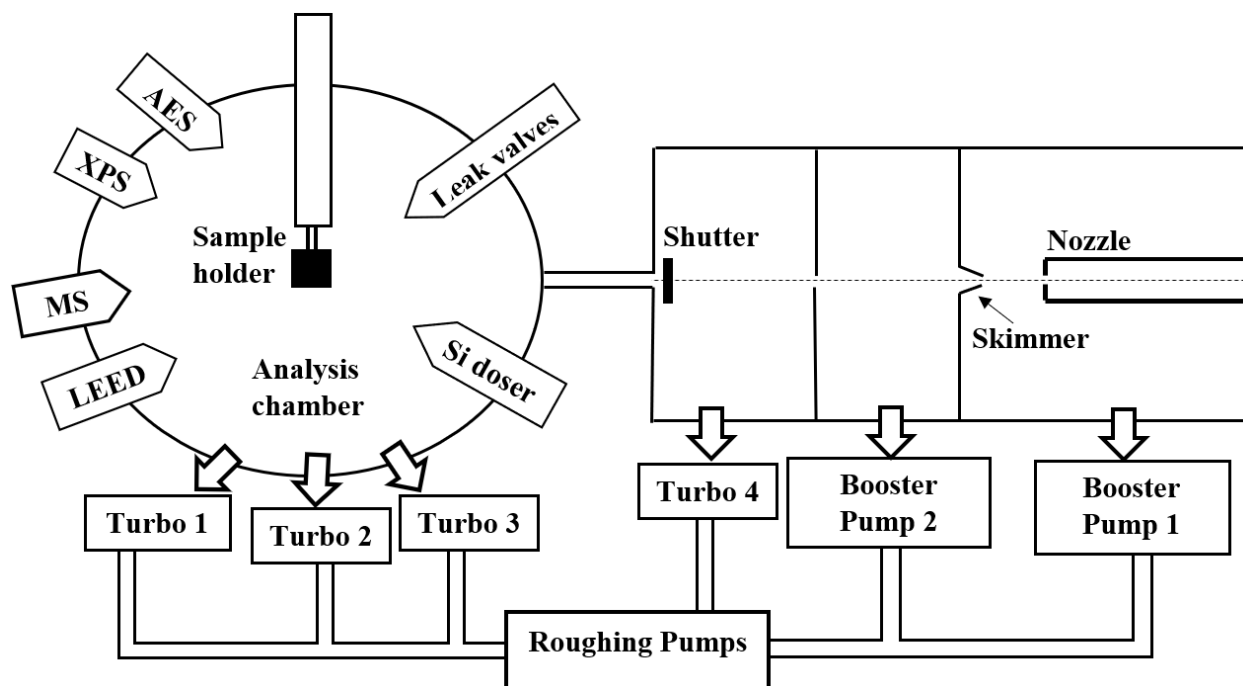


Figure 2.2. Schematic diagram of the UHV experimental setup utilized in this research

Burghaus group at North Dakota State University has two main UHV chambers utilized with several surface analytical techniques. All the UHV related projects described in this dissertation were carried out in either of those vacuum chambers. One chamber is equipped with low energy electron diffraction (LEED) as the major characterization technique, which will be called as “LEED chamber” hereon, and the other chamber is designed to carry out molecular beam scattering studies, which will be called as “beam scattering chamber” hereon. The LEED chamber is pumped by two Varian turbomolecular pumps with pumping speeds 550 l/s and 60 l/s (small turbo is attached to the sample manipulator) and an ion-getter pump, which are backed by a Leybold D65B rotary pump. This chamber is also equipped with an SRS RGA 100 residual gas

analyzer, SPECS ErLEED 3000D LEED/ AES system, a sputter gun and a couple of gas dosing needles. Sample/ substrate temperature can be controlled by liquid nitrogen cooling (up to 90 K) or electron beam heating (up to 2000K). A thermocouple (W–80%Ni /W–20%Cr) spot welded to the back side of the substrate was used to measure the sample temperature. The sample holder is attached to an XYZ manipulator, which allows the movement of the sample along X, Y and Z axis, and also rotation around the Z axis.

The beam scattering chamber has four different pumping stages, in which the first three pumping stages are specifically designed for the generation of supersonic molecular beams. A detailed description of these three pumping stages is included in section 2.5.2. The fourth stage is the analysis chamber, which is pumped by two Varian turbomolecular pumps with pumping speed 1000 l/s and 550 l/s, a Leybold 360 l/s turbomolecular pump, an ion-getter pump, and a Ti sublimation pump, backed by a Leybold D65B rotary pump. The analysis chamber is also equipped with a CMA based AES/ XPS system, two residual gas analyzers (SRS RGA 100) for TDS experiments and time of flight experiments, a sputter gun and a couple of gas dosing needles. A similar kind of sample holder with an XYZ manipulator is attached to the beam scattering chamber, as in the LEED chamber. An integrated schematic diagram of both LEED and beam scattering chambers are shown in Figure 2.2.

2.2. Auger electron spectroscopy

2.2.1. Historical background

Auger electron spectroscopy (AES) is a powerful surface analytical technique, which was developed in the 1960s with the development of the commercial ultra-high vacuum systems. This technique is based on the Auger process, discovered independently by two different scientists, Pierre Auger, and Lise Meitner in mid-1920s. Initially, Auger transitions were used to explain the

anomalies in the X-ray spectroscopic data. Later, this technique was independently developed as a surface probing tool to identify elemental/ chemical compositions.²³

2.2.2. Principles of AES

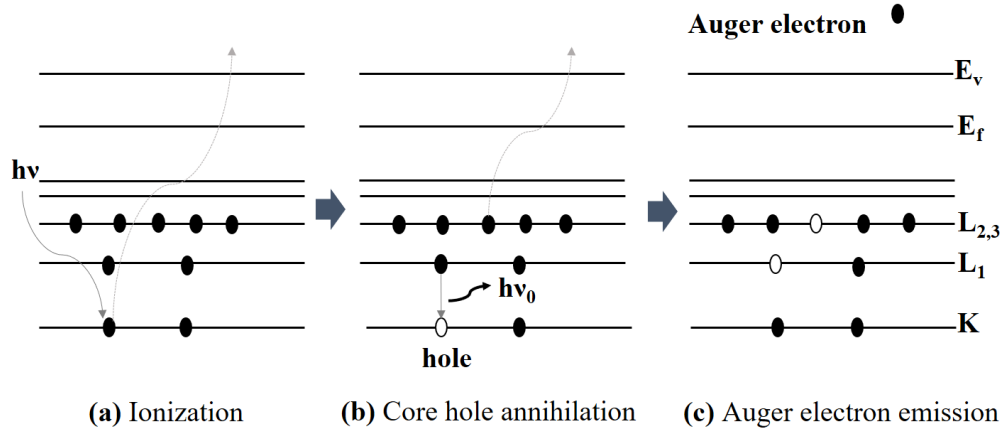


Figure 2.3. Auger emission process²⁴

Auger process is a secondary electron emission process from an excited atom, due to inter-state transitions. When an atom is excited by an electron beam or an X-ray beam with sufficient energy, it can be ionized by removing a core electron, leaving a core hole (Figure 2.3 (a)). The excited atom tends to relax either by X-ray emission or non-radiative Auger electron emission. In Auger emission process, the excited atom will be stabilized by the relaxation of an electron from the upper energy level to annihilate the core hole, by releasing energy equivalent to the difference of the orbital energies (Figure 2.3 (b)). Another electron in the atom can absorb this energy and will be emitted (Auger electron) if it acquires enough energy to overcome the orbital binding energy and the corresponding work function (Figure 2.3 (c)). Three different electronic states are involved in this Auger emission process, and the kinetic energy of the ejected Auger electron could be explained by considering the involved electronic states, as depicted in Figure 2.3. For instance, if the initial core hole is formed in the K shell after electron bombardment, an electron from the L_1 shell is relaxed to fill the core hole, and an electron from the $L_{2,3}$ shell is emitted by absorbing the

released energy in the second step, the kinetic energy of the emitted Auger electron can be given by $E_K - E_{L1} - E_{L2,3}$. Each element has their own characteristic Auger electron spectra because of their unique core electronic arrangements. Therefore, AES can be used to fingerprint elements.²⁵⁻²⁶

AES is a highly surface sensitive technique. Auger electrons escaped from 5-20 Å of the near surface region will reach the detector and the deeper surface electrons will be reabsorbed by the sample as they have very low kinetic energy.²⁷ To detect the low energy Auger electrons without any inelastic collisions, ultra-high vacuum conditions are required. Also, the kinetic energy of the ejected Auger electrons is independent of the incident electron beam, which could be typically 2-20 keV. A typical Auger electron spectrum consists of electronic transitions between neighboring orbitals of an atom. Lighter elements with the atomic number 3-14 have the most prominent KLL transitions. Elements with the atomic number of 14 to 40 exhibit LMM transitions predominantly. More heavy elements with an atomic number larger than 40 exhibits NOO transitions.²⁴⁻²⁵

2.2.3. Instrumentation

A PHI model 15-255G precession electron energy analyzer attached to a UHV chamber with a base pressure of 3×10^{-10} mbar was utilized as the Auger electron spectroscopic experimental setup. The analyzer comes with an internal electron gun as the probe for the AES experiments, three electron energy analyzers (a hemispherical retarding grid system, two cylindrical mirror analyzers) connected in series for the energy analysis of incoming Auger electrons, and an electron multiplier. The electron gun is attached to the inner cylinder of the energy analyzer, which is extended through the hemispherical retarding grid system, not to interfere with the grid system. A fixed electron beam current could be generated by applying 2-5 keV to the filament of the electron

gun. The diameter of the focused electron beam at the sample is about 1.5 mm (which is the size of the apertures between two cylindrical mirror analyzers and the exit slit).²⁸

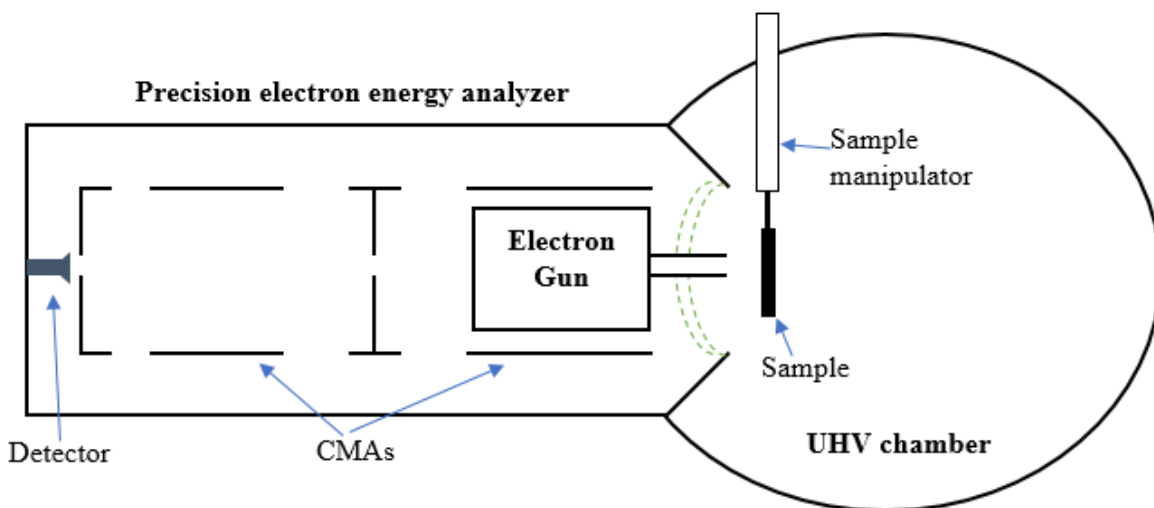


Figure 2.4. Schematic representation of the AES experimental setup in the Burghaus laboratory²⁸

After the electron bombardment of the sample surface, ejected Auger electrons are collected by the precision electron energy analyzer, which is placed in close proximity to the sample surface. For AES, the nonretarding operation mode of the energy analyzer is preferred because the ejected Auger electrons have very low kinetic energy compared to the photoelectrons generated by X-ray bombardment in XPS (the analyzer has the capability of detecting both Auger electrons and X-ray photoelectrons). Electrons enter the two-phase cylindrical mirror analyzer with their initial velocities. Then the electron current passing through the CMAs are amplified by the electron multiplier. As in the XPS mode, the resolution of the AES could also be improved significantly by using the retarding mode analysis. When using the retarding mode, pulse counting detection is preferred rather than directly detecting the analog signal, since the intensity of the signals is very low due to the applied retarding field.²⁸

A spectrum of kinetic energy of ejected Auger electrons as a function of the respective electron count ($N(E)$) is the output of the detector. But, conventional Auger spectra provides

$dN(E)/dE$ as a function of the kinetic energy of Auger electrons. The difference spectra are preferred in AES because, Auger peaks can be superimposed in a large continuous energy distribution, peak intensities can be very low and also there can be high background effects. Auger peaks are more easily recognizable by differentiating the energy distribution.²⁶

2.3. Low energy electron diffraction

2.3.1. Historical background

Low energy electron diffraction (LEED) is a powerful surface analytical technique which has been extensively utilized to study surfaces qualitatively, and quantitatively. Identification of lattice unit cells, overlayer structures, bond lengths, bond angles, and precise atomic positions of crystalline surfaces are possible using LEED. Even though the theoretical possibility of electron diffraction was predicted in 1924 by de Broglie, LEED was rapidly developed as a surface analytical tool in the mid-1960s. This slow progress was partly due to the rapid development of x-ray diffraction and the lack of sufficient theoretical work.²⁹ The first experimental observation of LEED was made by Davisson and Germer at Bell laboratories, with Ni (111) single crystal surfaces in the late 1920s.³⁰ At the same time, Thompson and Reid could record high energy electron diffraction patterns from celluloid surfaces.³¹ Both Davisson and Thompson were awarded the Nobel prize for physics in 1937 for their extensive experimental work in understanding electron diffraction. Considerable experimental development of LEED as a qualitative technique is evident in the 1960s, mainly due to the commercial availability of ion pumped ultra-high vacuum (UHV) systems and UHV compatible LEED optics. Also, availability of the Auger electron spectroscopic systems enables the characterization of chemical cleanliness of the sample surfaces prior to LEED experiments. More theoretical development of LEED is evident in the late 1960s and early 1970s, which helped to understand detailed surface structures more quantitatively.²⁹

2.3.2. Principles of LEED

X-rays penetrate deeply into the crystals because of the high energy. Therefore, X-ray diffraction is not much surface sensitive, even though it is a well-established crystallographic technique. Compared to X-rays, electrons do not penetrate deeply into the crystals, as they interact strongly with the matter (eg: repulsive interactions with atomic electron clouds). Also, electron energy can be varied easily to obtain the electron beams with comparable wavelengths with a respective atomic spacing of the sample of interest to avoid deep penetration, which enables the study of surface crystallographic structures. According to de Broglie's wave-particle duality, a beam of electrons can also be considered as a stream of electron waves. The wavelength of the electrons (λ_e) can be obtained by using the well-known de Broglie relation, $\lambda_e = h/\sqrt{2m_e V e}$, where h is the Planck's constant, e is the electronic charge and m_e and V are the mass and the acceleration voltage of the electrons respectively. For the energy in between 10-500 eV, the wavelengths of the electron beams are in the range of ~ 0.5 - 4.0 Å, which is comparable with the lattice spacings of most of the crystal structures.^{12, 32-34}

When a low energy electron beam is bombarded on a well-ordered crystalline surface, the incident electron wave will be backscattered by the localized electron densities of the surface atoms, which act as point scatters and hence an electron diffraction pattern will be generated. If the incident electron beam has a well-defined wavelength comparable with the atomic spacings of the surface, the penetration depth will be small (few atomic layers). Therefore, the observed diffraction pattern may contain substantial information about the two-dimensional periodicity of the crystalline surface. The diffraction pattern can be explained theoretically using a simple model, which is illustrated in Figure 2.5.

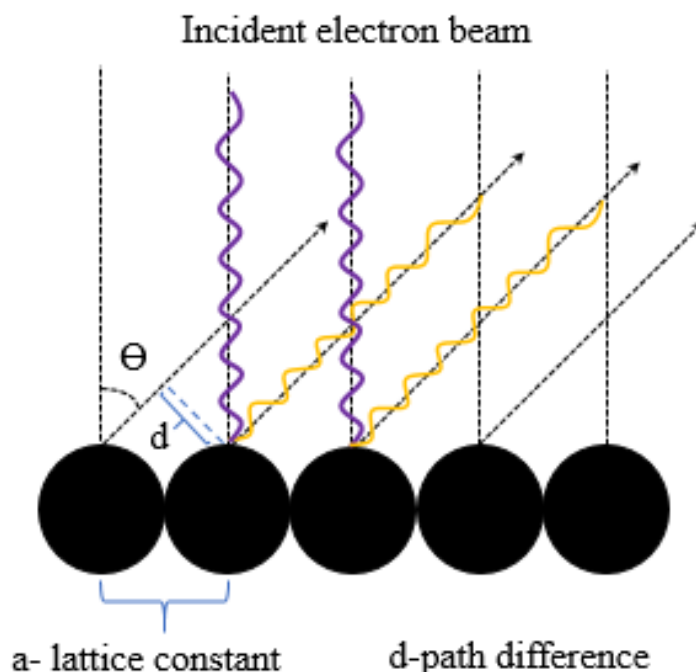


Figure 2.5. Electron diffraction by a one-dimensional array of atoms

Figure 2.5 depicts the scattering of an incident electron beam with an angle θ to the surface normal. The path difference (d) of the scattered radiation, $d = a \sin \theta$ where, a is the lattice constant, which can be simply obtained by considering the adjacent two-ray paths. These scattered periodic oscillations from the surface atoms (which are the scattering centers) may interfere destructively or constructively depending on the phase of the scattered wave. If the scattered waves are in phase, it will interfere constructively and if they are antiphase, destructive interferences may occur. Scattering from individual atoms are very weak but, scattering from a periodic array of a large number of scattering points with phase match to have constructive interferences of the scattered wave will provide intense diffraction patterns, characteristic to the surface lattice. In order to observe diffraction, Laue condition should be satisfied, which is the path difference of consecutive scattered beams should be equal to an integral number of wavelengths to observe constructive interferences ($d = a \sin \theta = n\lambda$, where n is the order of the diffraction).¹²

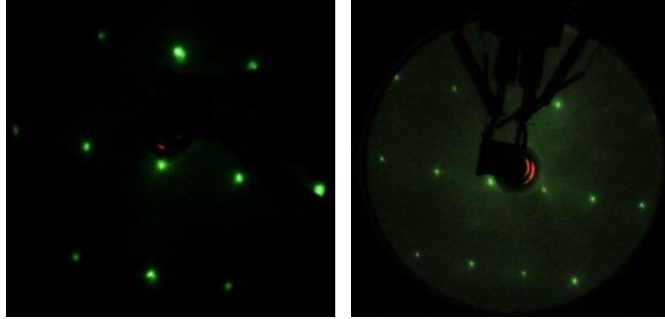


Figure 2.6. LEED patterns obtained for clean Mo(112) single crystal at 60 eV (left) and at 130 eV (right)

According to the equation $a \sin \theta = n\lambda$, the angle of diffraction (Θ) is inversely proportional to both the lattice constant and the square root of the electron energy ($\lambda \propto 1/\sqrt{E_k}$, E_k is the kinetic energy of the electron). For constant wavelengths, larger the real space lattice constant, smaller the scattering angle and hence smaller the corresponding distance in the diffraction pattern and vice versa. This reciprocal correlation can also be observed between the electron energy and the diffraction pattern. Therefore, as the energy of the electron beam increases, contraction of the diffraction pattern can be observed as depicted in the Figure 2.6.

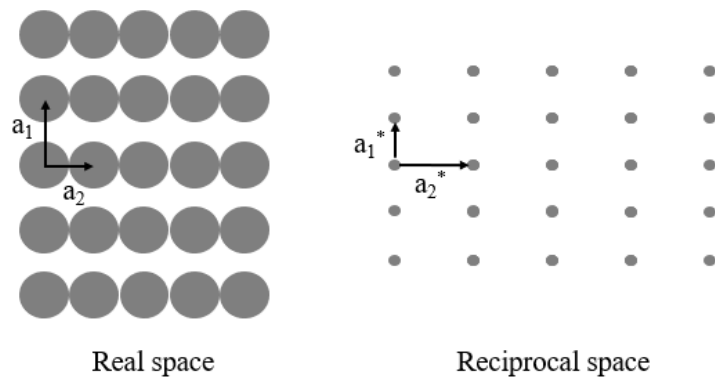


Figure 2.7. Schematic representation of the real space and the corresponding reciprocal space lattices

A typical crystalline surface will give a LEED pattern with a scaled representation of the reciprocal net of the surface structure. The correlation between the real space and the reciprocal space (obtained by LEED) can be understood mathematically by the concept of reciprocal vectors.

As depicted in Figure 2.7, if the two-dimensional real space lattice is defined by the vectors a_1 and a_2 , and the respective reciprocal space is defined by the vectors a_1^* and a_2^* , then the real space and the reciprocal space vectors have the relationships, $a_1 \cdot a_1^* = a_2 \cdot a_2^* = 1$ and $a_1 \cdot a_2^* = a_2 \cdot a_1^* = 0$, where a_1 is perpendicular to a_2^* and a_2 is perpendicular to a_1^* .¹² For an incident wavevector k_0 ($2\pi/\lambda_0$) and a scattered wavevector k ($2\pi/\lambda$) parallel to the sample surface, Laue condition for the diffraction can be given by $G_{hk} = k - k_0 = ha_1^* + ka_2^*$ (G_{hk} is any of the reciprocal lattice vectors related to a_1^* and a_2^*). Then the reciprocal lattice vectors can be given by the equations, $a_1^* = 2\pi[a_2 \times n/a_1(a_2 \times n)]$ and $a_2^* = 2\pi[a_1 \times n/a_2(a_1 \times n)]$, where n is a vector normal to the surface.²⁹

2.3.3. Instrumentation

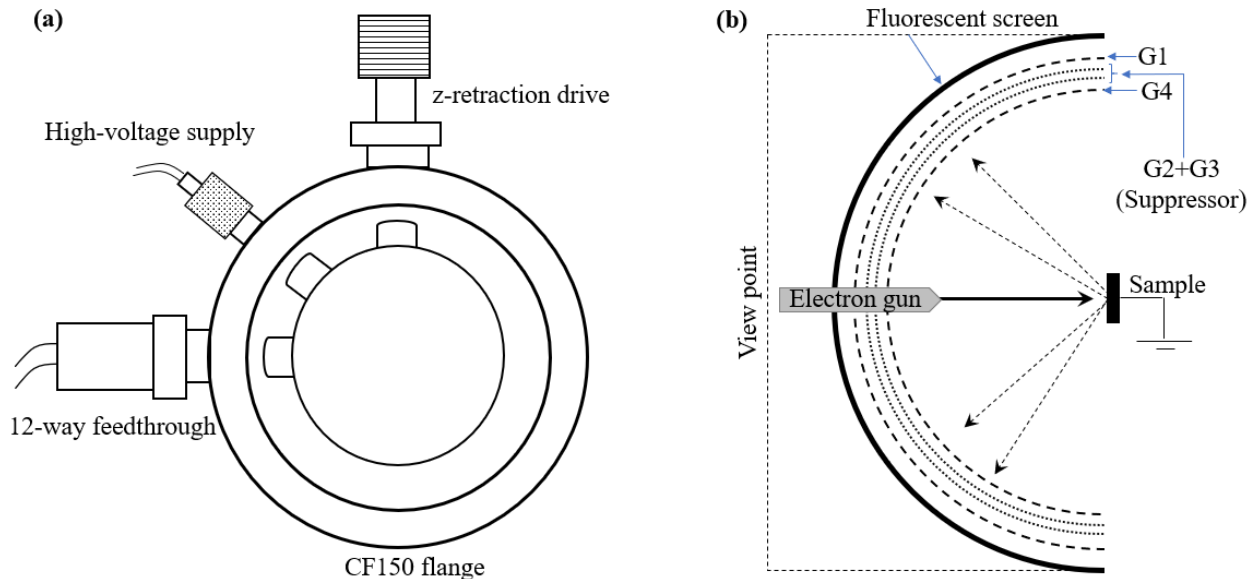


Figure 2.8. (a) Schematic representation of the ErLEED 150 optics,³⁵ (b) Main components of a typical LEED system¹²

SPECS ErLEED 150 with reverse view LEED optics attached to a UHV chamber via CF 150 flange (8" outer diameter) together with an ErLEED digital power supply (ErLEED 3000D)

was utilized to acquire LEED patterns of sample surfaces. The electron gun, the grid and the fluorescent screen are mounted on a base ring of the flange, inside the UHV chamber. The optics could be moved away or towards the sample using an inbuilt z-retraction mechanism. There is an integrated multi-segment shutter mounted in front of the grids, which is used to protect the optics when other experiments are running inside the UHV chamber. Schematic representation of the ErLEED optics mounted in the vacuum chamber and major components of a typical LEED system is illustrated in Figure 2.8.³⁵

The electron gun provides the necessary electron beam to probe the sample surface with energies between 0-1000 eV when the LEED mode is in operation. The ErLEED 3000D also has a retarding field analyzer mode in which the power supply can generate electron beams with energies up to 3000 eV for Auger electron spectroscopy or electron energy loss spectroscopy. In a typical LEED experiment, the electron energy is controlled in between 20-200 eV to probe the surface structures. To detect the elastically scattered low energy electrons without inelastic collisions, UHV conditions are necessary, which increases the mean free path of the electrons. The base pressure of the vacuum chamber was kept under 2×10^{-9} mbar during all the LEED experiments in this study.³⁵

The scattered electron beam passes four gold coated molybdenum grids (G_1 - G_4 in Figure 2.8 (b)) before striking the fluorescent screen. The grids G_1 , G_4 , and the sample are at ground potential to provide field-free space from the sample to the screen, to avoid any disturbances to the electron trajectories. This also helps to prevent sample charging during the cause of the electron bombardment. The suppressor grids (G_2 and G_3) are at negative potentials with respect to the sample, to keep away the secondary electrons or inelastically scattered electrons from the fluorescent screen. This reduces the background intensity of the recorded diffraction pattern by

showing only elastically scattered electrons and electrons with very small energy losses (energy losses less than 10 eV). A positive high voltage (~5-7 kV) is applied to the fluorescent screen to observe the diffraction pattern. ErLEED 150 consists of a semi-transparent back-view screen together with the usual front viewing option. With the back-view screen, the LEED pattern can be recorded without any obstructions such as the sample or the sample holder, and no additional window flanges are necessary.³⁵

LEED technique was extensively used in this work to qualitatively characterize the crystallinity of single-crystal surfaces, re-constructed overlayer structures, and crystalline thin films.

2.4. Thermal desorption spectroscopy

2.4.1. Introduction

Temperature programmed desorption (TPD) is a simple and well-established technique to study gas-surface interaction kinetics and thermodynamics. This technique is also known as thermal desorption spectroscopy (TDS) when the gas adsorption experiments are performed with well-defined single crystal surfaces in ultra-high vacuum conditions.³⁶ This technique has been extensively utilized by surface scientists and material chemists to study the heat of desorption processes,³⁷⁻³⁹ adsorbate-adsorbate interaction types,³⁷⁻³⁹ adsorbate-adsorbent interaction types,^{37, 39} molecularity of adsorption/ desorption processes (molecular or dissociative adsorption/ desorption),^{37, 40} phase transitions and quantitative coverage determination, identification of different adsorption sites on a surface and packing structures,⁴¹ surface reactions of heterogeneous catalytic systems⁴² and many more.

2.4.2. Experimental setup

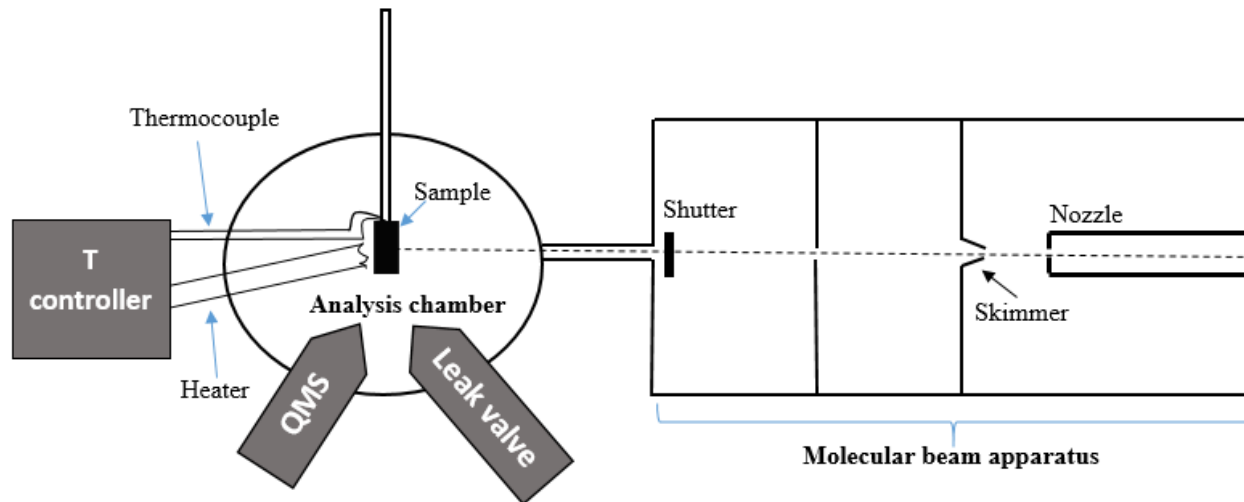


Figure 2.9. TDS experimental setup in the Burghaus laboratory.

In a typical TDS experiment, the gaseous precursor molecule (or molecules) of interest is dosed into the analysis chamber, while keeping the substrate (adsorbent) at relatively low temperature, in order to maintain a negligible desorption rate during adsorption. Gases were dosed either by backfilling the analysis chamber using a leak valve or by a supersonic molecular beam apparatus attached to the analysis chamber. After the adsorption process, the sample temperature is ramped employing a linear temperature program (see the section 2.13 for more details about the sample holder) and the desorbing molecular fragments (or reaction products) are detected by a quadrupole mass spectrometer. The mass spectrometer can be programmed to detect multiple mass fragments simultaneously (referred to as multi-mass TDS in this thesis) or a single mass fragment depending on the type of the experiment.

A residual gas analyzer from Stanford research systems (SRS RGA 100), which is capable of detecting the masses from 1-100 amu with 0.5 amu resolution was utilized as the gas analyzer. The RGA consists of a quadrupole probe as a mass filter (cylindrical rods with 0.25" diameter and 4.5" length), a standard Faraday cup (FC) detector (coupled with an electron multiplier), and an

open ion source with cylindrical symmetry, in which a thoria coated dual iridium filament is used as the ion (electron) source. The incoming gaseous molecules are ionized to positive ions by electron impact ionization. Then the masses are separated by the quadrupole mass filter and detected by the FC detector.⁴³

2.4.3. TDS theory

A typical TDS output is a plot of the partial pressure of the detected molecular species (intensity) as a function of desorption temperature, which is a convolution of the rate of desorption and the surface coverage. A maximum desorption temperature occurs because, the rate of desorption increases as the surface temperature increases, while the surface coverage decreases as the surface temperature increases.⁴⁴

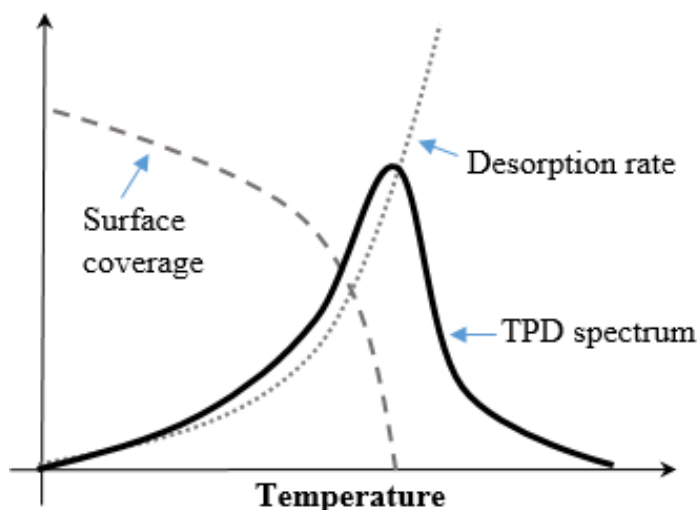


Figure 2.10. Schematic representation of a typical TPD spectra⁴⁴

The desorption kinetics can be determined by the so-called Polanyi-Wigner equation, which is an equation explaining the temperature dependence of the desorption rate. If the desorption rate of an adsorbed species A ($A_{(ad)}$) is explained by a rate coefficient k_d ($A_{(ad)} \rightarrow A_{(g)}$), then the desorption rate can be written as, $-\frac{d\theta}{dt} = k_d \theta^n$ (θ is the surface coverage of A, t is the

time, and n is the kinetic order of the desorption reaction). Also, the rate constant k_d can be expressed by the Arrhenius equation, $k_d = \nu e^{-E/RT}$ (ν is the pre-exponential factor, E is the desorption energy, T is the absolute temperature and R is the ideal gas constant). By combining the above equations with the heating rate, $\beta = \frac{dT}{dt}$, the so-called Polanyi-Wigner equation can be obtained, which is $-\frac{d\theta}{dT} = \frac{\nu}{\beta} \theta^n e^{-E_d/RT}$.^{33, 44}

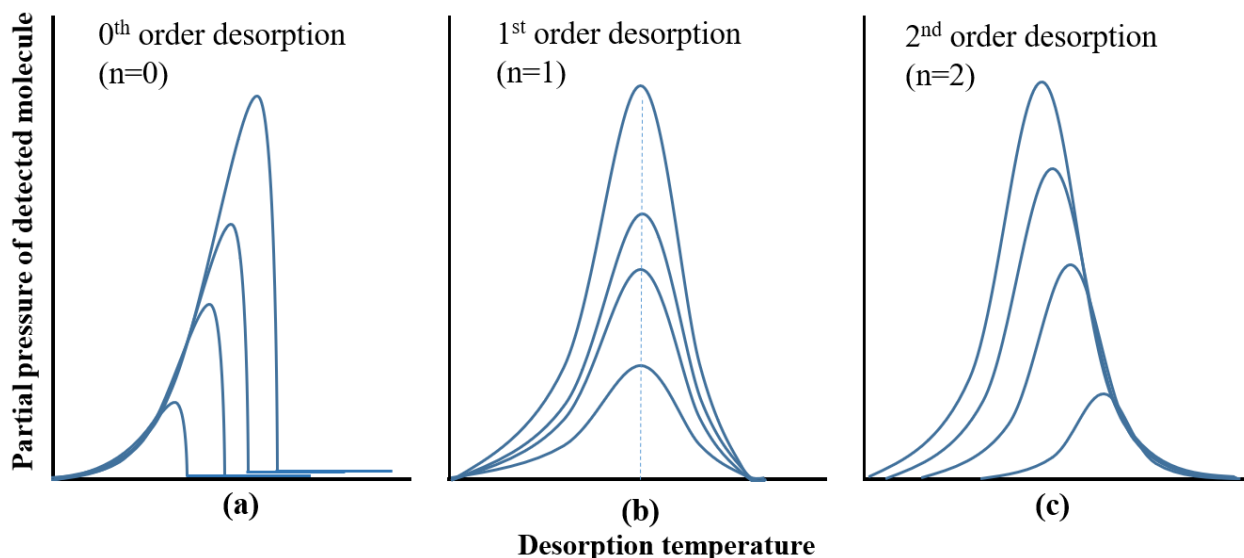


Figure 2.11. Schematic representation of TDS patterns for different desorption orders.

In a typical TDS experiment, several TDS curves are obtained at different exposures of the considering species. By observing the TDS data set, information such as molecularity of the desorption reaction (chemisorption, physisorption or dissociative desorption), effects of the adsorbate, phase transitions and different adsorption sites on the surface can be identified qualitatively.

0th order desorption has the characteristic curve shapes as depicted in Figure 2.11 (a). The peaks have shared leading edges due to the coverage independent desorption rates. Peaks are shifted to the higher temperatures with increasing coverage due to the intermolecular interactions of the adsorbates and the high adsorbate concentrations on the surface with higher exposures. A

similar type of interactions (0^{th} order) is observed when the adsorbate form clusters on the surface and/ or multi-layer desorption of the adsorbate. 1^{st} order kinetics have the characteristic coverage independent desorption temperatures and increasing desorption rates (ascending leading edges) with the increased exposure, as depicted in Figure 2.11 (b). This type of kinetics is evident when molecular physisorption or chemisorption without dissociation occurs on surfaces. 2^{nd} order kinetics is more often observed when the adsorbed molecules dissociatively desorbed from the surfaces. Characteristic TDS traces are shown in Figure 2.11 (c). The symmetric peaks are shifted towards the lower temperature with increasing exposure and the shared desorption tails are the major evidence for the 2^{nd} order kinetics.^{33, 44} Also, this kind of TDS traces could be observed when the molecularly adsorbed species influence repulsive-lateral interactions due to induced dipoles. The effect of repulsive lateral interactions are increasing with high exposures as a large number of molecules adsorbed in close proximity can cause steric repulsions progressively. To distinguish between dissociative desorption and molecular desorption with the repulsive lateral interactions, multi-mass TDS experiments (see section 3.53) can be used.

There are several reported quantitative data analysis techniques to obtain the order of the desorption, desorption energies, pre-exponential factors etc., utilizing the TDS peak temperatures and peak shapes, providing reliable results with fewer effects. Redhead analysis,⁴⁵ leading-edge analysis,⁴⁴ varying heating rate technique⁴⁶ are some examples. Techniques such as complete analysis⁴⁷ and inversion optimization analysis⁴⁸⁻⁴⁹ are some methods require more effort and also provides more accurate results. Redhead analysis and inversion optimization analysis were employed to extract quantitative information from TDS curves in this study.

2.4.3.1. Redhead analysis

In this method, TDS peak maximums are numerically converted to binding energies using the Redhead equation. The so-called Redhead equation is obtained by differentiating the Polanyi-Wigner equation with respect to the temperature. At TPD peak maximum, $\frac{d^2\theta}{dT^2} = 0$. Applying this derivative relationship to the Polanyi-Wigner equation, Redhead equation, $\frac{E_d}{RT_p^2} = \frac{\nu}{\beta} n\theta^{n-1} e^{-E_d/RT_p}$ can be derived, which is typically used to obtain the binding energies from the TPD peak temperatures. Here, E_d is the desorption energy and T_p is the TPD peak temperature. For an 1st order desorption process, the relationship between E_d and T_p is given by, $\frac{E_d}{RT_p} = \ln\left(\frac{\nu T_p}{\beta}\right) - 3.64$.⁴⁵ The desorption energy can be directly determined by measuring the TPD peak temperatures with assumed pre-exponentials.

2.4.3.2. Inversion optimization analysis

The so-called ‘inversion-optimization analysis’ is the mathematical inversion of the thermal desorption spectra to obtain the kinetic parameters for desorption processes, including the pre-exponential dependence, using Polanyi-Wigner equation. This technique has been employed to study coverage dependent desorption kinetics of small organic molecules on metal oxide surfaces by Kay et. al. for the first time.⁴⁸⁻⁴⁹

The Polanyi-Wigner equation for the 1st order desorption is, $r(\theta, T) = -\frac{d\theta}{dt} = \nu\theta e^{-E_d/RT}$.

To invert the Polanyi-Wigner equation, 1st order desorption (with physisorption) and coverage independent pre-exponential factor are assumed. Coverage dependent desorption energy can be

calculated by substituting the TPD curve in the inverted Polanyi-Wigner equation, $E_d = -RT \ln \left[-\frac{\left(\frac{d\theta}{dT}\right)}{\beta v \theta} \right]$, where $\beta = \frac{dT}{dt}$, is the heating rate and $\frac{d\theta}{dt}$ is the rate of the desorption, which is directly proportional to the TDS curve (TDS intensities). In our calculations, TDS peaks were normalized with respect to the monolayer desorption peak (onset of the condensation peak is considered as the monolayer adsorption) and the relative coverages of the sub-monolayer peaks were determined. For each exposure, at or below the monolayer coverage, $E(\Theta)$ curves were determined using inverted Polanyi-Wigner equation.⁴⁸

The binding energy curves obtained at different pre-exponential factors were fitted to an analytic function, $E_d = E_0 + Y\Theta + E_{def}e^{(-\theta/\theta_{def})}$.⁴⁹ In this equation, E_0 can be obtained by extrapolating the linear region of the binding energy curve back to zero coverage, which is corresponding to the defect free desorption energy of the adsorbate. The factor Y represents the adsorbate-adsorbate interaction, which can be repulsive-lateral interactions (negative) or attractive interactions (positive). The term E_{def} is the difference between actual binding energy calculated and the term E_0 , that compare the binding energy of the adsorbate on defect sites and the defect free sites. Term Θ_{def} includes the influence of the defect density on energy decay with increasing coverage.⁴⁸⁻⁴⁹

Then the complete set of thermal desorption spectra can be simulated by numerically integrating the Polanyi-Wigner equation, employing the parameters E_d and v . In our calculations, various binding energy curves were obtained at different pre-exponential factors and TDS curves were simulated for each pre-factor. Then, the experimental and simulated TDS curves were compared and the pre-factor which gives the best fits for a set of considered TDS curves is considered as the best pre-exponential for that adsorbate.

2.5. Molecular beam scattering

2.5.1. Introduction

Understanding the atomic or molecular collisions are fundamentally important to get insights into chemical processes. Reaction kinetics and energy transfer processes mainly depend on the collisions between the reactants. Molecular beam scattering is a type of technique that has been widely applied to understand the fundamental energy transfer processes in elementary reactions. Rates of elementary reactions, rate limiting steps and reaction mechanisms,⁵⁰⁻⁵¹ the dependence of the internal degree of freedom of reactants for the product formation⁵² etc., have been studied employing molecular beams with well-defined velocity distributions and controlled internal degree of freedom in the recent past. Also, coupled cross-molecular beams with LASER spectroscopy have been employed to get insights into the state to state reaction dynamics with controlled chemical reactivity.⁵³⁻⁵⁴

There are three major types of collisions, which are elastic, inelastic, and reactive collisions. Collisions with no energy transfer between the colliding species are elastic collisions, whereas inelastic collisions are collisions involving energy transfer between the internal degree of freedom of the participating particles. Reactive collisions are the collisions that drive chemical reactions, where the product formation is observed. Understanding all three types of collisions are important to get insights into the interatomic or intermolecular forces between the reactants. Molecular beam scattering experiments enable the study of each type of collisions for isolated elementary reaction steps, providing the details of the energy transfer processes.⁵⁵

There are two major types of molecular beams namely, effusive or thermal beams and supersonic molecular beams. Effusive molecular beams have small beam flux, a broad speed distribution, and a broad angular distribution. Therefore, control over the molecular beam energy

and internal degrees of freedom is very low. But, setting up effusive molecular beam systems are fairly cheap and simple compared to the supersonic molecular beams.⁵⁶ As the name implies, the supersonic molecular beams are the particle beams with the speed that exceeds the speed of sound. These molecular beams are more focused with large flux and low background pressure with narrow speed distributions. Also, the kinetic energy and the internal degrees of freedom of the molecular beam can be controlled over a wide range. But, setting up and maintenance of the supersonic beam systems are complex and expensive.⁵⁷⁻⁵⁸

2.5.2. Experimental setup

To generate supersonic molecular beams, gas particles initially at high pressure are pressed through a small nozzle (with a diameter of few micrometers) and then the stream of the particles are funneled through a series of differentially pumped vacuum chambers, through small orifices. Figure 2.12 depicts a schematic diagram of the differentially pumped UHV system used to obtain supersonic molecular beams in this study.

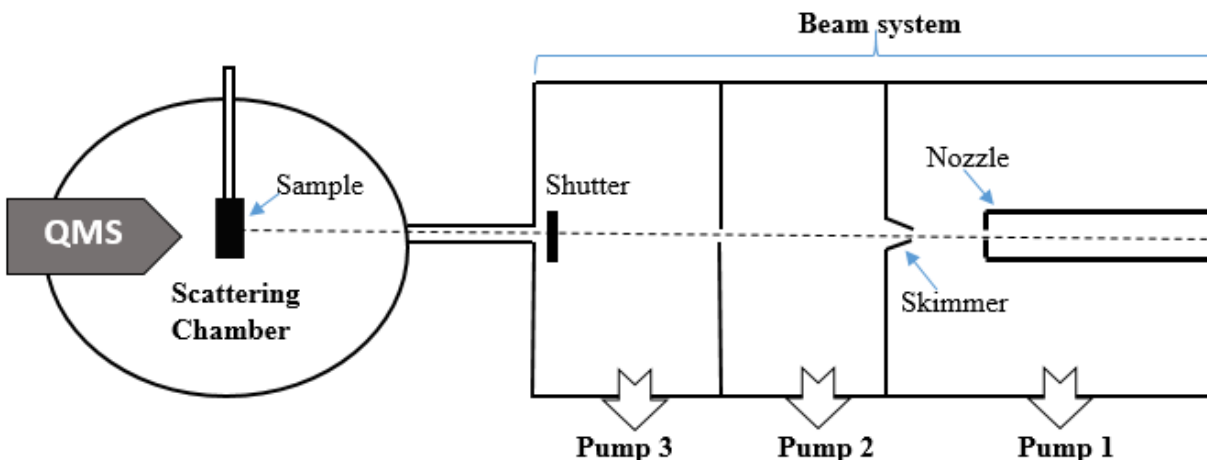


Figure 2.12. Schematic diagram of the molecular beam scattering experimental setup in the Burghaus laboratory⁵⁹

The first two stages of the beam system are pumped by two Varian diffusion pumps (VHS-10 with 6600 l/s and VHS-6 with 3000 l/s pumping speed respectively), backed by a combination

of a rotary and booster pumps (Leybold D65B and WSU500). The third stage is pumped by a head over mounted Varian V200 (200 l/s) turbomolecular pump. A Pt/ Ir electron microscope aperture (4mm of the outer diameter and 0.2mm thickness) with a hole diameter of 20 μ m is used as the nozzle plate, which is attached to the head counterpart of the steel metal tubing (nozzle). The nozzle is also attached to an adjustable x-y-z-tilt-manipulator. The differentially pumped beam system is attached to the scattering chamber, which is pumped by a combination of Varian V1000 and V550 turbomolecular pumps (pumping speeds of 1000 l/s and 550 l/s respectively) backed by a Leybold D65B rotary pump, maintaining ultra-high vacuum conditions (see section 2.1 for more details about the scattering chamber). The scattering chamber is equipped with SRS residual gas analyzers (RGA 100) for molecular beam detection and time of flight (TOF) experiments.⁵⁹

2.5.3. Molecular beam scattering theory

2.5.3.1. Supersonic molecular beams

Different types of molecular beams can be classified by a quantity called Knudsen number, which is the ratio between the mean free path of the particles inside the nozzle and the diameter of the nozzle aperture. Typical effusive beams are generated by dosing a gas through a large opening with a small source pressure. Mean free path of the particles inside the nozzle is large due to small source pressure and hence large Knudsen numbers are evident for thermal beams. When a gas expands adiabatically from a high-pressure source into vacuum through a tiny nozzle, a supersonic molecular beam with a narrow speed distribution can be generated. Due to high source pressure, mean free path of the particles are small and therefore, small Knudsen numbers are characteristic to supersonic molecular beams.

The gas inside the nozzle expands fast through the nozzle aperture due to the pressure difference, which makes the process adiabatic. The stored enthalpy of the particles at the state of

the viscous flow converted into kinetic energy along the flow direction and rest enthalpy of molecular flow along the direction of the beam.⁶⁰⁻⁶¹ Therefore, the temperature of the gas drops significantly, leading to a narrow speed distribution perpendicular to the beam direction. Transformation of the internal energy of the gas to the translational energy is responsible for the fast movement (supersonic speed) of the gas beam. To quantify the efficiency of the gas expansion, so-called Mach number (M) is used, which is the ratio of the speed of the beam to the speed of the sound in the surrounding medium.⁶²

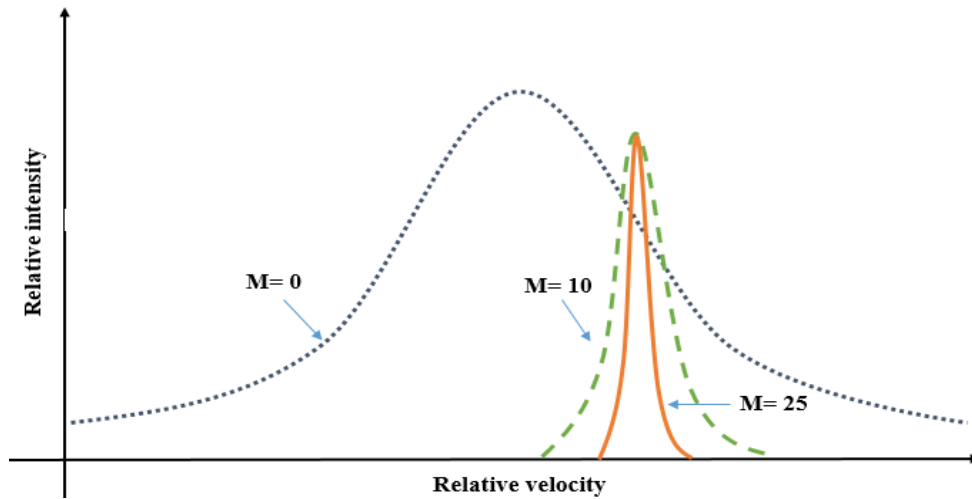


Figure 2.13. Schematic representation of the theoretical axial velocity distributions for a monoatomic gas with different Mach numbers.⁶³

Mach number increases with the nozzle pressure and the nozzle aperture diameter according to, $M_{max} \approx (p \times d)^{\frac{\gamma-1}{\gamma}}$. Here, p and d are nozzle pressure and nozzle diameter respectively, and γ is the heat capacity ratio. But, to have a large nozzle aperture diameter, pumps with huge pumping speed is necessary, which increases the cost of the instrument significantly. Aperture diameter should be optimized according to the available pumping speed, in order to have the optimum system performance. Mach number and the beam temperature related as, $T = T_0/[1 + 1/2(\gamma - 1)M^2]$.⁶¹ Here, T is the beam temperature and T_0 is the initial temperature of the

gas in the nozzle. As the speed of the beam increases, M increases and T decreases, narrower the speed distribution (see Figure 2.13).

2.5.3.2. Molecular beam energy

Characterization of the beam energy distribution and control over the beam velocity and internal degree of freedom are important for studying the reaction/ adsorption dynamics because the initial states of the reactants/ adsorbate and adsorbent play important roles in energy transfer processes. There are two major experimental techniques commonly used to vary the kinetic energy of the molecular beams. By changing the gas temperature prior to the gas expansion or by changing the composition of the gas mixture (seeding), molecular beam energy can be varied. In the former case, the temperature of the nozzle is typically changed by heating or cooling it down. In the latter case, lighter or heavier carrier gases can be used to change the speed of the molecular beam. When a fast-moving lighter gas collide with a slow heavy gas (reactant/ adsorbate), the speeds average out and hence the beam energy can be increased. Similarly, heavy carrier gases can be used to decrease the molecular beam energy. By changing the mixing ratios of carrier gases, internal degrees of freedom of the probe molecular beams can also be controlled.⁶⁴⁻⁶⁵ To calibrate the energy distributions of molecular beams, time of flight (TOF) experiments were utilized in this study.

2.5.3.3. Adsorption probability measurements

In this dissertation, the molecular beam scattering setup was mainly utilized as a gas dosing technique to study the adsorption dynamics of small molecules employing King and Wells type adsorption probability measurements.⁶⁶

When a beam of particles is introduced into a UHV chamber (e.g. Figure 2.12) without a sample on the way of the molecular beam (to an empty vacuum chamber), the base pressure of the

UHV chamber will be increased and it will reach a new equilibrium pressure, depending on the pumping speed of the system. In this case, the gas load of the UHV chamber is artificially increased by shooting the molecular beam and hence the total pressure of the chamber is increased. Figure 2.14-left depicts an example, in which a seeded n-butane particle beam in an empty vacuum chamber is characterized.

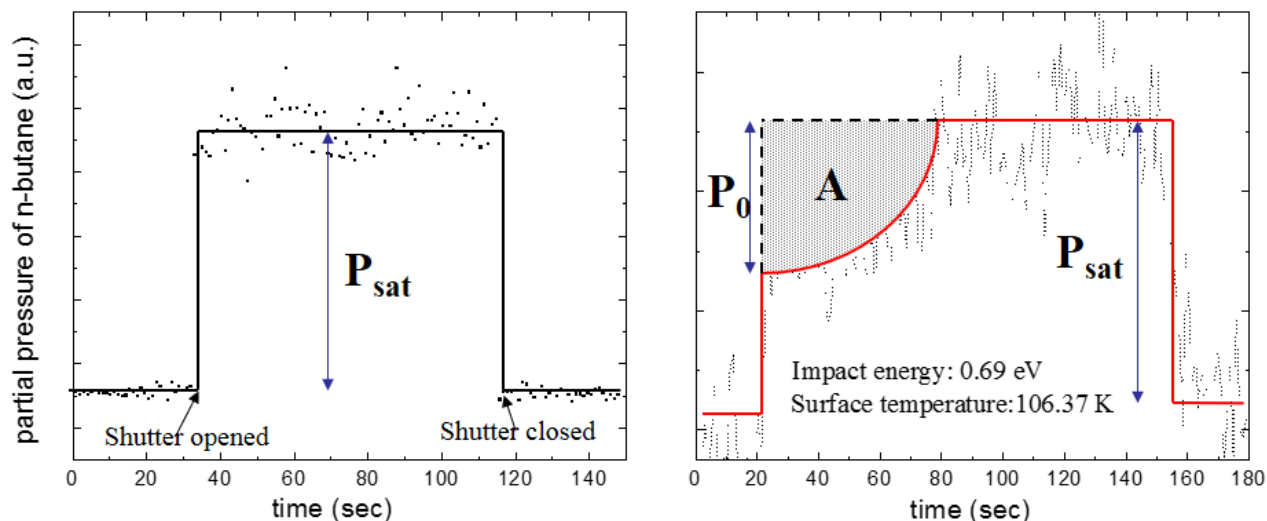


Figure 2.14 Seeded n-butane (3% n-butane in He) molecular beam characterization (left: n-butane molecular beam in an empty vacuum chamber, right: n-butane molecular beam interacting with a crystalline silica thin film on Mo(112))

When the particle beam is directed towards a sample surface in the UHV chamber where the particles have some affinity towards adsorption, a monolayer of particles will stick on the surface until all the available adsorption sites are occupied, if the correct surface temperature is maintained (just above the condensation temperature to avoid desorption of sub-monolayer adsorbates and also to avoid the formation of thick layers). An example adsorption transient of seeded n-butane adsorption on crystalline silica thin film on Mo(112) is depicted in Figure 2.14 (right). As indicated in the figures, the base pressure of the scattering chamber will suddenly increase as the shutter opened (which is used to switch on/off the beam into the scattering chamber). Then the base pressure will increase slowly as the available adsorption sites are

occupied by the incoming molecules. Eventually, it will rise to the saturation pressure with all the available monolayer adsorption sites are occupied. Using this pressure transient, some important parameter such as initial adsorption probability (or sticking probability, which determines the efficiency of the adsorption), coverage dependent adsorption probabilities, and surface coverage can be determined. The methods to determine the adsorption probabilities utilizing the pressure transients as depicted in Figure 2.14 was first proposed by King and Wells.⁶⁶

The adsorption probability is generally defined as the ratio of adsorption rate to the ratio of collision rate of particles on an adsorbent. If the adsorbent (surface) kept clean initially, the initial adsorption probability (S_0) can be determined, which is the ratio of initial pressure rise and saturation pressure ($S_0 = P_0/P_{sat}$, according to Figure 2.14). The incoming particle should dissipate part of their kinetic energy in order to adsorb on the surface. Therefore, the initial adsorption probabilities can be used to understand energy transfer processes (adsorption dynamics). Area above the pressure transient and below the saturation pressure (area A in Figure 2.14) is proportional to the surface particle density or the coverage (Θ). By integrating the area under the pressure transient, coverage dependent adsorption probabilities ($S(\Theta)$) can be determined at each point of the pressure transient. Typically, the signal to noise ratio of the mass spectrometer signal limits the adsorption probability measurement in-between 0.02-1 for King and Wells type experiments.

2.5.3.4. Activated and non-activated adsorption

The main objective of the adsorption probability measurement of this study was to determine the activated or non-activated adsorption behavior of small molecules on metal and semiconductor surfaces for catalysis related applications (see section 3.5.4.2.2 for experimental details). Initial adsorption probability (S_0) as a function of surface temperature and S_0 as a function

of impact energy were measured in order to determine the adsorption dynamics of considered species (see below for more details).

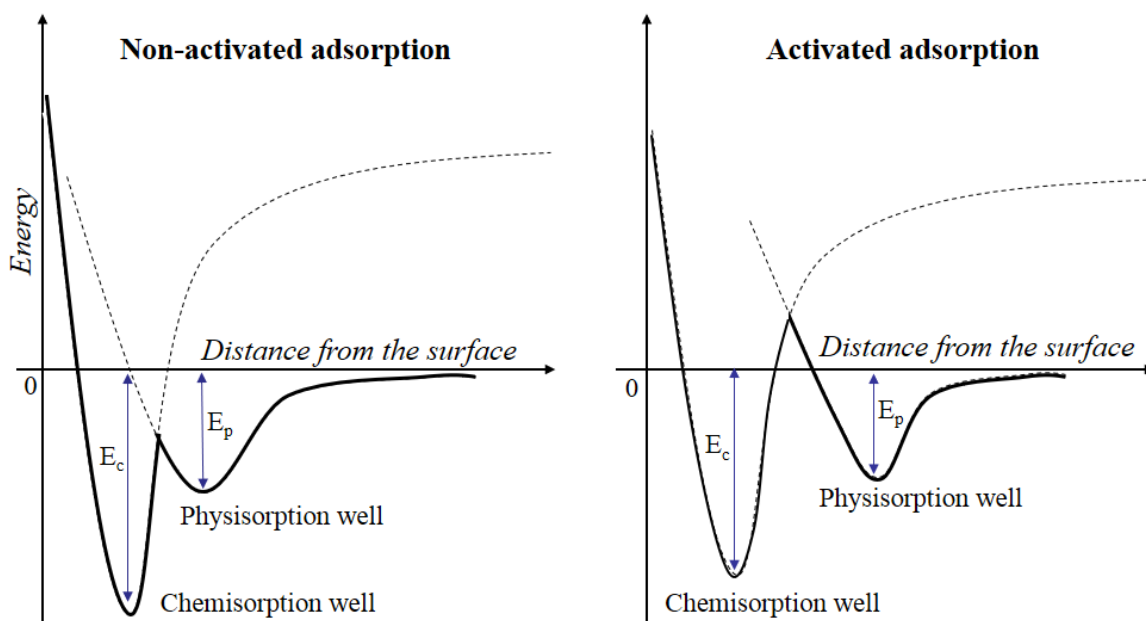


Figure 2.15. Lennard-Jones potential energy diagrams for activated and non-activated adsorption of a molecule as a function of the distance from the surface (adsorbent)⁶⁷⁻⁶⁸

Chemisorption is generally defined as the formation of strong covalent type bonding between adsorbate and adsorbent during the adsorption. In physisorption, weak van der Waals interactions are evident, resulting in small binding energies and large bond distances. In heterogeneous catalysis related applications, it is necessary to understand how the reactants adsorb on the catalytic surface or the molecularity of the adsorption process in order to understand the catalytic mechanisms and the kinetics of the catalytic processes. Therefore, distinguishing between the molecular adsorption (non-activated adsorption) and dissociative adsorption (activated adsorption) is vital. Temperature-dependent and energy dependent initial adsorption probability measurements can be used to clarify the molecularity of the adsorption processes.

Schematic diagrams of so-called Lennard-Jones potential energy surfaces for non-activated and activated adsorption are depicted in Figure 2.15. For non-activated adsorption, chemisorption

and physisorption potentials cross below the zero line, as there is no activation energy barrier to overcome during the molecular chemisorption process. A molecule should dissipate enough kinetic energy to the surface, in order to adsorb. For molecular adsorption, as the impact energy (E_i) or surface temperature (T_s) increases, the initial adsorption probability (S_0) would decrease because energy should be progressively transformed from the molecules to the surface (larger the impact energy, interaction time between the molecule and surface become shorter).⁶⁸⁻⁶⁹

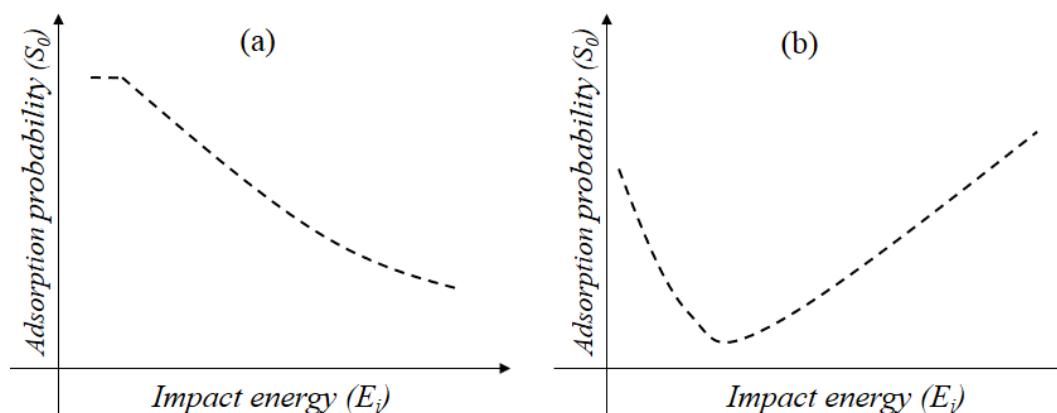


Figure 2.16. Schematic representations of the variation of initial adsorption probability as a function of impact energy for (a) molecular⁶⁹ and (b) dissociative adsorption.⁷⁰

In the case of dissociative adsorption, the chemisorption and the physisorption potentials cross above the zero line, means that there is an activation energy barrier to overcome in order to chemisorb dissociatively. The molecule may initially approach the surface through the physisorption potential. If it has sufficient energy to overcome the activation barrier, then it will chemisorb dissociatively, which is commonly known as direct chemisorption. Also, the molecule may temporarily undergo physisorption, from which it can either backscattered molecularly to the gas phase or it can overcome the chemisorption barrier eventually to form a dissociatively chemisorbed state, which is known as precursor mediated chemisorption.⁷¹ For low impact energies and surface temperatures, S_0 will decrease as the E_i and T_s increase, as the molecule tend to stay in the physisorption well since the energy is not enough to overcome the chemisorption

energy barrier. When E_i (or T_s) reaches the threshold value, which possesses enough energy to surmount the chemisorption energy barrier, a sudden increase of S_0 would be observed.⁷⁰ Then, as the E_i (or T_s) increase from this point, S_0 will again start to decrease, as the incoming molecule should dissipate more and more energy to the surface in order to adsorb.

2.6. X-ray photoelectron spectroscopy

2.6.1. Historical background

X-ray photoelectron spectroscopy (XPS) is a quantitative surface analytical technique, developed in 1967 by K. Siegbahn. XPS phenomenon is based on the photoelectric effect, which was discovered in 1887 by Heinrich Hertz and explained later by Albert Einstein in 1907. After the discovery of the photoelectric effect, several experiments have been conducted to record and explain the broadband of emitted photoelectron spectra as a function of velocity. Finally, Siegbahn and his co-workers published a comprehensive research study, explaining the utility of XPS, which was referred to as electron spectroscopy for chemical analysis (ESCA). Two years later, Siegbahn developed the first commercial XPS instrument together with an American company called Hewlett-Packard. Siegbahn was awarded the Nobel Prize in Physics in 1982, primarily for his work on XPS.⁷²⁻⁷³

2.6.2. Principles of XPS

XPS provides a quantitative chemical analysis of top 1-10 nm of the solid surfaces. Utilizing X-rays, a surface of a material can be excited to generate photoelectrons (photoelectric effect). In XPS, kinetic energies of the generated photoelectrons are analyzed, which contains elemental and chemical information of the respective material.

When the X-ray photons are bombarded on a sample surface, incident energy will be absorbed by the electrons in the surface atoms and they will escape the atom if they acquire enough

energy to overcome the binding energy to the nucleus and the corresponding work function. Electrons escaped from the deeper surface atoms will be reabsorbed by the sample and the electrons escaped from ~1-10 nm of the sample surface will reach the detector.⁷²

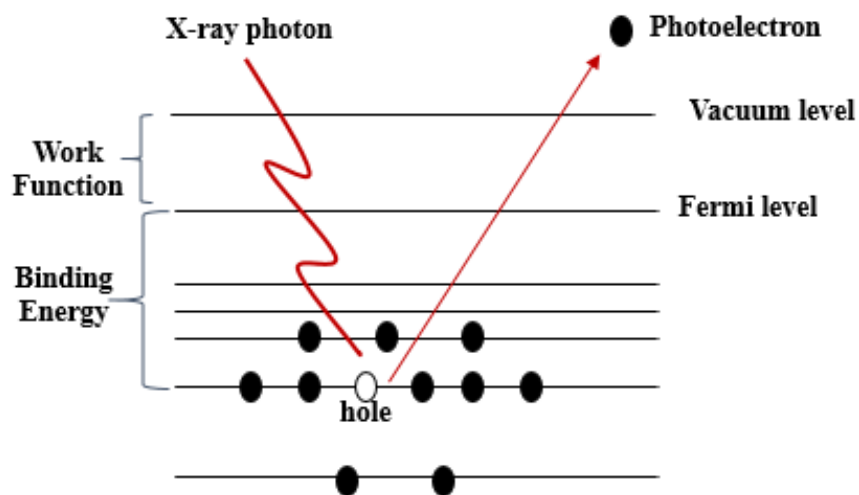


Figure 2.17. Photoemission process⁷²

The kinetic energy of the ejected photoelectrons depends on the binding energy of the core level shell, the work function of the material, as well as the incident X-ray energy. The photoemission will occur only when the sum of binding energy and work function is less than the incident X-ray energy. Therefore, the kinetic energy of the ejected photoelectrons increases with the incident X-ray energy and decreases with the binding energy of the core level. Also, the intensity of photoemission directly proportional to the intensity of incident X-ray photons. Each element has their own characteristic core electron arrangements and therefore, XPS can be used to fingerprint elements.

2.6.3. Instrumentation

A dual anode X-ray source and a cylindrical mirror analyzer (detector) are attached to a UHV chamber as depicted in Figure 2.18, which was utilized as the XPS experimental setup in this study. To detect the photoelectrons emitted by the sample after the bombardment of X-rays

without any inelastic collisions, high vacuum conditions are required. Mean free path of generated photoelectrons can be increased significantly by reducing the pressure up to the UHV range. The base pressure of the analysis chamber was maintained at 3×10^{-10} mbar by continuously pumping with turbomolecular pumps and an ion getter pump. An old fashion non-monochromatic dual anode X-ray source (PHI 04-548) consists of Al and Mg anodes is used as the probe. X-rays are produced by electron bombardment of either of the anodes with a heated thoriated tungsten filament. During the X-ray generation, a large amount of heat is generated and to dissipate the heat, the anode is water cooled.⁷⁴

The ejected photoelectrons from the sample surface are collected by the electron energy analyzer and separated according to their kinetic energies. There are two different types of analyzers, which are kinetic energy analyzers and deflection energy analyzers. Former separates the electrons according to their velocities and the latter separates the photoelectrons with different kinetic energies by forcing them through an electric field.

The XPS system is equipped with a PHI model 15-255G precision electron energy analyzer, which has the capability of detecting both X-ray photoelectrons and Auger electrons. The analyzer composed of an internal electron gun for Auger electron spectroscopy, an energy filter (electron energy analyzer) and an electron multiplier. In the analyzer part, there are three energy analyzers interconnected in series for the energy analysis of incoming electrons. A hemispherical retarding grid system is used to lower the kinetic energy of the incoming photoelectrons with a retarding field, and two cylindrical mirror analyzers (CMA) are used to accurately measure the energy. Generally, the energy resolution of a typical analyzer is defined as $\Delta E/E$ (ΔE -absolute energy resolution and E - kinetic energy of the electrons), which means the energy resolution could be significantly improved by decreasing the velocity of the electrons. The

generated electron current after the X-ray bombardment on the sample specimen (which exiting the analyzer) enters the electron multiplier and the multiplier amplifies the current to drive a lock-in amplifier. A spectrum of binding energy of ejected photoelectrons as a function of the photoelectron count (intensity) is the final output of the detector.²⁸

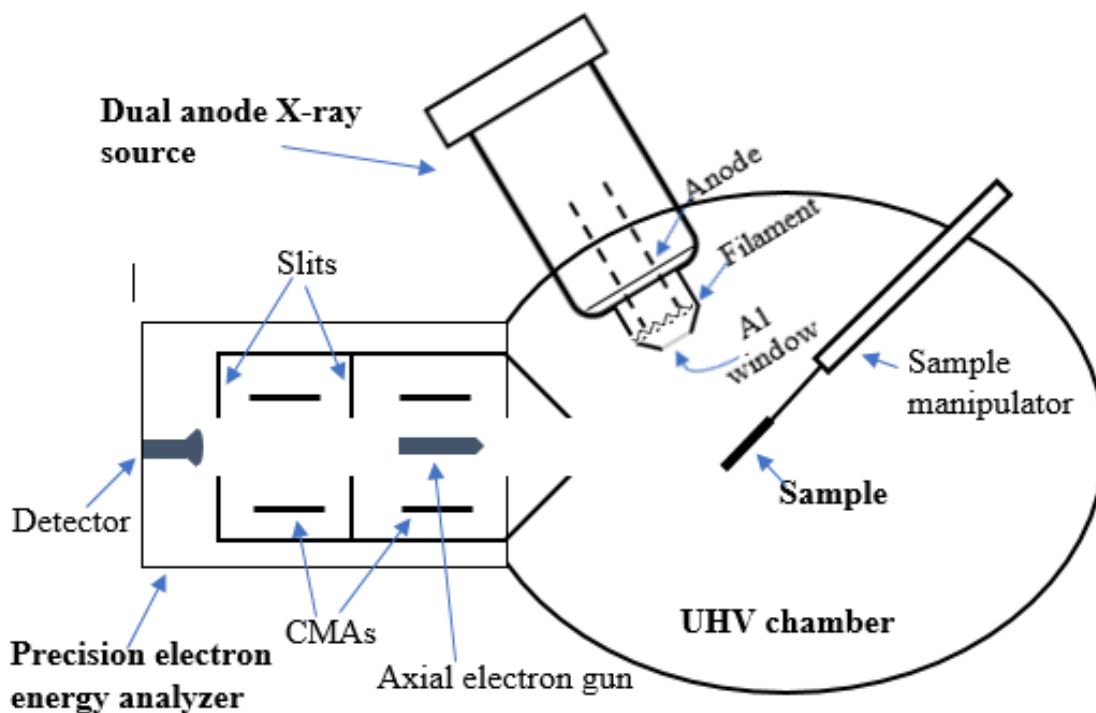


Figure 2.18. Schematic diagram of the XPS experimental setup in the Burghaus laboratory^{28, 74}

Typical XPS spectra consist of a discrete series of lines or peaks with the characteristic stepped background. Spectral lines or peaks can be core electron peaks, Auger electron peaks and/or valence band spectra. Majority of the XPS spectra consists of core electron peaks. Positions of these peaks/ lines can be used to identify elements and their electronic states. Intensities of these peaks to can be used to quantify the elements or compounds.

2.7. Ultraviolet-visible spectroscopy

2.7.1. Introduction

Ultraviolet-visible spectroscopy (UV-Vis) is one of the simple analytical tool used in the field of chemistry and biochemistry for qualitative and quantitative identification of materials. Interaction of the matter with the ultraviolet and visible radiation in the electromagnetic spectra is measured in this spectroscopic technique. In analytical and inorganic chemistry, UV-visible spectrometric techniques are extensively used to quantify inorganic molecules or ions. Several organic molecules, functional groups, complex biomolecules such as enzymes can also be analyzed utilizing UV-Vis techniques. Qualitative identification of compounds by matching the spectra with standards is one of the common applications of UV-Vis. Surface analysis is also possible employing both absorption and reflection spectroscopic modes depending on the transparency and surface roughness of the analyte.⁷⁵⁻⁷⁷

2.7.2. Theory

UV-vis is a type of electronic spectroscopic technique which involves intramolecular (Figure 2.19) or intermolecular (charge transfer) electronic transition by the interaction of the analyte with the UV or visible radiation.⁷⁵ Understanding the electronic structure of the molecule is necessary to get insights into this spectroscopic technique. Concepts of the molecular orbital theory can be used to understand the electronic structure of the polyatomic molecules.⁷⁶ In molecular orbital theory, bonds between the atoms are represented by molecular orbitals (MOs), which are considered as linear combinations of respective atomic orbitals. Those atomic orbitals (AOs) are combined by considering their relative energies and symmetry properties. Bonding MOs, anti-bonding MOs, and non-bonding MOs are three possible types of MOs. Bonding MOs are more stable than respective AOs (lower in energy), which contains a high concentration of

electron density in the region between the nuclei. Anti-bonding MOs have zero electron density between the nuclei, due to the cancellation of electronic wave functions, which have higher energy compared to the parent AOs. Electrons in non-bonding MOs have similar energy to the parent AOs and does not interact positively or negatively with the chemical bond.

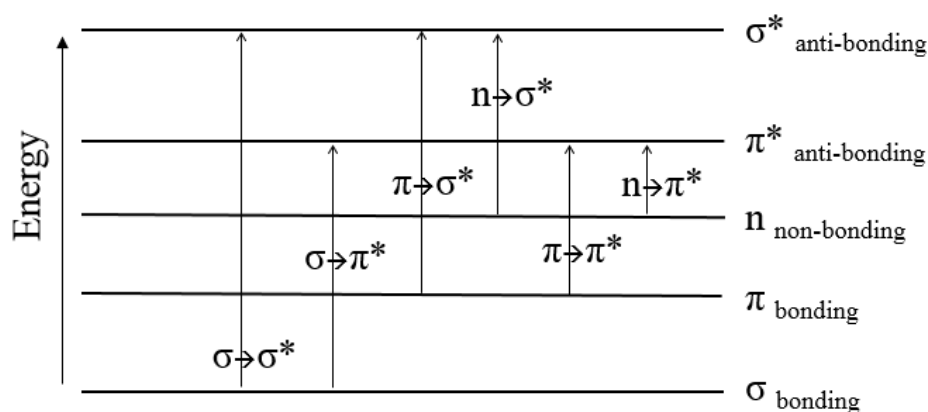


Figure 2.19. Possible electronic transitions in UV-Visible spectroscopy⁷⁵

Generally, single bonds have σ to σ^* transitions and occasionally n to σ^* transitions. These electronic transitions typically required higher energy than UV-Visible radiation ($\lambda < 200$ nm). Molecules with π electron systems and non-bonding electrons exhibit π to π^* and n to π^* electronic transitions, which generally required the energy in the range of UV-Visible region (200-800 nm). Transition metals and transition metal complexes exhibit absorption in the UV-Visible region due to electronic transitions between d electronic states. A similar type of behavior can be observed with lanthanides. UV-Visible absorption can also be observed due to charge transfer processes as well.⁷⁵

The experimental measurement of UV-Visible molecular absorption spectra involves bombarding the UV-Visible radiation on the analyte and measure the transmitted radiation through the sample (transmittance mode) or measure the reflected/ scattered radiation (reflection mode). The former is the most extensively used mode in which transparent liquids or thin films are

characterized. The latter method is applied for the analysis of surfaces or powders with high surface roughness. In such cases, reflection of the UV-Visible beam is not specular and therefore the transmitted intensity through the sample is too low to detect. In this sort of conditions, UV-Visible diffuse reflection spectroscopy (DRS) is generally utilized, in which diffusively reflected radiation from the sample is collected employing a suitable detector, such as semispherical collectors.⁷⁸

2.7.3. Instrumentation

In this project, UV-Visible transmittance mode was extensively used since the interested samples were transparent thin films (see section 4.3.1). If the radiation intensity of the incident beam is P_0 and the transmitted radiation intensity is P , then the transmittance (T) can be defined as, $T = P / P_0$. But. The molecular absorption (A) has a logarithmic relationship to the transmittance, which is defined as, $A = \log_{10} (P_0/P)$ or $A = -\log_{10} (T)$.⁷⁵

Varian Cary 50 bio UV-Visible spectrophotometer and Cary 5000 UV-Vis-NIR were used to analyzing perovskite thin films in this study (see section 4.3.1). The former is a simple and budget priced UV-Vis, which equipped with a xenon flash lamp as the radiation source, offering many advantages over traditional UV-Vis. This instrument is specifically designed for biological sample analysis in the range of 190-1100 nm, which includes inbuilt methods for kinetic data acquisition and interpretation. Cary 50 was mainly used in this project. The latter is a high-performance UV-Vis, which have superb photometric power in the 175-3300 nm range. Cary 5000 has the ability to analyze a variety of materials including various types of nanomaterials, with either transmittance mode or with diffuse reflection mode. Cary 50 only allows the transmittance mode.⁷⁹⁻⁸⁰

Cary 50 comes with a Xenon pulse lamp as the single source, that has a very long lifetime (3×10^9 flashes according to the Varian Cary 50 brochure). It can scan up to 24000 nm per minute,

which enables to scan the whole wavelength range in less than 3 seconds. Cary 50 equipped with a Czerny-Turner monochromator with approximately 1.5 nm fixed spectral bandwidth, and a dual silicon diode detector. The simplicity of the data acquisition and the high sensitivity of the instrument enabled fast and reliable qualitative analysis of perovskite thin films, which will be discussed in section 4.3.1.⁷⁹⁻⁸⁰

2.8. Scanning electron microscopy

Scanning electron microscopy (SEM) is a widely used imaging technique which has the capability of generating high-resolution images of a variety of sample surfaces employing a high energy electron beam as a probe. SEM can be used to obtain information such as topography and morphology, crystallographic structure, orientations of grains etc., of sample surfaces. Most of the SEMs have an in-built technique called energy dispersive X-ray spectroscopy (EDX) to analyze elemental and chemical composition. In this study, SEM was utilized as a supplementary technique to qualitatively characterize MAPbI₃ perovskite thin film surfaces (see section 4.3.1).

A typical SEM produces a high energy electron beam using either a thermionic emission gun or a field emission gun. By applying an acceleration voltage in between 5-200 kV, the energy of the produced electron beam can be controlled accordingly. Using a set of lenses, the produced electron beam is directed toward the sample. Three main characteristics of the electron beam are controlled by the electron lenses. Objective aperture reduces the beam angle to minimize the aberration effects. Condenser lens and objective lens help to control the beam current and working distance of the electron beam. Weak condenser lens produces high beam current which leads to a larger probe size and hence deteriorated resolution. Strong condenser lens leads to small beam current and smaller probe size, which leads to better resolution. Likewise, the incident electron beam can be controlled.

Once the incident electron beam hits the sample surface, it can produce characteristic X-rays, secondary electrons such as Auger electrons, backscattered electrons etc. In SEM, secondary and backscattered electrons are used to produce images of the specimen. Therefore, there can be two major types of detectors to detect secondary electrons and backscattered electrons. Detectors such as Everhart-Thornley detector facilitate the detection of both types of electrons.⁸¹

JEOL JSM-6490 LV SEM was used in this study to qualitatively characterize MAPbI₃ perovskite sample surfaces. This is a high-performance SEM which facilitates variable pressure modes, allowing the analysis of variety of samples such as polymers, nanomaterials fresh biological samples etc. Integrated Noran system six X-ray microanalysis system facilitates the analysis of the elemental composition of the materials.

2.9. X-ray diffraction

X-ray diffraction (XRD) is a well-established analytical technique, which is primarily used for the phase identification of crystalline materials. This technique can also be used to determine the unit cell parameters of crystalline, poly/microcrystalline materials. XRD was utilized in this study as a supplementary technique for the qualitative characterization of the MAPbI₃ perovskite samples and, to determine the different phases present in the characterized samples (see section 4.3.1).

X-ray source, sample holder, and the detector are the major components of a typical X-ray diffractometer. In the X-ray source, X-rays are generated by bombarding high energy electron beams on a target metal, such as copper. Typical X-ray diffractometers have monochromators to narrow down the probe X-ray beam to characteristic k_{α} or k_{β} radiation. This monochromatic X-ray beam is bombarded on the sample surface, which generates a characteristic diffraction pattern depending on the types of the atoms and the arrangement of the atoms in the crystal structure.

Single crystal X-ray diffraction and powder X-ray diffraction are two major available XRD techniques. Former needs a well-defined single crystalline sample, in which, unit cell dimensions, bond lengths, bond angles, details of the site ordering and the internal lattice structures can be determined. The latter is the most convenient method, which can be applied for crystalline, poly/microcrystalline powdered samples for the qualitative identification of materials, identification of different phases in materials and, determination of relative concentrations of each phase etc. Bruker AXS D8 Discover multi-purpose X-ray diffractometer was utilized to obtain powder XRD patterns of poly-crystalline MAPbI₃ perovskite thin films in this study.⁸²

3. FUNDAMENTAL SURFACE PROPERTIES OF TWO-DIMENSIONAL SILICA AND ZEOLITES

Zeolites and silica are some fascinating classes of materials, that have been extensively used in heterogeneous catalysis and semiconductor technology-based applications in many industrial processes. Understanding the fundamental properties of these materials are important and beneficial. Due to the lack of surface analogs and the insulating nature of these materials, they have been rarely studied utilizing UHV based powerful surface analytical methods. But, recent developments in the field of the crystalline silica film synthesis and understanding of the detailed chemical structures of silica opens new research interests in the field of surface science and heterogeneous catalysis.

Synthesis of mono-atom thick crystalline silica (silicatene) and conversion of the silicatene structures to 2D-zeolites are the main objectives of this research. We targeted heterogeneous catalysis related surface chemistry on silica and zeolites. Employing thiophene as a probe molecule, hydrodesulfurization (HDS) related surface chemistry on silica was studied extensively. The motive of this study was to deposit Mo nanoclusters on synthesized 2D-zeolites, that can be considered as a sinter-tolerant model catalyst for HDS reaction. Micropores of the zeolite framework can be utilized as the nucleation centers for the Mo metal cluster growth, which enables the fabrication of thermally rather stable catalyst with monodispersed Mo nanoclusters.

Fundamental surface properties and gas-surface interactions of silicatene and zeolites have not been explored in detailed employing powerful UHV based surface analytical techniques, which was targeted in this project. We introduced novel strategies to synthesize and characterize these challenging classes of materials. Detailed studies of gas-surface interaction kinetics and dynamics

related to HDS and support effects of silicatene (as a catalytic support) will be discussed in detail in this section.

3.1. Introduction

3.1.1. Silicatene and zeolites

Zeolites are mainly composed of aluminosilicates with microporous structures. Several naturally occurring zeolite structures have been identified with unique three-dimensional frameworks. Most of these zeolite frameworks are comprised of interconnected $[\text{SiO}_4]^{4-}$ and $[\text{AlO}_4]^{5-}$ tetrahedral molecular building units via oxygen atoms, keeping Al or Si atoms in the centers to form three dimensional networks of corner-sharing tetrahedra.⁸³⁻⁸⁴ 3D Zeolites have been extensively studied and developed as catalysts, catalytic supports, and sorbents owing to their microporous structures and large specific surface areas.⁸⁴

There are two major classes of zeolites namely 3D zeolites and layered (2D) zeolites. Former can be described as covalently bonded framework structures extended three-dimensionally, whereas the latter is covalently bonded framework structures propagated in only two-dimensions. Several types of layered zeolite materials have been synthesized with similar porosities and structures as 3D zeolites.⁸⁴ Synthesis of layered zeolite materials has attracted considerable attention in the recent past, not only due to catalysis related applications but also for technological applications such as semiconductor industry and microelectronic processing.⁸⁵ Therefore, it is worthwhile to explore the fundamental properties of these zeolitic materials employing highly sensitive surface analytical methods to understand the kinetics and dynamics of basic surface processes prior to technological applications.

However, it is rather difficult to study conventional zeolites employing surface analytical tools, mainly due to the insulating nature and the structural complexities. Surface charging arises

due to the electrical non-conductivity is a common problem encountered in the surface science experiments. By fabricating thin films of the respective material on a conductive metal substrate (that can dissipate the surface charge), surface charging effects can be minimized.⁸ Therefore, ultra-thin silicon dioxide films fabricated on metal and semiconductor supports attract considerable attention as 2D analogs to layered zeolite materials. Initially, poly-crystalline SiO₂ thin films have been thermally grown on single crystalline silicon surfaces, which resembles the structure of vitreous (amorphous) silica. Afterward, single crystalline silica thin films were grown on transition metal surfaces such as Mo(110), Mo(112), Ru(0001) and Pt(111).^{8, 85} Among these substrates, Mo(112) is found to be the most prominent substrate to synthesis silicatene films due to strong metal-oxygen bonding promoted by Mo surface atoms and the ability of Mo(112) crystal lattice to accommodate hexagonal structures without severe distortions.⁸⁵

Synthesis and characterization of these silicatene films are challenging and time-consuming. Initially, Goodman, et al., and Freund, et al., introduced well-controlled UHV based silicatene film fabrication techniques to the surface science community.⁸⁶⁻⁸⁷ Afterward, few other research groups, including our group (this dissertation work) described various silicatene preparation and characterization techniques on metal substrates.⁸⁸ Recently, these silicatene films were modified by co-deposition of Aluminum, initially by Goodman, et al., and then by Freund, et al., to form mixed Al₂O₃- SiO₂ thin films, which can be considered as 2D analogs to Zeolites.⁸⁹⁻⁹⁰ Formation of this ultra-thin zeolite-like structures on metal surfaces enables the study of fundamental surface properties of these materials employing powerful surface analytical techniques.

At the initial stage of silica/ zeolite film synthesis, low energy electron diffraction (LEED) has been widely used to study the surface crystallinity, while Auger electron spectroscopy (AES)

and X-ray photoelectron spectroscopy (XPS) has been used to obtain the elemental and chemical composition. Employing thermal desorption spectroscopic (TDS) techniques, stability and the gas-surface interaction kinetics of these thin films have been investigated.^{86-87, 89, 91} In the latter stage of silica film synthesis, sample morphology, and crystallinity has been extensively studied employing scanning tunneling microscopy (STM) together with density functional theory (DFT) calculations.⁹² We were able to come across a novel method to characterize the crystallinity of silica films based on the hydrophobic behavior of the films, utilizing a kinetic approach in this project.⁸⁸

One of the potential applications of 2D zeolite-like thin films targeted in this investigation was its use as a catalytic support for noble metal nanoparticles. Crystalline silica films resemble the bulk structure of silica, which consists of inert Si-O-Si bonds, that can be considered as a perfect platform for metal cluster deposition (physisorbed metal clusters in the microporous structure without a significant change in the electronic structure of the metal atoms). Supported catalyst metal/metal-oxide nanoparticle agglomeration during the catalytic processes is one of the major challenges encountered in the heterogeneous catalysis, that can eventually decrease the catalytically active surface area and hence the activity of the catalyst. By promoting strong catalyst-support interactions, agglomeration effects can be minimized. We hypothesized that the 2D zeolites with microporous structures have the ability to reduce the sintering effects of supported metal nanoparticle/ clusters by promoting strong metal-support interactions. Synthesis and characterization of silicatene/ zeolites and investigation of the structural and gas adsorption properties towards hydrodesulfurization related surface chemistry of thiophene will be discussed in this section.

3.1.2. Hydrodesulphurization

Hydrodesulfurization (HDS) is the process of removing sulfur from sulfur-containing compounds. HDS is an important step in petroleum refining, in which the contaminated natural gas is treated with hydrogen in the presence of the catalysts to form refined petroleum products. HDS is performed at elevated temperatures (320-440 °C) and pressures (10-150 atm) with supported heterogeneous catalysts.⁹³⁻⁹⁴ Transition metal sulfides such as MoS_x, WS_x, and CoMo or NiMo mixed sulfides supported on γ-Al₂O₃ and SiO₂-Al₂O₃ mixed oxides are used as catalysts most frequently.⁹³⁻¹⁰⁰ In order to improve activity, selectivity, specificity, and stability of the catalyst, a mechanistic understanding of the catalytic process, role of the catalyst, specific active centers of the catalyst, support effects etc., should be recognized. Therefore, several experimental and theoretical model studies have been conducted to understand the HDS catalytic process.

HDS of thiophene on different model catalytic systems such as MoS₂,^{96, 98} Co-Mo,¹⁰¹ Ni-Mo,^{99, 102} and few WS₂ based systems have been studied experimentally and theoretically to improve the catalytic systems and reveal the HDS mechanisms. Among these systems, MoS₂ supported on γ-Al₂O₃ has been studied extensively, which closely resembles the industrial HDS catalyst. Thiophene has been chosen as the probe molecule in most of the studies, because of the simplicity and the structural similarity of the other sulfur-containing complex hydrocarbons present in the crude petroleum.^{96-98, 100} Both aliphatic and aromatic sulfur-containing impurities are commonly encountered in crude petroleum. Other than thiophene, there are aromatic heterocycles such as benzothiophenes, dibenzothiophenes, substituted benzothiophenes etc., which are challenging compounds encountered in actual HDS processes. These are challenging compounds to utilize in surface science model studies as well. Typical molybdenum catalyst utilized in the studies are reduced by sulfidation from the common +6 oxidation state to +4 state,

forming MoS₂.⁹⁸ Molybdenum atoms with the oxidation number lower than +4 with sulfur vacancies are found to be the active catalytic centers.

Effect of the oxidation state of Mo, Mo-cluster sizes, Mo surface structures have been investigated to understand the active centers for HDS reaction.^{96, 98} Isolated Mo clusters with different oxidation states, Mo(ii) and Mo(iv) depicts similar reactivities to MoS₂. Furthermore, active sites with single Mo(iv), Mo(iv) dimers, and multiple atomic centers show similar reactivities, which indicates that the multiple-atomic centers are not necessarily required for the HDS reaction.⁹⁸ Based on kinetics model studies, two different types of desulfurization mechanisms are proposed, which are direct desulfurization (DDS) and hydrogenation followed by desulfurization (HYD).⁹⁶⁻⁹⁷ Based on the type of the mechanism, some researchers suggesting different active centers⁹⁶ while few studies have suggested the same active centers¹⁰³ for HYD and DDS routes. In most studies, MoS₂/ WS₂ edge sites found to be catalytically active while basal plane surfaces of MoS₂ seems to be catalytically inactive.⁹⁶ Still, much less is known about the actual active centers and there are considerable debates about the proposed mechanisms.

In DDS type pathways, the C-S bond of thiophene is directly cleaved before hydrogenolysis, leading to the formation of unsaturated hydrocarbons (alkenes), which can undergo hydrogenation afterward to form saturated hydrocarbons.¹⁰⁴ In HYD type, hydrogenation of both C=C bonds in thiophene is evident before C-S bond cleavage.¹⁰⁵ Two-point adsorption of the molecular thiophene on the catalytic surface followed by DDS or HYD, and then the desorption of alkanes/ alkene followed by regeneration of the catalytic surface by associative desorption of hydrogen sulfide is evident. The rate determining step of this HDS mechanism can be either carbon-sulfur bond scission or catalytic surface regeneration (desorption of H₂S). Therefore, it is important to study the fundamental gas-surface interactions of molecular thiophene and hydrogen

as the reactants, and n-butane, 1-butene, butadiene, tetrahydrothiophene, H₂S etc., as the products on the catalyst and the catalytic support to understand the mechanistic properties.

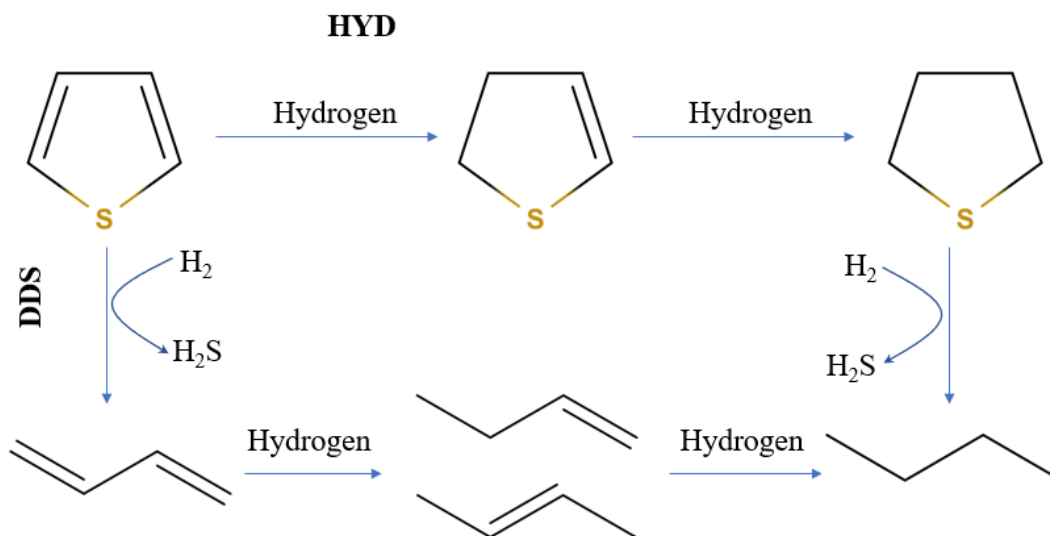


Figure 3.1. Schematic representation of the HYD and DDS pathways in catalytic HDS⁹⁷

3.2. Project structure

The first part of this project was synthesis and characterization of silicatene films on Mo(112). A chemical vapor deposition route was utilized as the fabrication method. Silicatene film growth was characterized by AES and XPS elementally. LEED was used to characterize the crystallinity of the silica films during the film growth. LEED alone was not good enough to confirm the crystallinity of silica and we introduced a novel chemical method, which utilizes water-TDS as a crystallinity characterization tool. As a part of this characterization, water adsorption on various silica thin films with different fabrication procedures was studied extensively.

The second part of the project was devoted to the study of small molecular adsorption on silicatene. We studied hydrodesulfurization related surface chemistry on silicate, in order to understand the potential support effects. Thiophene adsorption kinetics, short-chain alkane

adsorption trends, n-butane adsorption kinetics and dynamics, short-chain alcohol adsorption kinetics, and benzene adsorption kinetics and support effects were studied extensively utilizing TDS, molecular beam scattering, and AES.

As the third stage of the project, 2D-zeolites were synthesized by doping the silicatene films with Al (Al-doped silica and Al₂O₃/ SiO₂ mixed oxide thin films). Sample synthesis was characterized by AES. Chemical properties of silicatene and 2D-zeolites were compared by water-TDS experiments. Investigation of the fundamental gas adsorption properties on 2D-zeolites, fabrication of the Mo-doped hydrodesulfurization model catalyst, and studying the catalytic activity and stability employing thiophene as a probe molecule will be the future directions of this project.

3.3. Synthesis and characterization of silica thin films

3.3.1. Introduction

Synthesis of silica thin films on conducting substrates attracted considerable attention in the recent past to reveal the chemical and structural properties of silica, due to the importance of this material in several technological and catalysis-based applications.^{85-87, 90, 92, 106} Synthesis of thin films on conducting substrates enables the application of powerful surface analytical tools to understand the fundamental properties, which are not applicable with bulk silica or and zeolites, due to the problems associated with the surface charging. Even though there are a number of reports about the silica film synthesis, only two prominent surface science groups, led by D. W. Goodman and H. J. Freund were able to synthesis well-ordered ultra-thin crystalline silica films on conducting substrates, at the time we started our project in late 2014s to the best of our knowledge. Comprehensive gas-surface interaction studies related to heterogeneous catalysis related applications on silica or zeolites were not available. Therefore, we focused on the synthesis

of silicatene, chemical characterization, and fundamental gas-surface interaction studies on silicatene.

3.3.1.1. Choice of the substrate

At the early stages of silica film synthesis, thermally grown silica films on single crystalline silicon substrates were commonly studied, focusing on the Si-SiO₂ interface structures, motivated by microelectronics applications.^{85, 107-108} High temperatures (~700 K) and large oxygen exposures (~ 10¹¹ L) were required to oxidize silicon single crystals.⁸⁵ However, only amorphous silica films were reported, while the structural properties of the Si-SiO₂ interface remain questionable.

Thin and stoichiometric silica films were first reported by Goodman, et al., fabricated on Mo(110) supports. Silicon was vapor deposited at relatively low temperatures (~100 K) in 1×10⁻⁵ torr of oxygen pressure.¹⁰⁹⁻¹¹⁰ The choice of the substrate was simply due to the ease of cleaning the Mo single crystal surfaces and the ability to remove adsorbed oxides just by annealing at UHV. The gas phase precursor for the silica film preparation was SiO, which was formed by the oxidative etching of the heated silicon source in an oxygen atmosphere. As deposited silica films were amorphous, containing several SiO fragments adsorbed on the surface. By post-annealing at UHV, up to 1400 K, ordered thin films were prepared by fusing [SiO₄] units.¹¹⁰

The stability of the silica films synthesized on Mo(110) depended on the thickness. Thin films (<100 Å) were stable up to 1600 K while the thicker films (>100 Å) were stable up to 1900 K. But the surface structures (crystal structures) of the films were not revealed at this point (no LEED patterns has been observed).¹¹⁰ Later, a similar type of silica films on Mo(100) has been synthesized by the same research group.¹¹¹

Even though this was a good starting point for the thin silica film synthesis on metals, the long-range order of the films on Mo(110) and Mo(100) were low due to the lattice mismatch of

those substrates surfaces compared to the common polymorphic forms of silica. A few years later, employing a similar type of synthetic route, Freund, et al., fabricated a well-ordered silica thin films on Mo(112), in which the crystalline order of the films and hence the surface structures were successfully characterized by LEED.⁸⁶ Among the body-centered cubic Mo crystals, the ability of the Mo(112) surfaces to accommodate hexagonal silica structures without severer distortions was the key reason for the choice of the substrate in this study. Few more years later, both Goodman, et al., and Freund, et al., further characterize the crystalline structures of silica thin films on Mo(112) employing LEED⁸⁹ and scanning tunneling microscopy.¹¹² Considering the above reasons, we used Mo(112) as the substrate for the growth of the silica films in the current study.

3.3.1.2. Silica film characterization

Several surface analytical techniques such as AES, XPS, electron energy loss spectroscopy (ELS) or high-resolution electron energy loss spectroscopy (HREELS), TPD, LEED, STM etc., were utilized to characterize silica films.^{85-86, 106, 110, 112}

AES was widely used to understand the film growth characteristics, film thickness, deposition rates, elemental composition, chemical composition, and stoichiometry of the films. AES have distinct features at 91 eV and 76 eV for silicon (Si^0) and silicon dioxide (Si^{4+}) respectively. Even with a low-resolution AES instrument, these features can be distinguished due to the large chemical shifts, which is a huge advantage. Other than that, the Si^{4+} state has AES features at 63 eV and 59 eV.²⁶ With sensitive AES instruments, it is possible to detect different types of chemical states of silicon such as SiO , Si_2O , Si_2O_3 etc., since they have different AES chemical shifts.¹¹³⁻¹¹⁵ By detecting the attenuation of the substrate AES peak intensities (e.g. attenuation of Mo (186 eV) peak), film growth rates and film thickness were determined.^{87, 110}

Like AES, XPS also have different chemical shifts for the different oxidation states of silicon. For instance, Si_{2p} photoelectron line has distinct chemical shifts for silicon, silicides, silicon carbides, silicon nitrides, silanes, silicates, and silica in the range of 98 eV to 104 eV binding energies. With high-resolution XPS, different chemical structures of silica films, the presence of the impurities, and film stoichiometry were studied.^{86, 111}

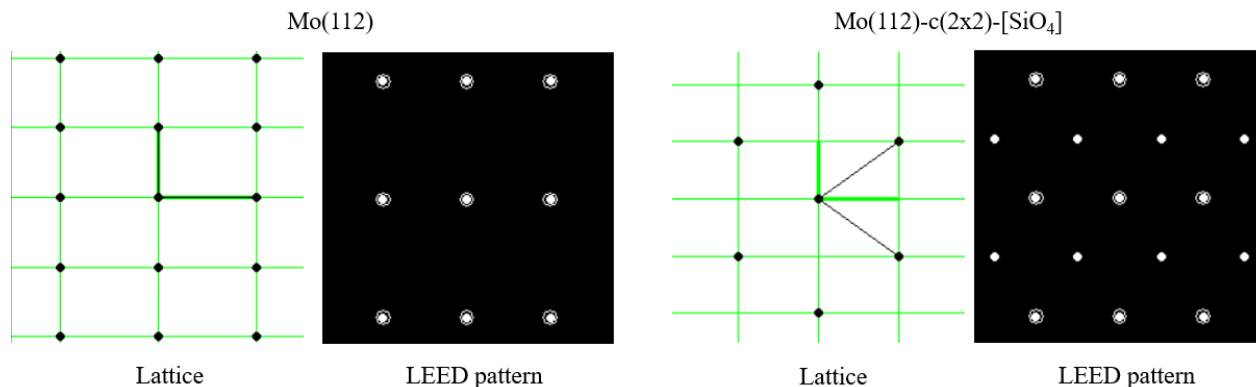


Figure 3.2. Simulated surface structures and LEED patterns of Mo(112) single crystalline surface and crystalline silica thin film on Mo(112) surface.

At the early stages of the silica film synthesis, LEED was the major technique for the crystallinity characterization. Film growth was also characterized by LEED.⁸⁶⁻⁸⁷ Change of the surface structures was detected by LEED before and after each silicon deposition cycles, during the silica film synthesis. Typical silica thin film with the long-range order must display a sharp hexagonal LEED pattern which arises from the overlapped diffraction patterns from the primitive rectangular surface unit cell of Mo(112) and the adsorbed silica layers with $c(2 \times 2)$ superlattice structure. Simulated LEED patterns corresponding to Mo(112) surface unit cell and a silica thin film on Mo(112) are depicted in Figure 3.2.

Stability of the silica thin films such as thermal effects was investigated mainly by ELS and TDS.¹¹⁰⁻¹¹¹ For example, even though the thin films are stable up to 1600 K, significant structural changes were observed according to ELS features at high temperatures. By temperature

programmed reaction studies, thermal desorption of silica thin films was studied, which enabled the investigation of maximum stable temperatures.¹¹⁰ Also, silica coverages were determined by deuterium adsorption studies, employing TDS by Freund, et al.⁸⁶

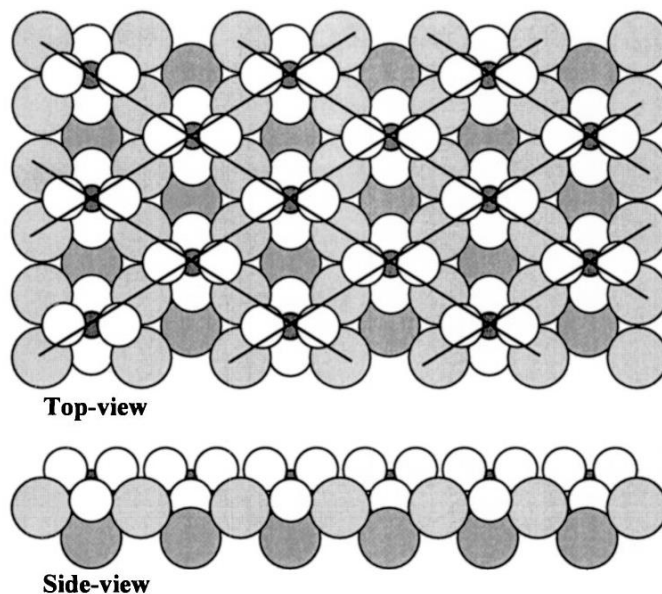


Figure 3.3. Schematic representation of the Goodman's cluster model of silica thin films on Mo(112), representing Mo(112)-c(2×2)-[SiO₄] structure. Copied from the ref.⁸⁷, with permission. Copyright (2004), The American Physical Society.

The most challenging part of the silica film characterization is the surface crystallinity. LEED, HREELS, and infrared reflection absorption spectroscopy (IRAS) were the widely used techniques in the early stages,^{86-87, 106} and STM was introduced to study the surface structures later.^{112, 116} With LEED, the crystal structure of the films, the effect of annealing on defect density etc., were determined.⁸⁶⁻⁸⁷ The epitaxial growth of silica thin films on the metal substrate was confirmed, rather than cluster or island formation, by observing the intensities of fundamental and superlattice LEED spots.^{86, 117} Combined LEED and HREELS studies suggested the formation of well-ordered monolayer structures of silica, having Mo(112)-c(2×2)-[SiO₄] structures. Unique phonon features were identified by HREELS, which were assigned to Si-O-Mo, rather than Si-O-Si in bulk silica.⁸⁷

Based on these observations, Goodman, et al., suggested a structural model for a silica thin film on Mo(112) for the first time. The model is commonly known as the ‘cluster model’, in which all four oxygen atoms in the $[\text{SiO}_4]$ units are directly bonded to the underlying Mo substrate, forming isolated $[\text{SiO}_4]$ clusters adsorbed on the surface, with long-range order. A schematic representation of the top view and the side view of a silica film on Mo(112) according to the cluster model is depicted in Figure 3.3. The absence of the phonon features corresponding to Si-O-Si in HREELS is a strong evidence for the cluster model.⁸⁷ But, this model was challenged later by Freund, et al., with combined STM and computational studies.¹¹² Surface structures and unit cell parameters of silica thin films were investigated with combined STM, IRAS, and theoretical studies.¹¹²

3.3.1.3. Structure of silica thin films on Mo(112)

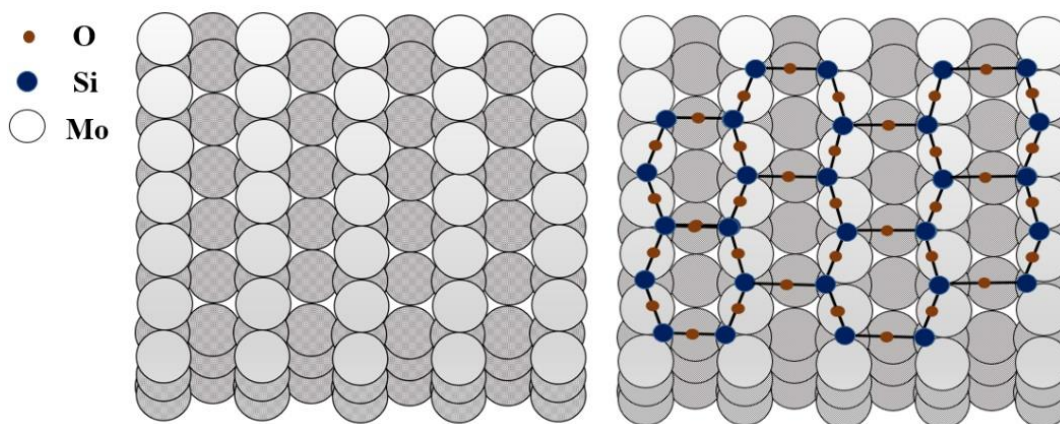


Figure 3.4. Schematic representation of the Mo (112) single crystal (left) and the Freund's structural model of the silica films on Mo(112) with a 2D network of corner-sharing $[\text{SiO}_4]$ tetrahedra superlattice (right).¹¹²

Detailed structural features of the silica thin films were revealed by Freund, et al., with a comprehensive study employing LEED, XPS, IRAS, and STM together with density functional theory calculations.¹¹² The honeycomb-like structure observed by high-resolution STM enables the calculation of the periodicities of the lattice, which are $\sim 5.2 \text{ \AA}$ and $\sim 5.4 \text{ \AA}$ along $[-3 \ 1 \ 1]$, $[-1$

-1 1] directions respectively, further confirming the $c(2 \times 2)$ silica overlayer structure obtained by LEED.^{86-87, 112} The honeycomb-like structures are formed by hexagonally arranged bumps, separated by $\sim 2.6 \text{ \AA}$.¹¹² A single peak at Si_{2p} region in the XPS confirmed the presence of the Si^{4+} state, while the presence of two distinct peaks at O_{1s} indicated the presence of two different oxygen species. According to the chemical shifts, the oxygens were identified as Si-O-Si oxygen and Si-O-Mo oxygen, which suggested that each silica group is bonded to the Mo substrate, as well as to the neighboring silica groups. With these experimental results, Freund, et al., suggested a structural model of corner-sharing $[\text{SiO}_4]$ tetrahedra, with one oxygen bonded to the underlying Mo substrate and the other three oxygens extending the two-dimensional network by the interaction with the neighboring $[\text{SiO}_4]$ tetrahedra. They further confirm this structural model by DFT calculations, ruling out the cluster model proposed by Goodman, et al.^{87, 112}

3.3.2. Results and discussion

Silica thin films were synthesized on Mo(112) employing a chemical vapor deposition technique. Film growth was characterized by AES, LEED, and XPS. Different synthetic methods were analyzed chemically utilizing a water-TDS technique. In this regard, water adsorption on Mo(112) substrate, the oxidic precursor of Mo(112) (Mo(112)-p(1 \times 3)-O), and silica thin films obtained with different preparation procedures were studied comprehensively. Our results indicate that the wettability of the silica thin films strongly depends on the quality of the films, defect densities, as well as the details of the preparation procedures. We introduced water-TDS as a powerful tool to distinguish between well-ordered and defected silica thin films, which seems to be more sensitive than standard LEED (section 3.4.2.2).

3.3.2.1. Substrate preparation and characterization

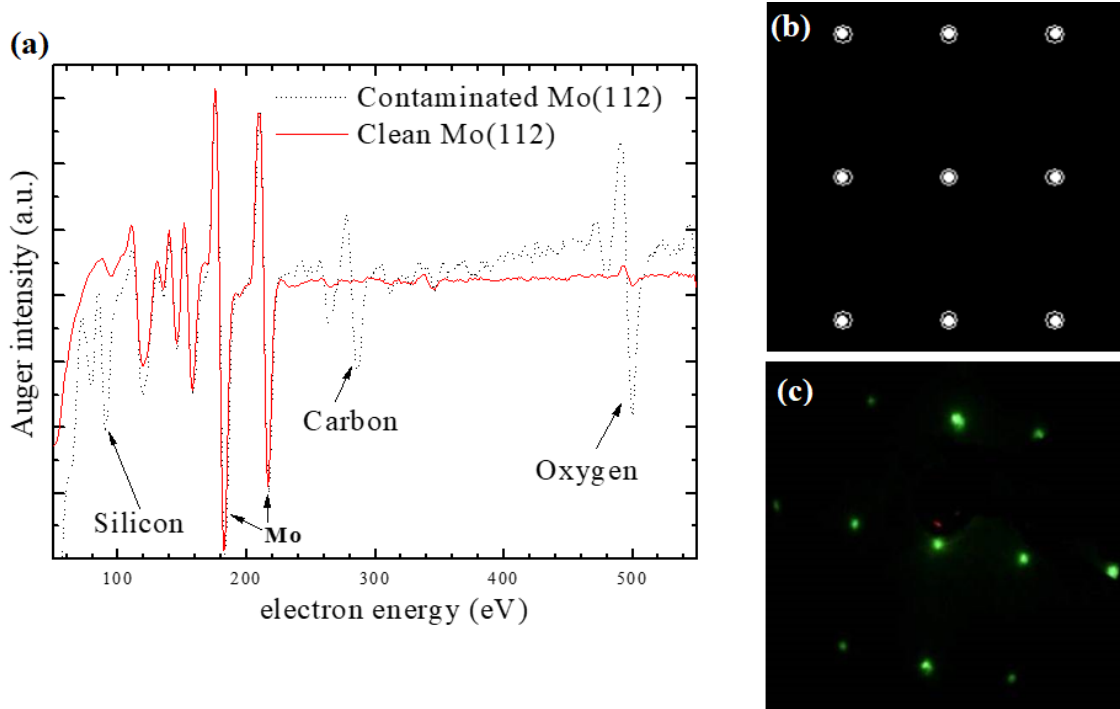


Figure 3.5. Characterization of the Mo(112) substrate (a- AES of contaminated and clean Mo(112), b-Simulated LEED pattern of Mo(112) surface, c-The LEED pattern obtained for clean Mo(112) at 58 eV)

As received Mo(112) single crystal was cleaned by several cycles of Ar⁺ ion sputtering (2 keV, sample current 1.0 μ A, 40 min per cycle), followed by annealing/ flashing at UHV (up to 1600 K) to remove adsorbed carbon and oxygen impurities. If the sample is contaminated with a significant amount of silicon during silicon deposition trials, the sample was annealed at UHV and at oxygen ambient up to 1400 K to obtain clean surfaces. Sample cleanliness was characterized by AES and LEED. As depicted in figure 3.4 (a), a small AES feature at 500 eV is evident on the clean surface, which is characteristic of oxygen. Since the silica film was synthesized on an oxygen overlayer structure, we did not attempt to remove all the residual oxygen as we are adding oxygen to the surface subsequently.

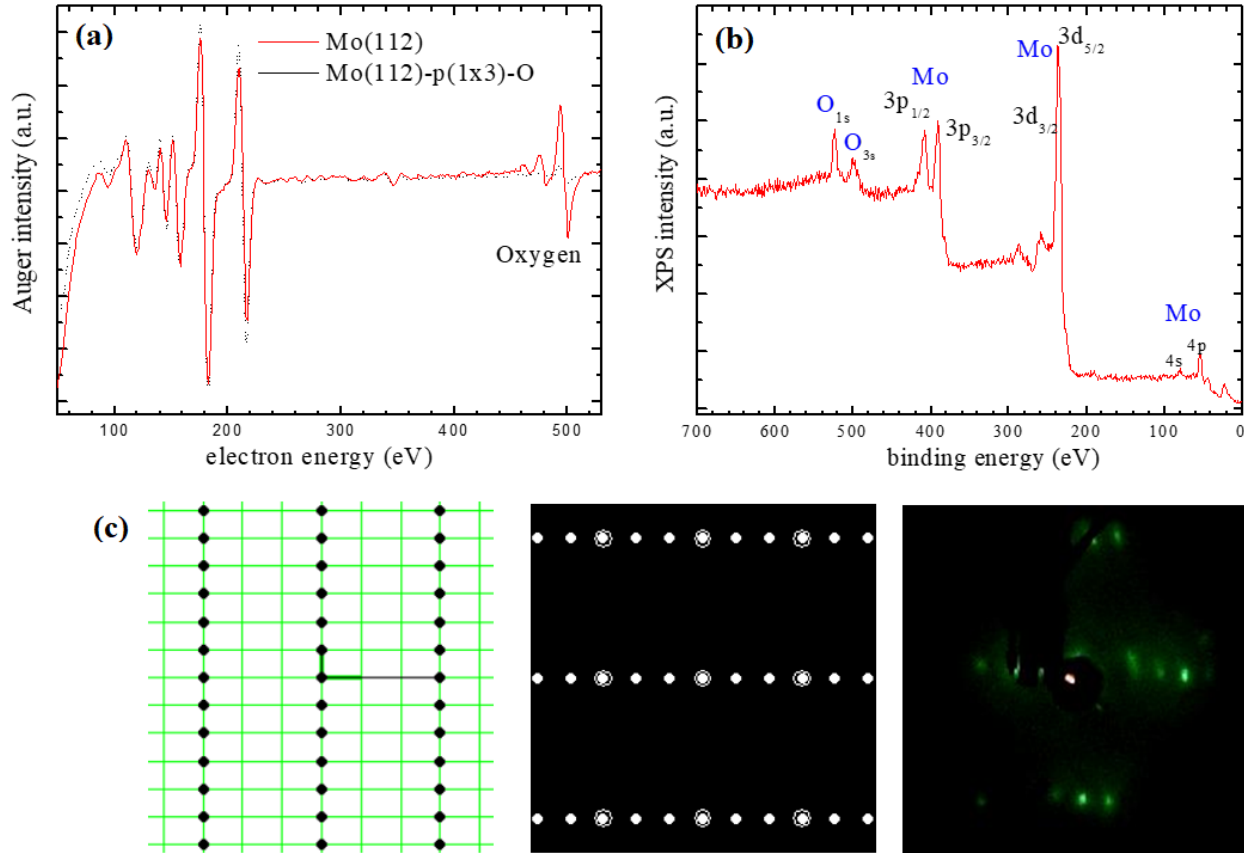


Figure 3.6. Characterization of the oxidic precursor of Mo(112) substrate (a- AES of clean and oxidized Mo(112), b- XPS of oxidized Mo(112), c- Mo(112)-p(1×3)-O simulated superlattice, simulated LEED pattern, and LEED pattern obtained at 58 eV from left to right)

Our silica film preparation procedure was derived by combining Goodman's⁸⁷ and Freund's^{86, 112} fabrication methods. Prior to the silicon deposition step, an oxygen reconstructed Mo(112) surface was prepared. Mo(112)-p(1×3)-O overlayer structure was obtained by annealing the surface at 900 K in $7\text{-}9 \times 10^{-8}$ mbar oxygen pressure for approximately 5 minutes. Multiple oxidation steps were performed if necessary until the required reconstruction pattern is obtained, as the quality of the film was dependent on the initial oxidic precursor structure. Mo(112)-p(1×3)-O structure is explained as a missing-row type reconstruction induced by oxygen, forming an oxide-like surface.¹¹⁸ These oxidic precursor structures have been studied for the epitaxial growth of oxide films such as MoO₃, MgO, TiO₂, and SiO₂ etc., which have potential applications in

heterogeneous model catalysis.¹¹⁸⁻¹¹⁹ The oxide precursor was characterized by AES, LEED, and XPS. Preparation of the well-ordered oxide precursor assisted the epitaxial growth of the SiO₂ thin film on Mo(112).

3.3.2.2. Silica thin film synthesis

Three different nanofabrication methods were tested by combining Goodman's and Freud's methods to obtain well-ordered crystalline silica thin films. In all three methods, silicon was vapor deposited on Mo(112) at variable conditions utilizing a home-made silicon doser (see Figure 3.7), which was designed to evaporate silicon by a heated tungsten filament in contact with a silicon rod.

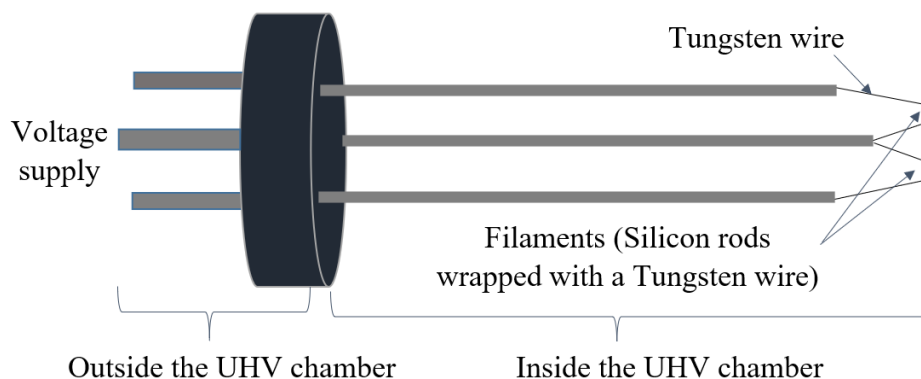


Figure 3.7. Schematic diagram of the home-made silicon doser

In our first method, the silica films were prepared by evaporating silicon onto the oxygen pre-covered Mo(112) substrate. Here, silicon was vapor deposited onto the Mo(112)-p(1×3)-O surface followed by annealing at 800 K for 5 minutes in a 2.5×10^{-7} mbar oxygen environment. Then the surface temperature was increased to 1150 K for an additional 5 minutes (in a similar oxygen background). This procedure was repeated until a constant Si-to-Mo Auger peak ratio was obtained and a sharp hexagonal LEED pattern was seen. The fabrication method used here is closest to the procedure described by Goodman, et. al.⁸⁷

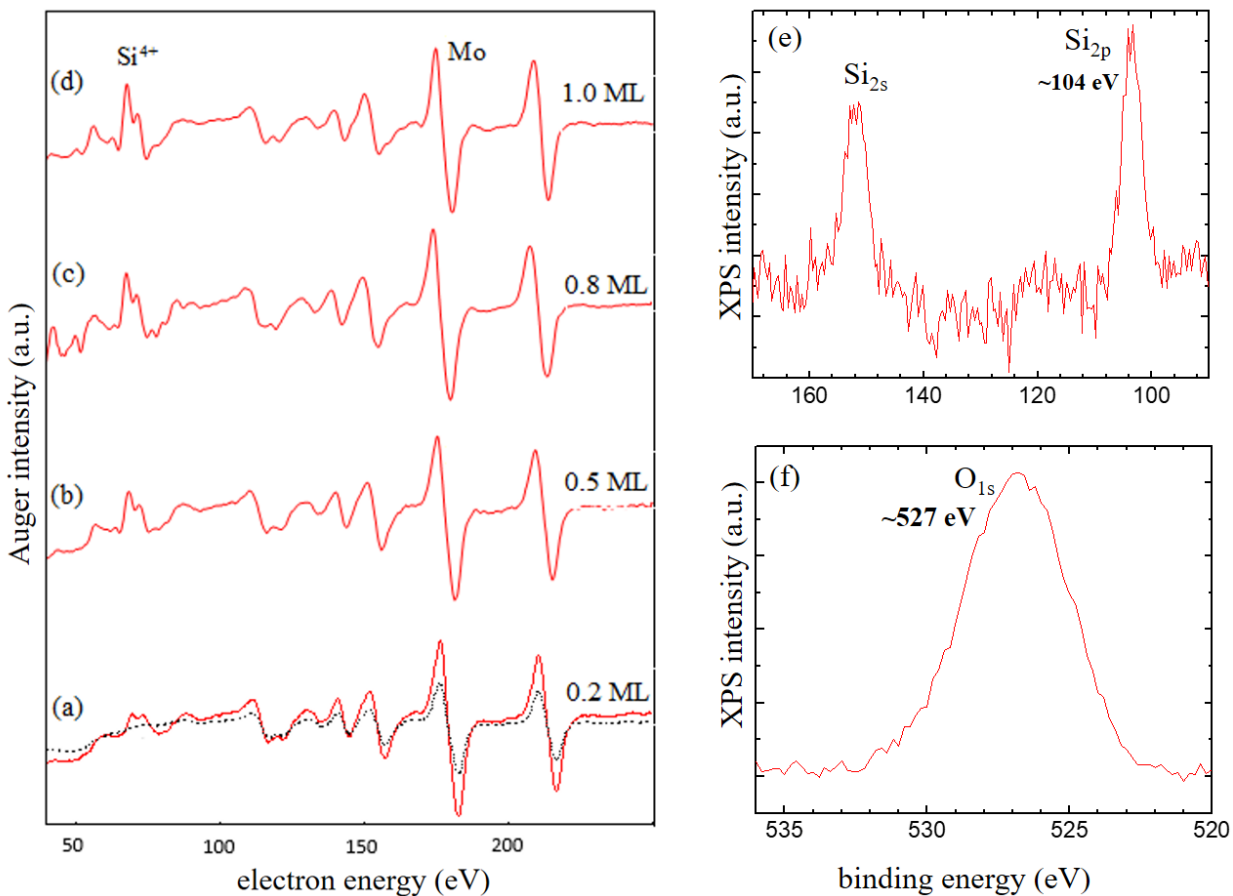


Figure 3.8. (a) to (d)-AES of silica thin films on Mo (112) after each Si dosing and oxidation cycle (In (a), dotted line indicates the clean Mo (112) support), e, f- Characteristic XPS photoelectron lines for silicon (Si_{2p} , Si_{2s}) and oxygen (O_{1s}) for a silica thin film.

Figure 3.8 depicts the silica film growth characteristics investigated by AES in our first method. Silica coverages at different initial silicon fluxes were calibrated according to the monolayer silica film, which was identified due to the self-termination growth of the silica thin films at 1150 K. At lower temperatures (<1150 K), the multi-layer growth of silica thin films was observed. Experimentally, silicon was dosed until a constant silica (Si^{4+}) to molybdenum ratio is achieved, which can be considered as ~1 ML. After forming a monolayer of silica, silica to molybdenum peak ratio remained constant unless the oxygen annealing temperature is decreased. It is possible to form multilayers of silica by controlling the oxygen annealing temperature and pressure.

The crystallinity of the thin films was always depended on annealing temperatures. Large annealing temperatures resulted in a decrease of the Si^{4+} AES peak intensity and disappearance or weakening of the LEED pattern, presumably by desorption of SiO_2 film. Smaller oxygen annealing temperatures resulted in amorphous films, which contained silica together with unreacted silicon impurities, according to AES and LEED. With the preparation method 1, a LEED pattern with high-intensity spots and a low background was observed, which is usually assumed to indicate a surface of high crystallographic order. Also, hexagonal LEED pattern is an evidence for the formation of $\text{Mo}(112)\text{-c}(2\times 2)\text{-}[\text{SiO}_4]$ structure.

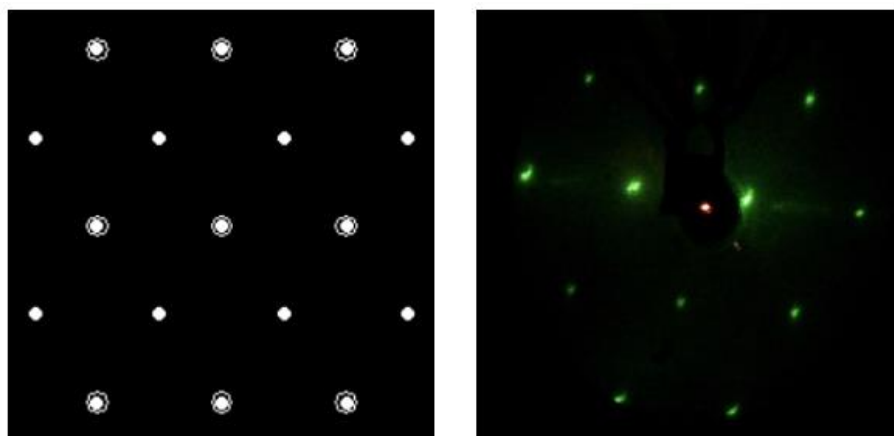


Figure 3.9. Simulated (left) and experimental (right, at 58 eV) LEED patterns obtained for silica thin films on $\text{Mo}(112)$.

In the second nanofabrication method, silicon was vapor deposited on $\text{Mo}(112)\text{-p}(1\times 3)\text{-O}$ with simultaneous oxygen annealing at 900 K in 7×10^{-8} mbar oxygen atmosphere for approximately 6 minutes, which is a single-step method contrast to the method 1. The third method is identical to the second method, in which additional UHV annealing steps were utilized to obtain more ordered silica thin films. Second and third methods are closer to the Freund's technique.¹¹²

Effect of the temperature on silica thin films is depicted in Figure 3.10. Structural changes on the silica thin film already starting to appear even at 860 K, as indicated by LEED.

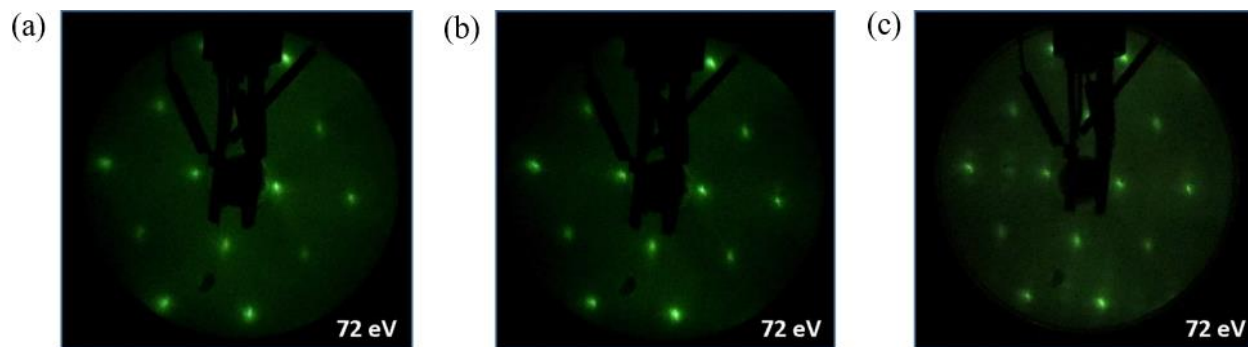


Figure 3.10. LEED patterns obtained after preparation of the silica film on Mo (112) using method III as described above ((a) After water TDS, (b) after flashing to 800 K, (c) after flashing to 860 K).

3.3.3. Summary: Synthesis and characterization of silica thin films

With all three methods, we were able to obtain crystalline silica thin films on Mo(112), identified by characteristic hexagonal LEED patterns, corresponding to Mo(112)-c(2×2)-[SiO₄] overlayer structures. But, the quality of the silica films cannot be determined with LEED and AES alone, as the isolated silica clusters and point defects etc., cannot be identified with these techniques. To identify the presence of isolated silica clusters, other types of defects and oxygen-rich/ oxygen-poor structures of silica, STM and infrared techniques have been utilized in recent studies.¹²⁰ To distinguish between high-quality and defected silica films, a chemical kinetic method was utilized in this study (section 2.4), which appeared to be a more sensitive tool to characterize the crystallographic order, compared to standard LEED.

3.4. Water adsorption on silica thin films

3.4.1. Introduction

Understanding the wetting properties of the surfaces such as silica and zeolites are important because water covers most of the solid surfaces and therefore it plays important roles in electrochemistry, electronic devices, and heterogeneous catalysis. The terms wetting, and non-

wetting are common in surface science, which refers to the epitaxial growth (layer by layer growth) and cluster growth respectively. The same concepts are described as hydrophilic and hydrophobic in the nanoscience and engineering fields. Water contact angle measurements were used in engineering type studies, which are typically carried out in ambient conditions.¹²¹⁻¹²² This type of studies may create problematic situations due to adsorbed impurities and therefore, UHV-based surface spectroscopic studies have been extensively used to understand the water wetting properties of different model systems (see table 2.4.1).

TDS is a simple and effective kinetic tool, which can be used to distinguish between hydrophilic vs hydrophobic interactions, molecularity of the adsorption (molecular vs dissociative adsorption), and dissociation mechanisms. For the surfaces possessing hydrophobic interactions, molecular adsorption of water, typically desorb at low temperatures is evident, which follows 0th order desorption kinetics starting from the smallest exposure.^{37, 123} Formation of the two-phase regimes, like water clusters or nanodroplets, which shrink in size as the temperature increases, and also feeds the desorption process can be observed in hydrophobic desorption kinetics.¹²⁴

Coverage independent desorption is typical for water adsorption on hydrophobic surfaces, starting from sub-monolayer exposures. As the exposure increases, monolayer TDS peaks shifts to a higher temperature, since it takes longer to desorb a large amount of water. Low temperature leading edges of the TDS peaks are lining up, which is an indication of the coverage independent desorption rates. Also, the exponential rise of the leading edges is typical.^{37, 123, 125} In the case of hydrophilic surfaces, favorable interactions between water and the surface are typical, as the name implies. Water-surface interactions can be strong physisorption, molecular chemisorption, dissociative chemisorption etc., which shows drastically different TDS features compared to the water adsorption on hydrophobic surfaces.¹²⁶⁻¹²⁷ Typically, more than one TDS peaks are common,

in that the sub-monolayer peaks can show either no temperature shift or shifting towards lower temperature with increased exposure. 1st order desorption, which is qualitatively characterized by no temperature shifts in the TDS peaks can be seen in the cases of physisorption or molecular chemisorption

Table 3.1. Surface science studies of water adsorption on hydrophilic and hydrophobic surfaces

System	Hydrophobic	0 th order kinetics?	Number of TDS peaks	Method	Ref.
Au(111)	Yes	Yes	1	UHV, TDS	128
O-Au(111)	Yes	Yes	1	UHV, TDS	129
D ₂ -Ni(111)	Yes	Yes	1	UHV, TDS	130
D ₂ -Pt(533)	Yes	Yes	1	UHV, TDS	131
Octane-Pt(111)	Yes	Yes	1	UHV, TDS	132
Water-Pt(111)	Yes	Yes	1	UHV, TDS	133
Antimony(111)	Yes	Yes	1	UHV, TDS	134
Cu(111)	Yes	Yes	1	UHV, TDS	135
Polycrystalline Cu	No	No	1	TDS	37
Ag(011)		Yes	---	HREELS	136
HOPG	No	No	4	UHV, TDS	126
HOPG	No	Yes	1	UHV, TDS	124
HOPG	No	No	3	UHV, TOF-SIMS, TDS	127
HOPG	Yes	---		Ambient, contact angle	124
HOPG	Yes	---		Ambient, AFM	137
Silica wafer	Yes	Yes	1	TDS	37
CVD graphene/silica	No	No	1	TDS	37
CVD graphene/Cu	Yes	Yes	1	TDS	37
PVD graphene/Ru(001)	Yes	Yes	1	TDS	123

When water adsorbed dissociatively, 2nd order kinetics are expected, in which the TDS peaks shift towards the lower temperature with increased exposure at sub-monolayers. A similar type of TDS peak patterns can be observed with 1st order desorption because of the increased repulsive-lateral interactions between the adsorbed water molecules in close proximity as the exposure increases.^{37, 126-127} In both cases, low-temperature TDS features do not line up, characteristic to coverage dependent desorption. At multi-layer water exposures, typical water

condensation is seen in most of the studies, characterized by 0th order kinetics (see section 2.4.3 for more details about the desorption kinetics).^{37, 125}

3.4.2. Results and discussion

UHV based TDS was utilized in this study to investigate the water wetting properties of crystalline silica films and the support effects. Water was adsorbed at low temperatures (90-120 K) on considered surfaces, where the desorption rates are negligible. Then, the surface temperature was ramped linearly and the desorption fragments (water/ fragments of water) was detected simultaneously by a quadrupole mass spectrometer (QMS). We expected to see 0th order desorption for strictly hydrophobic surfaces and 1st or 2nd order desorption for strictly hydrophilic surfaces at sub-monolayer coverages. It is rather difficult to determine the actual saturation exposures precisely due to different water structures possibly formed and the traditional double-layer model.¹²⁵ But, it can be safely assumed that the exposures below 1 Langmuir (one-second gas exposure at 1×10^{-6} torr) will automatically guarantee sub-monolayer exposures since a molecule cannot adsorb with an adsorption probability larger than one. Therefore, TDS features observed at exposures below 1 Langmuir are critical in determining hydrophilic/ hydrophobic characteristics.

We expected to see hydrophobic characteristics for the silica thin films due to the inert nature of Si-O-Si bonds in silica. According to the electronic structure of silica, silicon has low energy empty d orbitals and oxygen has nonbonding electron pairs in p or spⁿ hybrid orbitals. This can result in partial π bonding character in which filled p or spⁿ electrons in oxygen will be shared with the empty d orbitals of silicon. Due to this partial π bond character, the Si-O bond length is shorter and significantly stronger than expected,¹³⁸ which is responsible for the inertness of silica. On the other hand, the presence of point defects and dangling bonds (unsaturated valences) can

lead to the formation of hydrophilic adsorption sites such as Si-H, Si-OH, Si-O. Also, water can be dissociatively chemisorbed on defected sites. Therefore, the presence of defects and dangling bonds may lead to hydrophilic adsorption of water on silica.

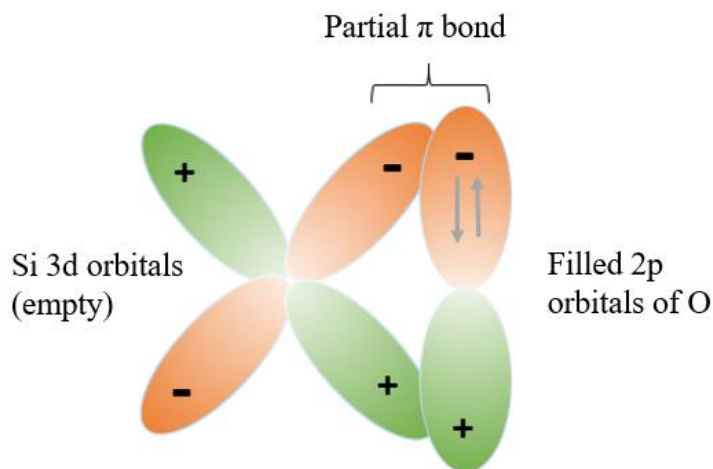


Figure 3.11. Schematic molecular orbital representation of the partial π bond character of Si-O bonds in silica

The Mo support or Mo-O structure can be considered as hydrophilic due to several factors. Functional groups such as Mo-O, trace amounts of Mo-OH, Mo-H etc., may form hydrogen bonds with water. Also, trace amounts of defects can cause dissociative adsorption of water. Since the pore size (diameter) of crystalline silica thin films is estimated to be $\sim 3\text{-}4 \text{ \AA}^{139}$ and the molecular diameter of water in the condensed phase is approximately 2.76 \AA^{140} with 0.96 \AA of O-H length and 104.5° H-O-H angle, water may snug-fit into the 2D silica or sink into the pores, geometrically. Graphene can be considered as a structural analog to silica, which has lattice vectors $a_1=a_2=2.46 \text{ \AA}$, a similar pore size to silica.¹⁴¹ But, water doesn't diffuse through the graphene layers, as the π -electron cloud of graphene prevents the diffusion.^{123, 140} Therefore, it is not only the geometrical concerns but also the electronic structure of the thin film will strongly affect the transparency of the water molecules through the nonporous structure. If water diffuses through the silica thin films, strong chemisorption, which may lead to hydrophilic characteristic can be expected.

In this study, we tried to understand how the chemical properties of the epitaxial silica film affected by the support, whether or not the van der Waals interactions penetrate through the support, which is also referred as the transparency of the thin films, whether these films resemble bulk silica properties or new chemical properties, and also the wetting properties in terms of hydrophilic/ hydrophobic adsorption behavior employing TDS.

3.4.2.1. Water adsorption on Mo(112) and Mo(112)-p(1×3)-O

Water adsorption on Mo(112) support and the oxidic precursor of the Mo(112) was studied. Figure 3.12(a) and (b) depicts a set of TDS curves obtained for the water adsorption on clean Mo(112) crystal. The exposures, χ , given in Langmuir (L), was varied until multi-layer desorption is evident, starting from very small exposures ($\chi \sim 0$ L). Low-temperature molecular desorption of water rules out the dissociative chemisorption, that have been observed in previous studies.^{37, 123} Above ~ 2 L, low-temperature edges of the TDS curves are lined up (see figure 3.12 (b)), which indicates the coverage independent desorption (0th order kinetics), which is due to condensation of water (multi-layer formation structure). The condensation peak is labeled as c peak, which shifts to higher temperatures as the exposure increases (indicated by the dotted line in the figure 3.12 (b)) since the desorption of a large amount of water takes longer time. At sub-monolayer exposures, which is below 2L according to the condensation feature (typically, condensation feature can be qualitatively used to identify the multi-layer formation, below which the sub-monolayer desorption features are present), the TDS peaks shift to lower temperature with increased exposure. Also, the initial rise of the desorption edges does not align, which certainly indicates that the surface is not hydrophobic.

The absence of the 0th order kinetics at sub-monolayer exposure rules out the strict-hydrophobicity. But, the lower desorption temperatures of molecular water indicates weak

physisorption-like interactions between the water and the Mo(112) crystal. The change of the monolayer to the multi-layer regime is identified by the change in the direction of the peak shifts at lower and higher exposures. The condensation appeared at $\sim 2L$ is consistent with the epitaxial growth of the water layers, typical for quasi-hydrophilic surfaces. Presence of one TDS peak at submonolayer coverages with a narrow peak width (~ 25 K) is an indication of a well-ordered Mo(112) surface.

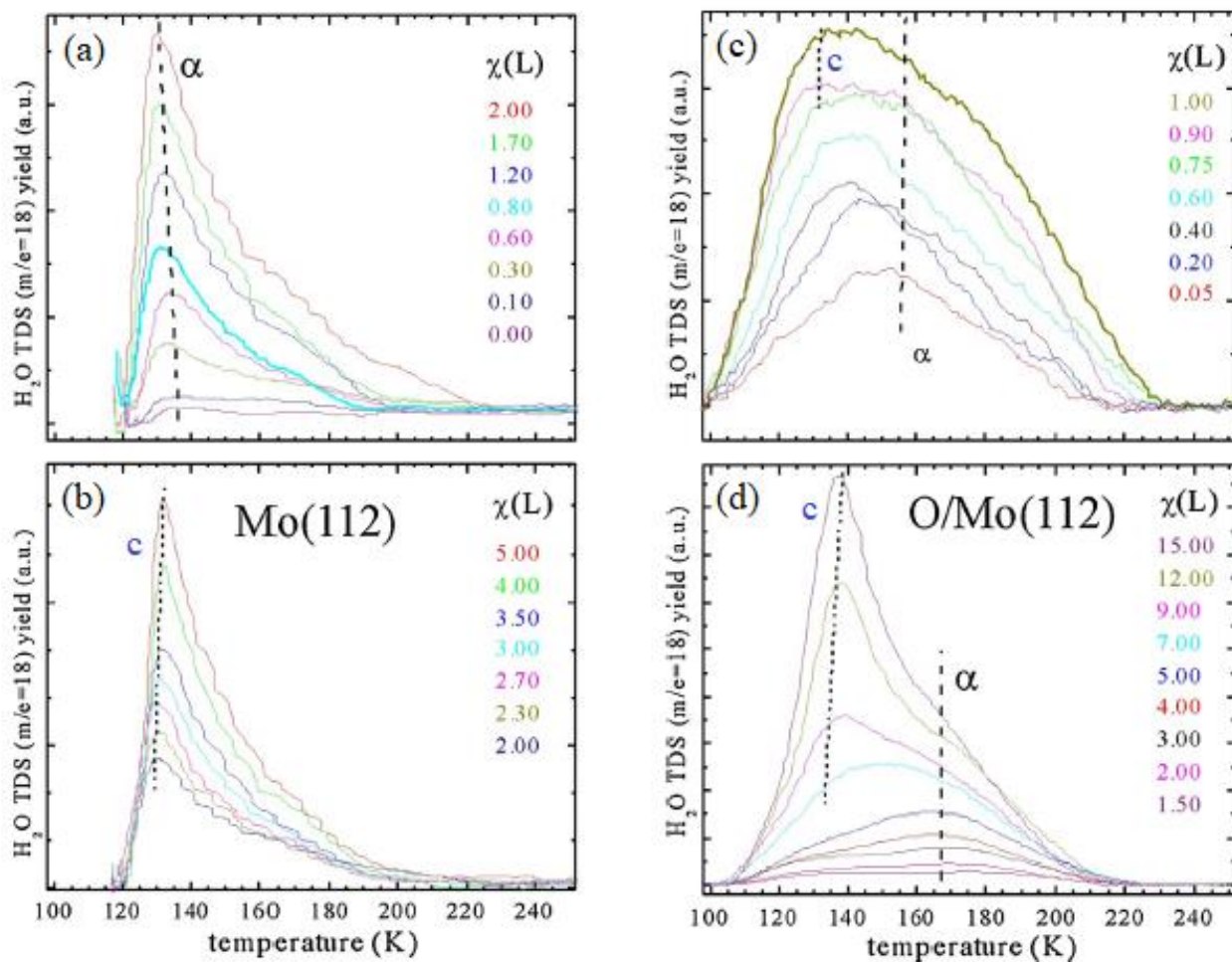


Figure 3.12: Water TDS for Mo(112) (at lower (a) and larger (b) exposures) and Mo(112)-p(1 \times 3)-O (at lower (c) and larger (d) exposures). Exposure is given in Langmuir (1L \sim 1s exposure at 1×10^{-6} torr)

A similar type of TDS experiment was carried out with Mo(112)-p(1 \times 3)-O surface, which can be considered as the actual support for the silica film synthesis. A set of water TDS curves as

a function of the desorption temperature for the oxidic precursor is depicted in Figure 3.12 (c) and (d). Two well-separated TDS peaks is a characteristic feature for hydrophilic interactions. The β peak again indicates the water condensation at large exposures attributed to 0th order kinetics. The α peak is assigned to the desorption of water in the sub-monolayer regime. A distinct increase in the TDS peak width (~85 K) is an indication of the presence of chemically distinct adsorption sites on the surface. The Mo-O sites on the added raw reconstructed surface and the Mo sites on the original surface are potentially different adsorption sites, other than the trace amount of defects/dangling bonds that may present on the surface.

Contrast to the oxidic precursor, the Mo(112) surface does not have clear TDS peak separation which is obviously due to the different binding strengths of the surface-water bonds. Water-water interactions and the water-surface interactions may be comparable since the condensation and sub-monolayer features have very similar desorption temperatures in the case of Mo(112). Both Mo(112) and the oxidic precursor are not strictly-hydrophobic, attributed by water TDS data.

3.4.2.2. Water adsorption on silica thin films

Water adsorption on silica thin films was studied employing TDS. The relationship between the crystallographic order of the silica thin films with the details of the sample preparation, including UHV annealing was investigated with water TDS. Figure 3.13(a) and (b) depicts the LEED patterns obtained for silica thin films on Mo(112) employing method I and II respectively. Both LEED patterns indicate high crystallographic order attributed by high-intensity spots with the low background for the Mo(112)-c(2×2)-[SiO₄] superlattice of silica. Figure 3.13 (c) and (e) represent water-TDS datasets at lower and higher exposures for the 2D silica films obtained by

method I. The data qualitatively looks quite similar to the desorption from the clean Mo(112) surface, which shows low-temperature molecular desorption of water with small TDS peak widths.

But, the leading edges of the first 3 TDS curves, which are from 0-0.7 L do not line up, indicating coverage dependent desorption kinetics at lower coverages. Also, it is clearly evident that the peaks from 0-0.7 L shifted to a lower temperature (see the dotted line in Figure 3.13 (c)) with increasing exposure, not strictly following the 0th order kinetics. Therefore, silica thin films obtained from the 1st method are not strictly hydrophobic.

The same experiment was repeated for the silica thin films obtained by the second method, which is depicted in Figure 3.13 ((d) and (f)). In this situation, leading edges of the TDS features are lining up from the initial exposure and the TDS peak positions shift to higher temperatures with the increased exposure for the entire range, indicating a strictly hydrophobic surface attributed by 0th order desorption kinetics.

In the method III, the effect of the annealing temperatures on the crystallinity of the silica thin films was investigated. Fabricated silica structures were exposed to different temperatures at UHV and interaction with water was investigated by TDS. As the annealing temperatures exceed 860 K, structural changes started to appear in the LEED patterns, as well as in the water TDS curves. At 860 K, sub-monolayer TDS peaks deviate from the 0th order desorption kinetics (as depicted in Figure 3.14 (c)), which was not indicative until 800 K. At 910 K (Figure 3.14 (d)), the deviation is severe, in which the surface looks more hydrophilic (e.g. the desorption peak temperatures for the 0.2 L exposures are increased from ~136 K to ~140 K as the annealing temperature increased from 860 K to 910 K). As indicated from all the TDS data for water adsorption on silica thin films up to this point, only the method II resulted in a strictly hydrophobic

surface while the annealing temperatures critically determine the wetting properties of silica thin films in the method III.

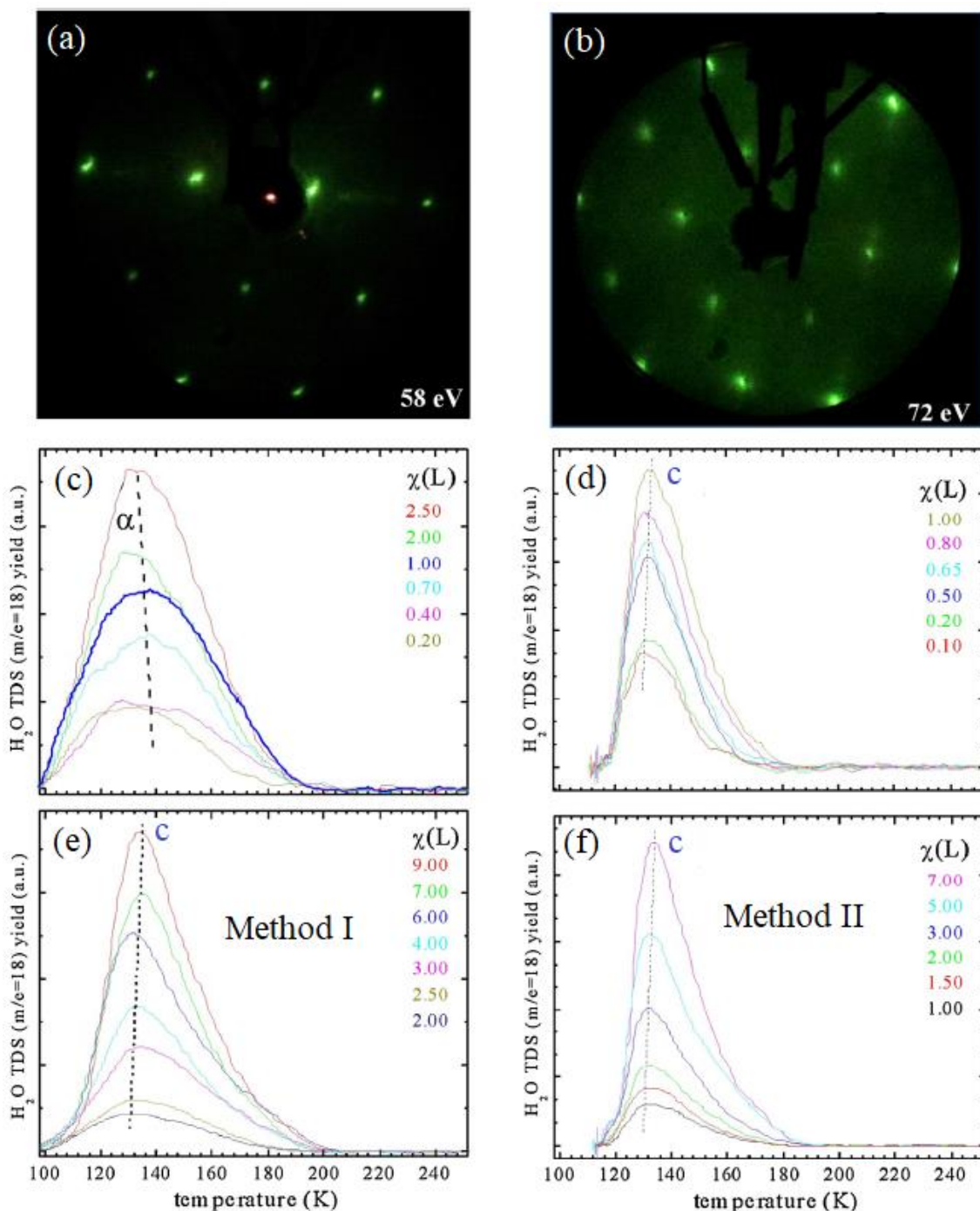


Figure 3.13. (a), (b): LEED patterns of Mo(112)-c(2×2)-[SiO₄] obtained from method I and II, (c)-(f): water TDS curves obtained for the same surfaces ((c) and (e)- Lower and larger exposer of water adsorbed on silica films from method I, (d) and (f)- Lower and larger exposer of water adsorbed on silica films from method II)

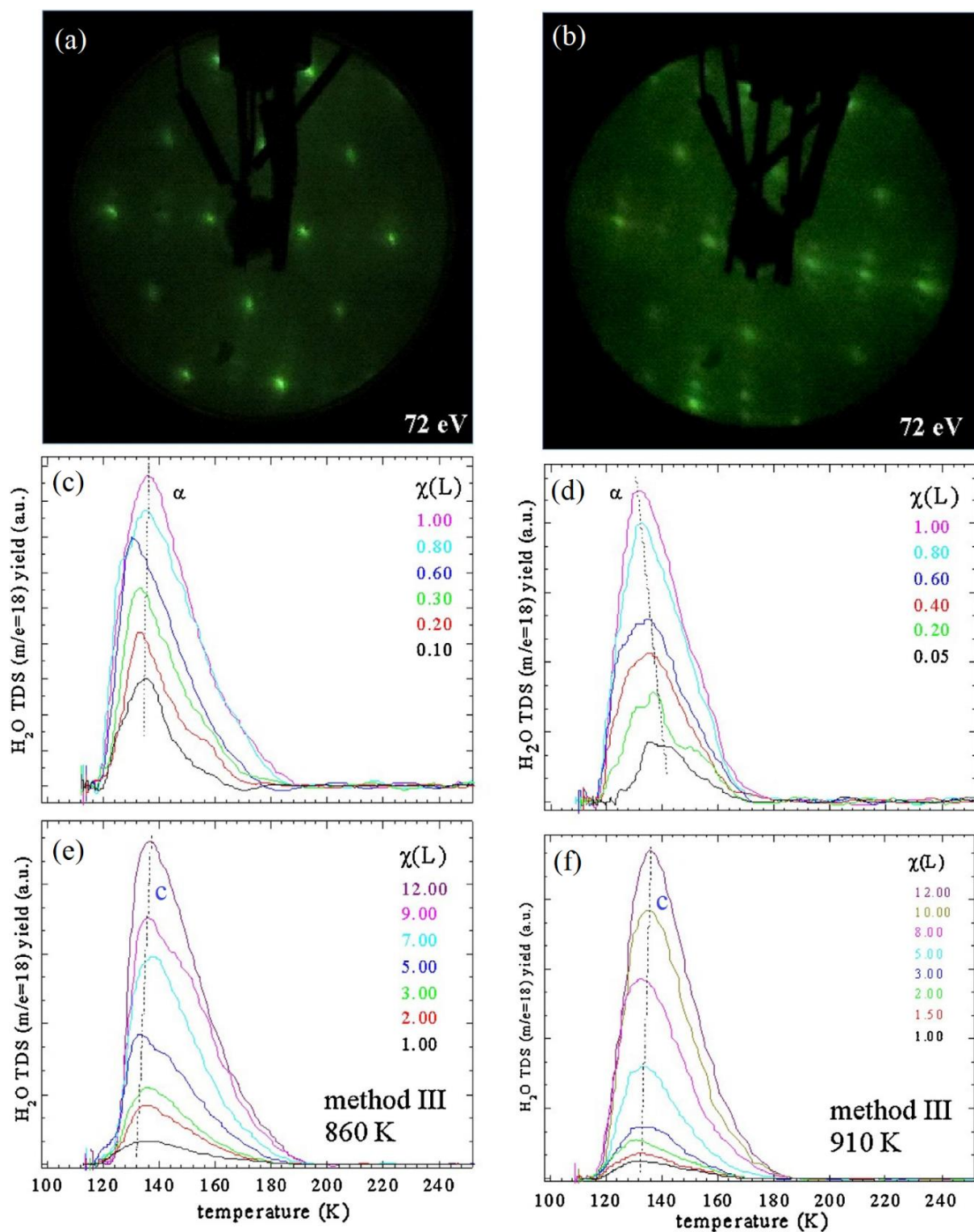


Figure 3.14. (a), (b): LEED patterns of Mo(112)-c(2×2)-[SiO₄] obtained from method III after annealing to 860K and 910 K, (c)-(f): water TDS curves obtained for the same surfaces ((c) and (e)- Lower and larger exposer of water adsorbed on the surface annealed to 860 K, (d) and (f)- Lower and larger exposer of water adsorbed on the surface annealed to 910 K)

However, the quality of the LEED patterns obtained in the methods I, II, and up to 860 K of annealing temperatures in method III appeared to be quite similar. Flashing beyond 860 K resulted in hydrophilic-like surfaces, which also somewhat resembles the hexagonal LEED structure up to 910 K, characteristic to the crystalline silica thin films.

Si-O-Si chains making the 2D-silica structure are inert and therefore, hydrophobic behavior was observed for the crystalline silica films in our study. However, the oxidic precursor of Mo(112) is hydrophilic as indicated by water-TDS since Mo-O surface can facilitate hydrogen bonding with water. Also, we observed quasi-hydrophilic character in Mo(112) substrate. Our silica film preparation methods I and II provide oxygen-rich silica structures, whereas in the 3rd method oxygen-poor structures were obtained, mainly due to different initial oxidation and post-annealing conditions utilized. If the pore structure of silica allows the penetration of water through the film (transparency), or if the van der Waals interactions between the silica film and water are induced by the substrate, we expected to see hydrophilicity with reference to the wetting properties of the support. Also, oxygen-rich and poor substrates should give distinct TDS features in case of transparency. For e.g., the oxygen-rich substrate with excess oxygen adsorbed on the Mo(112) surface should increase the hydrophilicity, which can increase the TDS peak temperatures.

The exact adsorption sites for water on silica surfaces are not known precisely at sub-monolayer exposures. But, there should be distinct TDS features reflecting different adsorption sites with hydrophobic and hydrophilic behavior at the sub-monolayer range if water penetrates through the silica film, which seems not to be the case, depicted by TDS data.

On the other hand, prior experimental and theoretical works indicate that the surface defects such as distortions of SiO₄ tetrahedra, non-bonding oxygen atoms, unsaturated valences etc., are responsible for the hydrophilicity of the silica wafer and amorphous silica.¹⁴²⁻¹⁴³

Theoretical simulations indicate that the defects on the silica surface can induce strong electrostatic fields, which are not common on the pristine supports.¹⁴² Because of that, even dissociative chemisorption of water can be expected on defected silica structures.¹⁴⁴

As depicted by our TDS data, Mo(112)-p(1×3)-O is the least hydrophobic surface. Mo(112) is also not hydrophobic, as it has some weak physisorption interactions with water. For the silica thin films, the detailed preparation conditions and the annealing temperatures determine the wetting properties. Also, in our measuring conditions, wetting seems to be independent of whether the film is oxygen rich or oxygen-poor, which suggest that the water molecules do not penetrate through the nonporous silica even though the geometrical size may just allow that. No water intercalation was also observed.

Higher UHV annealing temperatures increase the hydrophilicity of the silica films. But, until up to a point of significant deformation, hexagonal LEED patterns were observed for silica. High-quality silica films give TDS traces with a smaller width, because of chemically equivalent adsorption sites whereas, the deformed silica films have larger TDS peaks corresponding to chemically inequivalent adsorption sites.

Chemically different adsorption sites such as terminal oxygen, Si, Mo-O and Mo are available on the system. TDS data rules out the transparency of the silica films, which eliminates the substrate effects on the wetting properties. Therefore, peak broadening can be mainly due to the presence of point defects, isolated silica clusters, dangling bonds etc., that can increase the inhomogeneity of the surface. These defects would not significantly change the LEED patterns, but it would affect the wetting properties and reflected by TDS. Therefore, most hydrophobic silica films would be crystallographically more ordered ones with the least amount of defects. As indicated in this study, water TDS can be quantitatively used to measure the defect density of silica

thin films, which is more sensitive than the standard LEED techniques. With that conclusion, high UHV annealing temperatures may induce defects by desorbing Si/ SiO_x traces from the silica films, which can increase the hydrophilicity.

3.4.3. Summary: Water adsorption on silica thin films

The focus of this study was to investigate the water wetting properties and support effects of crystalline silica thin films grown on Mo(112), rather than water adsorption geometries and electronic structures. Water adsorption on epitaxial silica thin films, Mo(112), and Mo(112)-p(1×3)-O was studied. TDS was introduced as a characterization tool to assist the formation of a rather difficult to fabricate two-dimensional silica structures.

Mo(112) surface is not strictly hydrophobic but the oxidic precursor is clearly hydrophobic. Wetting properties are independent of the oxygen-rich or oxygen-poor nature of the silica thin films. Water does not penetrate through the nonporous silica films and there are no any conclusive pieces of evidence for the support assisted adsorption of water.

Wetting properties of the silica thin film strictly depend on the preparation procedure and the post-annealing conditions. Lower quality films are not hydrophobic whereas the high-quality silica films are strictly hydrophobic. Therefore, water-TDS is a sensitive tool to distinguish between well-ordered and defected silica thin films.

3.5. Desulfurization-related surface chemistry on 2D-silica film

Thiophene and small chain alkane adsorption kinetics and dynamics on silica thin films were studied employing multi-mass TDS and molecular beam scattering at UHV. The monoatomic thick crystalline silica films (silicatene) grown on Mo(112) was characterized by AES, LEED, and water-TDS as described in sections 3.3 and 3.4. Thiophene is a standard probe molecule for study HDS and n-alkane are major reaction products. Silicatene can be considered as a potential catalytic support for catalytic HDS. Therefore, support effects on the desulfurization related surface chemistry were investigated comprehensively in this section. Also, chemical reactivity of silicatene and silica wafer towards small molecule adsorption was compared quantitatively.

3.5.1. Experimental procedures

All the experiments were carried out in a UHV chamber equipped with a triply differentially pumped molecular beam apparatus. The experimental setup is described in section 2.1.3. The sample temperature was controlled between 90 K to 1600 K with liquid nitrogen cooling (together with He gas bubbling) and electron beam heating respectively, for the TDS measurements of condensed alkanes (low-temperature limit) and the sample cleaning and oxidation (high-temperature limit). The thermocouple reading was calibrated (± 5 K) by TDS measurements of condensed small molecules, which is illustrated in table 3.2.

Silicatene films were prepared on Mo(112) single crystal surface by vapor depositing silicon on Mo(112)-p-(1 \times 3)-O oxygen overlayer structure at 900 K in 7×10^{-8} mbar oxygen pressure. Further UHV annealing and oxygen annealing steps were used to improve the crystallinity of the silica thin films. Samples were characterized by AES, LEED, and water-TDS as described in section 3.3.1.2.

TDS and molecular beam scattering were utilized to determine the adsorption kinetics and dynamics of considered molecules on silicatene. TDS peak positions were numerically converted to binding energies using Redhead analysis (see section 2.4.3.1 for more details) with an assumed pre-exponential factor $1 \times 10^{13} \text{ s}^{-1}$. The chain-length dependent desorption kinetics for alkanes were analyzed using ‘inversion optimization analysis’ (direct inversion of the Polanyi–Wigner equation, see section 2.4.3.2 for more details). A constant heating rate, which amounts to 1.6 K/s was used in all TDS experiments. Backfilling and molecular beam techniques were utilized as gas dosing methods in TDS. Liquid alkanes/ thiophene were degassed by several freeze-pump-thaw cycles and the cleanliness was characterized by mass spectrometric measurements prior to TDS. For dynamics experiments, molecular beam apparatus was used. 3% n-butane seeded in He was used as the probe alkane. The impact energy (E_i) of n-butane was controlled by changing the nozzle temperature (see Figure 2.1.2). E_i for seeded n-butane was determined by a time of flight (TOF) setup. Adsorption probabilities were determined using King and Well’s method (see section 2.5 for more details).

Table 3.2. Thermocouple calibration by in-situ TDS

Adsorbate	Condensation Temperature (K)	
	Experimental	Reported
Isobutane	108	105 ⁴⁹
n-Pentane	127	125 ^{39, 145}
Thiophene	134	131 ¹⁴⁶
Methanol	145	153 ³⁹
Benzene	149	153 ¹⁴⁷

In-situ calibration of the thermocouple with TDS condensation peak temperatures of small organic molecules are listed here.

3.5.2. Sample characterization

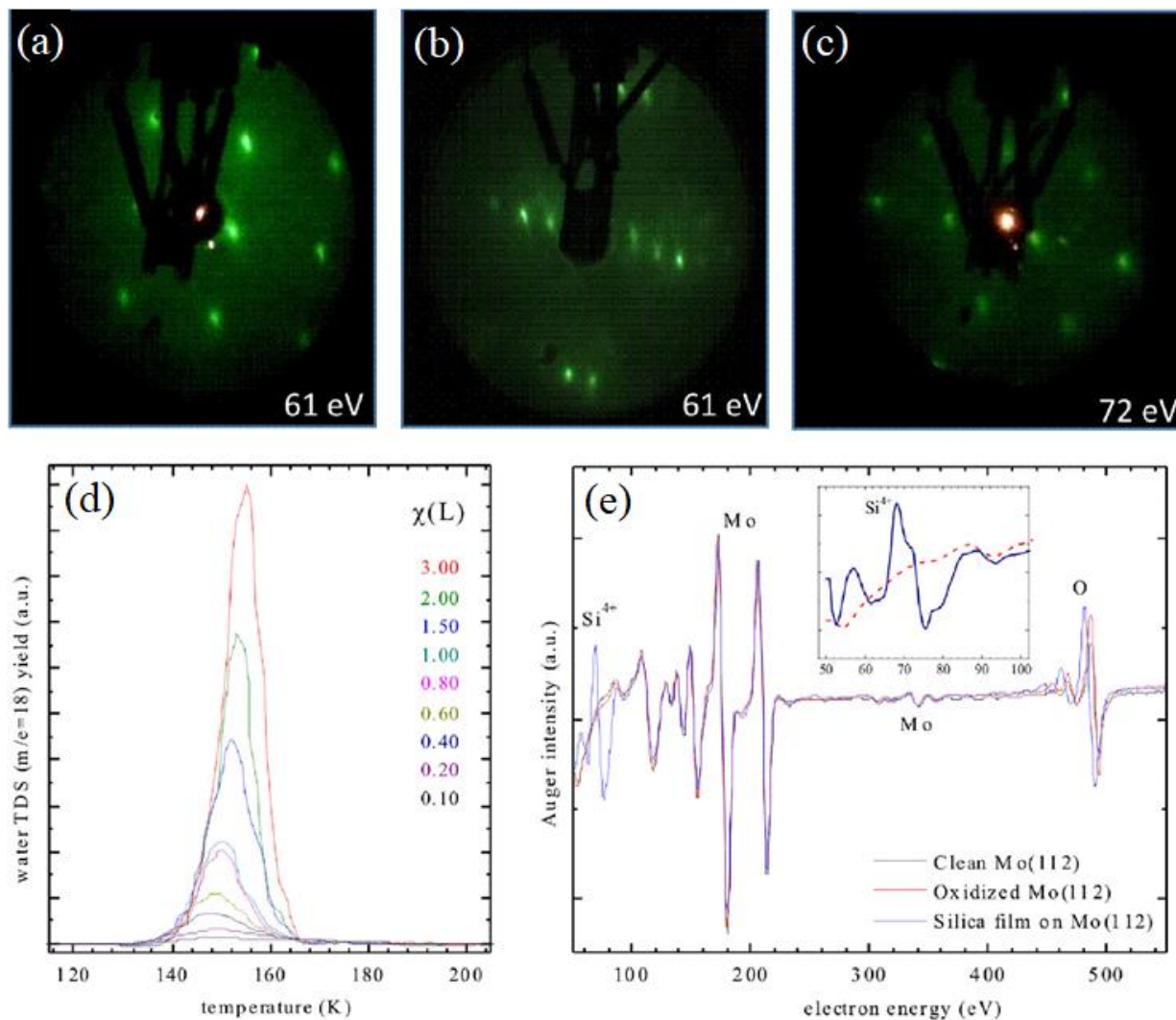


Figure 3.15. LEED characterization of (a) Mo(112), (b) Mo(112)-p-(1×3)-O, (c) Mo(112)-c(2×2)-[SiO₄]; (d) Water TDS curves on silicatene as a function of temperature; (e) AES of Mo(112), Mo(112)-p(1×3)-O, and silicatene film on Mo(112).

A crystalline silicatene film was obtained on Mo(112) with Mo(112)-c(2×2)-[SiO₄] superlattice as depicted by LEED (Figure 3.15(c)). The impurity levels of the silicatene were below the sensitivity limit (<0.01) of our CMA based AES system, which indicates no unwanted impurities on Mo(112), Mo(112)-p(1×3)-O and the silicatene film (Figure 3.15(e)). As depicted by water TDS data (Figure 3.15(d)) on the silicatene, the leading edges of the TDS curves line up well below the saturation exposures (< 0.4 ML) with peaks shifts to higher temperatures (with

increasing exposure), indicating 0th order kinetics over the entire concentration range. Therefore, the surface is hydrophobic. Several different silicatene films were synthesized and studied throughout the project, which was initially characterized as described here. Old silica films were removed by Ar⁺ sputtering and high-temperature annealing.

3.5.3. Thiophene adsorption kinetics

3.5.3.1. Introduction

A discussion about the HDS process, catalytic HDS of thiophene, and thiophene HDS mechanisms are included in the section 3.1.2. Investigation of the influence of the silicatene support toward HDS of thiophene is the main purpose of this study. Because the silica films are synthesized on Mo(112), one can speculate that the thiophene bond activation may be observed owing to the influence of the underlying metal support, as Mo is catalytically active towards thiophene HDS. To the best of our knowledge, two-dimensional crystals such as silicatene have not been studied as model catalytic supports for HDS yet. Traditionally, HDS was studied on Mo and MoS₂ single crystals. Nanostructures such as nanoclusters, nanotubes, nanoparticles etc., have been considered as catalysts and catalytic supports in recent surface science model studies.¹⁴⁸⁻¹⁵⁰

Nanoparticles have different physical, chemical, and electronic properties compared to their bulk counterparts such as micropower and single crystals, which attract fundamental interest towards the fabrication of the nanocatalysts. They exhibit novel properties such as enhanced catalytic properties and chemical reactivity, increased strength and conductivity, unusual absorption characteristics etc., which are crucial in catalysis related applications.¹⁵¹ More controlled fabrication of supported nanocatalysts with uniform particle distributions enhance the homogeneity of heterogeneous catalysis, leading to new concepts such as single atom catalysis.¹¹

There are significant structural changes in the surfaces of silicatene and silica wafer, which may also have different chemical properties even though both are made up of inert Si-O bonds. Silicatene has long-range order two-dimensionally whereas silica wafers are thick SiO₂ layers on natural bulk silica or thermally grown thick oxide layers on a silicon wafer, typically polycrystalline. Surfaces of the silicatenes usually have very small defect densities and the saturated Si-O-Si bonds are responsible for the chemical inertness. But, silica wafer contains defects and unsaturated valences, which may contain reactive functionalities. Prior studies on thiophene and alkane adsorption on silica wafer indicates the molecular physisorption interactions since the bond activation requires reactive metal surfaces.^{145, 148} Since silicatene is grown on Mo(112) and Mo is an active metal towards thiophene and alkanes,¹⁵²⁻¹⁵³ it is interesting to investigate how the support influence the adsorption properties of silicatene, prior to utilizing it as an HDS model catalytic support.

3.5.3.2. Results and discussion

Figure 3.16 (a) depicts a set of TDS curves for thiophene adsorption on silicatene as a function of exposure, that follows standard desorption kinetics. Low exposure desorption is dominated by a single peak from 140-160 K, which is labeled as α . The α peak shifts to lower temperature with increased exposure and saturated at 12 L. Subsequent growth of a second peak is observed at relatively high exposures, which is labeled as c-peak. c-peak is consistent with standard 0th order kinetics in which the lower temperature flanks are aligned and peaks shifts towards the high-temperatures with increased exposures. Therefore, c-peak is the characteristic condensation feature (multi-layer formation) for thiophene and the onset of the c-peak can be identified as the one monolayer (1 ML) coverage. Consequently, α -peak can be assigned as the sub-monolayer desorption of thiophene. At very low exposures, (<0.6 L), a minor desorption peak

is evident with 172 K of peak temperature (44.0 kJ/mol) is evident, which is labeled as β in the inset of the Figure 3.16 (a). This peak becomes a shoulder superimposed on the α -peak at larger exposures (>06 L). With respect to the 1ML coverage estimation of the TDS peaks, coverage of β -peak estimated to be 0.10-0.15 ML.

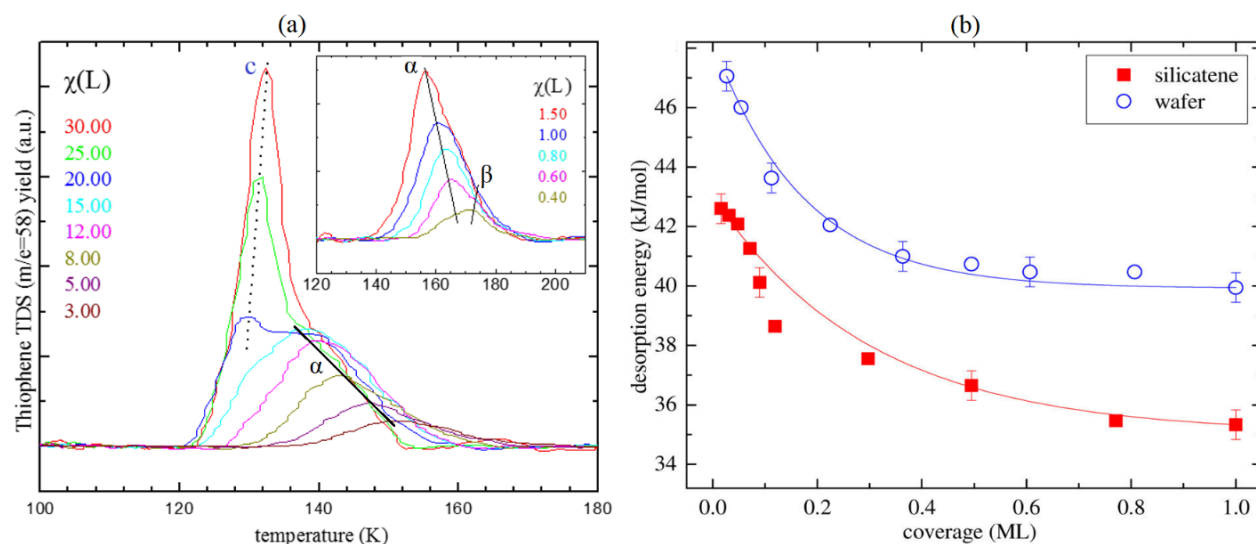


Figure 3.16. (a) TDS curves obtained for thiophene desorption from silicatene as a function of exposure ($m/z=58$ amu was detected, which is the most intense fragmentation mass of thiophene), (b) Binding energies for thiophene adsorbed on silicatene (α -peak) and silica wafer (extracted by the ref.³⁹) as function of exposure calculated with Redhead analysis using the pre-exponential $1 \times 10^{13} \text{ s}^{-1}$.

Epitaxially grown silicatene has a nonporous structure, that can expose the underlying Mo substrate for adsorbates. The pore size of silicatene ($\sim 3\text{-}4 \text{ \AA}$ in diameter¹³⁹) and the molecular size of thiophene (the maximum molecular diameter of thiophene is $\sim 4.6 \text{ \AA}$ according to Gaussian calculations) are comparable, which can possibly influence the bond activation of thiophene adsorbed on silicatene, unlike in silica wafer³⁹ as Mo is an active metal towards thiophene. Also, macroscopic defects such as holes in the silicatene can directly expose Mo substrate, resulting in activated adsorption. Other than that, the van der Waals interactions may be transferred through the silicatene without direct contact with the Mo substrate, which may also be resulted in activated

adsorption or strong chemisorption. Therefore, molecularity of thiophene adsorption was investigated by multi-mass TDS and AES.

Decomposition of thiophene may result in sulfur and/ or carbon deposition on the substrate, that can be easily detected by AES. Our CMA-based AES system can detect impurities less than 1% of the monolayer (0.01 ML). Also, sulfur has higher AES sensitivity compared to Mo, Si, and O, which are the major elements detected in the silicatene spectra (AES relative sensitivity factor for sulfur is ~ 0.9 , as compared with ~ 0.35 for Mo and Si, and ~ 0.5 for oxygen¹⁵⁴). Also, adsorbed impurities such as sulfur, carbon fragments etc., may lead to site blocking effects, which may have resulted in sample history dependent desorption of thiophene. As depicted in figure 3.17 (a), AES before and after thiophene adsorption are identical. Sulfur would have significantly increased the intensity of AES peak at 152 eV.¹⁵⁴ Similarly, TDS data were well reproducible irrespective to the sample history, clearly indicating the molecular adsorption of thiophene on silicatene.

Furthermore, the mass spectrometric fragmentation pattern of gaseous thiophene was collected separately during the thermal desorption of adsorbed thiophene on silicatene (multi-mass TDS). The collected mass fragments replicate the gaseous mass spectra of thiophene (figure 3.17 (a)-(d)). Additionally, all the fragments desorb at the same temperature with similar TDS peak shapes attributed to the molecular desorption. Therefore, we rule out thiophene bond activation on silicatene and also the support effects. It seems like the atomically thin silica layer completely passivate the substrate effects.

The TDS peaks α and β (Figure 3.16 (a)) can be assigned to the sub-monolayer desorption of molecularly adsorbed thiophene as indicated by the multi-mass TDS and AES data (since no dissociative adsorption or substrate effects). The c-peak is the characteristic condensation feature

of thiophene. The β -peak can be assigned to the desorption from defected sites, which is less than 0.15 ML according to coverage estimations.

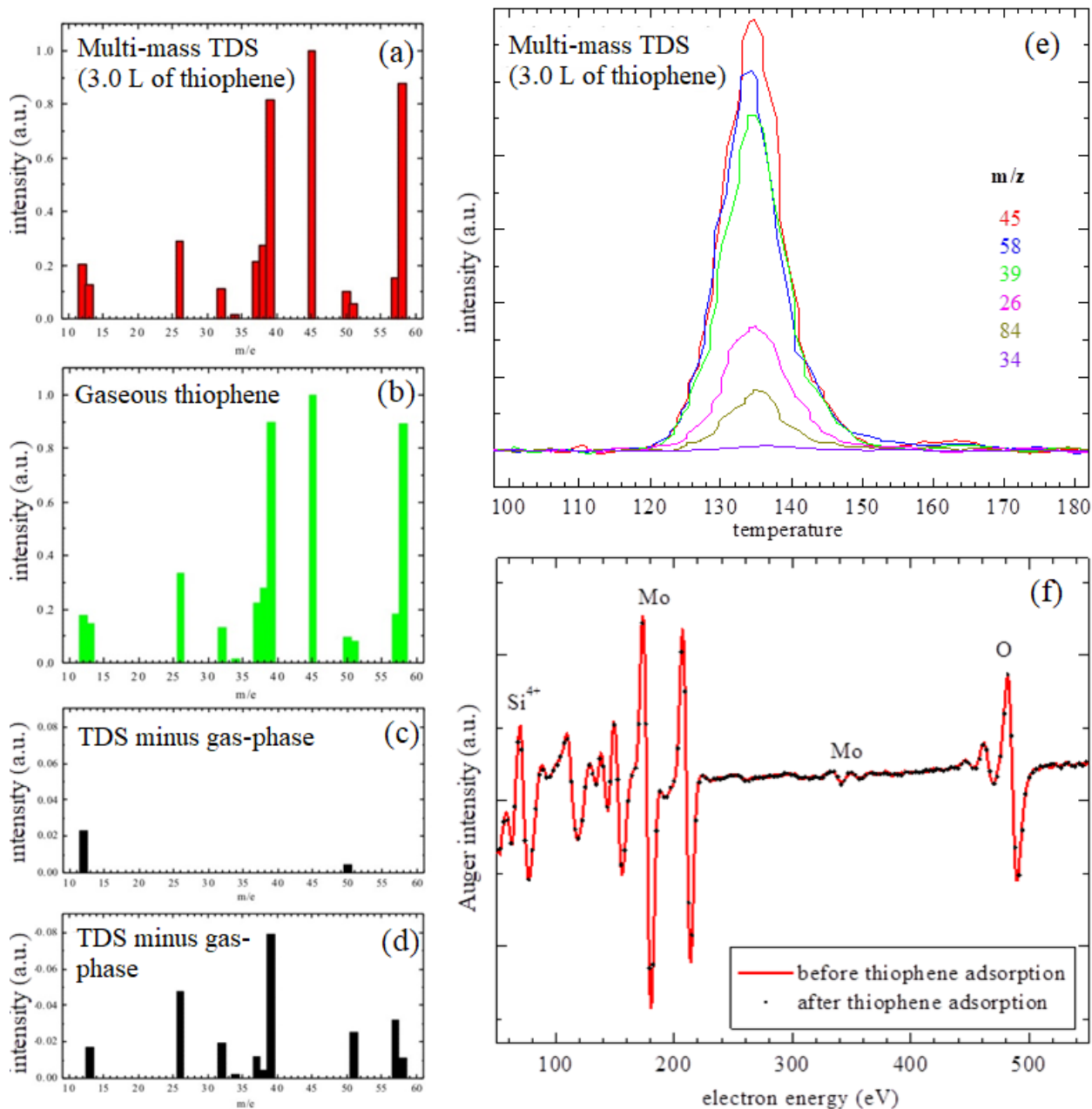


Figure 3.17. (a) Multi-mass TDS fragments of gaseous thiophene desorbed from silicatene, (b) Mass spectra of gaseous thiophene, (c) & (d) Difference spectra (Normalized multi-mass TDS intensity minus corresponding gas-phase mass fragment intensity) Positive and negative values of the difference in panels (c) and (d) respectively.

A similar type of molecular adsorption/ desorption kinetics for thiophene on polycrystalline silica wafer was evident in prior studies.³⁹ But, TDS curves are broader and the sub-monolayer to multi-layer peak separation is not clearly seen in the silica wafer. This may be related to the crystalline order of the silica wafer. Presence of the chemically distinct binding sites with slightly different binding energies due to the polycrystallinity may cause broader TDS peaks.

Binding energies of thiophene adsorption was determined using Redhead analysis. TDS peak maximums were numerically converted to binding energies assuming 1st order desorption pre-exponential ($1 \times 10^{13} \text{ s}^{-1}$), which is typical for molecular adsorption. The coverages were obtained by integrating the ($\alpha + \beta$) TDS peaks and normalizing the peaks with respect to the 1 ML peak, which is the onset of the condensation peak. Coverage-dependent binding energies for silicatene and silica wafer are depicted in Figure 3.16(b).

At a quick glance, the TDS peak shifts at sub-monolayer exposures qualitatively look like second order desorption kinetics (see Figure 2.11). This type of kinetics can be observed as a result of activated (dissociative) adsorption or due to the presence of energetically inequivalent adsorption sites on the surface. Activated adsorption is safely ruled out by multi-mass TDS and AES data. If the surface is inhomogeneous, the adsorbate can sample different adsorption sites by diffusion on the surface after adsorption, which will eventually have adsorbed on the most active sites (sites with the greatest adsorption energies) initially. Hence, the desorption energies will be decreased with increasing surface coverage. Since the silicatene films are crystalline the surface is very homogeneous besides some random defects. Therefore, there cannot be energetically inequivalent adsorption sites which can cause 2nd order-like desorption kinetics. The reason for the TDS peak shifts in our case is mainly due to the repulsive-lateral interactions caused by adsorbates, which was observed in prior studies with polar physisorbed molecules.^{148, 155} Thiophene is a polar

molecule with 0.83 D of polarity. Physisorbed polar molecules with close proximity can cause repulsive lateral interactions due to induced dipoles. As the adsorbate concentration increases, the steric hindrance increases, and hence low desorption energies were observed at sub-monolayer.

Binding energy (E_d) for thiophene adsorption on pristine silicatene sites is 42.6 kJ/mol and it is 1.4 kJ/mol lower for defected sites (β -peak). E_d decreases with increasing coverage, consistent with repulsive lateral interactions between the adsorbates. The reactivity of silicatene is relatively low compared to the polycrystalline wafer, indicated by thiophene desorption energies (figure 3.16(b)). This may be mainly due to the higher defect density of silica wafer including various grain boundaries.

3.5.3.3. Summary: Thiophene adsorption on silicatene

Non-dissociative physisorption of thiophene on silicatene is evident with no support effects. Thiophene binding energy on pristine silicatene amounts to be 42.6 kJ/mol, which decreases with surface concentration, consistent with repulsive-lateral interactions between the adsorbed species with close proximity. Coverage-dependent binding energies for thiophene on silicatene are smaller than that of polycrystalline silica wafer, may be mainly due to the surface defects and functionalities on silica wafer.

3.5.4. Alkane adsorption kinetics and dynamics

3.5.4.1. Introduction

The motivation for the study of alkane adsorption kinetics and dynamics on silicatene was that alkanes are one of the major reaction products of catalytic HDS. Therefore, it is potentially important to understand the adsorption properties of alkanes on silicatene, which is a potential HDS catalytic support.

More fundamentally, adsorption of small organic molecules such as n-alkanes on epitaxial thin films attracted attention due to their applications in self-assembled systems (e.g. self-assembled monolayers on gold surfaces,¹⁵⁶ hydrocarbon separation and purifications, bio-sensors, and hydrocarbon storage etc.¹⁵⁷⁻¹⁵⁹ For example, epitaxially grown graphene, which is a structural analog to silicatene have been studied extensively for similar types of applications recently.^{88, 158, 160} However, graphene shows weak physisorption-like interactions with n-alkanes, which affected by the underlying substrate according to experimental and theoretical studies.^{88, 158} Historically, adsorption of short-chain hydrocarbons on metals and metal oxides have been studied for catalysis related applications mainly.^{155, 161}

Silica wafer can be considered as the chemically closest analog for silicatene. Adsorption of short-chain alkanes on silica wafer has been studied for heterogeneous catalysis related applications. In this regard, adsorption properties such as support effects and binding energies were determined at UHV.³⁹ Bulk thermodynamic properties have also been studied at ambient conditions.¹⁶¹⁻¹⁶³ Alkanes from butane to nonane (C₄-C₉) seems to have physisorption-like interactions with silica wafer while the adsorption dynamics are dominated by precursor states.³⁹

3.5.4.2. Results and discussion

3.5.4.2.1 Alkane adsorption kinetics

Alkane TDS peaks structurally similar to thiophene data qualitatively. Lower exposures are dominated by α -peak, which saturates about 3L exposure (Figure 3.18). A minor desorption peak is evident at lower exposures (see the insets), labeled as β . At larger exposures, another structure (c-peak) grows in intensity with the exposure. Lower temperature molecular desorption peaks of all considered alkanes rule out the activated adsorption. Therefore, α and β peaks are assigned to the molecular desorption at sub-monolayer coverages as well as the c-peak to

condensation (multi-layer formation) of alkanes. Like in the thiophene TDS, β -peak can be assigned to the desorption of alkanes from defects, such as step edges.

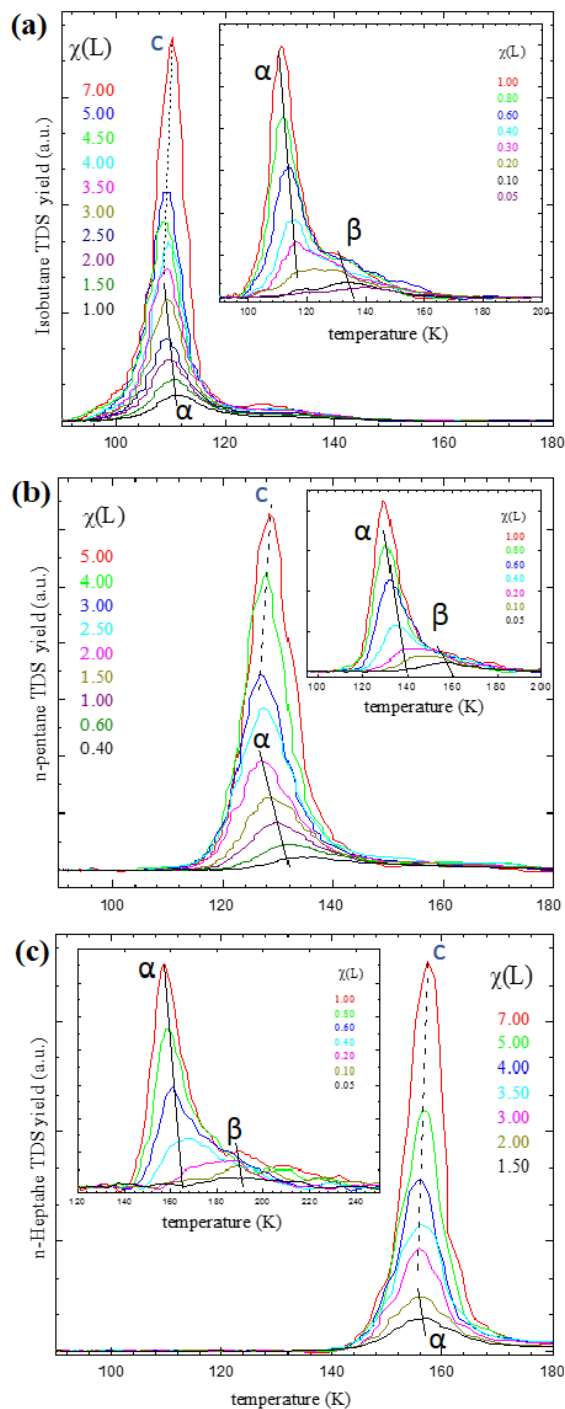


Figure 3.18. TDS curves for (a) Isobutane (C_4H_{10}), (b) n-pentane (C_5H_{12}), (c) n-heptane (C_7H_{16}) adsorption on silicatene as a function of exposure of each alkane (data for small exposures are given in insets)

α and β peaks are shifted to lower temperature with increasing exposure as a result of repulsive lateral interactions caused by adsorbed alkanes in close proximity. In the case of alkane, both repulsive^{162, 164} and attractive¹⁶⁵ lateral interactions have been seen in previous studies. TDS peak shifts to higher temperature with exposure have been observed for alkane adsorption with attractive lateral interactions.¹⁶⁵ The c-peak has the characteristics of 0th order kinetics with common leading edges and higher temperature peak shifts with exposure, corresponding to alkane condensation.

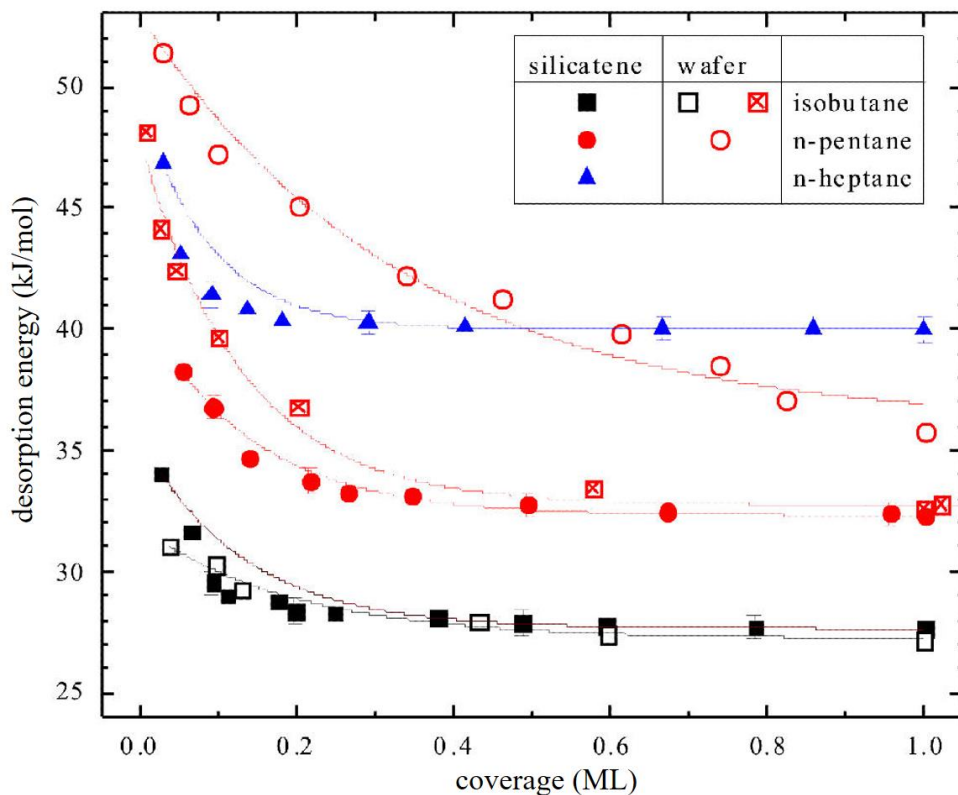


Figure 3.19. Coverage-dependent binding energies (E_d) for alkanes adsorbed on silicatene and silica wafer. E_d for silicatene was determined using the Redhead analysis with assumed pre-exponential $1 \times 10^{13} \text{ s}^{-1}$. E_d for silica wafer was extracted from ref.³⁹ (the same pre-factor was used).

Identical temperature axis in Figure 3.18 enables the comparison of desorption temperatures of alkanes, which indicates chain length dependent desorption temperatures. The desorption temperatures increase with the alkane chain length, which is typical for molecular physisorption. As depicted in the insets (Figure 3.18), the desorption temperatures appear to

increase by 20 K for each added methylene bridge (-CH₂-) with the TDS peak shapes unaffected. The binding energy corresponding to 20 K shift is estimated to be 2 kJ/mol with an assumed pre-exponential $1 \times 10^{13} \text{ s}^{-1}$ with chain length independent desorption kinetics.

To have a more quantitative comparison, alkane desorption energies (binding energies, E_d) were determined using Redhead analysis (see section 2.4.3.1). TDS peak maximums were numerically converted to binding energies for sub-monolayer exposures assuming 1st order desorption kinetics (TDS peaks were normalized considering the onset of the condensation peak as the monolayer coverage). Even though the exact pre-exponential factors are not known, $1 \times 10^{13} \text{ s}^{-1}$ is a standard pre-factor, generally acceptable for molecular adsorption, which was used to parameterize the kinetics in this study. This parameterization allows the direct comparison with previous studies.^{39, 148, 166} Determination of the exact pre-factors is important to understand the exact binding energies. Higher pre-factors will give higher numerical values of E_d due to kinetic compensation effects while the desorption rates remain unaffected. Therefore, even with an assumed pre-factor, trends of the binding energies can be compared, as they are independent of the choice of the pre-factor. A comprehensive study of pre-factor dependent kinetic parameters is included below.

The silicatene surfaces considered in this study contains 0.10-0.15 ML of defect density, as depicted in TDS data (Figure 3.18, β -peak). The exponential decay of E_d with coverage below $\sim 0.15 \text{ ML}$ is mainly because of the adsorption of alkanes on defects rather than repulsive lateral interactions. To obtain the alkane adsorption on pristine silicatene sites (defect-free parameters), the linear sections of the binding energy curves were extrapolated to zero coverage limit and the E_d data are shown in Table 3.3 for comparison.

The reactivity of silicatene in terms of alkane adsorption can be compared with poly-crystalline silica wafer using the binding energy data. Both silicatene and silica wafer have weak physisorption interactions with considered alkanes in this study. Similar to thiophene adsorption study, silica wafer is slightly reactive than silicatene as indicated by binding energies, possibly due to the higher defect concentration on the poly-crystalline silica wafer surfaces compared to crystalline silica films. The binding energies of alkanes increase with the chain length for both surfaces, mostly due to the electrostatic interactions.

Table 3.3. Binding energies for alkanes on defect-free silicatene and silica wafer adsorption sites.

Surface	Probe molecule	Binding energy (kJ/mol)
Silicatene	Isobutane	29.6
Silica wafer	Isobutane	29.6 ³⁹
Silicatene	n-pentane	33.6
Silica wafer	n-pentane	46.9 ³⁹
Silicatene	n-heptane	40.7

In the Redhead analysis, only the TDS peak maximums are considered, which is a reliable technique to compare the common trends in desorption kinetics. This method works best when the molecular sizes are quite similar. Since we used alkanes with different chain lengths (C₄ to C₇) in this study, so-called inversion optimization analysis was applied to the TDS data, which enables more accurate determination of coverage dependent desorption energies and pre-exponential factors as well. Contrast to Redhead analysis, the inversion optimization method uses the entire shape of the TDS curve. A comprehensive discussion about the theory behind the inversion optimization analysis is included in section 2.4.3.2.

An example illustrating the above analysis method is depicted in Figure 3.20. Briefly, the coverage dependent binding energies can be extracted from the TDS curves by applying inverted Polanyi–Wigner equation (Figure 3.20 (b)) to each point of the TDS curve (which is proportional

to the desorption rate). Ideally, a perfect TDS dataset would result in the same binding energy curve ($E_d(\theta)$ vs θ curve) for different initial coverages (Figure 3.21). A general binding energy curve for a particular experimental TDS data set can be obtained by varying the pre-exponential factor.

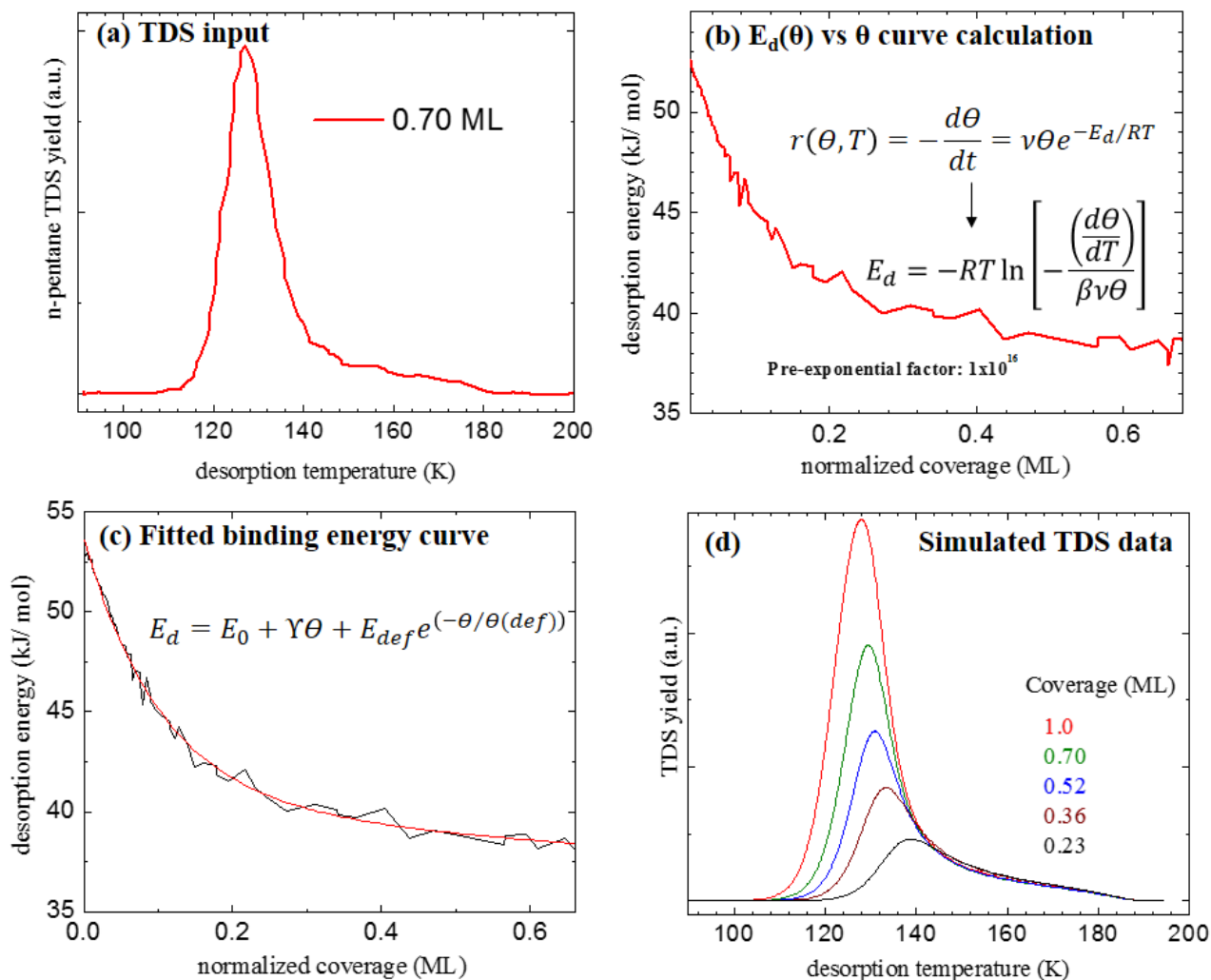


Figure 3.20. Application of the inversion optimization analysis technique to simulate TDS data for n-pentane adsorption on silicatene (experimental TDS curve corresponding to 0.7 ML n-pentane exposure was used as an example. All the equations are explained in section 2.4.3.2)

Then, the complete TDS data can be simulated by numerically integrating the Polanyi–Wigner equation, using a parametrized version of the binding energy curve obtained in the prior step (more details about the parameterization can be found in section 2.4.3.2). The pre-factor,

which generates the best-fitted data (simulated) to the experimental TDS is considered as the best pre-exponential for that particular adsorbate (alkane).

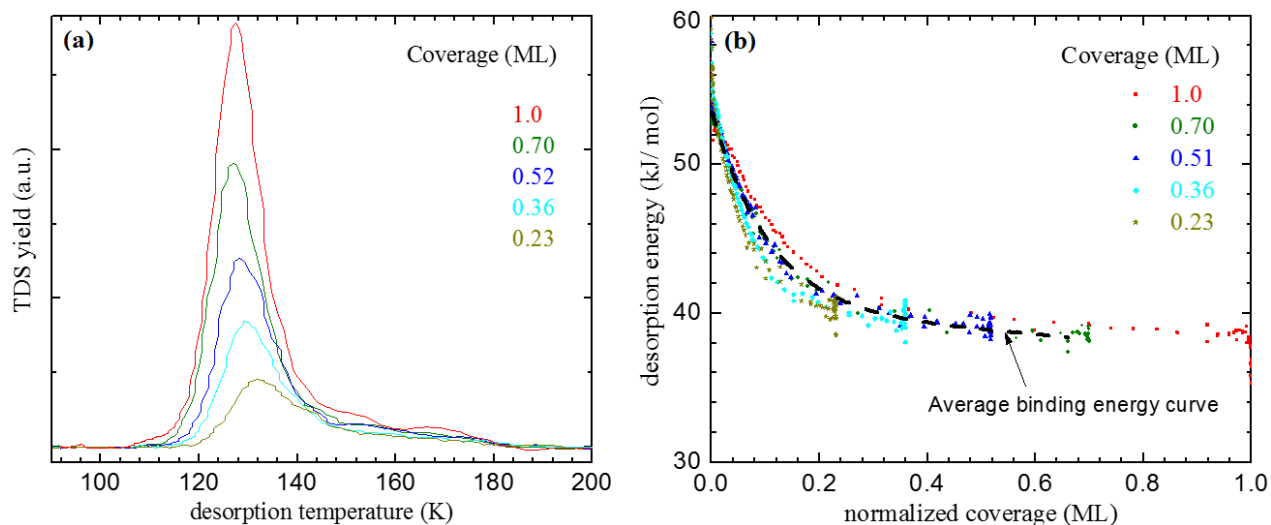


Figure 3.21. (a) Experimental n-pentane TDS curves for silicatene, (b) corresponding $E(\theta)$ vs θ curves obtained for each TDS curve by applying the inverted Polanyi–Wigner equation.

The best fits (TDS simulations) obtained for the alkane TDS in this study are shown in Figure 3.22 (left panel). Reasonable fits to the experimental TDS were generated by varying the pre-exponential factor. The objective was to fit an entire TDS dataset for different initial exposures, rather than a single TDS curve. The effect of the pre-exponential factor to the shape and the position of the TDS curves are illustrated in Figure 3.22 (right panel) with an example.

The pre-exponential determined by the direct inversion of the Polanyi–Wigner equation in conjunction with the fitting procedure clearly indicates the chain length dependence of the pre-factor, consistent with earlier reports.¹⁶⁵ The variation of the pre-factor with chain length has been correlated to the entropy effects in early studies,¹⁶⁵ that depends on the size and the shape of the molecules. The pre-exponentials are increasing with the chain length from 1×10^{15} - 1×10^{18} s⁻¹, when going from C₄ (isobutane) to C₇ (n-heptane).

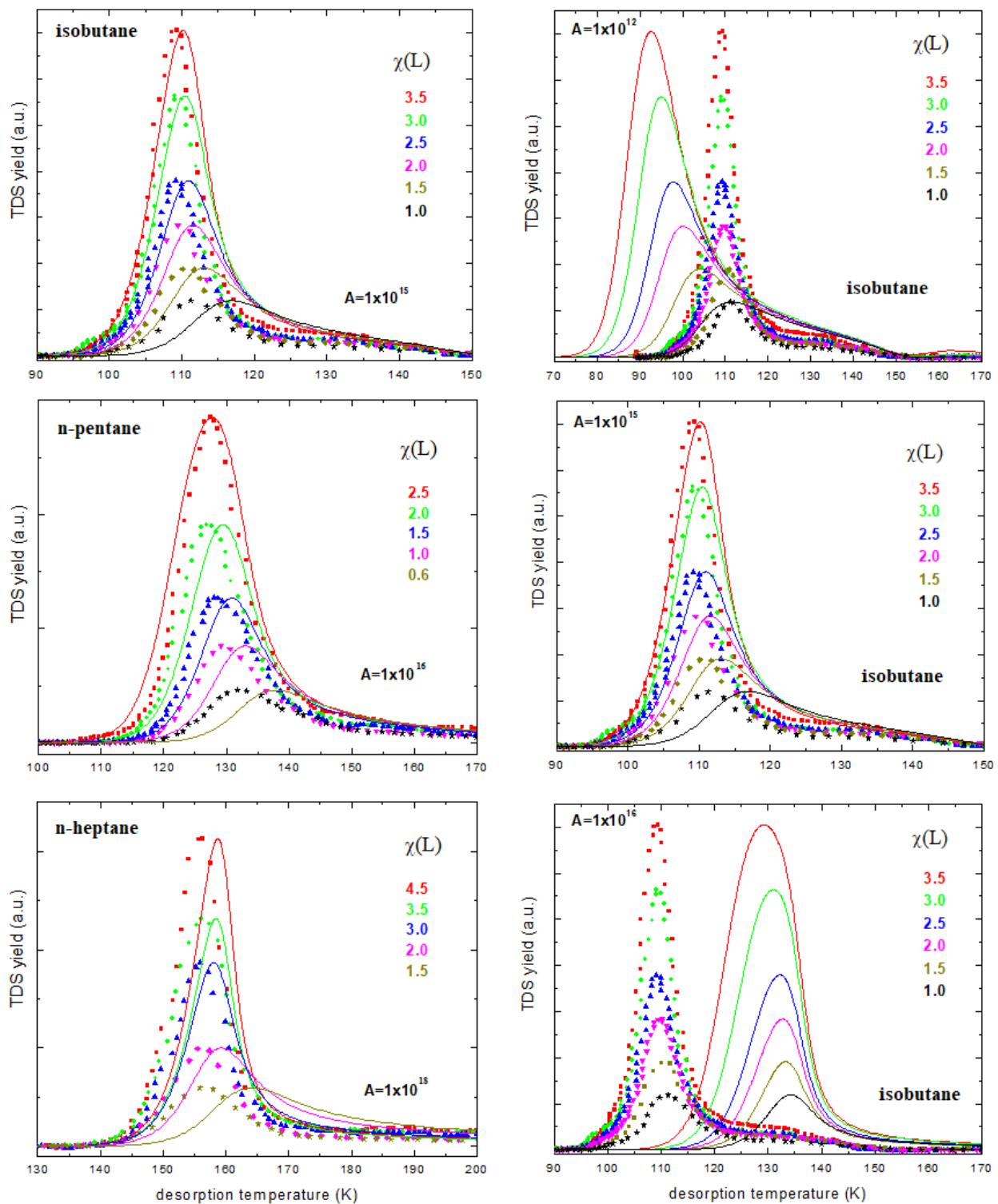


Figure 3.22. Left panel- Experimental (symbols) and simulated (solid lines) TDS of isobutane, n-pentane, and n-heptane (top to bottom), with best-fitted pre-exponentials (A). Right panel- Effect of the pre-exponential to the shape and the position of the simulated (solid lines) TDS curves (for isobutane TDS)

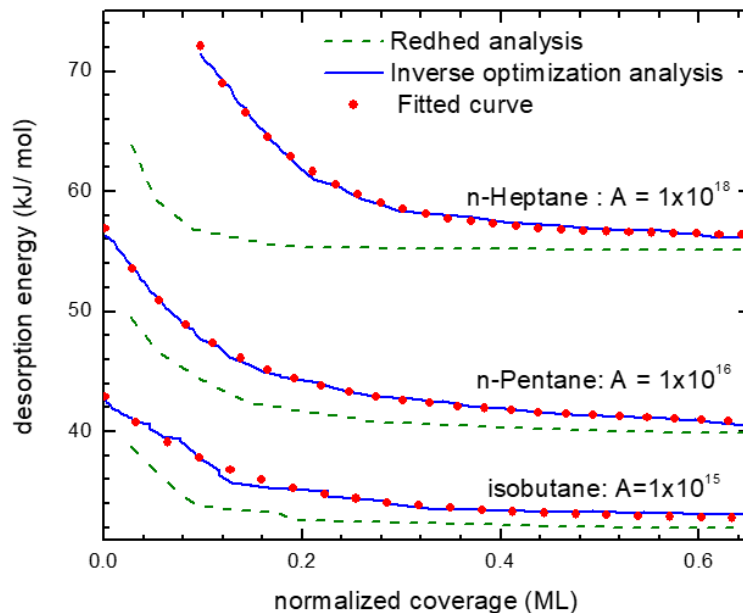


Figure 3.23. Coverage-dependent binding energies obtained from best-fitted pre-exponentials for isobutane, n-pentane, and n-heptane. Binding energy curves obtained from inversion optimization analysis and Redhead analysis are compared (with the same pre-factors)

The best fitted $E_d(\theta)$ vs θ curves for each alkane obtained from inversion optimization and Redhead analysis are shown in Figure 3.23. The same pre-exponential factor yields quite similar coverage-dependent binding energy curves irrespective to the method for short-chain alkanes. But the pre-factor should be assumed in Redhead analysis, which may lead to errors with larger molecules.

Table 3.4. Parameterization of $E_d(\theta)$ vs θ curves obtained from inversion optimization analysis according to the function $E_d = E_0 + \Upsilon\theta + E_{def}e^{(-\theta/\theta_{def})}$ (energies are in kJ/mol).

Alkane	Fit parameters			
	E_0	Υ	E_{def}	Θ_{def}
Isobutane	33.28	-0.86	9.69	0.13
n-pentane	42.83	-3.23	14.24	0.10
n-heptane	56.34	-7.23×10^{-5}	40.15	0.10

3.5.4.2.2 Alkane adsorption dynamics

Alkane adsorption dynamics on silicatene was investigated employing n-butane as the probe alkane. Supersonic molecular beams of n-butane were generated utilizing the molecular

beam apparatus (see section 2.5 for more details). It is possible to generate supersonic molecular beams with liquids but generating a stable beam flux with liquid sources are challenging. Therefore, seeded n-butane in helium gas (3% n-butane in He) was used as the probe molecule, which is a room temperature gaseous alkane. Temperature-dependent and energy dependent initial adsorption probabilities (S_0) of n-butane on silicatene was determined using King and Well's technique.

S_0 as a function of surface temperature (for constant impact energy, $E_i=0.70$ eV) is shown in Figure 3.24 (a). S_0 remain constant initially at 0.45 ± 0.03 up to ~ 115 K until it starts to drop down with the temperatures beyond 115 K. The adsorption probabilities below 107K was not considered because n-butane condenses ~ 107 K and starts to form multi-layers, which was determined by TDS experiments. King and Wells type techniques are not applicable to multilayer adsorption.

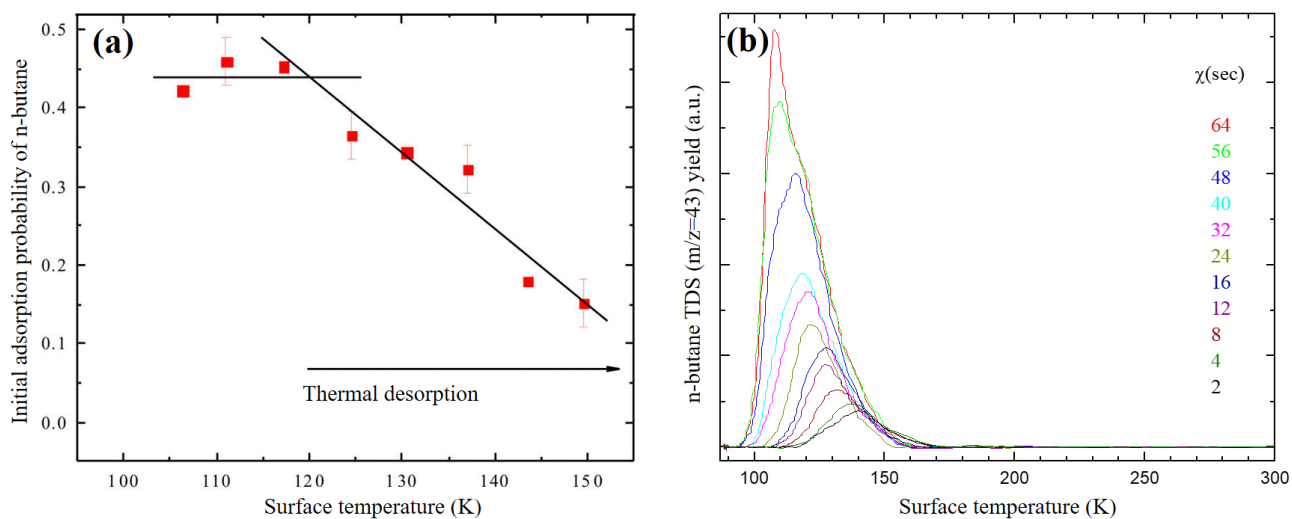


Figure 3.24. (a) Initial adsorption probability as a function of surface temperature for n-butane adsorption on silicatene at a constant impact energy of 0.7 eV, (b) n-butane TDS curves for silicatene as a function of exposure time.

The onset temperature of the S_0 decrease coincides with the onset of the thermal desorption (~ 120 K) of alkanes as indicated by the TDS and adsorption probability measurements, reflecting

the balance of adsorption and thermal desorption. The constant S_0 at lower temperatures is characteristic of non-activated molecular adsorption, which was also confirmed by TDS experiments.

The initial adsorption probability of n-butane decreases with the impact energy, as indicated in Figure 3.25. The decrease of S_0 with the impact energy is another indication for the non-activated adsorption of n-butane on silicatene. As the impact energy increases, more energy needed to be dissipated to the surface for the molecule to be adsorbed and therefore, the adsorption efficiency decreases with the impact energy. The decrease of the adsorption efficiency with the impact energy is a characteristic feature of non-activated physisorption. Theoretically, the bond activation is possible at smaller impact energies (< 0.7 eV). Unfortunately, our experimental lower limit was 0.7 eV. But, the TDS experiments confirmed the non-activated adsorption of n-butane on silicatene.

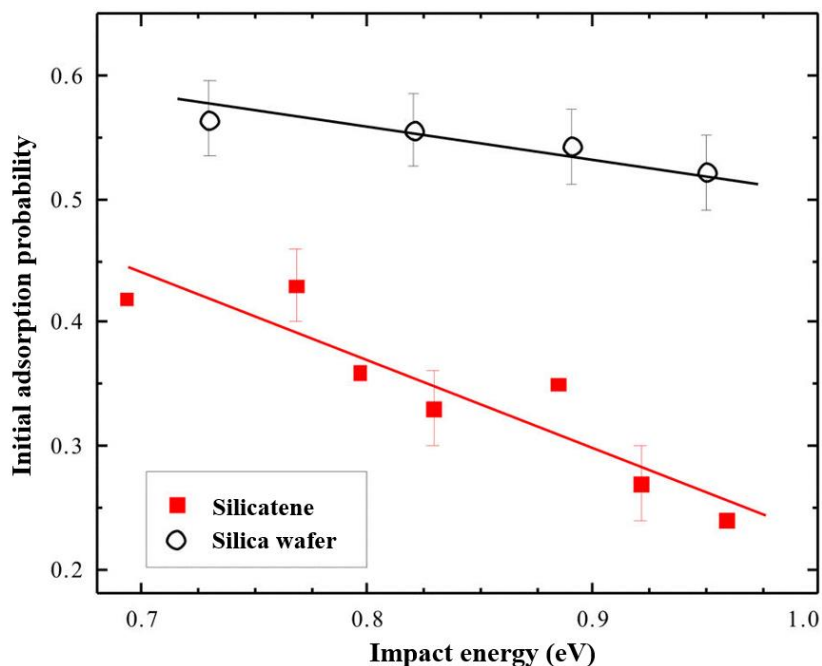


Figure 3.25. Initial adsorption probability as a function of impact energy for n-butane adsorption on silicatene at a constant surface temperature ($T_s=110$ K).

The reactivity of silicatene and silica wafer can also be compared using the initial adsorption probabilities. As indicated in Figure 3.25, S_0 is distinctly larger for silicatene than silica wafer and hence the reactivity of silica wafer is high compared to silicatene, in terms of alkane adsorption. Inhomogeneity of silica wafer due to the presence of surface defects and dangling bonds can increase the adsorption probabilities significantly, which can promote efficient energy transfer with the impinging molecules.

3.5.4.3. Summary: Alkane adsorption kinetics and dynamics

Short chain alkane adsorption kinetics and dynamics were investigated employing TDS and molecular beam scattering, and the results were compared with literature data of silica wafer. All alkanes physisorbed molecularly on silicatene. Adsorption energy increases with the chain length, which is typical for electrostatic interactions. Alkane binding energy decreases with the coverage attributed to the repulsive-lateral interactions caused by steric factors. Silica wafer seems to be more reactive than silicatene according to kinetics and dynamics results. Alkane chain length dependence of the kinetic parameters was investigated by so-called inversion optimization analysis. The pre-exponential increases with the size of the molecule. The chemical reactivity of inert silicatene is not affected by the reactive Mo support, according to TDS and molecular beam scattering results.

3.6. Benzene adsorption on silicatene

Benzene adsorption on silicatene, Mo(112)-p(1×3)-O, and Mo(112) were investigated employing TDS. Fundamental interest was to investigate how the planar aromatic compounds like benzene interact with inert silicatene, which can be considered as an ideal molecule to explore the surface-molecule anisotropic properties. A comprehensive study of support effects of benzene

adsorption on silicatene was performed to figure out whether or not the van der Waals interactions are penetrated through the atomically thin silicatene layers.

3.6.1. Introduction

Benzene is a standard aromatic probe molecule that has been extensively used in heterogeneous catalysis related surface science model studies. Benzene adsorption on transition metals,¹⁶⁷⁻¹⁶⁸ metal oxides,¹⁶⁸⁻¹⁶⁹ transition metal carbides,^{167, 170} graphite,¹⁷¹ and graphene¹⁵⁷ has been studied experimentally and theoretically to understand the molecule-surface and molecule-molecule anisotropic properties. On metal surfaces such as Mo(100) and Mo(110), chemisorbed benzene layers with aromatic ring plane parallel to the surface plane for the first molecular layer and perpendicular to the surface plane for the second molecular layer have been observed with spectroscopic techniques.¹⁶⁷⁻¹⁶⁸ Benzene seems to have relatively weak interactions with oxygen modified metal surfaces, which adsorbed on those surfaces with the aromatic plane tilted away from the surface plane, according to spectroscopic studies.¹⁶⁷ In a theoretical study, benzene adsorption on graphite and MoS₂ have been modeled to understand the effect of the insulating materials in scanning tunneling microscopic imaging and the tunneling current.¹⁷¹ Benzene adsorption on carbide modified surfaces such as Mo₂C has been investigated to model benzene hydrogenation catalysis. Dissociative chemisorption of benzene on Mo₂C has been observed, which deactivates the catalyst because of strong interactions between benzene and the carbide modified surfaces.¹⁷⁰ In a single study, benzene adsorption on silicatene was investigated by Goodman et al., with vibrational spectroscopy, which concludes parallel physisorption of benzene with surface oxygen atoms on silicatene. In this case, layer-by-layer growth of benzene has been observed for the first three monolayers of benzene. This is mainly due to the close matching of the

lattice parameters of benzene and silicatene, which facilitate parallel packing with electrostatic interactions and with a minimum amount of distortions.¹⁶⁹

In most of these studies, benzene adsorption geometries and electronic structures have been demonstrated. Very few studies were devoted to benzene adsorption kinetics and support effects on benzene adsorption.¹⁵⁷ Benzene adsorption on Mo(112) and Mo(112)-p(1×3)-O has not been investigated. These metal and metal oxide supports are potential catalysts in liquefaction of coal, HDS, NO_x reduction etc. This study is focused on the investigation of benzene adsorption kinetics on silicatene and support effects with TDS.

3.6.2. Experimental procedures

Silicatene films were synthesized on Mo(112) at UHV following the procedure described in section 3.3.1.2, and characterized by LEED, AES, and water-TDS (Figure 3.15). Benzene was dosed by backfilling the vacuum chamber with exposures given in Langmuir (1L= 1×10⁻⁶ torr exposure for 1 second). Benzene binding energy on silicatene, Mo(112), and Mo(112)-p-(1×3)-O were determined from the TPD peak positions using the Redhead analysis and the standard pre-exponential factor 1×10¹³ s⁻¹. TDS heating rate was kept constant for all experiments, which amounts to 1.6 K/s.

3.6.3. Results and discussion

3.6.3.1. Benzene adsorption kinetics on silicatene

A set of TDS curves obtained for benzene on silicatene as a function of benzene exposure is depicted in Figure 3.26. At lower exposure, a single peak (α) is evident, which shifted to lower temperature with the exposure. This peak shift is consistent with repulsive lateral interactions due to steric factors since no benzene dissociation or surface inhomogeneity (which can possess multiple adsorption sites and 2nd order-like desorption kinetics) is conclusive. The π electron cloud

of benzene may be polarized when it approaches the surface, which can eventually form induced dipoles and the repulsive-lateral interactions are mainly arises due to this type of polarization effects of the adsorbates. Also, there can be repulsive hydrogen-hydrogen interactions between the physisorbed benzene molecules, adsorbed parallel to the surface plane in close proximity.

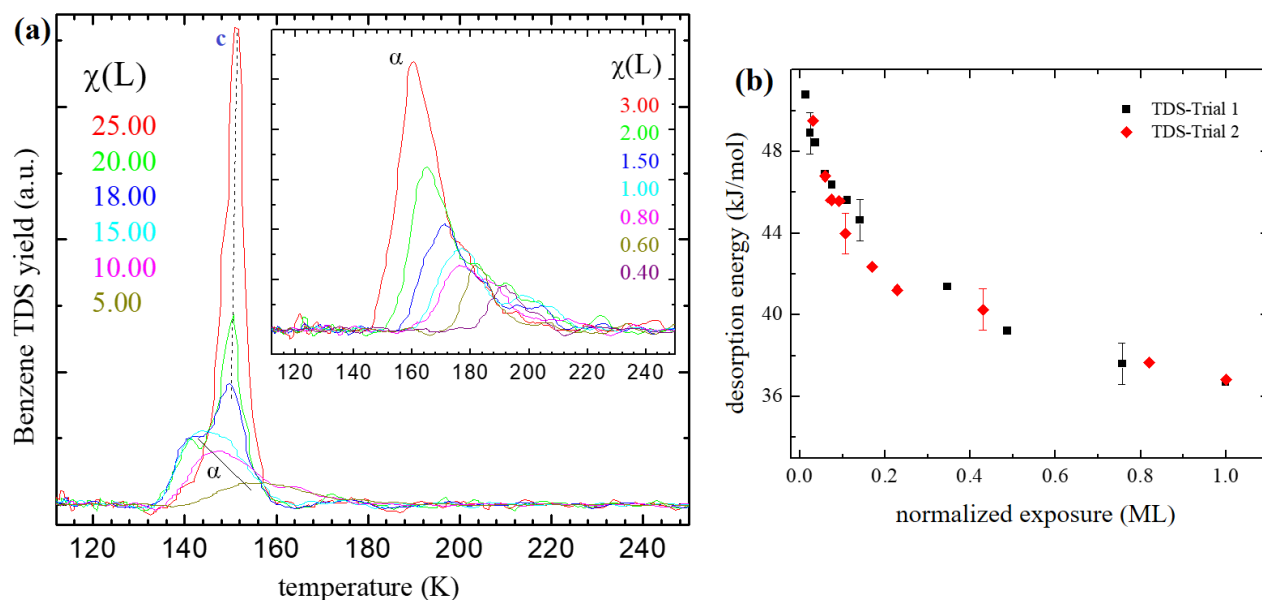


Figure 3.26. (a) TDS curves obtained for benzene adsorbed on silicatene as a function of benzene exposure, (b) coverage dependent binding energies for benzene adsorption on silicatene (different data points refer to different TDS datasets)

A second peak (c-peak) starts to appear around 15 L exposure while the α -peak saturates. The c-peak continue to grow with the exposure. The lower temperature flanks of the c-peak lineup and the peaks shift to higher temperatures with the exposure, consistent with 0th order kinetics. Therefore, the c-peak can be assigned to the condensation of benzene with multi-layer formation structures. A special feature in the TDS phase transition from a monolayer to the multi-layer regime, that was not observed in either alkanes or thiophene adsorption is evident in benzene TDS, which is that the condensation peak temperature of benzene is larger than the final monolayer peak temperature (~10 K). This might be due to the higher binding energy between the benzene

molecules in the condensed phase compared to the binding energy between the benzene and silicatene. The general shape of the benzene TDS data was well reproducible.

Structurally similar TDS data have been observed in previous studies. For example, methyl iodide (CH_3I) adsorbed on $\text{TiO}_2(110)$ show structurally similar desorption kinetics,¹⁷² in which the different adsorption sites on TiO_2 and different adsorption geometries of CH_3I causing the unusual TDS peak shifts. Similarly, benzene adsorption geometry can play an important role in the desorption kinetics at the phase transition regime in this study.

According to previous studies, benzene tends to adsorb on silicatene with its aromatic ring parallel to the surface plane.¹⁶⁹ Since the unit cell parameters of silicatene and the molecular size of benzene has a close match, a two-dimensional layer of benzene adsorbed with the aromatic plane parallel to the surface may be formed. This adsorbed benzene layer can assist the formation of somewhat strong non-covalent π - π stacking interactions (non-covalent attractive interactions between aromatic π -electron cloud containing molecules, like benzene) with incoming benzene molecules, during multi-layer adsorption. The orientation of the initial benzene layer will play an important role in the strength of the π staking, as it depends strongly on the adsorption geometries. As an example, benzene adsorption on silica wafer does not have this type of TDS peak shifts at monolayer-multilayer phase transition regime (usual desorption kinetics). Since the polycrystalline wafer has surface inhomogeneity, it can have stronger interactions with initial benzene layer (compared to silicatene) and at the same time, the bonding geometries of the benzene layer may not be perfectly planer (e.g. there can be benzene molecules adsorbed on defects with tilted geometries), unlike in the case of silicatene. Therefore, the strength of the multilayer π stacking interactions in the case of benzene adsorption on silica wafer may be weaker compared to the case of silicatene due to the surface inhomogeneity of monolayer benzene structures.

A similar type of benzene adsorption kinetics has been observed on some metal oxide surfaces (e.g. MgO(100)/Mo(100)¹⁷³) in previous studies, which also suggest that the coverage dependent geometric arrangement of benzene can cause this type of effects. Benzene tends to adsorb with the aromatic plane parallel, tilted, or perpendicular to the surface plane depending on the concentration, which would certainly affect the binding energy and the TDS peak positions.

3.6.3.2. Support effects of benzene adsorption

Benzene adsorption on Mo(112) and Mo(112)-p-(1×3)-O was studied to reveal whether there are any influences of the underline support in adsorption kinetics of benzene on silicatene. Benzene adsorption on Mo(110) and Mo(100)^{168, 171} have been studied earlier, which show strong chemisorption of benzene on considered Mo supports. But, benzene adsorption on Mo(112) and the oxidic precursor used in the silicatene synthesis were not studied before. Since the silicatene films grow epitaxially on Mo(112) forming more stable 2D layers compared to Mo(110) and Mo(100) due to the close matching of the unit cell parameters of silicatene and Mo(112) surfaces (which can accommodate hexagonal structures, like silicatene without severe distortions), we expected to see strong chemisorption of benzene on Mo(112). Because, like silicatene, Mo(112) may also accommodate epitaxial benzene layers without structural distortions (since the unit cell parameters of silicatene and the bond parameters of benzene are comparable). On the other hand, unlike silicatene, Mo(112) is chemically reactive and hence it can form more strong covalent types bonds with the π electron cloud of benzene. Therefore, favorable structural and chemical properties may lead to the formation of much stable epitaxial benzene layers.

Mo readily adsorb oxygen even at UHV to form oxidized structures and therefore, the cleanest Mo(112) obtained in this experiment has about 0.15 of AES O-to-Mo peak ratio, measured with the AES sensitivity factors taken into account. This impurity oxygen content was difficult to

remove with Ar⁺ sputtering or UHV annealing. But, this surface shows the rectangular LEED pattern characteristic to clean Mo(112), which suggest that the oxidation of the surface is random and it is in the trace concentration levels. The oxidic precursor of Mo(112) has an AES O-to-Mo ratio of ~0.40, which is approximately consistent with the stoichiometry of the Mo(112)-p(1×3)-O overlayer structure (O/Mo= 0.33).

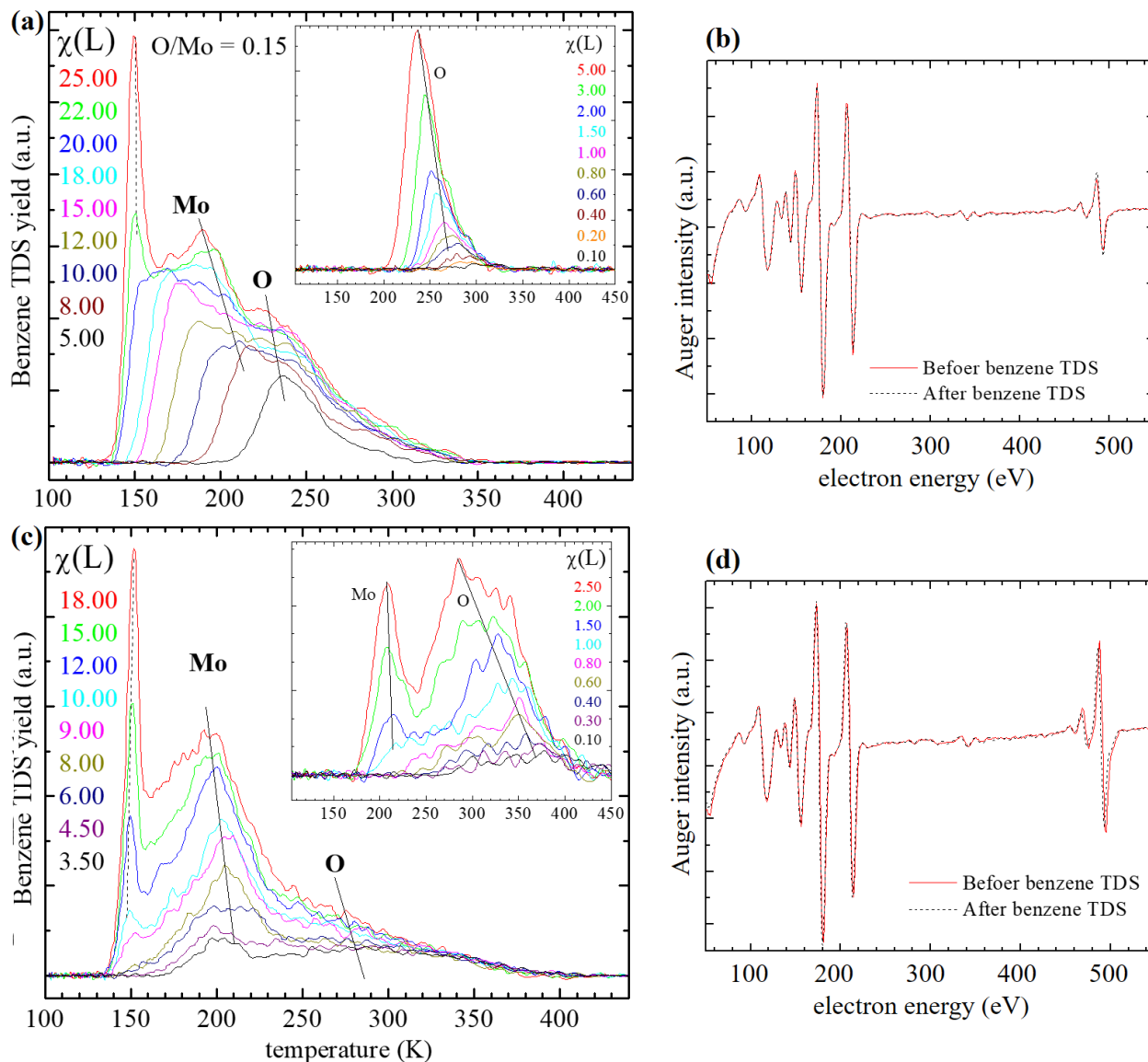


Figure 3.27. Sets of benzene TDS curves as a function of benzene exposure on, (a) Mo(112) and (b) Mo(112)-p(1×3)-O. AES data comparing the elemental composition of, (a) Mo(112) and (b) Mo(112)-p(1×3)-O before and after the benzene adsorption experiments.

Benzene adsorbed molecularly on both Mo(112) and Mo(112)-p-(1×3)-O surfaces. Molecular desorption was evident below 400 K (Figure 3.27). The AES further confirms the non-activated adsorption since no residual carbon impurities were detected on both surfaces after the benzene TDS experiments (Figure 3.27 (b) and (d)). The TDS follows standard kinetics, unlike in the case of silicatene. At a quick glance, two broad desorption peaks are evident at lower exposures, which saturates with exposure to form a sharp feature at higher exposure (c-peak). c-peak does not saturate with the exposure, that has common leading edges at lower temperatures, characteristic to 0th order kinetics. Therefore, the c-peak is assigned to the condensation of benzene, forming multi-layer structures.

A broad TDS peak within the range of 200-400 K is evident at the lowest benzene exposures, which is most distinct for the Mo-O surface (inset of the Figure 3.27 (c)), where the desorption temperatures are greater compared to the Mo(112) surface. This peak is assigned to benzene desorption from oxygen sites or in the vicinity of oxygenated species on the Mo(112) surface (O-peak). A second broad desorption structure, which centered around 200 K is evident on both surfaces. The Mo(112) TPD is dominated by this feature, on which a small shoulder peak (O-peak) superimposed. Therefore, this peak is assigned to benzene desorption from clean Mo sites (Mo-peak). The oxygen reconstructed Mo surface has several different adsorption sites,¹²⁰ which is clearly reflected by the TDS feature within 250-400 K in the Mo-O surface (Figure 3.27 (c)). However, TDS cannot provide exact peak assignments for different adsorption sites in the oxygen reconstructed surface. Also, the higher temperature feature in the Mo(112) surface correlates with the surface impurity oxygen content, as characterized by AES.

Benzene molecule is small enough to sample different adsorption sites on the Mo(112) surface even if it adsorbed perfectly flat on the surface. This is possible because the Mo(112) ridge-

and-through structures are separated by 4.5 Å and the distance between the Mo atoms along the rows is about 2.5 Å,¹⁷⁴ while the molecular diameter of benzene is about 2.8 Å.

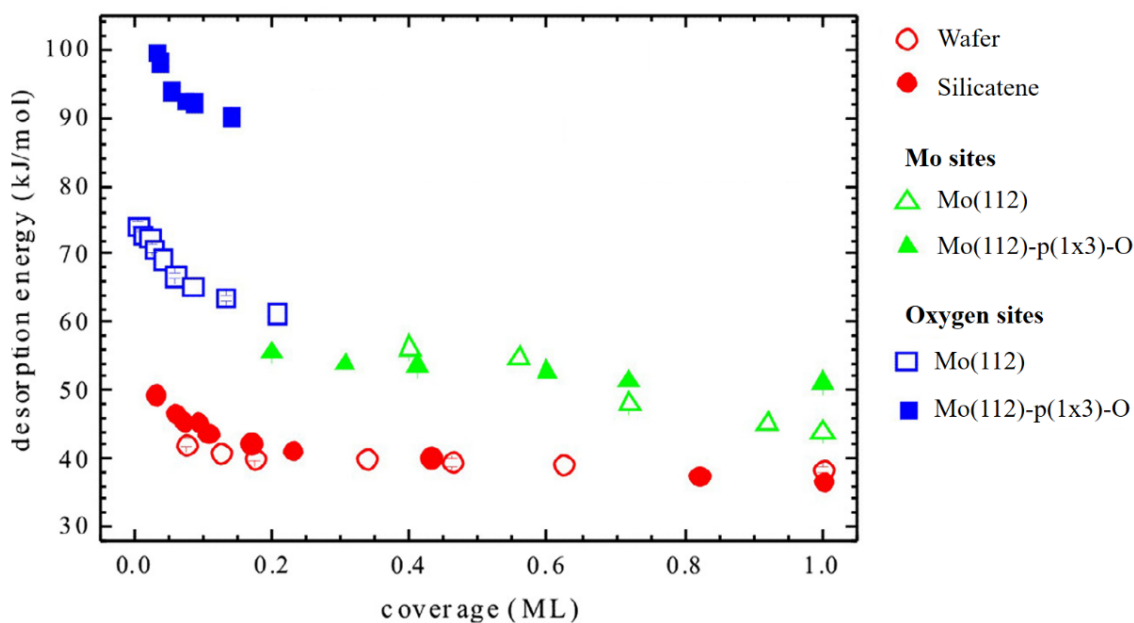


Figure 3.28. Coverage-dependent binding energies for benzene adsorption on silicatene, silica wafer, Mo(112), and Mo(112)-p(1×3)-O obtained by Redhead analysis using a 1st order exponential of $1 \times 10^{13} \text{ s}^{-1}$.

According to TDS, benzene binds more strongly on oxygen adsorption sites than Mo sites. Also, benzene-oxygen interactions on the oxygen reconstructed surface seem to be higher than that in the Mo(112) surface (residual oxygen), as reflected by the desorption temperatures (240-400 K and 200-320 K respectively). The formation of oxygen-induced reconstructed surface required a quite large temperature (~900 K), which indicates the strong oxidic character of the surface. Different binding energies would relate to the differences in the surface charge distributions. The oxygen atoms making up the p(1×3)-O structure are more strongly bonded to the surface compared to the residual oxygen adsorbed on the surface, as reflected by the preparation temperatures. The π electron density on oxygen may be shared with the vacant Mo d orbitals (Mo: [Kr] 4d⁵, 5s¹), forming $p\pi$ -d π interactions. This partial π bond character may lower the electron density of oxygen valance band, which forms the reconstruction pattern. Therefore, the surface oxygen may have

more electrophilic character compared to the residual oxygen adsorbed on the surface at ambient temperature. On the other hand, benzene is a good nucleophile, which is susceptible to electrophilic attack because of its delocalized π electron cloud. Therefore, the π electron cloud of benzene would be shared with surface oxygen atoms, which results in strong chemisorption-like interactions. Therefore, oxygen sites on Mo(112)-p(1 \times 3)-O exhibits higher benzene binding energies compared to Mo(112) and silicatene.

Benzene adsorption energies on different supports are compared quantitatively in Figure 3.28, which contains the coverage dependent binding energies of benzene adsorption determined using the Redhead analysis. Benzene has weak physisorption-like interactions with silicatene and silica wafer, showing the binding energies between 40-50 kJ/mol, typical for benzene adsorption on less reactive surfaces. A similar type of binding strengths has been observed for benzene on graphitic systems.¹⁵⁷ Even though the shapes of the TDS curves for benzene on silicatene and silica wafer³⁹ are different, the absolute binding energies agree within experimental uncertainties. Benzene strongly chemisorbed on the Mo support and on the oxidic precursor, as depicted by the corresponding binding energies. The Mo binding sites on both Mo(112) and Mo(112)-p(1 \times 3)-O have quite similar binding energies, which corroborates the Mo peak assignment. Benzene binding energies on different oxygen sites are quite different, consistent with the qualitative discussion about the electronic structural differences of the oxidic surfaces.

The monoatomic thick silica layers have quite different chemical properties compared to the underlying support according to the TDS data. Therefore, silicatene is non-transparent chemically for benzene adsorption and there is no any influence of the support for the benzene adsorption on silicatene, unlike its structural analog graphene.¹⁵⁷

3.6.4. Summary: Benzene adsorption on silicatene

Benzene adsorption on silicatene, Mo(112), and Mo(112)-p(1×3)-O were studied employing TDS. Benzene adsorbed molecularly on all considered surfaces. Weak physisorption of benzene on silicatene and strong chemisorption of benzene on Mo, and Mo-O are evident. Benzene desorption kinetics on silicatene is rather unusual, which depicts higher temperature molecular condensation features compared to the monolayer desorption structures. This could be mainly due to slightly strong benzene-benzene interactions in the condensed phase compared to benzene-silicatene interactions. The kinetics of benzene adsorption on silicatene and the underlying support are quite different, showing the non-transparency of the van der Waals interactions through the atomically thin silica layer.

3.7. Alcohol adsorption on silicatene

Short-chain alcohol (methanol, ethanol, 1-propanol, 1-butanol, 1-pentanol) adsorption kinetics on silicatene was investigated employing TDS. The fundamental interest was to understand the binding energies of the alcohols on silicatene, chain-length dependence of the desorption processes, and the reactivity of silicatene compared to silica wafer in terms of alcohol adsorption.

3.7.1. Introduction

Alcohols are important feedstocks in chemical industries and transportation (e.g. fuel additives), which are used as reactants, and also formed as reaction intermediates and products in several different catalytic transformations.^{120, 175} Therefore, reference data (molecularity of adsorption, desorption energy etc.) of alcohol adsorption is useful to make improvements in industrial processes.

Adsorption and decomposition of methanol and propanol on metals, metal oxides, metal carbides, alloys, silicon, silica wafer, and graphite etc., have been studied experimentally and theoretically,^{161, 176-182} mainly for fuel cell related applications. Methanol is a convenient fuel, which is a stable liquid with low volatility, high energy density, and broad liquid temperature range. Therefore, electrochemical methanol oxidation reaction has attracted considerable attention. Most of the methanol oxidation catalysts are platinum-based metal nanoclusters (Pt, Pt/Ru, Pt/Pd alloys etc.) supported on porous carbon materials and metal oxide supports.¹⁸³⁻¹⁸⁴ Other than methanol, adsorption studies devoted to alcohol adsorption, especially longer chain alcohols are rare. Generally, molecular adsorption of alcohols on less reactive surfaces (such as noble metals, graphite, and silica) and activated adsorption leading to dehydration, isomerization, hydrogenation, and decomposition on reactive surfaces (Mo, Ni, Mo₂C) have been observed.

3.7.2. Experimental procedures

Silicatene films were synthesized on Mo(112) at UHV following the procedure described in section 3.3.1.2, and characterized by LEED, AES, and water-TDS (Figure 3.15). Methanol, ethanol, 1-propanol, 1-butanol, and 1-pentanol were dosed by backfilling the vacuum chamber with exposures given in Langmuir ($1\text{L} = 1 \times 10^{-6}$ torr exposure for 1 second). Alcohol binding energies on silicatene were determined from the TPD peak positions using the Redhead analysis and the standard pre-exponential factor $1 \times 10^{13} \text{ s}^{-1}$. TDS heating rate was kept constant for all experiments, which amounts to 1.6 K/s.

3.7.3. Results and discussion

Thermal desorption profiles of alcohols adsorbed on silicatene as a function of exposure are depicted in Figures 3.29 and 3.30. The left and the right column containing the smaller and the larger exposures of alcohols respectively. Same temperature scales are used in each column for the

qualitative comparison of desorption temperatures. The gas-phase equilibrium structures of alcohols were obtained by Gaussian calculations and are shown in the left column together with TDS curves. Also, the elemental composition of silica films before and after alcohol adsorption determined by AES are shown in the right column (insets).

A single feature, labeled as α is evident at lower exposures, which shifted to lower temperatures with the exposure as highlighted by a solid line (direction of the peak shift). Similar to alkane and thiophene adsorption studies, the peak shift is due to repulsive-lateral interactions since dissociative adsorption and/ or surface inhomogeneity are not evident. Dissociative adsorption or bond activation of alcohols can be ruled out due to the lower temperature molecular physisorption structures and homogeneous silicatene structures were characterized by LEED and water-TDS experiments (Figure 3.15).

For larger alcohols, a small tail is appearing, which is due to the readsorption effects caused by differences in the pumping speed (the pumping speeds for the alcohols seems to be decreased with the molecular size). The peak temperature range of the α -peak is increased with the size of the molecule, characteristic to the molecular physisorption effects.

At larger exposures, α -peak saturates and another peak (c-peak) started to appear, which shifted to larger temperatures with the exposure. Similar to alkane and thiophene adsorption studies, c-peak is the characteristic condensation structures (due to multi-layer adsorption) of alcohols, that have common lower temperature leading edges representing 0th order desorption kinetics. Therefore, the α -peak is the sub-monolayer desorption of alcohols.

The exposures needed to initially observe the c-peak increases with the molecular size (e.g. $\chi=3.5$ L for methanol but $\chi=10.0$ L for 1-butanol for the initial appearance of the c-peak). This appeared to be counter-intuitive since it was expected to observe lower saturation exposures with

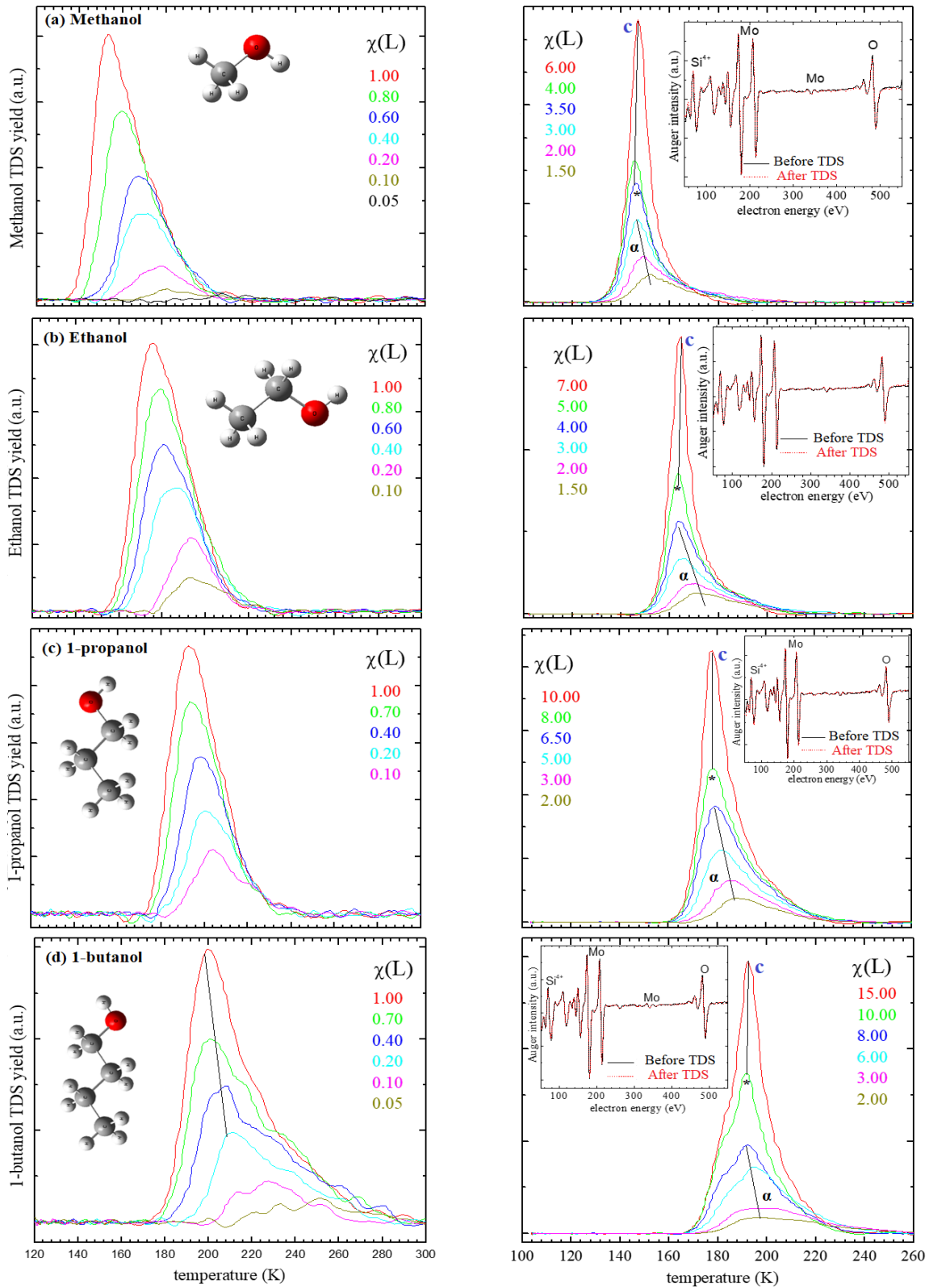


Figure 3.29. Methanol, ethanol, 1-propanol, and 1-butanol TDS as a function of exposure (left-smaller exposures, right-larger exposures, insets- AES before and after alcohol adsorption)

the molecular size considering the surface area of the alcohols. However, the exposure dependence suggested that the adsorption probability of the alcohols decrease significantly with the molecular size, may be due to the steric hindrance caused by the probe molecules adsorbed on the surface. The steric effects (repulsive) increases with the molecular size.

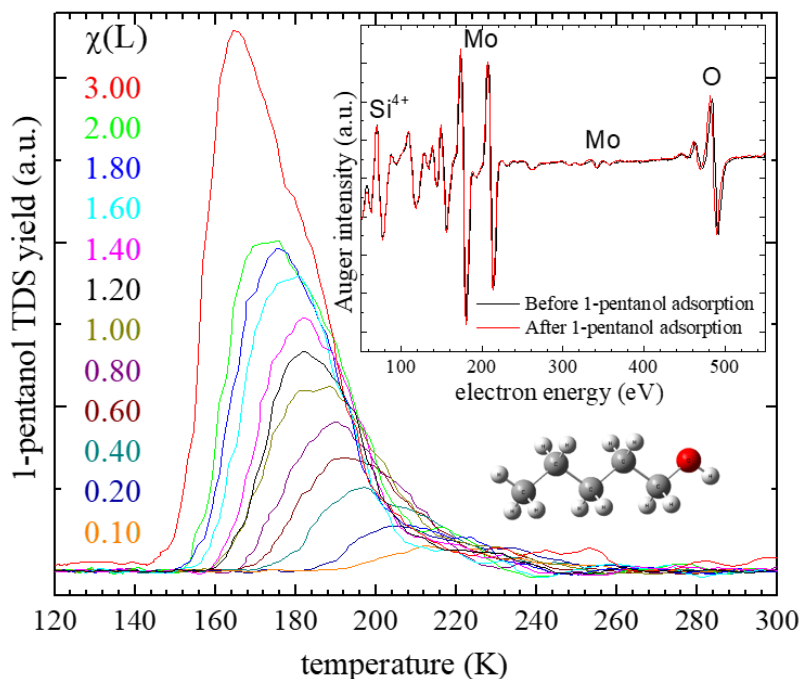


Figure 3.30. 1-pentanol TDS curves on silicatene as a function of exposure (inset- AES characterization before and after TDS)

Measuring actual adsorption probabilities of alcohols utilizing molecular beams are cumbersome since the generation of the supersonic molecular beams of liquid alcohols is challenging. Also, when the chain length increase, there can be different adsorption geometries, which can cause this type of exposure dependence. For instance, long-chain alcohols may adsorb on the surface with tilted geometries, rather than laying down flat on the surface. With the size of the molecule, the tilt angle would change and also the alkyl-alkyl interactions between the adjacent adsorbates, which may lead to a size-dependent monolayer molecular density. However, the latter

effect (adsorption geometry dependence) can be ruled out since we observed only repulsive-lateral interactions irrespective to the molecular size of the alcohols.

Alcohol desorption energies were quantitatively compared using Redhead analysis (see Figure 3.31). The coverages were calculated by integrating the TDS peaks and normalizing with respect to the monolayer desorption peak (which is the onset of the condensation structure).

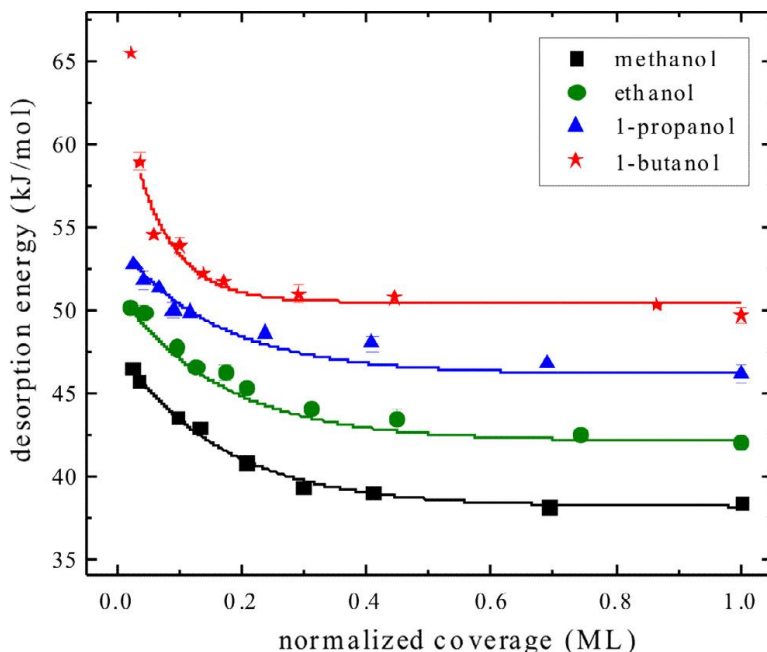


Figure 3.31. Coverage-dependent binding energies of methanol, ethanol, 1-propanol, and 1-butanol on silicatene calculate using Redhead analysis (a first order pre-exponential of $1 \times 10^{13} \text{s}^{-1}$ was used)

Table 3.5 shows the desorption energies at zero coverage limit, together with literature data of alcohol adsorption on carbon nanotubes (CNTs) for comparison. Reference data for alcohol physisorption are rather limited since most of the prior studies dealt with alcohol bond activation chemistry, for instance, electrocatalysis of methanol oxidation etc. Biding energy increases with the molecular size, consistent with the physisorption-like interactions. For each alcohol, binding energy decreases with the coverage, due to the repulsive lateral interactions caused by polar physisorbed alcohols. For convenient comparison of binding energies, the E_d vs θ curves were

parameterized according to $E_d(\text{methanol}) = 9.68e^{(-\theta/0.166)} + 38.13$, $E_d(\text{ethanol}) = 9.15e^{(-\theta/0.165)} + 42.10$, $E_d(\text{propanol}) = 7.91e^{(-\theta/0.161)} + 46.13$, $E_d(\text{butanol}) = 13.98e^{(-\theta/0.164)} + 50.48$, where E_d is in kJ/mol.

Prior studies on propanol adsorption on Mo(110) indicates dissociative adsorption.¹⁸⁵ Also, alcohol bond activation on Mo₂C and Ni surface have been observed. Therefore, we expected to see activated adsorption or strong chemisorption of alcohols, if there are any influences of the underlying support (Mo(112)). But, Mo(112)-c(2×2)-[SiO₄] is not reactive (for alcohol bond activation or chemisorption) even though the silicatene films are atomically thin, which suggest that there are no support effects of alcohol adsorption on silicatene grown on Mo(112).

Table 3.5. Zero coverage limit ($\theta < 0.02$) of the binding energies calculated using the Redhead approximations for alcohol adsorption on silicatene and CNTs¹⁸⁶

Alcohol	Silicatene		CNTs ¹⁸⁶
	T _p (K)	E _d (kJ/mol)	
Methanol	180	46.5	55.3
Ethanol	194	50.2	58.8
1-propanol	203	52.8	58.1
1-butanol	251	65.55	61.2

Binding energies were determined with the approximated equation $E_d = RT_p \left[\ln\left(\frac{\nu T_p}{\beta}\right) - 3.64 \right]$ by considering 1st order desorption of adsorbed alcohols ($\nu = 1 \times 10^{13} \text{ s}^{-1}$)

3.7.4. Summary: Alcohol adsorption on silicatene

Short chain alcohols (methanol, ethanol, 1-propanol, 1-butanol, 1-pentanol) adsorption on silicatene was investigated employing TDS. Molecular physisorption of all considered alcohols with binding energies increasing with the chain length was observed, which show zero coverage binding energies between 46.5-65.5 kJ/mol. Adsorption kinetics of alcohols on silicatene and Mo are quite different, which rules out support effects.

3.8. Two-dimensional zeolite synthesis

3.8.1. Introduction

Surface science analogs of zeolites (2D zeolite thin films) are rare and difficult to synthesize. The primary focus of this study is to synthesize a 2D zeolite thin film using a silicatene film as the starting precursor. 2D silicatene can also be considered as a type of 2D zeolite, which has interconnected $[\text{SiO}_4]^{4-}$ tetrahedral units as the primary building blocks with no Al content. Si to Al ratio plays an important part in chemical properties of zeolites. The strategy is to convert the silicatene film into a zeolite film by doping Al. The purpose of converting silicatene into a more reactive zeolite-like thin film is to address the problem of catalyst stability. Catalyst nanoparticle agglomeration during the catalytic processing conditions (at high temperatures and pressures) is a major problem encountered in several catalytic processes. Providing strong catalyst-support interactions is the common strategy to avoid this problem. 2D zeolites with non-zero Al/Si ratio can be considered as more reactive supports compared to silicatene (Al/Si=0). When the Al content is increased in zeolites, improved reactivity has been observed in prior studies for bulk zeolites. Polarities of the zeolites can be manipulated by changing the Al content. It has been observed that the Zeolites with high Al contents are more polar compared to the zeolites with low Al contents.¹⁸⁷

Structures and properties of several naturally occurring and synthetic bulk zeolites (layered or 3D) have been studied extensively. More than 232 types of unique zeolite frameworks have been identified.¹⁸⁷⁻¹⁸⁹ These bulk zeolites have microporous structures constructed by interconnected aluminosilicate tetrahedral units as the primary building blocks. There are several framework structures reported (secondary building units (SBU)), forming complex ring structures by interconnected alumina or silica tetrahedral units.¹⁸⁷ For instance, ZSM-5 (Zeolite Socony Mobile-5) is a commonly used 3D zeolite for heterogeneous catalysis related applications.¹⁹⁰⁻¹⁹¹

ZSM-5 belongs to the pentasil zeolite family, which formed with interconnected pentagonal rings, formed by corner-sharing aluminosilicate tetrahedral units. One pentasil unit has eight interconnected five-membered rings. The framework structure formed by interconnected pentasil units is known as MIF framework (which is the SBU of ZSM-5). The vertices of the framework are composed of Al or Si atoms, while the oxygen bridges interconnecting the pentasil units. Likewise, these aluminosilicates building blocks can be linked in various possible ways to form different types of mesoporous zeolite ring structures (from 4 membered to 12 membered rings).¹⁸⁷

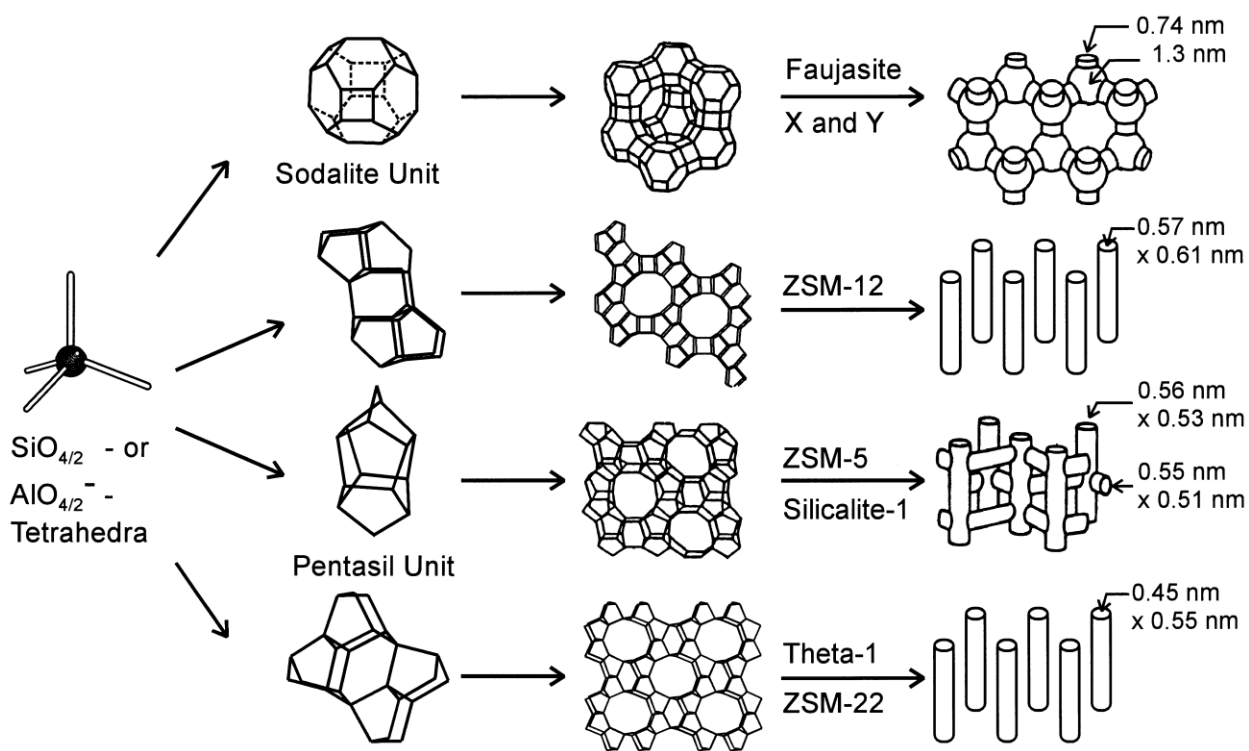


Figure 3.32. Some example zeolite framework structures with corresponding 3D zeolites (Reprinted from Solid State Ionics, 131, Jens Weitkamp, Zeolites and catalysis, 175-188., Copyright (2000), with permission from Elsevier).

The concept of 2D zeolite thin films was first introduced by Goodman, et al., in 1994.⁸⁹ They synthesized $\text{Al}_2\text{O}_3/\text{SiO}_2$ mixed oxide thin films by depositing Al on amorphous silica films grown on Mo(100) substrates, followed by several high-temperature annealing steps (up to 1200 K) to completely oxidize Al to Al^{3+} . These mixed oxide structures have been extensively

characterized employing AES, XPS, and TPD. Reduction of a significant portion of Si^{4+} to Si^0 , formation of Si-O-Al bonds by Al^{3+} replacing Si^{4+} in the precursor, diffusion of aluminum oxide into the bulk of the silica surface, and the desorption of volatile SiO as a result of the solid-state reaction have been observed. The starting precursor (silica thin film) was not crystalline and a huge amount of silicon deposited on the surface was also evident. Importantly, the mixed oxide thin films somewhat resemble the electronic properties of bulk aluminosilicates such as glass and zeolites.⁸⁹

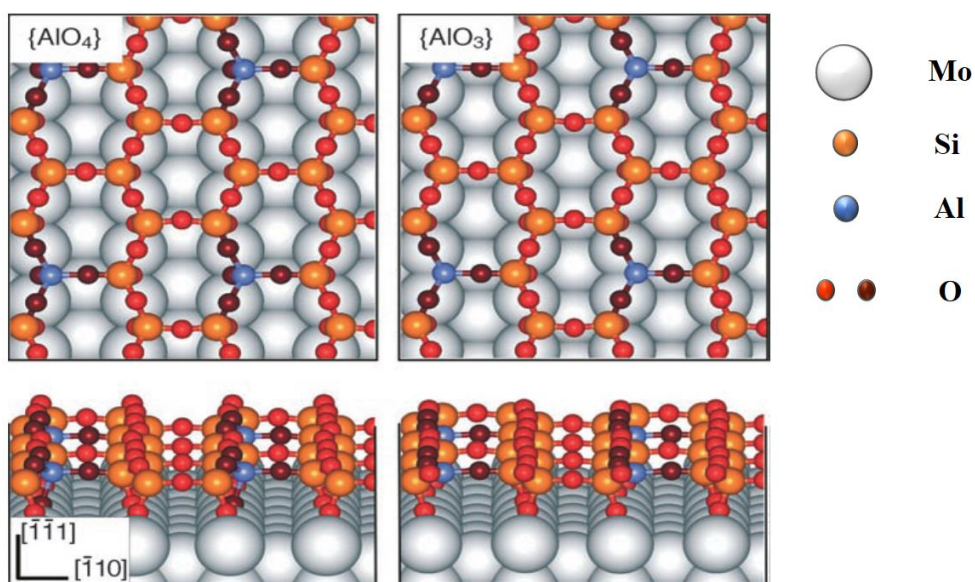


Figure 3.33. Proposed models of the top view and the side view (top and bottom respectively) of the Al-doped silicatene films (Reprinted from *Angewandte Chemie (international edition)*, 45, Dario Stacchiola et al., *Synthesis and Structure of Ultrathin Aluminosilicate Films*, 7673., Copyright (2006), reprinted with permission from Wiley online library (John Wiley and Sons)).

Later, in 2006, Freund et al., introduced crystalline 2D aluminosilicate thin films by co-deposition of silicon and aluminum on Mo(112) substrates in an oxygen ambient. They were able to obtain crystallinity (long-range order) by post-annealing these thin films, which have been characterized by LEED and STM. According to XPS investigations, Si and Al atoms in the film are fully oxidized. Furthermore, according to STM observations, the Al-doped silica resembles the honeycomb-like structure of 2D silicatene films, which was discussed in section 3.3.1.3.¹⁹²

The focus of the current study is to use the sequential synthetic technique originally proposed by Goodman, et al., with relevant modifications to obtain crystalline 2D-zeolite structures with tunable Al/Si ratios. As the starting precursor, silicatene films grown on Mo(112) were used and the target was to optimize the Al deposition flux and the oxidation/ annealing conditions to obtain a crystalline 2D-zeolite thin film.

3.8.2. Experimental methods

Silicatene films were synthesized on Mo(112) substrates and characterized as described in section 3.3. H₂O/D₂O adsorption kinetics was investigated using TDS. Metallic Al was vapor deposited on silicatene films using a home-made metal doser (prepared by 99.9% Al rods wrapped with a tantalum filament and designed to evaporate Al by the heated tantalum filament). Al flux and oxidation conditions were varied to obtain Al₂O₃/ SiO₂ mixed oxide thin films (or Al₂O₃ clusters on silicatene, which was formed with large Al flux and oxygen annealing at 900-1000 K at oxygen ambient) and Al-doped silicatene (with small Al flux and several UHV annealing steps up to 1200 K). 2D-zeolite film growth was extensively characterized by AES. Water-TDS (H₂O/D₂O) was used as the chemical (reactivity) characterization technique.

3.8.3. Results and discussion

Different oxidation states of Si, as well as Al, can be distinctly identified using AES. Si⁰, Si⁴⁺, Al⁰, and Al³⁺ oxidation states have major AES peaks at 92, 76, 68, and 51 eV respectively.¹⁵⁴ The CMA based AES in our lab has an energy resolution of 0.6-1.6% with non-retarding analyzer mode, and therefore 2D-zeolite film growth was characterized by AES. Figure 3.34 (a) depicts AES data of a typical silica thin film grown on Mo(112), which has the characteristic Si⁴⁺ major peak ~ 76 eV. Figure 3.34 (b) indicates the sequential growth of an Al₂O₃ film on clean Mo(112). The purpose of this pure Al₂O₃ film growth on Mo(112) was to characterize the different oxidation

states of Al by AES chemical shifts experimentally. Also, understanding the behavior of the deposited metallic Al at higher temperatures (with and without oxygen) is essential to deduce 2D-zeolite growth mechanisms.

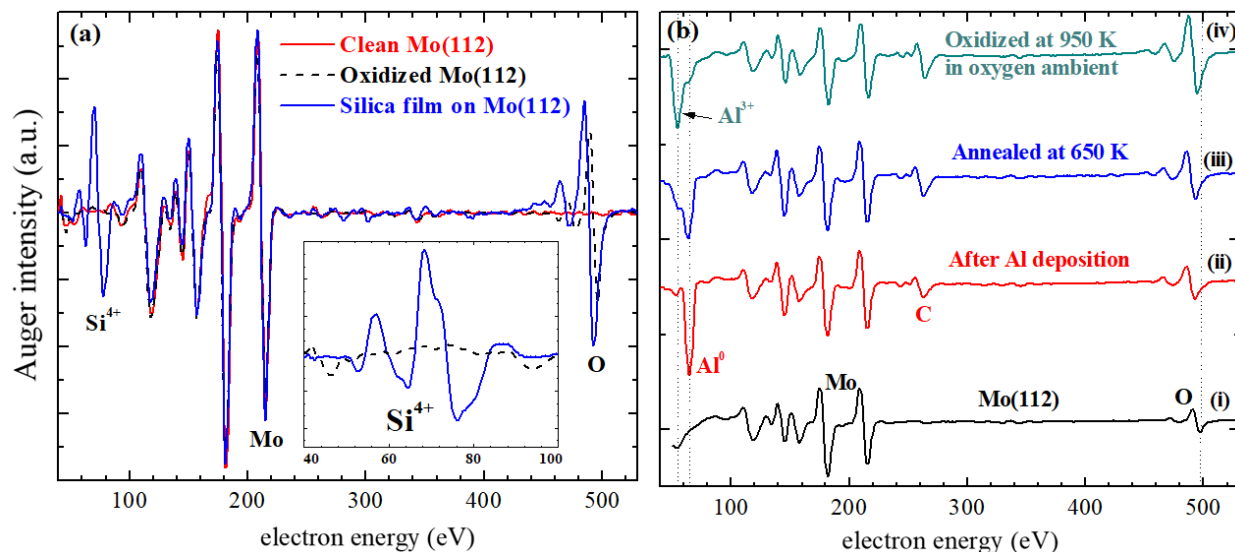


Figure 3.34. (a) Characterization of a silica thin film grown on Mo(112), (b) sequential growth of an Al_2O_3 thin film on clean Mo(112)

The Mo(112) substrate was exposed to a large Al flux at room temperature (300 K) to obtain an Al-deposited substrate (Al film on Mo(112)- Figure 3.34 (b)-(ii)). Auger spectra of Al deposited thin films indicate the characteristic Al^0 AES feature at 68 eV. Annealing the Al-deposited substrate at 650 K leads to a small reduction of the Al^0 peak intensity, with a superimposed Al^{3+} feature on the Al^0 peak, and also with an increased oxygen content of the surface, indicated by AES (see Figure 3.34 (b)-(iii)). A trace amount of background water in the UHV chamber and the residual oxygen adsorbed on the Mo(112) surface may be responsible for the oxidation of Al^0 to Al^{3+} at 650 K. Limited amount of oxidation sources could have hindered the complete conversion of Al to Al_2O_3 . By oxygen annealing the surface in the next step, a significant part of remaining metallic Al was oxidized to form an Al_2O_3 thin film, leaving only traces of Al atoms on the surface. Characteristic Al^{3+} AES feature at 51 eV with a small

superimposed shoulder Al peak (to the right of the Al^{3+} peak) is evident in AES (see Figure 3.34 (b)-(iv)).

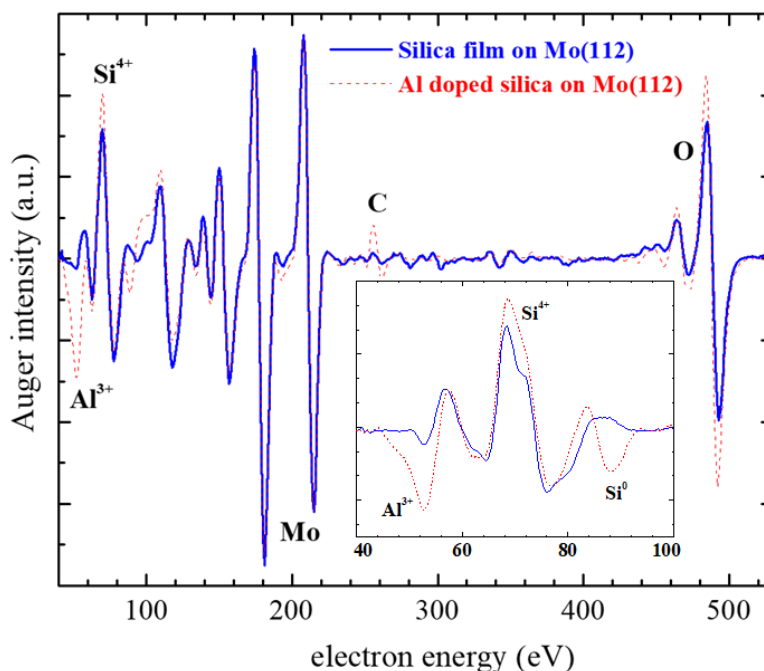


Figure 3.35: AES characterization of a silicatene film (solid blue line) and a $\text{SiO}_2/\text{Al}_2\text{O}_3$ mixed oxide thin film on Mo(112) substrate.

$\text{SiO}_2/\text{Al}_2\text{O}_3$ mixed oxide thin films were synthesized on Mo(112) using a silicatene film as the starting precursor. A small amount of Al was deposited on the silicatene thin film followed by oxygen annealing at 900 K to obtain the mixed oxide structure. As depicted in Figure 3.35, deposited Al is oxidized to Al^{3+} . A trace amount of Al^0 may be remaining on the surface, which is not detectable due to the broad Si^{4+} peak. Also, partial reduction of the SiO_2 thin film is evident according to AES (reduction of Si^{4+} to Si^0 is characterized by AES feature appearing at ~92 eV, corresponding to Si^0). A slight increase in the oxygen intensity is coming from the Al_2O_3 clusters formed (during Al oxidation process) on the SiO_2 thin film. Therefore, the surface consists of SiO_2 , Al-doped silica (evident by partial reduction of the silicatene structure), and Al_2O_3 clusters. These $\text{SiO}_2/\text{Al}_2\text{O}_3$ mixed oxide films expected to be chemically more reactive compared to the inert

silicatene films. Since the amount of Al introduced to the silicatene film is very small, ~80% of the mixed oxide structure resembles the original silicatene structure, which was estimated considering the O-AES peak intensities before and after Al deposition and oxidation (slight structural change is due to the formation of the Al₂O₃ clusters, as well as traces of Si and Al). Also, uniform distribution of the Al³⁺ sites (either doped Al³⁺ in the silicatene structure or Al₂O₃ clusters) were evident according to multiple AES scans recorded at different sample positions.

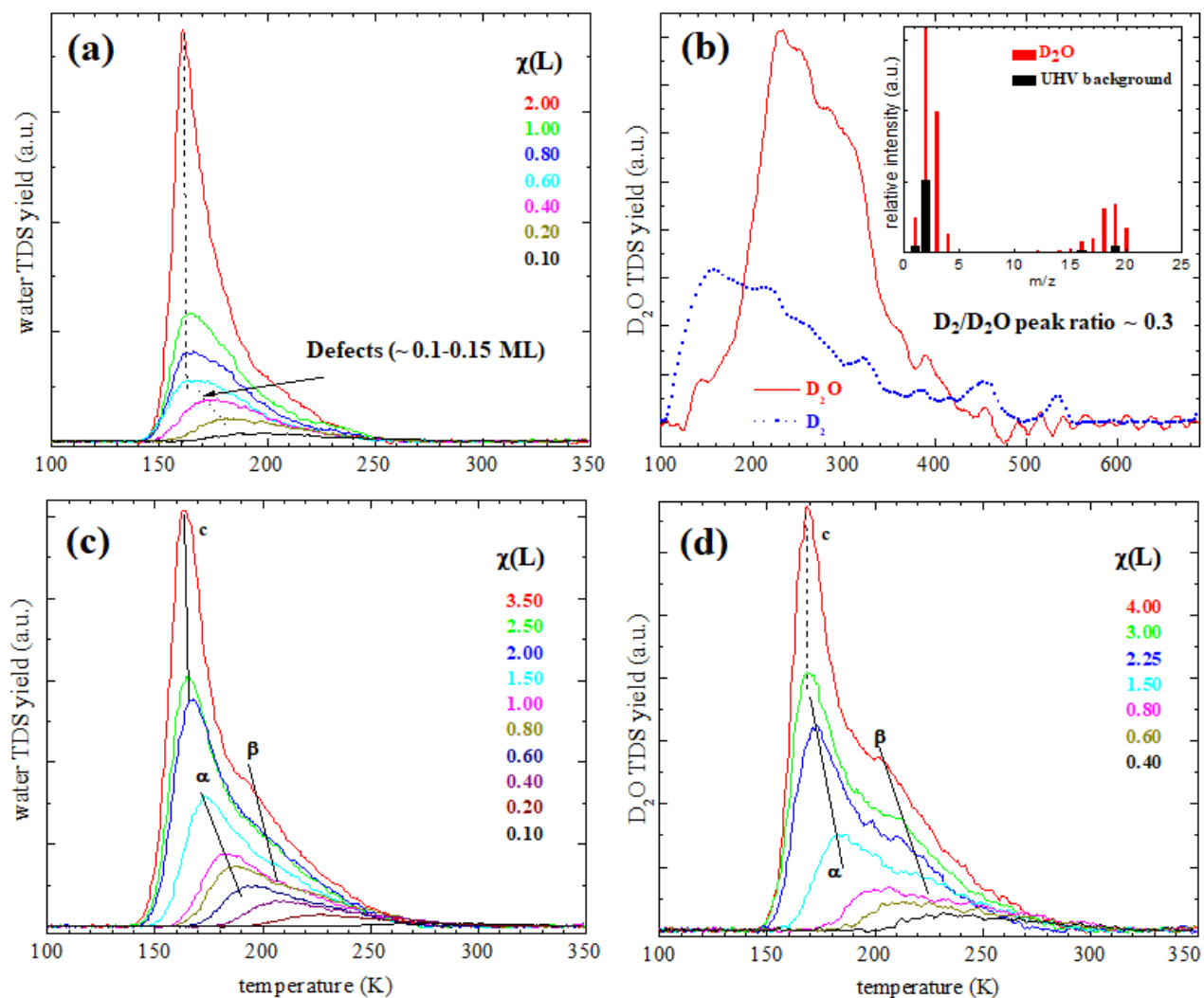


Figure 3.36. (a) Water TDS on a silicatene film, (b) desorption profiles of D₂O and D₂ after ~ 1.0 Langmuir of D₂O adsorption on SiO₂/ Al₂O₃ mixed oxides, (c) Water TDS on mixed oxide thin films, (d) D₂O TDS on mixed oxide thin films

Chemical reactivity of the mixed oxide thin films was characterized by H₂O/ D₂O TDS experiments. Water TDS of a typical inert silicatene film (with ~ 0.10-0.15 ML of defects) is depicted in Figure 3.36 (a) for comparison (which is the initial precursor used for the mixed oxide (zeolite) film growth). The initial lower temperature peak shift with the exposure up to ~ 0.6 L is due to the trace amount of defects (inhomogeneity). Starting from 0.6 L, lower temperature leading edges of TDS traces are lining up, which is characteristic of 0th order desorption kinetics. Therefore, silicatene films are hydrophobic. On the other hand, hydrophilic interactions of water with synthesized mixed oxide thin films is evident, as depicted in Figure 3.36 (c).

At exposures above 2.0 L (Figure 3.36 (c)), lower temperature leading edges of TDS peaks aligning, characteristic to 0th order kinetics (c-peak). c-peak can be assigned to the condensation (multi-layer adsorption) of water on mixed oxide thin films. At exposures below 2.0 L, two distinct TDS features are evident. Both shifted to lower temperatures with exposure, consistent with repulsive lateral interactions of the polar physisorbed molecules and/ or surface heterogeneity. Both explanations are possible on this mixed oxide surface. [SiO₄]⁴⁻ and [AlO₄]⁵⁻ are the major adsorption sites while Al₂O₃, traces of Al, Si, and defects may also act as potential adsorption sites. Defects, Al, and Si sites, as well as poly-crystalline Al₂O₃ clusters deposited randomly on the surface may have the highest binding energies due to unsaturated valances. Even water dissociation is possible on these type of adsorption sites.⁹¹ Therefore, the β-peak is assigned to these minor adsorption sites. According to prior studies with 3D zeolites, it has been shown that the polarity of the zeolite structure can be controlled by Si to Al ratio. Inert zeolites have low Al content (high Si/Al ratio), which are hydrophobic, while polar zeolites have high Al content with hydrophilic character. Replacing Si⁴⁺ by Al³⁺ in the [SiO₄]⁴⁻ unit in the silicatene structure increase the net negative charge and hence polarity of the structure. Therefore, Al-doped silica exhibit high

hydrophilicity compared to silicatene (Al/Si=0). α -peak is assigned to water adsorption on $[\text{SiO}_4]^{4-}$ and $[\text{AlO}_4]^{5-}$ binding sites, which also exhibit coverage dependent desorption, contrast to inert silicatene.

To investigate the molecular/ dissociative adsorption behavior of water on $\text{SiO}_2/\text{Al}_2\text{O}_3$ mixed oxide structures, a multi-mass D_2O TDS experiment was used. Simply, D_2O was adsorbed on mixed oxide thin film by backfilling the vacuum chamber (~ 1.0 L). Then, the sample temperature was ramped from 95-700 K and D_2 , D_2O were detected using the residual gas analyzer. H_2/D_2 and O_2 are major dissociation products of water (which was observed for water adsorption on reactive substrates in prior studies¹²⁵) and therefore D_2 was detected. D_2O was used because of the large UHV background pressure of H_2 (H_2 couldn't be detected without background interferences if H_2O was used). Figure 3.36 (b) depicts the multi-mass traces of D_2 and D_2O . The inset of Figure 3.36 (b) compares the gas-phase mass scan of D_2O (thin red bars) with the UHV background mass scan (thick black bars). Introduced D_2O into the vacuum chamber (1.0 L by backfilling) seems to exchange isotopes with background H_2 , which may be the reason for the presence of masses (m/z) 3(HD), 4(D_2), 18(H_2O), 19(HOD) in relatively high intensities. The low-temperature D_2 peak may be from the molecularly adsorbed D_2 on the substrate, from the background (after isotope exchange), which has a relatively low-intensity peak compared to the D_2O peak (Figure 3.36 (b)). Also, if water dissociates, D_2 desorption temperature would have been much higher (dissociation products, such as D_2 , O_2 desorb usually above 250 K on oxide surfaces¹²⁵).

Figure 3.36(d) depicts the D_2O adsorption TDS curves on mixed oxide thin films as a function of D_2O exposure. This TDS data set is identical to the water-TDS data set for the same substrate (Figure 3.36(c)), suggesting that there are no significant isotope effects for the water

adsorption on $\text{Al}_2\text{O}_3/\text{SiO}_2$ mixed oxide thin films or TDS is not sensitive enough to detect any isotope effects.

3.8.4. Future directions

Conversion of the silicatene films to an Al-doped silica structure resembling the original silicatene structure without Al_2O_3 contaminants will be important, which can possess more specific binding sites to catalyst nanoparticles. A hydrodesulfurization model catalyst can be prepared by depositing Mo nanoparticles on Al-doped silicatene structures. Polarity introduced by Al doping may enhance the stability of the catalyst by promoting strong catalyst-support interactions. Specificity of the catalytic support may introduce more homogeneity to the catalyst. The polarity of the support can be tuned accordingly by changing the Al/Si ratio. The catalytic activity and stability can be characterized by employing thiophene as a probe molecule.

3.8.5. Summary: 2D-Zeolites

Al_2O_2 and $\text{SiO}_2/\text{Al}_2\text{O}_3$ mixed oxide (2D-zeolite) thin films were grown on Mo(112) and silicatene films respectively using molecular beam epitaxy. Film growth was extensively characterized by AES. Chemical reactivity of 2D-zeolite thin films was compared with inert silicatene using H_2O and D_2O as probe molecules. 2D-zeolite structures are hydrophilic compared to the hydrophobic silicatene. Polarity introduced by Al incorporation into the silicatene structure may be the major cause of the reactivity together with trace amounts of defects, Si, and metallic Al. Like in 3D zeolites, the polarity of 2D-zeolites can also be tuned by changing Si/Al ratio, as indicated by this study.

4. GAS-SURFACE INTERACTIONS ON METHYLAMMONIUM LEAD IODIDE PEROVSKITES

Lead halide perovskites are a fascinating class of material for solar cell related applications, which shows record efficiency in the recent past. However, poor thermal and chemical stability prevent industrial applications. This study investigated the possible thermal degradation mechanisms, effects of impurities on thermal stability, and improvement of stability by surface passivation (by introducing protective ligands) of methylammonium lead iodide perovskites.

4.1. Introduction

Methylammonium lead halides are organic-inorganic hybrid solid materials with perovskite structure. The chemical formula of these materials can be generally given as $\text{CH}_3\text{NH}_3\text{PbX}_3$, where X can be Cl, Br, I or combination of these halides, to form lead halide perovskites. These materials have been extensively studied in the recent past experimentally and computationally for solar-to-electric power conversion, light emitting diodes, LASERs, and photodiodes etc.¹⁹³⁻¹⁹⁸

Lead halide perovskites attracted considerable attention as the light harvesting active material in third generation solar cells owing to high power conversion efficiencies and available low-cost solution phase fabrication techniques.^{196, 198} Compared to traditional silicon-based solar cells, which required complex and expensive fabrication techniques such as chemical/ physical vapor deposition, molecular beam epitaxy etc., at higher temperatures (>1000 °C) and at UHV conditions, perovskite solar cells can be processed employing simple wet chemistry fabrication techniques with standard laboratory environments.^{193, 196, 199} These perovskite solar cells were introduced in 2009 and the power conversion efficiencies were increased from 3.8% to 25.2 % within a decade,^{195, 198} showing the fast advancement of the perovskite solar cell technology.

4.1.1. Advantages

High absorption coefficients of lead halide perovskite materials enable the absorption of complete visible spectra with ultra-thin films. High absorption coefficients are required property for the light-harvesting materials of solar cells in order to absorb efficiently. The estimated absorption coefficients of thin films of these materials found to be ten times greater than that of typical ruthenium-based molecular dyes used in dye-sensitized solar cells. Because of the high absorption coefficients with a wide range of absorption in the solar spectrum from UV to IR regions, most of the incoming radiation can be absorbed by thin layers of lead halide perovskites.²⁰⁰⁻²⁰¹

Lead halide perovskites have direct band gaps, which is an added advantage for solar cell related applications. Indirect band gap materials do not absorb light efficiently, which required thick layers of materials (e.g. first and second generation silicon solar cell materials are few hundreds of micrometers thick²⁰²), whereas thin-film solar cells like perovskite solar cells are made up of very thin active layers for harvesting light ($< 1\mu\text{m}^{197}$).

The charge carrier diffusion length, which is defined as the average distance the charge carriers move in a semiconductor before recombination, plays an important role in photovoltaic cells. Long diffusion lengths of the charge carriers are important and lead halide perovskites have charge carrier diffusion lengths exceeding 10 micrometers.²⁰³⁻²⁰⁴

4.1.2. Limitations

Even though these hybrid perovskite materials possess several advantages for solar cell related applications, the real world industrial applications are limited due to the short-term and long-term instability of these materials, degrading to form PbI_2 with time, which has a completely different electronic structure compared to the initial perovskite structure.²⁰⁵⁻²⁰⁶ The sensitivity of

these materials to moisture, oxygen and other ambient gases, intrinsic thermal degradation, degradation due to the influence of voltage, UV light etc., are major concerns.²⁰⁷⁻²⁰⁹ Also, the lead toxicity is another major issue associated with organo-lead halide perovskites. Replacing Pb with Sn in the perovskite structure would solve the toxicity problem but the solar cell performance decreases significantly.²¹⁰⁻²¹¹ Several studies have been performed in order to understand the degradation mechanisms, as well as to improve stability. Most of the studies were focused on thermal and moisture degradation of organic-inorganic lead halide perovskites.^{205-209, 212}

Due to instability in polar solvents such as electrolytes, organo-halide perovskites can be hardly applied to liquid state solar cells in industrial applications. For instance, rapid dissolution of $\text{CH}_3\text{NH}_3\text{PbI}_3$ (MAPbI_3) perovskite materials have been observed in Γ/I_3 electrolyte, decreasing the power conversion efficiencies drastically.²⁰⁶ However, post-modification of perovskite layers by aluminum oxide prevented the degradation in liquid state cells, which also seemed to be suppressing the carrier recombination.²¹³ Similarly, post-modification of perovskite layers by aluminum oxide in solid-state solar cells has introduced some moisture-stability, compared with the non-modified perovskite layers.²⁰⁶ Other than Al_2O_3 , hydrophobic protecting layers such as oligothiophene hole transport layers have been successfully used to improve the stability in humid conditions.²¹⁴ In some studies, typical Ag or Au electrodes were replaced by carbon-based electrodes, that introduced significant moisture stability at ambient conditions, in which the thick carbon electrodes acting as a protecting layer for the perovskites.²¹⁵

Furthermore, amine mediated metal oxide chemical inhibition layers have been introduced to chemically neutralize the mobile ionic defects in the perovskite layers. Chemical inhibition successfully maintained about 80% of the solar cell's initial power conversion efficiency, even after 200 hours in ambient conditions without any encapsulation.²¹⁶ Doped hole transport layers

seem to be acting as deactivators for perovskites even though they improve the device performance in short-term. The dopants react with perovskites and decrease the long-term stability.²¹⁷ By introducing non-doped charge transport layers such as fullerenes, conjugated small molecules, and zinc oxide nanocrystals etc., device stability has been improved.²¹⁸ Self-degradation of the lead halide perovskites due to ion contamination is another challenge for device stability. It has been found that the ionic defects cause the self-degradation by ion movement from the perovskite layer to electrode-electron transport layer interface.²¹⁹ Integrated organic chemical inhibition layers (OCIL) into the perovskite active layer have been successfully used to prevent the ion migration from perovskites. For instance, integrated fulleropyrrolidine mixtures into the perovskite layers efficiently passivated the electrodes from perovskites by trapping halide anions transport from perovskites to electrodes, which improves the stability of the active layers.²¹⁸

Even though there are several studies attempted on stability improvement of lead halide perovskites with some advances, still, the organo-halide perovskite solar cells have very little market significance due to insufficient stability.

4.1.3. Perovskite structure

The perovskite crystal structure can be generally explained by the chemical formula ABX_3 , which ideally forms a cubic crystal structure with $[BX_6]$ corner-sharing octahedra in which the cationic A occupied in the center of 12-fold coordination site generated by eight of $[BX_6]$ octahedra (Figure 4.1). A and B are two cationic species, both bonded to X anions, where the A atom typically larger than B. The coordination numbers of A and B atoms can be reduced due to the distortions of the structure.²²⁰⁻²²¹ The name perovskite is derived from the mineral calcium titanate with the ABX_3 crystal structure explained above ($CaTiO_3$), which named as perovskite after the Russian mineralogist, Perovski, L.A.

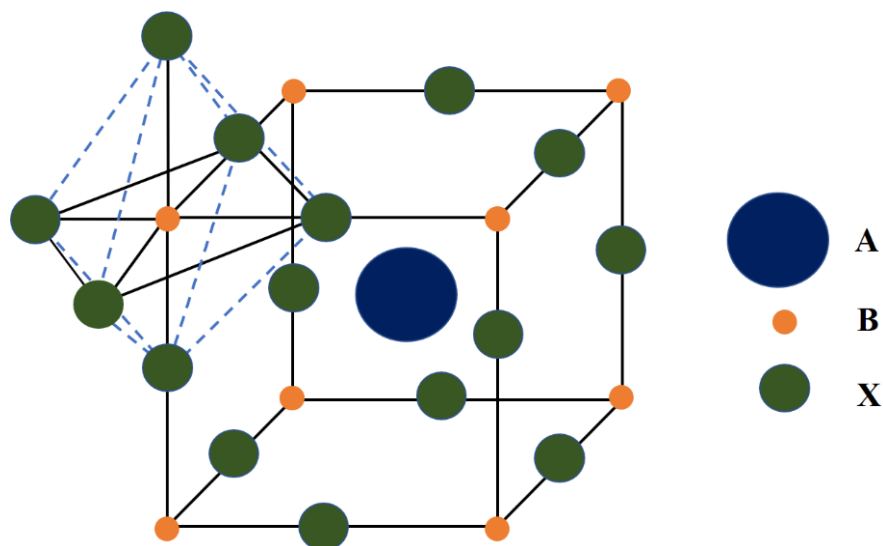


Figure 4.1. Schematic representation of the ideal cubic perovskite structure ABX₃ with a three-dimensional network of [BX₆] corner-sharing octahedra, forming 12-fold cavities containing cationic A.²²²

There is a large family of naturally occurring compounds containing the perovskite structure. Generally, the perfect cubic perovskite structure is not commonly encountered. Even the mineral perovskite (CaTiO₃) has a slightly distorted structure, which has been determined to have an orthorhombic crystal structure.^{220, 223} SrTiO₃ is an example of a naturally occurring mineral with ideal cubic perovskite structure.²²¹ Initially, these natural perovskite minerals were studied for their magnetic and electric properties arises due to the reduced symmetry of the distorted structures. Several different types of naturally occurring minerals with perovskite structure and synthetic perovskites have been discovered with potential applications such as high temperature capacitors, metallic conductors, catalysts, superconductors, insulators, giant magnetoresistance devices, light harvesting materials for solar cells etc.^{222, 224} Among these minerals, bridgmanite, which is a silicate perovskite [(Mg, Fe)SiO₃] is considered as the dominant silicate mineral on the earth.²²⁴

Synthetic organic-inorganic hybrid perovskite materials were first introduced to the field of photovoltaic cells by Akihiro Kojima et al. They synthesized nanocrystalline CH₃NH₃PbI₃ and CH₃NH₃PbBr₃ particles on TiO₂ films, which were used as the light absorbing active layers in the

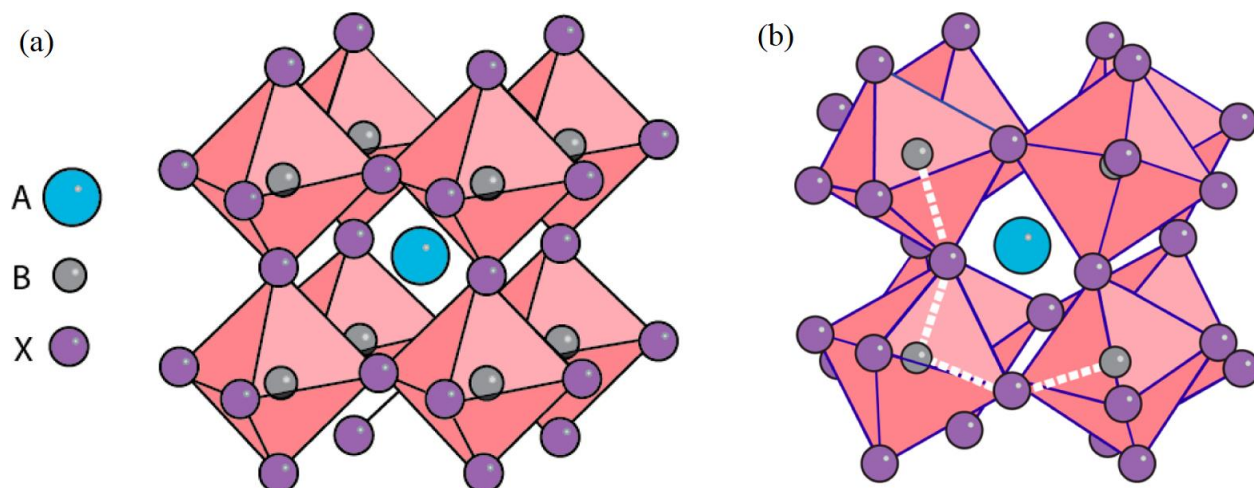


Figure 4.2. (a) Symmetric cubic phase and (b) less symmetric orthorhombic phase of the perovskite crystal structure (Adapted with permission from ref.¹⁹⁴ Copyright (2017) American Chemical Society)

photovoltaic cells for the first time.¹⁹⁵ The crystal structures of $\text{CH}_3\text{NH}_3\text{PbX}_3$ were determined by powder x-ray diffraction, which found to be having the crystalline structures belong to perovskite family. According to their x-ray diffraction peak assignments, $\text{CH}_3\text{NH}_3\text{PbI}_3$ was identified as tetragonal perovskites while $\text{CH}_3\text{NH}_3\text{PbBr}_3$ with cubic perovskite structures.¹⁹⁵ With the fast advancement of the perovskite solar cell technology, the structures of $\text{CH}_3\text{NH}_3\text{PbX}_3$ hybrid perovskites have been studied extensively in the past few years. Most of these hybrid perovskites consist of inorganic lead halides (or tin halides) and organic methylammonium sublattice. Other than methylammonium, formamidium ($\text{CH}_3(\text{NH}_2)_2^+$) and Cs^+ were also common as the A cation in the perovskite structure. In MAPbX_3 perovskites, cationic Pb^{2+} is octahedrally coordinated with the anionic X^- (halide anion) forming corner-sharing octahedra with the cationic methylammonium ion having the 12-fold coordination. Other than ideal cubic unit cell structures, tetragonal and orthorhombic symmetries have also been identified.²⁰⁵ The different polymorphic forms of MAPbX_3 is correlated to the orientation of the methylammonium ion in the crystal structure. More ordered MA ions resulted in the orthorhombic phase while more disordered MA ions resulted in

the cubic phase.²²⁵ Also the crystallization conditions affects the final polymorphic form. For instance, ambient conditions favor the formation of tetragonal phase.²²⁶ The organic methylammonium cation plays the important role of charge stabilization of the perovskite structure. But, the stability of the organic cation seems to be the main barrier for the commercialization of lead halide perovskite solar cells, which tend to degrade forming methyl iodide and PbI₂ more often due to self-degradation or as a result of temperature and moisture effects. However, the degradation mechanisms are not known very clearly, which is a major hindrance for stability improvement.

4.1.4. Degradation mechanisms of MAPbI₃

Several studies have been conducted in order to understand the thermal, moisture, and self-degradation mechanisms of MAPbI₃.^{200, 205-208, 212} Formation of yellow colored lead iodide together with volatile methylamine were commonly encountered. The MAPbI₃ perovskites tend to degrade in the air and low vacuum (10⁻² torr), which was rapidly accelerated by temperature and relative humidity conditions.²⁰⁵ In the presence of water, deprotonation of methylammonium cation, forming volatile CH₃NH₂ and HI leaving PbI₂ have been observed.²⁰⁶ Other mechanisms involving hydrated perovskite intermediates, forming similar products were also proposed recently. In the latter case, by in situ absorption spectroscopy and GIXRD measurements, hydrated perovskite intermediates containing PbI₆⁴⁻ has been identified, which then eventually decomposed into CH₃NH₂, HI, and PbI₂. The formation of the hydrated intermediate can be given by, 4CH₃NH₃PbI₃ + 2H₂O ↔ (CH₃NH₃)₄PbI₆·2H₂O + 3PbI₂.²¹²

According to computational calculations, thermodynamic surface degradation of the MAPbI₃ perovskites is mainly due to the creation of volatile molecular defects. Molecular vacancies such as HI and MAI with non-ionic character caused more favorable dissociation than

ionic (e.g. MA^+) or atomic (e.g. Pb, I, H etc.) defects. Creation of thermodynamic defects was accelerated by high temperatures, which somewhat explains the instability of MAPbI_3 at high temperatures.²⁰⁵ Avoiding the internal vacuum spaces (defects) of the MAPbI_3 crystals by compact and highly crystalline growth of the material might increase the stability by minimizing the internal thermodynamic degradations. Also, by efficiently passivating the surface, thermodynamic degradation of the organohalide perovskites can be minimized, which is the strategy used in our study as well.

Furthermore, combined experimental and theoretical studies have been carried out to determine the thermal degradation mechanisms of MAPbI_3 . Thermogravimetric studies coupled with mass spectrometry at ambient pressure and inert conditions (He environment) suggested that the thermal degradation of MAPbI_3 releases CH_3I and NH_3 , which also further confirmed by DFT calculations.²⁰⁷ This is in contrast with the mechanisms predicted in some other studies (e.g. ref.²⁰⁶), that suggest the formation of CH_3NH_2 and HI as final products (PbI_2 common in both cases) in humid environments. Therefore, in the presence and the absence of humidity, different dissociation mechanisms are possible.^{206-207, 212}

4.1.5. Synthesis of MAPbX_3 perovskite thin films

The high efficiency of MAPbI_3 perovskite solar cells highly depends on the quality of the perovskite thin film used as the light harvesting layer. The perovskite thin films should have preferred crystallographic orientations with homogeneity and high crystallinity, large-grained microstructures with fewer vacancies, residual PbI_2 impurity free flat surfaces, and large enough contact areas for hole transport layers etc.^{193, 227} Several attempts have been made to obtain high quality perovskite crystals by optimizing preparation techniques with controlled reaction

conditions such as temperature, reaction time, chemical compositions etc., selecting different precursors, introducing surfactant ligands and many more.^{196, 227-230}

The ability of the synthesis of high-quality semiconductor thin films employing low-cost solution-based fabrication techniques is an advantage of perovskite solar cells compared to the conventional silicon-based solar cells. Simply, by combining stoichiometric amounts of PbX_2 and $\text{CH}_3\text{NH}_3\text{X}$ in solvents such as DMF and drop casting the precursor solution on the required substrate followed by spin coating to prepare a thin homogeneous film and drying out the solvent, self-organized nanocrystalline MAPbX_3 thin films can be prepared.¹⁹⁵ This basic preparation method has been improved significantly during the past few years to enhance the stability and reproducibility.

Reduction of the bulk defect density of perovskites is a major challenge, which induces intrinsic degradation. Increasing the size of the crystals and the crystalline quality of the grains are some approaches to reduce bulk defect density.¹⁹⁶ By varying the precursor concentrations, using mixed solvents, thermal annealing etc., some control over the defect densities have been achieved.²³¹⁻²³² Also, using solution based hot-casting techniques, continuous and defect-free organohalide perovskite thin films with large (millimeter size) crystalline grains were obtained recently.¹⁹⁶

Using lead acetate as the precursor, ultra-smooth perovskite thin films were obtained, which seems to have smaller grain sizes compared to the perovskites prepared by lead halide sources.²³³ The grain sizes could be increased by solvent-annealing methods and using lead acetate-lead halide mixed sources. Using lead acetate precursors, enhanced reproducibility and low hysteresis were observed together with structural flexibility enabling the synthesis of perovskite nanowires, nanorods, nanoparticles etc.²³⁴⁻²³⁵ Furthermore, with the lead acetate

precursor, perovskite thin films with higher light absorption ability, efficient electron transport, and faster electron excitation to the electron transport layer was observed. Also, the introduction of acetic acid to the precursor solution prevented the decomposition of perovskite crystals, improving the purity of the thin films.²²⁷

In a study focused on the synthesis of ligand-mediated inorganic perovskites (CsPbBr_3), different surfactant ligands were utilized to obtain various perovskite crystal shapes and sizes. Carboxylic acid and amine ligands with different sizes were used to dissolve PbBr_2 precursor, followed by reacting it with CsOAc . Depending on the carbon chain lengths of the surfactant ligands, nanoplates, nanocubes etc., of perovskites were obtained, in which the particle sizes were strongly depended on the sizes of the surfactant ligands. For instance, thinner nanoplates were obtained with shorter chain amines.²²⁹ By tuning the shapes and sizes, the optoelectronic properties of these materials can be optimized, which are important in further applications.

Other than the solution deposition techniques, there are vapor phase deposition techniques such as chemical vapor deposition,²³⁶ thermal vapor deposition^{37, 237} etc., utilized to fabricate organohalide perovskite thin films. Aerosol-assisted chemical vapor deposition (AACVD), which allows the transportation of non-volatile liquids into the reaction chambers for CVD has been successfully utilized to synthesize high-quality MAPbI_3 thin films at ambient pressure. Aerosol-assisted MAPbI_3 films were deposited using a precursor solution of PbI_2 and $\text{CH}_3\text{NH}_3\text{I}$ in DMF, on to a TiO_2 coated glass substrate, where the film growth occurred at $200\text{ }^\circ\text{C}$. Cubic phase was dominant initially, which was transformed into a tetragonal phase after several days. No impurity PbI_2 was observed according to XRD measurements after several days of storage at a dry atmosphere. Ability to scale up the synthesis is an advantage of this ambient pressure AACVD technique.²³⁶

Vapor deposition at high vacuum conditions has also been employed to synthesis organohalide perovskite thin films. Using a dual-source evaporator, $\text{CH}_3\text{NH}_3\text{I}$ and PbCl_2 have been simultaneously deposited onto a TiO_2 coated FTO substrate at high vacuum, where $\text{CH}_3\text{NH}_3\text{I}$ and PbCl_2 were heated to 116°C and 320°C respectively. By changing the deposition rates, times, and relative compositions of the precursors, different film thicknesses ranging from 125-500 nm were obtained. Optimum device performance has been observed with 330 nm thick perovskite films. The main advantage of this vapor deposition technique over solution phase deposition is the ability to scale up the process with conventional processing techniques already available industrially with infrastructures.²³⁷ However, the solution phase deposition of organohalide perovskite thin films is more promising for the commercialization due to the simplicity, low-cost, and fewer energy requirements.

The objective of this study is to improve the thermal stability of the hybrid MAPbI_3 perovskite thin films synthesized using a solution deposition technique at ambient, employing a carboxylic acid surface passivation layer. Furthermore, thermal degradation mechanisms, effects of residual impurities on thermal degradation, and small molecule adsorption properties were investigated experimentally and theoretically.

4.1.6. Carbon dioxide adsorption studies

Carbon dioxide is a standard probe molecule used in surface science for several model studies.²³⁸⁻²⁴² The surface chemistry and gas-surface interactions of CO_2 attracted much attention of a broad range of research fields including surface, materials, and environmental sciences, catalysis, energy etc. The interest in carbon dioxide chemistry increased recently, mainly due to environmental concerns. Since CO_2 is a greenhouse gas which affects global warming, capturing CO_2 (storage), converting it to value-added feedstocks in the chemical industry etc., are popular

topics nowadays.²³⁸⁻²⁴² Bond activation of CO₂, which is an inert molecule in the gas phase has been studied extensively on reactive metal surfaces for the applications such as methanol synthesis, higher alcohol synthesis, methane synthesis, reverse water-gas shift reaction (CO formation), and many more.^{238, 241, 243-245}

Molecular orbital diagram of the gas-phase linear CO₂ molecule is depicted in Figure 4.3. Ground state CO₂ is a linear molecule with two C=O bonds. A carbon atom with four valence electrons (C-1s² 2s² 2p²) and two oxygen atoms with six valence electrons in each atom (O-1s² 2s² 2p⁴) combined to fulfill their octets, forming two C=O bonds with sixteen valence electrons. By linearly combining the valence atomic orbitals, six sigma (bonding and anti-bonding) molecular orbitals and six π molecular orbitals (bonding, anti-bonding, and non-bonding) can be formed. Sixteen valence electrons are occupied in four sigma bonding molecular orbitals, and two π molecular orbitals, including one non-bonding molecular orbital. Each of these filled π molecular orbitals is doubly degenerated.²³⁹⁻²⁴⁰

First excited state electronic structure of CO₂ is analogous to that of NO₂, where one electron is excited to 2 π^* anti-bonding orbitals. The geometry of the excited state CO₂ found to be bent, rather than the linear configuration. Reduction of CO₂ during the adsorption processes favored the formation of anionic CO₂ (CO₂⁻) with seventeen valence electrons, which also tend to form bent geometries rather than linear configurations. The negative charge is more towards the oxygen atoms, because of the electronic shift towards oxygen, forming ~ 135° of O-C-O angles.^{238-240, 246}

Physisorption of CO₂ on low index metal/ metal oxide surfaces have been observed, which was commonly characterized by small desorption temperatures or binding energies, and large surface- CO₂ bond distances, experimentally and theoretically. Typically, close-packed low index

surfaces are inert and not active towards CO₂ adsorption, except there are defects and steps on the surface.

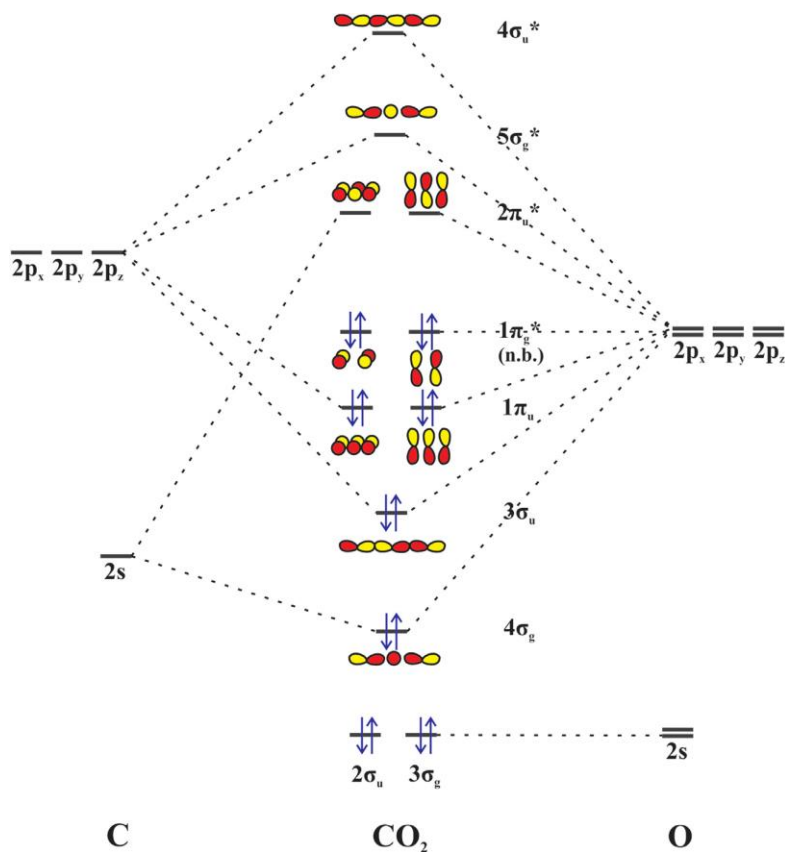


Figure 4.3. Molecular orbital diagram of the gas-phase carbon dioxide (Reprinted from Surface Science Reports, 71, Taifan et al., Surface chemistry of carbon dioxide revisited, 597., Copyright (2016), with permission from Elsevier)

When higher the coordination of the ordered surface, lower reactivity has been observed, which is the general trend for physisorption-like interactions.^{123, 247} Also, adsorbate assisted adsorption (attractive lateral interactions) has been observed with CO₂ physisorption.²⁴⁸ Most of the time, physisorbed CO₂ seems to have linear configurations, adsorbed with linear upright/ tilted or parallel to the surfaces. Typically, physisorbed CO₂ desorption below 200 K have been observed with TDS experiments²⁴² while the multi-layer formation (condensation) temperature ~ 80 K.²⁴⁹

Molecular chemisorption or dissociative chemisorption of CO₂ have been observed on high index surfaces such as stepped surfaces (e.g. stepped Cu), powders, and reactive metal surfaces

such as Ni (e.g. Ni(110)) etc.^{123, 250-252} The adsorption geometry of chemisorbed CO₂ and CO₂⁻ seems to be bent rather than linear configurations. Bent geometries of CO₂ are more reactive since the bending induces the charge distribution in the molecule, which influences further charge transfer by bond making or breaking. Mixed CO₂ configurations containing linear and bent structures have been observed for surfaces with weak chemisorption-like interactions.¹²³ Carbonate formation is a commonly encountered chemisorption form of CO₂ on metal oxides, which is assisted by the surface oxygen. MgO and CaO are some example model surfaces that readily form carbonates with CO₂.²⁵³

CO₂ adsorption on MAPbI₃ perovskites has not been studied previously using experimental techniques. The motivation for this study was to investigate the influence of atmospheric CO₂ on the stability of the organohalide perovskite thin films, as the ambient pressure synthesized perovskites contained a significant amount of CO₂ (adsorbed) even the synthesis carried out in a dry nitrogen atmosphere, which was observed with UHV characterizations (see Figure 4.8 and Figure 4.10). CO₂ adsorption on structurally similar perovskites such as BaTiO₃,²⁵⁴ SrTiO₃,²⁵⁵ LaMnO₃²⁵⁶ etc., have been studied previously. For instance, CO₂ strongly chemisorbed on oxygen vacant sites of the LaMnO₃, while weak physisorption-like interactions were observed on metallic sites. Similar to CO₂ adsorption on certain metal oxides, carbonate formation on oxygen surface sites of the LaMnO₃ have also been observed.²⁵⁶ Even though the structures have similarities, chemical properties of MAPbI₃ and above inorganic perovskites are quite different.

4.1.7. Formic acid adsorption studies

Formic acid adsorption on several different metals, metal oxides, and semiconductor surfaces have been investigated experimentally and theoretically for fundamental interests as well as applied catalysis perspectives.^{194, 254, 257-260} Fundamentally, formic acid is the simplest molecule

containing the carboxylic acid functional group, which make it important and simple enough probe molecule for carboxylic acid-related adsorption studies. For instance, bio-oil decomposition mechanisms on transition metal surfaces have been investigated for the purpose of understanding C-O and C-C bond breaking mechanisms, employing formic acid as a probe molecule.¹⁹⁴ In the catalysis perspective, formate is an important intermediate commonly encountered in industrial catalytic processes, such as methanol synthesis. Also, formic acid has been observed as an industrial waste product of several organic transformations.^{257, 261} Also, formic acid adsorption on supported reactive metals such as Ni have been investigated for the purpose of hydrogen production from formic acid.²⁵⁹

Activated adsorption of formic acid on most of the surfaces was observed with quite a similar type of dissociation mechanisms. At temperatures greater than 400 K, adsorbed formic acid typically forms the formate (HCOO) intermediate, by dehydrogenation. Eventually, dissociative desorption of adsorbed formate, forming CO₂ and hydrogen typically observed. Low-temperature formate formation has also been seen with the coadsorption of oxygen (in the cases of oxidation or hydrolysis). Thermodynamically, formic acid has the ability to directly decomposed into CO and H₂O, without going through formate intermediate, which has been only observed in theoretical studies.²⁶² Formation of CHO, COOH intermediates have also been proposed in a recent theoretical study of formic acid adsorption on Cu(111) surfaces.²⁶³ CHO formation is observed in the current study, which seems to be a major dissociation product of formic acid.

Even though we considered the fundamental adsorption kinetics and dissociation mechanisms of formic acid on MAPbI₃ perovskites, the major motivation of this study is to investigate the ability of an adsorbed layer of formic acid to passivate the degradation mechanisms of MAPbI₃.

4.2. Experimental procedures

4.2.1. Materials

The methylammonium triiodoplumbate ($\text{CH}_3\text{NH}_3\text{PbI}_3$) precursor solution (1.37 g/ml in 40% DMF) was purchased from Sigma Aldrich. Indium-doped tin oxide (ITO) glass slides were used as the substrate for the perovskite thin films, which were also purchased from Sigma Aldrich ($25 \times 25 \times 3 \text{ mm}^3$ ITO glass slides). ITO glass slides were cut into $10 \times 10 \times 3 \text{ mm}^3$ pieces to fit our UHV sample holder. For UHV gas adsorption experiments, research grade gasses (pure CO_2) were purchased from Praxair and analytical grade liquids (formic acid) were purchased from Sigma Aldrich. Gases were dosed into the vacuum chamber by backfilling technique. Liquids were degassed by numerous freeze-pump-thaw cycles to degas the liquids prior to use in the experiments, which were attached to the UHV chamber by a metal-glass flange through a leak valve.

4.2.2. UHV experimental setup

The same experimental setup explained in section 2.1.3 was used. AES was used to characterize the elemental composition of perovskite thin films, PbI_2 thin films, and ITO substrate. Temperature programmed desorption was used to determine the thermal stability and small molecular adsorption kinetics. The lowest accessible temperature for the gas adsorption experiments was $\sim 90 \text{ K}$ with liquid nitrogen cooling (accompanied with He gas bubbling), and the highest temperatures used for the thermal stability tests were $\sim 875 \text{ K}$. Binding energies of adsorbed gases were determined using Redhead analysis, in which the TDS peak positions were numerically converted to binding energies assuming 1st order desorption pre-exponential, $1 \times 10^{13} \text{ s}^{-1}$.

4.2.3. Ambient pressure experiments

A commercial spin coater (P6700 from Specialty coating system Inc.), as well as a home built one were employed to spin coat the perovskite films at dry nitrogen atmosphere. Samples synthesized in ambient were characterized using UV-Visible (both transmittance and reflectance mode spectrums were collected using Varian carry 50-Bio and Varian carry 5000 UV-Vis-Nir (see section 2.7) respectively), XRD (Bruker AXS D8 Discover multi-purpose X-ray diffractometer (see section 2.9)), SEM and EDX (JEOL JSM-6490 LV scanning electron microscope coupled with EDX(see section 2.8)). Additionally, the perovskite film thicknesses were estimated using a surface profiler (P11 from Tencor).

4.2.4. Perovskite synthesis

Ambient pressure solution processed synthesis technique was used to fabricate MAPbI_3 perovskite thin films, which was derived from a reported procedure.¹⁹⁶ ITO coated glass substrates were washed with water, acetone, and methanol prior to the thin film deposition. 60 μl of the methylammonium triiodoplumbate precursor solution maintained at 70 $^{\circ}\text{C}$ was added to the ITO substrate (10 \times 10 mm^2) using a micropipette, and subsequently spin coated for 30 seconds at 3300-4000 rpm in a dry nitrogen atmosphere. The spin-coated sample was then heated on a hot plate at 100 $^{\circ}\text{C}$ in a flow of dry nitrogen, for 10 minutes. As prepared samples were stored in a nitrogen filled container to avoid atmospheric contamination until mounted on a UHV sample holder. UHV mounted samples were degassed up to 380 K. Heating beyond this temperature accelerates dissociation mechanisms. Also, sample cleaning using inert gas sputtering destroys the thin films eventually. Therefore, cleaning the samples after preparation at ambient conditions is limited, but inert UHV environment avoids further sample contamination by residual gas adsorption. Several perovskite thin films were synthesized since the samples were either decomposed or changed

irreversibly during the course of the experiments. Perovskite thin films were characterized at ambient prior to transfer into the UHV chambers.

4.3. Results and discussion

4.3.1. Characterization of MAPbI₃ perovskite thin films

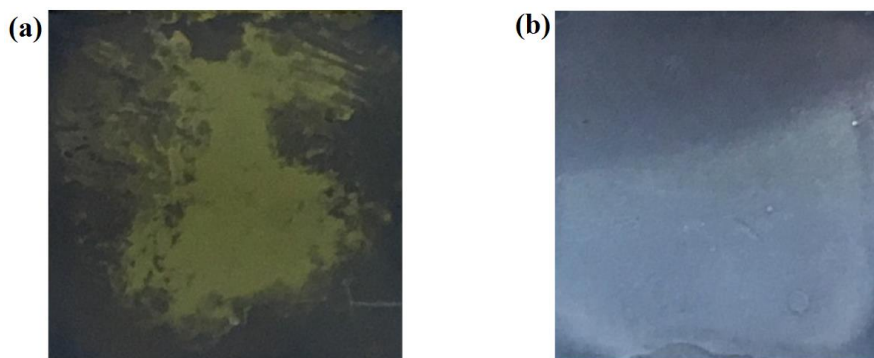


Figure 4.4. (a) A photo of decomposed MAPbI₃ forming PbI₂ as a result of overheating (~200⁰C) during the synthesis, (b) A photo of a good MAPbI₃ perovskite thin film (photos were taken using a digital camera)

UV-Visible absorption spectroscopy (UV-Vis) has been widely used to characterize organohalide perovskites experimentally. Also, there are several theoretical studies about the absorption spectra of organohalide perovskites enabling the comparison of experimental optical absorption spectra.^{193, 201, 203-204} We used the UV-Vis as the primary characterization tool for the perovskite synthesis due to the simplicity and non-destructiveness of the technique, as well as to connect our UHV-based experimental work with prior literature reports. Figure 4.5 depicts the UV-Visible absorption spectra of several MAPbI₃ perovskite samples that have been synthesized in different stages of the current study. The variation of the intensities of the absorption spectra observed among the different samples is mainly caused by the differences in the film thicknesses. The film thickness of a MAPbI₃ perovskite thin film was measured using a surface profiler, which amounts to be (648±75) nm. Since the surface profiling is a destructive technique, samples couldn't be further used after measuring the film thickness.

Perovskite samples synthesized in our study had the typical dark gray color, as depicted in Figure 4.4. Also, the perovskite thin films look somewhat transparent to the naked eye, which may be due to the sub-micron thickness of the thin films. Broad optical absorption band centered around 750 nm indicates the successful chemical transformation of the methylammonium triiodoplumbate solution to the corresponding organohalide perovskite structure according to several previous reports.^{193, 201, 203-204, 264} Deposition of carbon impurities from traces of dust, residual air, oil etc., is difficult to avoid during the synthesis (at ambient pressure) unless atomically clean environments (e.g. UHV) are employed. Therefore, it was expected to observe an absorption band around 200-350 nm, which can be from carbon black, carbon quantum dots, and graphene etc.²⁶⁵⁻²⁶⁷

However, the ITO glass substrate has a strong absorption band around the same spectral region, which is interfering (overlapping) with the carbon absorption band (because of the strong absorption of the ITO coated glass substrate at UV spectral region, the relative absorption intensity of the thick substrate (~ 3mm) is significantly high compared to the MAPbI₃ thin film).²⁶⁸ Therefore, using the UV-Vis in transmission mode, it was difficult to distinguish the carbon absorption band. But, the reflectance mode UV-Vis enabled the detection of the carbon absorption band since the reflected signal from the sample surface is analyzed when diffuse reflection (DRS) mode is used with minimum interferences with the deep sample surface.

MAPbI₃ perovskites can be decomposed into PbI₂ due to several factors (intrinsic degradation, thermal and moisture effects etc.), which appear in yellow color. For the degraded perovskite thin films, typically a sharp decrease of the optical absorption in the 530-800 nm region with the characteristic absorption feature around 510-530 nm for PbI₂ has been observed,^{199, 206} which is also evident in our study for deteriorated samples (Figure 4.5 (c)). Generally, the onset of

the absorption band centered at 750 nm tend to shift to lower wavelengths with the decomposition of the perovskite structure, which did not observe in our case. Therefore, the UV-Vis obtained here are typical for good perovskite samples.

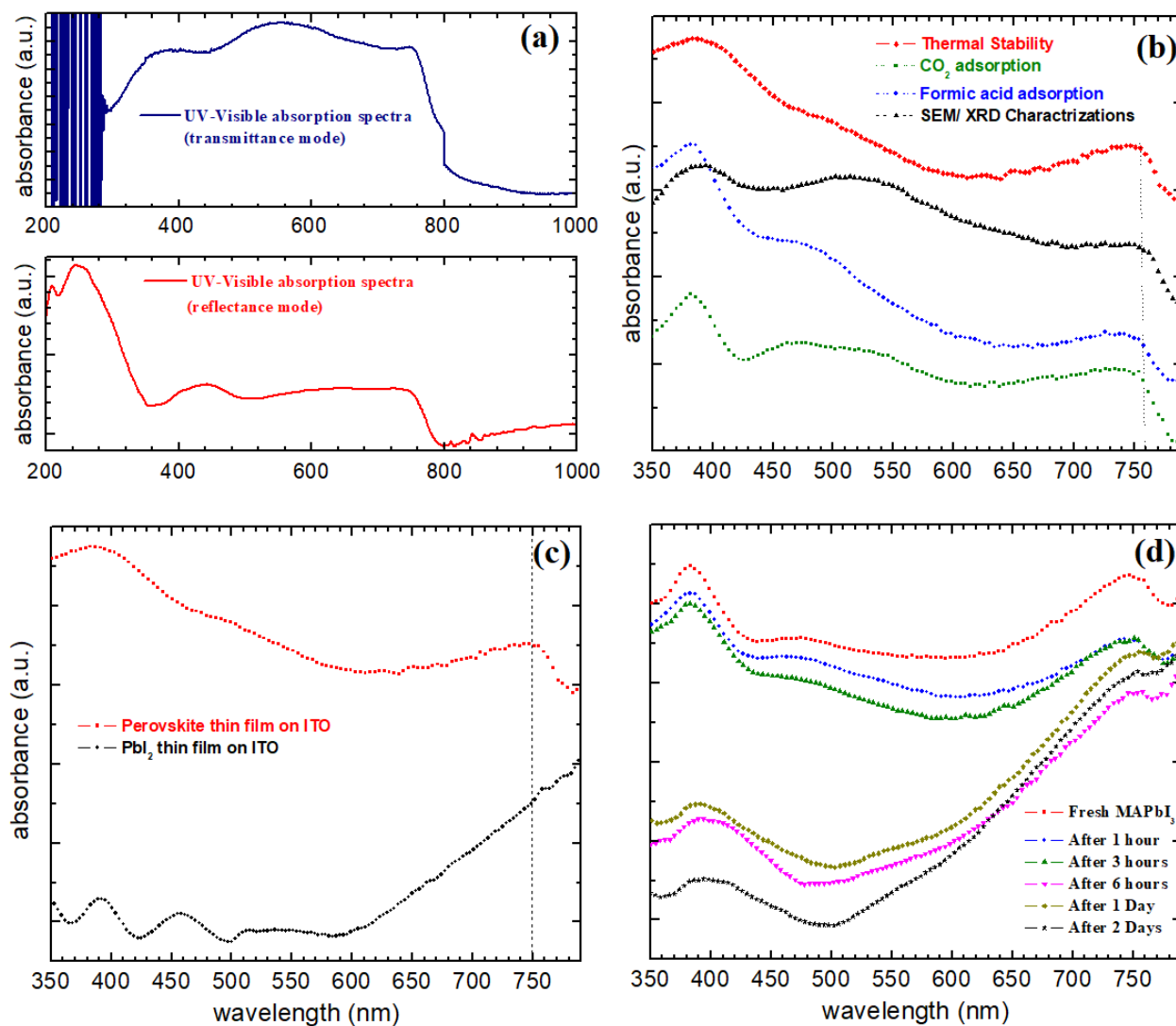


Figure 4.5. (a) UV-visible absorption spectra of a typical MAPbI₃ perovskite thin film synthesized in the study (using the UV-Vis transmittance mode (top panel) and the diffuse reflectance mode (bottom panel)), (b) Absorption spectra of perovskite thin films employed in each step of the study, (c) comparison of absorption spectra of MAPbI₃ perovskites and PbI₂ thin films (which was obtained by high temperature annealing the perovskite thin films), (d) Absorption spectra of a MAPbI₃ perovskite thin film kept at ambient conditions for 48 hours.

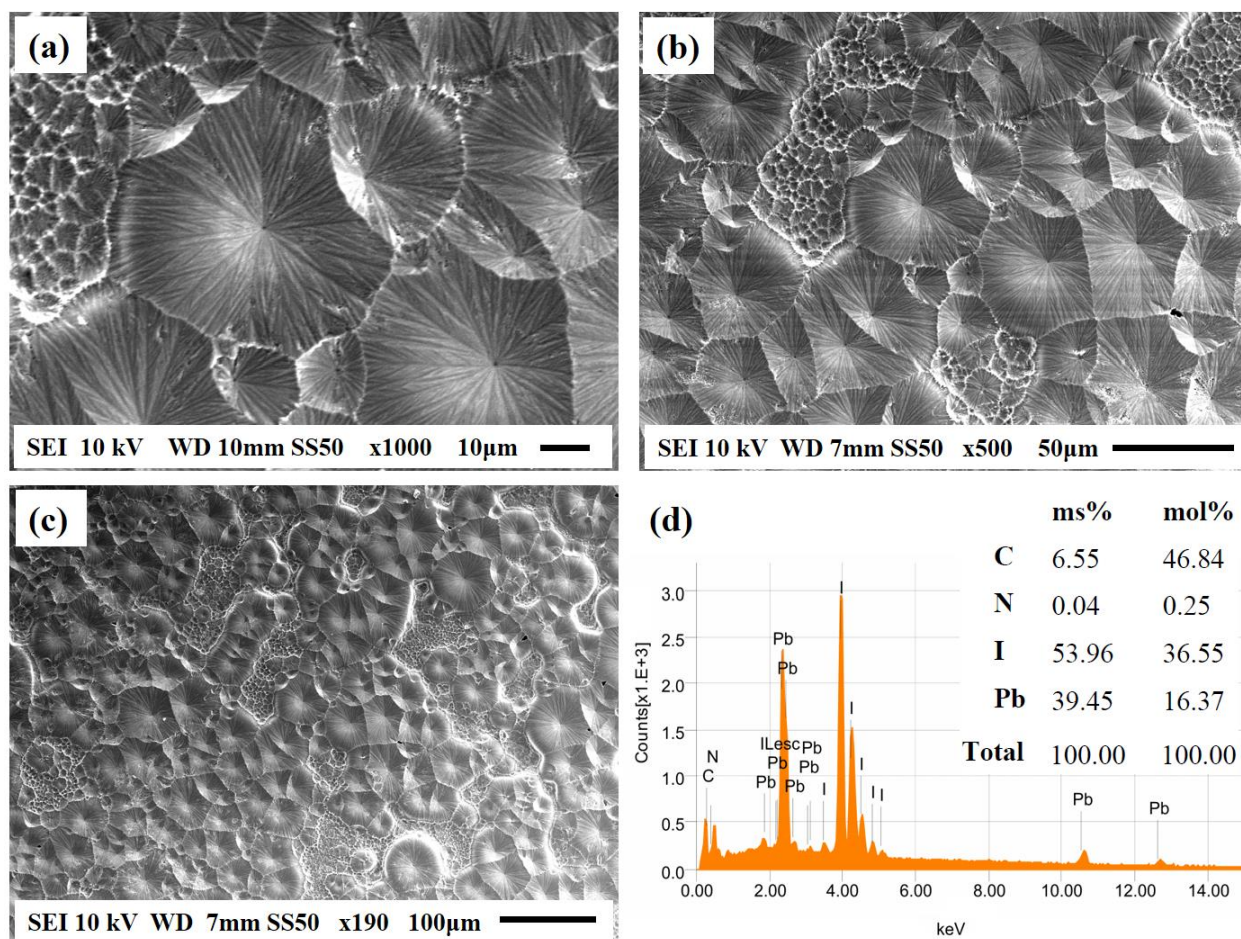


Figure 4.6. (a)-(c) SEM microstructures of MAPbI₃ perovskite thin films with different magnifications, (d) EDX spectra of the same sample illustrating the elemental composition.

As depicted in Figure 4.6 (a) to (c), SEM images with leaf-like structures in each grain were observed, consistent with prior works.¹⁹⁶ The microstructure within each grain are qualitatively identical for both small and large grains. Defects, such as pin-holes free grains with uniform overlayers were obtained with somewhat large grain sizes. EDX spectra (Figure 4.6 (d)) depicts the elemental composition of the same perovskite thin film, which confirms the presence of all the elements Pb, I, C and N (Since hydrogen have no core electrons, core-electron XPS/EDX are not possible. Valence electron of H (1s¹) participated in the chemical bonding can generate XPS/ EDX signal but it will be overlapped with the valence electron bands of the other surface atoms²⁶⁹), with their relative mass and molar percentages. EDX confirms the presence of excess

carbon, which is also qualitatively consistent with AES (see Figure 4.8). According to the stoichiometry of the MAPbI_3 perovskite structure, carbon to iodine molar ratio should be 0.33 but, here it is about 0.80. Therefore, the sample is carbon contaminated due to the ambient pressure synthesis, which is difficult to avoid completely without atomically clean environments. The EDX molar ratio of lead to iodine is 1: 2.3, which is somewhat closer to the expected stoichiometry (1:3).²⁷⁰

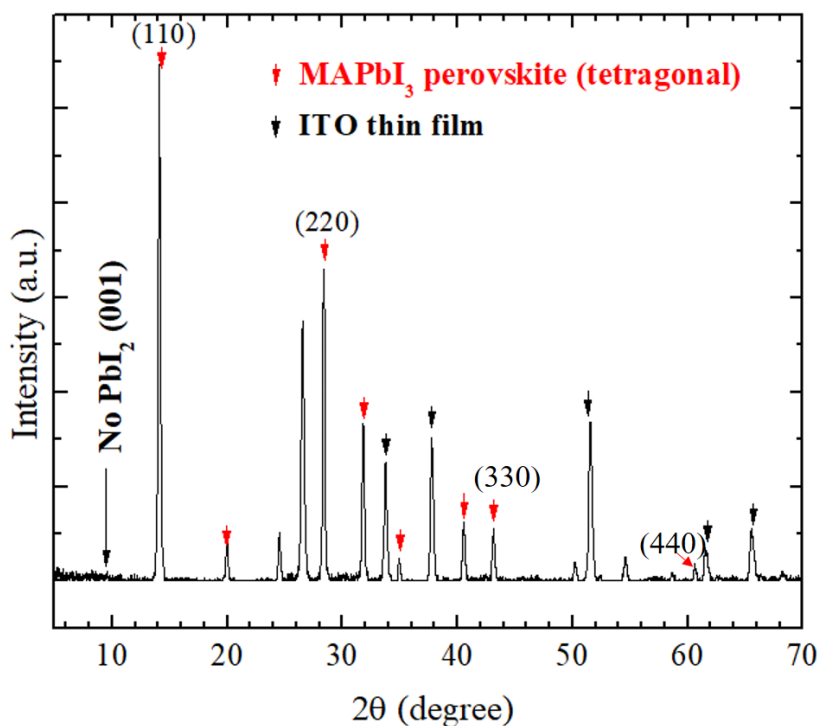


Figure 4.7. X-ray diffraction pattern obtained for a MAPbI_3 perovskite thin film synthesized in this study. Phase (tetragonal)^{196, 199, 204} and the substrate peaks²⁷¹⁻²⁷² were identified by comparison with the literature reports.

Powder XRD pattern of a MAPbI_3 perovskite thin film was obtained to identify the stable phases and possible impurities of fabricated perovskite thin films. The diffraction pattern obtained here closer to the tetragonal phase of MAPbI_3 perovskites compared to the literature reports. Main diffraction peaks at 14.2° and 28.4° are from (110) and (220) planes of MAPbI_3 perovskite thin films.^{199, 204} Any diffraction peaks characteristic to PbI_2 was not observed, which further confirms

the complete conversion of the precursor for the corresponding perovskite structure without leaving traces of PbI_2 impurities.¹⁹⁶

After performing the ambient pressure characterization of the MAPbI_3 perovskite thin films, the elemental composition was characterized employing AES at UHV, which has not been applied for the characterization of MAPbI_3 perovskites so far. Auger electron spectra of an ambient pressure synthesized MAPbI_3 perovskite thin film after immediately transferred into the UHV chamber is depicted in Figure 4.8 (a- dotted line). AES indicate the presence of elements Pb, I, C, N, O, and Sn, which are originated from the perovskite thin film, adsorbed impurities, as well as from the underlying substrate. Determination of the relative concentrations (and percentages) of each element is complicated due to different AES sensitivity factors and screening effects. For example, AES sensitivity for Pb is much smaller than Carbon, but the methylammonium carbon is occupied in the 12-fold coordination site, covered by the octahedra cages formed by electron-dense Pb and I, which can cause significant suppression of the C and N Auger signals compared to the Pb and I signals. Also, different types of carbons such as adsorbed CO_2 , CO, C, etc., are possible, which further increase the complexity for the quantification.

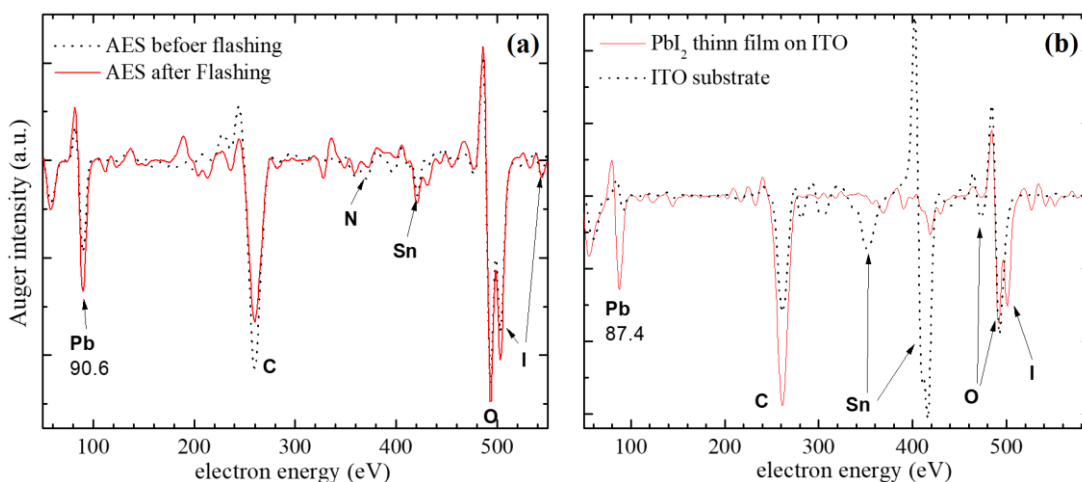


Figure 4.8. AES spectra obtained for (a) MAPbI_3 perovskite thin films, (b) PbI_2 thin films (obtained by UHV annealing the MAPbI_3 perovskite thin film), (c) ITO substrate (obtained by removing the PbI_2 film by Ar^+ sputtering).

Even though the probe electron beam with 2 keV can penetrate through the sub-micron thick perovskite film, the escape lengths of typical Auger electrons are around 5-20 Å.²⁷ Therefore, the small substrate peak at 420 eV should be from a trace amount of defects exposing the substrate or from areas with ultra-thin MAPbI₃ perovskite films, which enable the escape of substrate Auger electrons. With the AES probe electron beam, approximately 1.8 mm² of the sample area is analyzed, and hence the largest grain-size is about 50-60 μm in diameter (according to SEM), defects along the grain boundaries may expose the underlying surface.

Significant carbon and oxygen peaks can be observed in AES. Carbon can be mainly from adsorbed impurities such as residual gases, oil, dust etc., during ambient pressure synthesis other than the methylammonium cation. Also, during thermal desorption studies of perovskite thin films, a huge amount of carbon dioxide desorption from the surface was detected, which may be responsible for a significant portion of the AES carbon peak (see Figure 4.10). Similarly, a significant percentage of oxygen seems to be from adsorbed water vapor during the ambient pressure synthesis/ storage, which was also determined by thermal desorption studies of MAPbI₃ perovskite thin films at UHV.

The solid line in Figure 4.8 (a) shows the elemental composition of the perovskite thin film after UHV flashing to ~380 K. Carbon AES intensity decreased due to the partial desorption of carbon impurities and/ or diffusion of the impurities into the bulk of the sample. Also, the intensity of the Pb AES peak increased may be due to the partial desorption of adsorbed impurities and hence reduced screening effects.

Figure 4.8 (b) depicts the AES of PbI₂ thin film and ITO substrate. The former was obtained by thermal decomposition of MAPbI₃ perovskite thin film, simply by annealing at ~ 600 K. The ITO substrate was obtained by wiping out the perovskite/ PbI₂ films, by Ar⁺ sputtering and high-

temperature annealing (~ 900 K). Characteristic features for Sn and O together with impurity carbon for the ITO substrate can be observed. The indium as a dopant of the ITO is below the detection limit of the AES system. When the perovskite/ PbI_2 thin films are completely desorbed from the substrate, the double peak feature around 500 eV from I and O converts to a single peak (oxygen). Even the thin films (perovskite/ PbI_2) are completely removed from the surface, still, a significant impurity carbon peak is evident. As well known in the surface science, any surface exposed to air can cover with residual gas, oil, dust etc., which can generate an amorphous layer of carbon deposited on that particular surface.¹²³⁻¹²⁴ Therefore, as received substrates are usually covered with an amorphous carbon layer, which is difficult to remove completely with ambient pressure cleaning techniques (e.g. washing with different solvents). Because of that, the perovskite thin film is actually grown on an amorphous carbon layer. A glove box filled with N_2 can significantly reduce the amount of gaseous impurities but cannot produce atomically clean environments to prevent the carbon deposition completely.

Even though we expected to see an ideal sandwich structure of glass/ ITO/ perovskite, it turned out that the thin film system resulted in a more intricate structure, containing multiple impurity carbon layers on top of each glass/ ITO/ perovskite layers, predicted based on AES and EDX results. However, the sample fabrication technique employed in this study is fairly common, simple, and suitable for industrial solar-cell related applications.

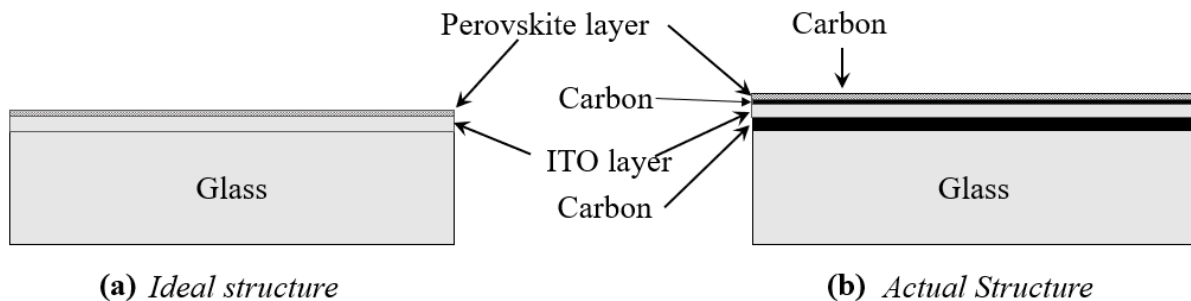


Figure 4.9. Schematic representation of the cross-sections of ideal structure (a) and the real structure (b) of the perovskite thin films grown on ITO coated glass slides.

4.3.2. Thermal stability of MAPbI₃ perovskite thin films

Pristine MAPbI₃ perovskite thin films are not stable at ambient conditions. Water adsorption, thermal effects, UV radiation, intrinsic effects etc., can reduce the lifetime of these thin films at ambient conditions. According to the early studies, these perovskite thin films start to degrade around 348 K (~ 75⁰C) at ambient conditions under illumination while the films are not stable above 386 K (~ 95⁰C) even in dark,²⁷³ which make it difficult for the application of any detailed quantitative kinetics experiments. The gradual degradation of perovskite thin films to PbI₂ at low vacuum (~ 10⁻² Torr) has been observed as a result of isothermal annealing at 150⁰C. Complete degradation of the perovskite structure by losing the volatile components was observed within 14 hours in the same study at low vacuum.²⁰⁵ Such a low stability prevents the application of any UHV cleaning techniques such as high-temperature annealing and inert ion sputtering. Rapid flashing to ~ 380 K at UHV was used to clean (degas) the samples at UHV, which doesn't change the elemental composition of the samples. Obviously, higher stability of the MAPbI₃ perovskite thin films at UHV can be expected compared to the ambient conditions due to the inert atmosphere. Before the application of any kinetics experiments, it is worthwhile to understand the thermal degradation temperatures of these perovskite thin films at UHV, which has not been studied previously. Also, understanding the thermal degradation mechanisms and highest stable temperature limits are essential in order to apply any meaningful kinetic experiments, which can be helpful to develop and characterize sample stabilization mechanisms.

Multi-mass thermal desorption experiments were utilized to understand the degradation temperatures of MAPbI₃ perovskite thin films in this study. After degassing and characterization of the elemental composition of perovskite thin films, sample temperature was ramped linearly from ~100 K to 750 K and desorbing volatile molecular fragments from the perovskite thin film

were detected using a residual gas analyzer. After the thermal ramp, the elemental composition of the sample was analyzed by AES.

Figure 4.10 (a) depicts the thermal desorption profiles of detected masses desorbing from the perovskite thin film during the thermal ramp as a function of surface temperature. With our residual gas analyzer, only masses below $m/z=100$ (SRS RGA 100) could be detected and also, only four different masses could be detected simultaneously with optimum sensitivity. The molecular fragments to be detected were decided based on known degradation mechanisms of MAPbI_3 perovskites and by trial TDS experiments.

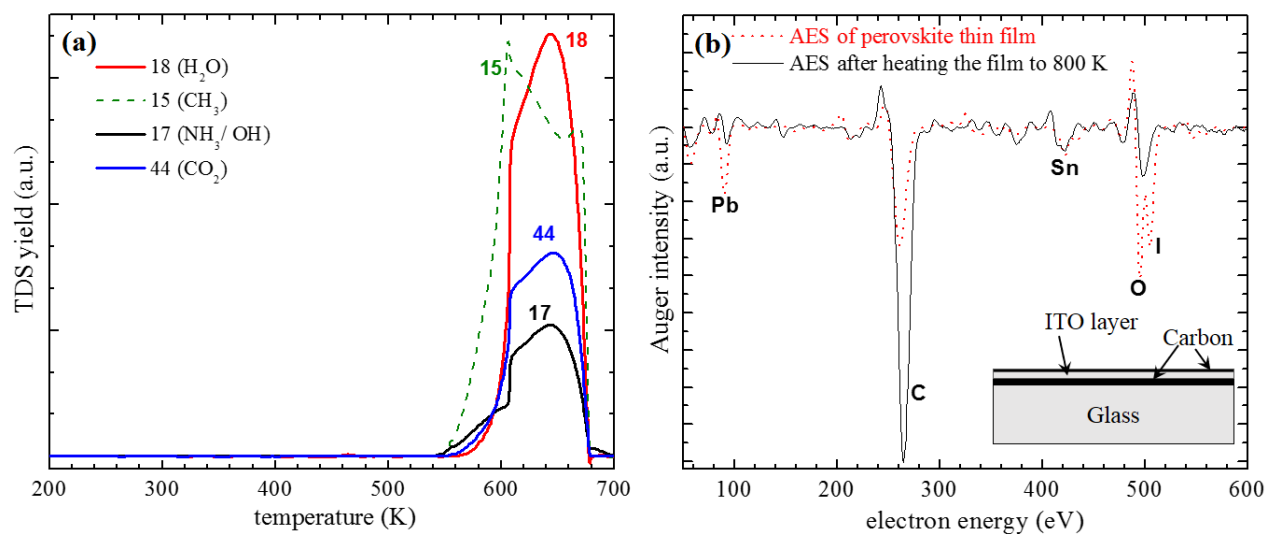


Figure 4.10. (a) Thermal desorption profiles of detected mass fragments as a function of surface temperature during a linear thermal ramp (1.6 K/s) of pristine MAPbI_3 perovskite thin films at UHV, (b) AES before and after the thermal degradation of the perovskite thin films.

Two major reaction pathways have been identified for the degradation of MAPbI_3 perovskite in the presence and absence of moisture. In the presence of humidity, catalytic reduction of MAPbI_3 perovskites forming CH_3NH_2 , HI, and PbI_2 is the major degradation mechanism, while the intrinsic degradation in the absence of humidity resulted in CH_3I , NH_3 , and PbI_2 mainly.^{205, 207} Parent masses of species such as PbI_2 , CH_3I , HI ($m/z= 358, 127,$ and 149 respectively) could not be detected directly by our mass spectrometer because of their higher masses. Both CH_3NH_2 and

CH₃I have CH₃ fragment (at m/z= 15) in their gas phase mass scans. Therefore, CH₃ was the major mass fragment detected for the identification of the thermal degradation of MAPbI₃ perovskite thin films.

Other than the CH₃ fragment, NH₃ was also detected, which is a potential product of intrinsic degradation of MAPbI₃ perovskites. But, the detection of NH₃ parent mass was somewhat interfered by the OH fragment of desorbing water from the perovskite thin films. Furthermore, chemisorbed water and carbon dioxide during the ambient pressure synthesis/ storage were also desorbed during the thermal desorption of perovskite thin films, which were identified by detecting m/z= 18 and 44 respectively.

As depicted in Figure 4.10 (a), gas desorption (H₂O/ CO₂) and decomposition of pristine perovskite thin films start above 540 K simultaneously at UHV, with TDS peak maximum around 640 K. No gas desorption was detected below 500 K, indicating the strong chemisorption of residual gases such as CO₂ and H₂O on perovskite thin films. Compared to ambient pressure decomposition temperatures, perovskite thin films are much stable at UHV, which may be simply due to the inert environment provided by UHV. Most of the volatile molecular fragments were desorbed by ~ 700 K and further ramping the sample temperature to ~ 850 K resulted in desorption of other decomposition fragments (e.g. PbI₂) leaving traces of Pb atoms on the ITO coated glass substrate as indicated by AES (Figure 4.10 (b)).

According to our TDS data, the mechanism forming CH₃I, NH₃, and PbI₂ is plausible, which is the favorable degradation pathway in the absence of water. Both degradation mechanisms are possible in which the intrinsic degradation may be predominant due to the inert UHV atmosphere. Even at UHV conditions, previously contaminated MAPbI₃ perovskites (with moisture) can induce degradation and therefore, initial synthesis and storage conditions are critical

for the long-term stability of organohalide perovskite thin films (at least the moisture degradation pathway could be avoided). More TDS data would be necessary in order to determine the exact degradation mechanisms.

Compared to the AES of pristine perovskite, Pb and I peak intensities are decreased significantly after the thermal ramp. The double peak feature around 500 eV converted to a single peak due to the desorption of iodine as CH_3I , HI etc. A small Pb peak is detectable may be from trace amounts of atomic lead or PbI_2 . The carbon peak intensity significantly increased after the thermal degradation. Since the initial state of ITO thin film is not atomically clean, it was expected to see a layer of carbon underneath the perovskite thin film. Auger excitations from that carbon layer dominate the AES carbon peak of deteriorated perovskite structure since the screening factors from perovskite layer is nonexistence. Thermal ramps below 600 K kept the epitaxial PbI_2 films adsorbed on ITO layer which was investigated for small molecule adsorption in later studies (Figure 4.13 (a)).

The desorption temperatures of both H_2O and CO_2 are too large for physisorption interactions. For instance, physisorption of water on non-reactive surfaces such as graphene,³⁷ silica,⁸⁸ gold¹²⁹ etc., desorb below 200 K. Similarly, molecularly physisorbed CO_2 desorb below 300 K with binding energies in the range of 20-40 kJ/mol.²³⁸ By assuming 1st order desorption kinetics with the pre-exponential factor of $1 \times 10^{13} \text{ s}^{-1}$, the desorption energy corresponding to $\text{CO}_2/\text{H}_2\text{O}$ TDS peak temperatures $\sim 640 \text{ K}$ amounts to 170 kJ/mol, which is significantly higher for even molecular chemisorption.

These unusually high binding energies can be due to associative desorption of dissociatively adsorbed CO_2 and H_2O on perovskite thin films, or due to co-adsorption effects. For CO_2 chemisorbed on metal oxides (e.g. CaO , MgO) forming carbonates have depicted similar

desorption temperatures in previous studies. Carbonates are usually formed on oxygen terminated adsorption sites on metal oxide surfaces. However, MAPbI₃ perovskites do not directly possess oxygen adsorption sites. Carbonates bind on surfaces with polydentate adsorption geometries, where the adsorbate interacts with multiple surface adsorption sites simultaneously, forming strong chemisorption-like interactions. This type of geometries is possible in inhomogeneous surfaces, such as perovskites.

Co-adsorption of CO₂ and H₂O is another possible way of having large desorption energies, which can form bicarbonates, carbonic acids etc. Bicarbonate formation has been observed on defected TiO₂ surfaces, which eventually desorbed as CO₂ at 214 K.²⁷⁴ CO₂ co-adsorption with water have also been observed on Pd surfaces, via carboxylate (bent CO₂⁻) formation. However, the desorption temperatures are around 200 K.²⁷⁵ Since the perovskite possess large pore structures, so-called Knudsen diffusion of molecularly adsorbed CO₂ inside the internal volume (adsorption/ desorption inside the pores) can cause higher desorption temperatures. We also conducted several blind experiments including the dissociated perovskite (PbI₂ thin films), the ITO substrate (Figure 4.13 (a and b)), and the sample holder which ruled out CO₂ desorption from the background at higher temperatures. A minor H₂O desorption peak from the sample holder was detected at higher temperatures, which is few orders of magnitude smaller in intensity compared to the water desorption peak of perovskite structures (see Figure 4.11 (a)- dotted lines). Furthermore, impurities such as alkali metals can cause higher desorption energies for CO₂,²³⁸ which can be excluded in this study according to AES characterization of perovskites (CMA based AES used in this study can detect impurities up to ~ 1% of a monolayer).

Adsorption of water on perovskites, water-induced dissociation mechanisms etc., have been studied extensively related to MAPbI₃ perovskites stabilization studies since water is one of

the most corrosive contaminants causes catalytic degradation of such organohalide perovskite structures. But, the unusually high binding energy of carbon dioxide on MAPbI₃ perovskites have not been observed and investigated according to the best of our knowledge. In order to investigate this unusual adsorption/ desorption kinetics, we further studied CO₂ adsorption on MAPbI₃ perovskite thin films experimentally and theoretically.

4.3.3. Carbon dioxide adsorption on MAPbI₃ perovskite thin films

Carbon dioxide was adsorbed on MAPbI₃ perovskite thin films and desorption kinetics were studied employing TDS. 2.0 L of CO₂ was dosed by backfilling the UHV chamber, keeping the substrate ~100 K during the gas dosing. Then, the sample temperature was ramped linearly, and desorption traces were detected using a residual gas analyzer. Same molecular fragments captured in the prior study were analyzed in this case as well. At a quick glance, TDS traces are much broader and onsets of the desorption peaks, as well as the TDS peak temperatures, are significantly smaller (by ~100 K) compared to the prior study (see Figure 4.11). Lower desorption temperatures reflect greater surface concentrations of CO₂ after the additional dose of CO₂, which can be arises due to the repulsive-lateral interactions caused by adsorbed CO₂ molecules. Differences in the shapes of the TDS scans may be mainly due to the variation of the sample morphology. According to the TDS temperatures, it seems like additional CO₂ concentration destabilize the perovskite thin films. Compared to pristine perovskites, which started to thermally dissociate around 560 K (estimated considering the onset of the CH₃ TDS peak), thermal dissociation of CO₂ dosed perovskites already started ~400 K. In both cases, perovskite dissociation and CO₂/ H₂O desorption happens at the same time.

Multiple stabilization mechanisms acting simultaneously on adsorbed CO₂ may be responsible for the large desorption energies, which is quite unusual for CO₂ surface chemistry.

The porous structure of MAPbI₃ perovskites enables surface/ sub-surface reactions as well. To identify possible CO₂ stabilization mechanisms on MAPbI₃ perovskite structures, DFT calculations were conducted collaboratively as a part of this project.

Numerous surface binding sites were considered for molecular adsorption of CO₂ and H₂O on the MAPb₃ perovskite thin films computationally. According to DFT calculations, molecular adsorption of CO₂ and H₂O resulted in 12 kJ/mol and 42 kJ/mol binding energies respectively, which are way below the experimentally observed binding energies (150-170 kJ/mol). Adsorption of carbonic acid (H₂CO₃) as a result of a possible co-adsorption reaction, CO₂ + H₂O → H₂CO₃ is also assumed, which yielded a desorption energy amounts to 53 kJ/mol on perovskite surfaces. The presence of water (adsorbed) on perovskite surfaces is clearly evident according to the experimental thermal desorption studies and it is typical for any real-world application, which could facilitate above co-adsorption reaction. Significantly increased binding energy was observed (121 kJ/mol) with multi-site interactions (polydentate adsorption) between the perovskite surface and the H₂CO₃-H₂O van der Waals complex formed by further co-adsorption of H₂CO₃ with excess water.

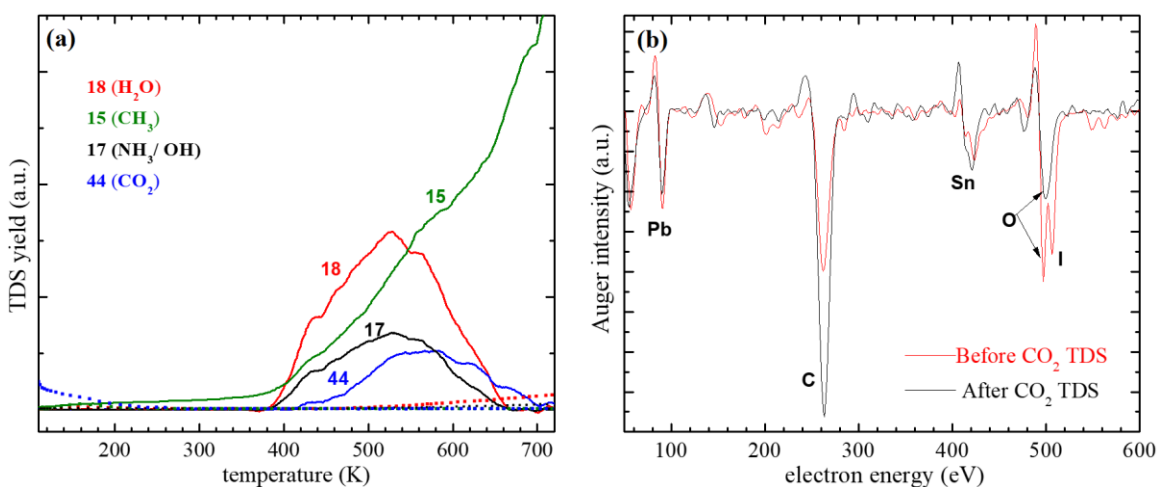


Figure 4.11. (a) TDS traces of 2.0 L of CO₂ adsorbed MAPbI₃ perovskite thin films (dotted lines are the desorption profiles from sample holder/ background), (b) AES of perovskite thin film before and after CO₂ adsorption experiments.

Defect-mediated stabilization of co-adsorbed CO₂ and H₂O embedded on the perovskite structure gives rise to quite similar desorption energies for experimental results. It is possible for the co-adsorbed CO₂ and H₂O to stay in the equilibrium, H₂CO₃ ↔ HCO₃⁻ + H₃O⁺. Occupation of the H₃O⁺ in the cationic vacancies (CH₃NH₃⁺ vacancies) and HCO₃⁻ in the anionic vacancies (I⁻) in the perovskite structure was assumed in this case. Since the perovskites are synthesized in ambient conditions, adsorbed water can induce the formation of such defects by catalytic reduction of the structure to form CH₃NH₂ and HI, and these vacancies (CH₃NH₃⁺ and I⁻) can be occupied by HCO₃⁻ and H₃O⁺ ions. This model gives the closest binding energy for the experimental results, which amounts to 166 kJ/mol (compared with the 170 kJ/mol of the experimental binding energy). Similar types of stabilization mechanisms have been observed in colloidal lead halide perovskites.²⁷⁶ Here we are comparing the binding energies of CO₂/ H₂O co-adsorption with desorption energies of respective molecules from as prepared perovskites (low coverage limit) rather than with excess CO₂ dosed perovskites in the follow-up experiment (high coverage limit) since the calculated desorption energies are for low coverages of CO₂.

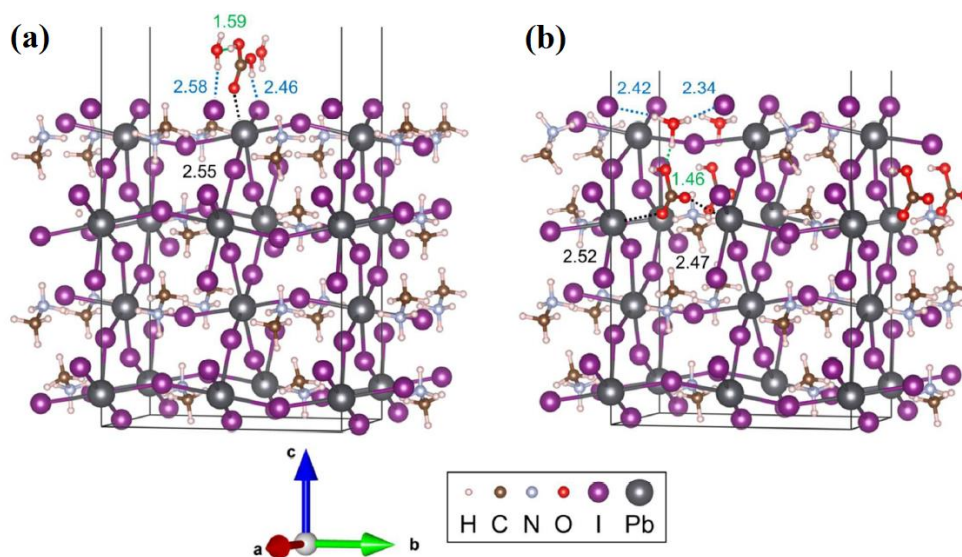


Figure 4.12. Computational models of MAPbI₃ perovskites forming (a) H₂CO₃-H₂O van der Waals complex, (b) the defect structure with embedded HCO₃⁻ and H₃O⁺ (models were prepared by Yulun Han).²⁷⁷

Several structural and chemical factors are affecting the CO₂ stabilization according to the above-explained mechanism. Conservation of the crystal structure by replacing I⁻ and CH₃NH₃⁺ defects in the original perovskite structure by HCO₃⁻ and H₃O⁺ respectively induces electrostatic interactions, which may lead to the morphological stabilization of the adsorbed CO₂/ H₂O as well as the perovskite structure by further degradation. Formation of HCO₃⁻ can lead to the chemical stabilization of CO₂. Also, the complexation of HCO₃⁻ with Pb²⁺ in the perovskite lattice can lead to the formation of lead (ii) bicarbonates (Pb(HCO₃)₂), which is a stable naturally occurring compound. Similarly, the H₃O⁺ cation can be stabilized electrostatically by neighboring anions. This co-adsorption process can be considered as a sub-surface reaction, rather than bulk or solid-state reaction since the active sites considered for the bicarbonate formation is an anion vacancy (I⁻) in the perovskite lattice formed below ~4.5 Å of the outer surface layer.

Table 4.1. Experimental and theoretical CO₂ binding energies on MAPbI₃ perovskite thin films

Method	System	E _d (kJ/mol)
Experimental	As prepared surface	170
	CO ₂ adsorbed (2.0L) surface	153
DFT	Surface-CO ₂	12
	Surface-H ₂ O	40
	Surface-H ₂ CO ₃	53
	Surface- (H ₂ O + H ₂ CO ₃)	121
	Surface- (H ₃ O ⁺ + HCO ₃ ⁻)	166

Thermal desorption of HCO₃⁻ may lead to the desorption of molecular CO₂ into the gas phase leaving adsorbed OH, which is indeed 1st order with respect to the HCO₃⁻ concentration. Desorption of adsorbed OH (OH_(ad)) may be stimulated by adsorbed H (H_(ad)) on the surface from the UHV background (even a UHV chamber has a significant residual H₂ background unless specialty pumps were not utilized to reduce the hydrogen background pressure). Assuming the decomposition of HCO₃⁻ to CO_{2(g)} as the rate determining step and H_(ad) + OH_(ad) → H₂O_(g) as a fast

process followed up by the decomposition of HCO_3^- , simultaneous desorption of the CO_2 and H_2O can be explained, which is reflected by the desorption temperatures in both pristine and CO_2 dosed MAPbI_3 perovskite thermal desorption studies.

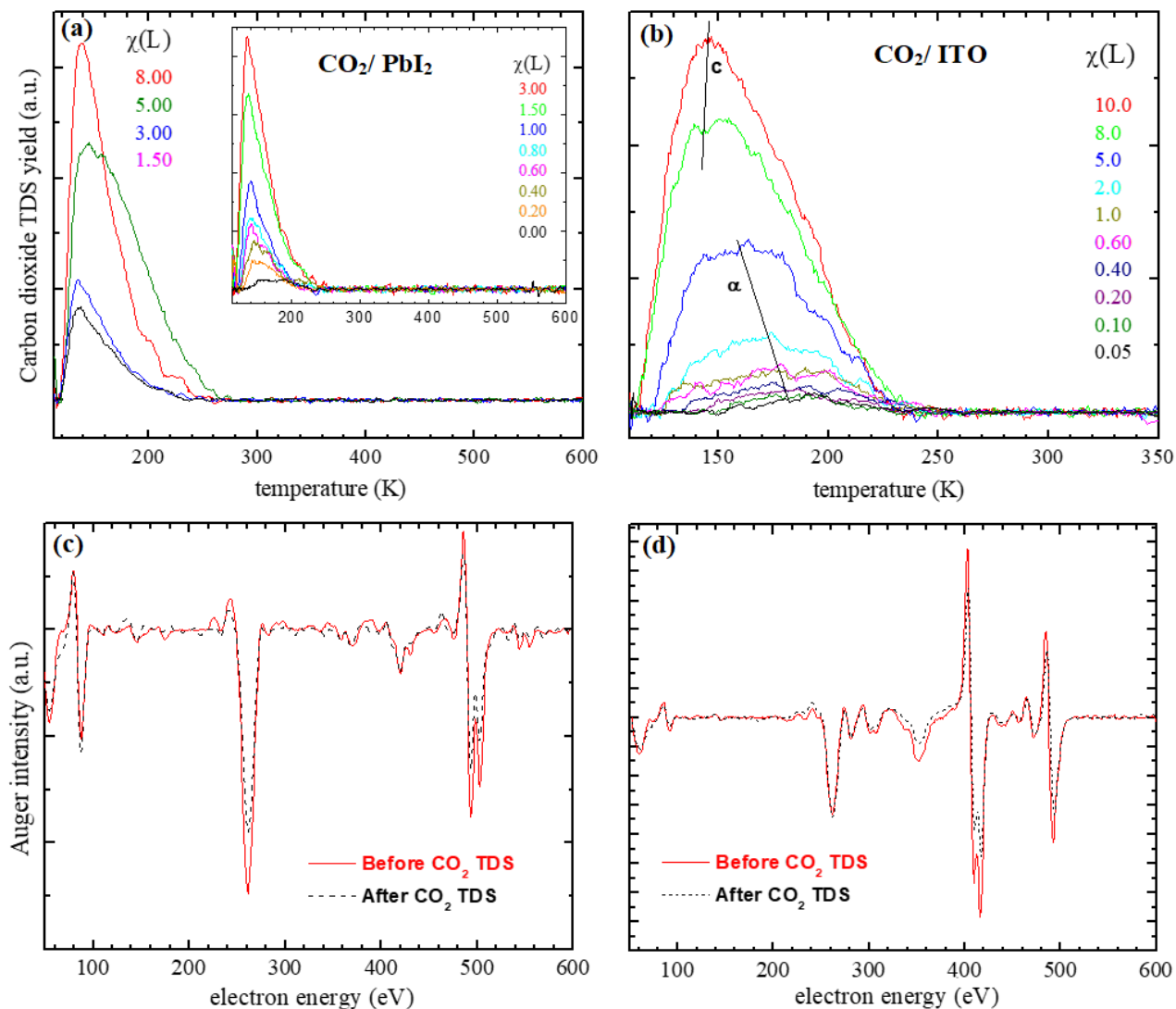


Figure 4.13. Carbon dioxide adsorption on the substrate ((a) CO_2 TDS on PbI_2 , (b) CO_2 TDS on ITO, (c) AES of PbI_2 thin film before and after CO_2 adsorption, (d) AES of the ITO substrate before and after CO_2 adsorption)

Initial stabilization of the perovskite structures even with high adsorbed water content may be due to the occupation of HCO_3^- and H_3O^+ in the defected sites initially created by the catalytic reduction of the MAPbI_3 perovskite structure by adsorbed H_2O at ambient, removing CH_3NH_2 and

HI. Contrast to MAPbI₃ perovskites, carbon dioxide exhibits weak physisorption-like interactions with dissociated perovskites (PbI₂ thin films) and ITO substrate, as reflected by TDS peak temperatures for carbon dioxide adsorption on those substrates (Figure 4.12 (a and b)).

4.3.4. Formic acid adsorption on MAPbI₃ perovskite thin films

Formic acid adsorption kinetics on MAPbI₃ perovskite thin films, thermally dissociated perovskites (PbI₂ thin films), and ITO substrate were studied employing TDS and AES at UHV. Background effects (e.g. effects of the sample holder etc.) were studied by replacing perovskite/ITO/ glass substrate by an inert silica film grown on Mo(112) and performing a similar type of kinetics experiments for formic acid adsorption (similar to formic acid adsorption kinetics on perovskites).

Formic acid was dosed ($\chi = 20.0$ L) by backfilling the vacuum chamber while keeping the fresh MAPbI₃ perovskite thin film ~ 100 K initially. Then, the sample temperature was ramped using a constant heating rate (1.6 K/s) and desorbing molecular fragments were detected by a residual gas analyzer. Thermal desorption profiles of detected molecular fragments as a function of surface temperature is depicted in Figure 4.14 (a). Prior to this thermal scan, potential thermal desorption fragments dissociatively/ molecularly desorbed from the perovskite thin films after adsorbing different concentrations of formic acid were analyzed in order to identify the most important fragments desorbing from the surfaces, which could help to understand the adsorption/ desorption mechanisms.

The parent mass of formic acid ($m/z = 46$) was detected along with $m/z = 28$ and 29 corresponding to CO and CHO, which are the major mass fragments appeared in the gas phase mass spectra of formic acid. Purpose of the detection of the above molecular fragments was to identify the molecularity of the adsorption process. Also, formaldehyde (CHOH, $m/z = 30$) found

to be a major desorption product, which was also detected during the thermal desorption studies.

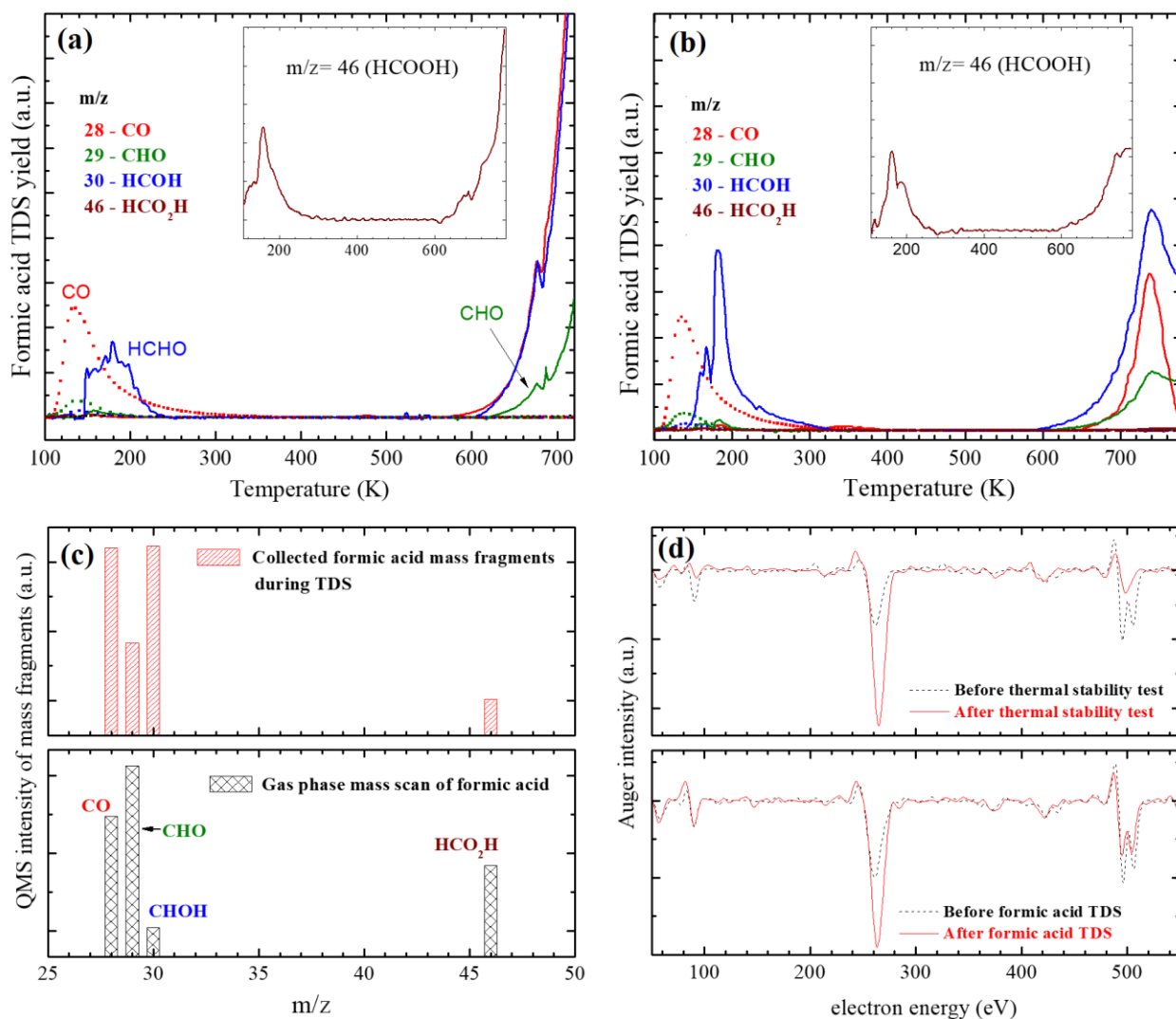


Figure 4.14. (a) Desorption profiles of formic acid fragments adsorbed ($\chi = 20.0$ L of formic acid) on perovskite thin films (solid lines) and silica thin films (dotted lines) as a function of surface temperature, (b) desorption profiles of formic acid fragments for a second dose of 20.0 L of formic acid after the 1st TDS experiment, (c) comparison of the gas phase mass scan (only four selected masses were compared) of formic acid (bottom panel) with the integrated TDS peak intensities of collected mass fragments of desorbed formic acid fragments from perovskite thin film (top panel), (d) comparison of the AES spectra of perovskite thin films before and after thermal stability test (top panel) with the AES spectra of perovskites before and after formic acid TDS (bottom panel).

After the first thermal ramp, a second TDS experiment was performed using the same perovskite thin film. Similar to the previous case, 20.0 L of formic acid was dosed, and the sample temperature was ramped from 100-800 K at a rate of 1.6 K/s (Figure 4.14 (b)). Since the sample

temperature was ramped to ~ 750 K during the 1st TDS experiment, we expected to see a significant difference in the TDS peak positions in this case with the hypothesis of the perovskite sample degraded at that temperatures (which is > 540 K), reflected by prior thermal stability and CO₂ adsorption experiments (see Figure 4.10 and 4.11). However, the TDS traces look quite similar (in terms of peak positions), only with some intensity differences of respective peaks.

The TDS traces collected during the 1st thermal ramp were integrated, and the peak areas are depicted in Figure 4.14 (c- top panel). Also, a part of the gas-phase mass spectrum of molecular formic acid is depicted in the bottom panel in the same figure for the comparison. At a quick glance, the intensity ratios of the formic acid gas-phase mass fragments and that of the formic acid desorption fragments collected during the thermal desorption study are quite different. This is a direct indication for the activation adsorption of formic acid on MAPbI₃ perovskite thin films.

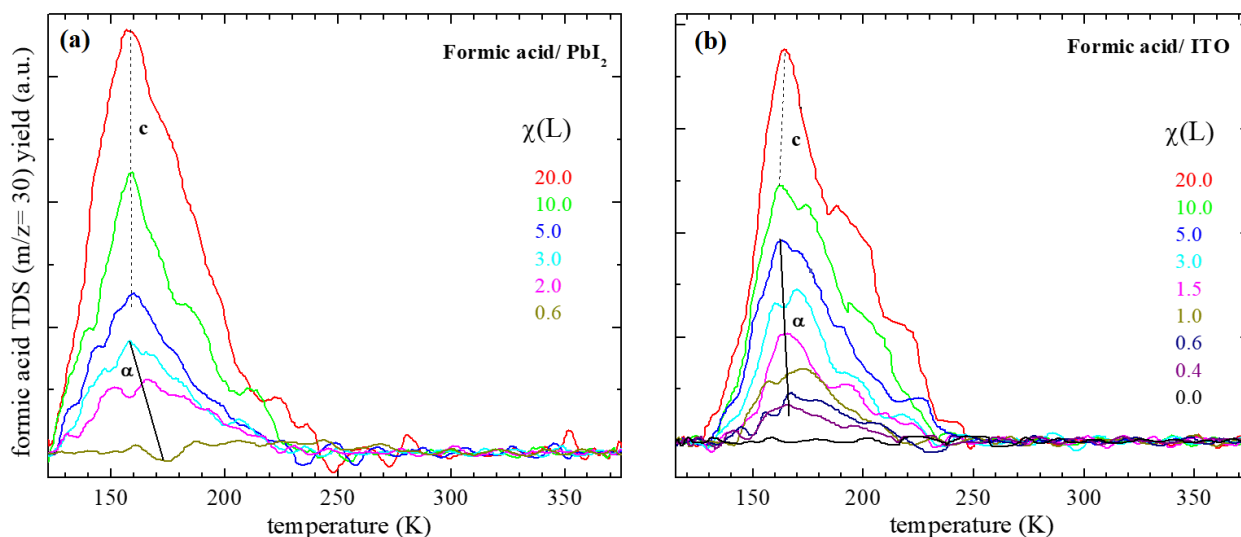


Figure 4.15. Formic acid TDS curves as a function of exposure on (a) PbI₂ thin films, (b) ITO substrates.

Background thermal desorption profiles of formic acid (desorption from silica samples) are depicted in Figures 4.14 (a) and (b) with dotted lines. Only low-temperature desorption peaks are evident and therefore, background effects, reabsorption effects etc., at higher temperature

involving the sample holder can be ruled out. Also, formic acid adsorption on the PbI_2 thin films (thermally dissociated perovskites) and the ITO substrate was investigated to further understand any background/ substrate effects on formic acid adsorption/ desorption kinetics. Only low-temperature desorption peaks are evident in both PbI_2 and ITO TDS experiments as depicted in Figure 4.15. Identification of the monolayer saturation exposures/ multi-layer formation limit was another objective of this experiment as the monolayer-multilayer peak separation can be clearly observable. Furthermore, by comparing the TDS peak patterns/ desorption temperatures with perovskite data, chemical differences/ similarities of the perovskites layers before and after TDS experiments can be identified.

In PbI_2 and ITO TDS experiments, the desorbing mass fragments with the highest intensity were detected to have the highest mass-spectrometric sensitivity. $m/z= 30$ was detected, which was the most intense mass fragment rather than the parent mass of formic acid ($m/z= 46$). As depicted in Figure 4.15, two TDS peaks are evident in both kinetics experiments, which can be identified with the direction of the peak shifts with the exposure. TDS peaks are shifted to lower temperatures with the exposure at the beginning, consistent with the repulsive lateral interactions caused by already adsorbed species (steric repulsion) as well as the chemical inhomogeneity of the considered surfaces. The latter case may be the dominant factor, reflected by AES data (e.g. PbI_2 thin films may contain PbI_2 , ITO, carbon, and traces of perovskite adsorption sites, which may have cumulative effects for the adsorption/ desorption kinetics. See Figure 4.8 (b) for the AES of PbI_2 and ITO thin films).

When the exposure reaches to ~ 5.0 L, the direction of the TDS peak shift is reversed. A higher temperature shift of the TDS peaks with the exposure and the shared leading edges at low temperatures are characteristic features of 0^{th} order kinetics, which reflects the multi-layer

adsorption regime of formic acid. Therefore, the onset of the condensation peaks (c-peak) can be considered as the monolayer adsorption limit. Required exposure to obtain monolayer coverage is ~ 5.0 L in both cases. The α -peak is the sub-monolayer desorption peak of formic acid.

The binding energies of formic acid on PbI_2 and ITO were determined using the α -peak positions together with the Redhead approximations, which found to be 41-44 kJ/mol and 42-45 kJ/mol respectively on PbI_2 and ITO. The onset of the TDS peak is about 160 K irrespective to the substrate, which is a characteristic feature of the condensation peak.

Formic acid was adsorbed on MAPbI_3 perovskite thin film by dosing 20.0 L, which is about four times larger than the monolayer exposure for PbI_2 / ITO substrates, determined by prior TDS experiments. The objective was to cover the entire surfaces of MAPbI_3 perovskite thin film with a layer of formic acid and to study the stability of the thin films with thermal treatments. Formic acid adsorption-desorption kinetics were also investigated. Large exposure of the probe molecule was dosed assuming the perovskite thin films have a larger surface area due to its porous structure, compared to the PbI_2 / ITO thin films. As indicated in Figure 4.14 (a), CHOH is a major desorption fragment along with CO and CHO fragments. Compared to the gas-phase mass spectrum of formic acid, the relative intensity of CHOH is significantly high, clearly indicating the dissociative adsorption of formic acid. Desorption peaks centered around 180 K is multi-layer adsorption regime of formic acid since a huge initial exposure is used. Monolayer desorption peaks appear > 600 K, showing a huge binding energy of formic acid to the perovskite thin film. The binding energy of formic acid is even greater than that of CO_2 and H_2O to the perovskite surfaces.

The second thermal ramp of perovskite thin films with adsorbed formic acid (20.0 L) generates structurally similar TDS peaks, with slight intensity differences. The vertical axis of Figure 4.14 (a) and (b) are identical, enabling the comparison of the peak intensities qualitatively.

Structural similarity suggesting the retention of the perovskite structure without severe deteriorations as the sample temperature increased (up to 750 K), contrast to the previous experiments regarding the thermal stability of MAPbI₃ perovskites (severe dissociations occurred above 540 K). If the perovskite thin films dissociated completely to PbI₂ or ITO, higher temperature formic acid desorption peaks could not be observed. However, the intensity of the higher temperature peaks is somewhat smaller in the second thermal ramp, which may be due to the partial dissociation of perovskite thin films at high temperature. Reduced surface area due to the partial dissociation of the perovskite thin films may result in a smaller saturation exposure. Also, traces of PbI₂/ ITO may also be sampled by adsorbing formic acid. These are the possible factors for the increased intensity of lower temperature desorption peak in the second TDS experiment.

AES compositional analysis further confirms the structural stability of the perovskite thin films after formic acid adsorption. Even after applying two thermal ramps from 100-750 K, retention of a significant portion of the perovskite structure is evident according to AES as well (Figure 4.14 (d)-bottom panel). The AES of perovskite thin films before and after the thermal treatment with adsorbed formic acid have quite similar peak patterns with some differences in the peak intensities. Lowering the peak intensities at Pb, I regions are consistent with the partial dissociation of the perovskite thin film, which was also reflected by TDS. The significant intensity increase in the AES carbon peak may be due to the dissociatively adsorbed formic acid fragments embedded on the surface. Much higher temperature annealing may be necessary to remove those fragments, which can eventually destroy the remaining perovskite structure. However, a similar type of thermal treatments (heating from 100-750 K) without adsorbed formic acid layers

completely destroyed the perovskite structures, reflected by the Auger scans in Figure 4.14 (d)-top panel.

Competitive adsorption of formic acid with the adsorbed impurities such as water and carbon dioxide are possible, which would lead to the sample stability. As shown in previous studies, the corrosive reduction is a major decomposition pathway for the organohalide perovskite thin films induced by water. Since the adsorption energy of water on perovskite thin films is significantly lower than that of formic acid (water desorbed at 400-600 K where the formic acid desorption starts > 600 K), adsorption of formic acid would be thermodynamically favored over water due to the formation of strong chemical bonds, reflected by TDS temperatures. Therefore, surface concentrations of water may be reduced, subsequently lowering the corrosive effects of water. Also, strongly bonded formic acid would reduce the thermal vacancy formation by surface diffusion of constituent ions, as the diffusion activation energies are proportional to the binding energies. Reduced corrosive reduction by water and inhibited diffusion mediated degradation would enhance the thermal stability of the MAPbI₃ perovskite thin films with the adsorbed formic acid layer.

Dissociative adsorption indicated by TDS experiments draw our fundamental interests towards the adsorption/ desorption mechanisms of formic acid on MAPbI₃ perovskite thin films. Even at low temperatures, a significant HCHO peak is evident, suggesting the dissociative adsorption on impact. Desorption of molecular formic acid ($m/z=46$) is observed at the multi-layer regime, as well as in the monolayer regime (at higher T), which are shown in the insets of the Figures 4.14 (a) and (b). The relative concentration of molecularly desorbed formic acid is quite low compared to the other desorption fragments. Low-temperature desorption peak is from condensed molecular formic acid where the high-temperature desorption structure could be from

associatively desorbed dissociated fragments, forming molecular formic acid. Dissociation of adsorbed formic acid via formate intermediate on metal/ metal oxide surfaces has been observed in previous studies. Unfortunately, adsorbed states of formic acid intermediates could not be detected with our experimental techniques. CHO is another potential intermediate/ reaction product which has been predicted theoretically. A significant amount of CHO desorption is evident in the current study as well. CHO could be formed by either direct dissociation of molecular formic acid on impact or through the formate intermediate. Recombinative desorption of CHO with adsorbed H can form CHO_H, which is a major desorption product detected. Further dissociation of CHO can yield CO, which is also detected in TDS. Furthermore, molecular desorption of CHO is also evident.

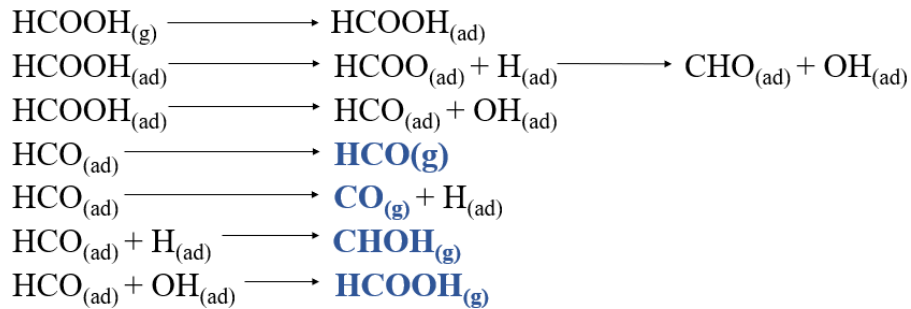


Figure 4.16. Possible adsorption/ desorption pathways of formic acid on MAPbI₃ perovskite thin films proposed based on the detected desorption fragments (detected fragments are highlighted in blue color)

Even though we observed some thermal stability of MAPbI₃ perovskite thin films with a passivation layer of formic acid, exact binding sites of formic acid with such a high binding energy, actual form of the formic acid adsorbed on the surface (molecular/ dissociated fragments), sample stabilization mechanisms, and formic acid desorption mechanisms etc., must be revealed prior to any real-world applications. Also, the effect of the adsorbed formic acid layer on the electronic properties of the MAPbI₃ perovskites will be critically important in solar-cell related applications.

Therefore, further experimental and theoretical studies are necessary to get insights into the formic acid adsorbed MAPbI₃ perovskite system.

4.4. Summary and conclusions

Methylammonium lead iodide (MAPbI₃) perovskite thin films were synthesized on ITO coated glass slides at ambient employing a solution processed synthesis technique. MAPbI₃ thin films were characterized by UV-visible spectroscopy, XRD, SEM, and EDX at ambient, as well as by AES at UHV. Thermal stability, small molecular adsorption, and stabilization mechanisms of MAPbI₃ perovskite thin films were studied employing UHV based thermal desorption techniques as well as computational methods.

MAPbI₃ perovskite thin films are stable up to 540 K at UHV due to the inert environments. Ambient pressure synthesis and storage can readily contaminate the samples with residual CO₂ and H₂O indicated by TDS and AES. Carbon dioxide and water bind strongly to the MAPbI₃ perovskite thin films. Co-adsorption of carbon dioxide with water on defected sites replacing I⁻ and CH₃NH₃⁺ defects by HCO₃⁻ and H₃O⁺ respectively in the perovskite structure lead to the strong binding of carbon dioxide to the surface, with 153-170 kJ/mol of binding strength. However, a high amount of carbon dioxide concentrations decreases the thermal stability of MAPbI₃ perovskite thin films.

Formic acid adsorption on perovskite thin films was investigated to understand the ability of a molecular layer of formic acid to act as a protective chemical inhibition layer. Formic acid adsorbed perovskite thin films are thermally more stable than pristine perovskite thin films. Strong bonding of the formic acid to the perovskite surface may prevent the corrosive reduction by water and also reduce the thermal degradation by ionic diffusion. More experimental and theoretical

studies may be necessary to get insights into the MAPbI₃ perovskite-formic acid system prior to any real-world applications.

REFERENCES

1. Hudson, J. B., *Surface Science: An Introduction*. Wiley: 1998.
2. Ertl, G.; Küppers, J., *Low Energy Electrons and Surface Chemistry*. VCH: 1985.
3. Gao, F.; Goodman, D., Model Catalysts: Simulating the Complexities of Heterogeneous Catalysts. *Annual Review of Physical Chemistry* **2012**, *63*, 265.
4. Somorjai, G. A., *Introduction to surface chemistry and catalysis*. Wiley: 1994.
5. Kelley, R. D.; Goodman, D. W., *Catalytic methanation over single crystal nickel and ruthenium: Reaction kinetics on different crystal planes and the correlation of surface carbide concentration with reaction rate*. 1982; Vol. 123.
6. Strongin, D. R.; Carrazza, J.; Bare, S. R.; Somorjai, G. A., The importance of C7 sites and surface roughness in the ammonia synthesis reaction over iron. *Journal of Catalysis* **1987**, *103* (1), 213-215.
7. Chen, M. S.; Goodman, D. W., The Structure of Catalytically Active Gold on Titania. *Science* **2004**, *306* (5694), 252.
8. Kim, Y. D.; Wei, T.; Goodman, D. W., Identification of Defect Sites on SiO₂ Thin Films Grown on Mo(112). *Langmuir* **2003**, *19* (2), 354-357.
9. Chen, P. J.; Goodman, D. W., Epitaxial growth of ultrathin Al₂O₃ films on Ta(110). *Surface Science* **1994**, *312* (3), L767-L773.
10. Yang, X.-F.; Wang, A.; Qiao, B.; Li, J.; Liu, J.; Zhang, T., Single-Atom Catalysts: A New Frontier in Heterogeneous Catalysis. *Acc. Chem. Res.* **2013**, *46* (8), 1740-1748.
11. Zhang, W.; Zheng, W., Single Atom Excels as the Smallest Functional Material. *Advanced Functional Materials* **2016**, *26* (18), 2988-2993.
12. Clarke, L. J., *Surface crystallography: an introduction to low energy electron diffraction*. Wiley: 1985.
13. Henk, J., Chapter 10 - Theory of low-energy electron diffraction and photoelectron spectroscopy from ultra-thin films. In *Handbook of Thin Films*, Singh Nalwa, H., Ed. Academic Press: Burlington, 2002; pp 479-526.
14. Hermann, K., Periodic overlayers and moire patterns: theoretical studies of geometric properties. *J Phys Condens Matter* **2012**, *24* (31), 314210.
15. Woodruff, D.; Woodruff, D. P.; Delchar, T. A., *Modern Techniques of Surface Science*. Cambridge University Press: 1994.
16. Oura, K.; Lifshits, V. G.; Saranin, A.; Zotov, A. V.; Katayama, M., *Surface Science: An Introduction*. Springer Berlin Heidelberg: 2003.
17. Laidler, K. J.; Meiser, J. H., *Physical chemistry*. Benjamin/Cummings Pub. Co.: 1982.
18. Burghaus, U.; Vattuone, L.; Gambardella, P.; Rocca, M., HREELS study of CO oxidation on Ag(001) by O₂ or O. *Surface Science* **1997**, *374* (1), 1-8.

19. Zeinalipour-Yazdi, C. D., On the possibility of an Eley-Rideal mechanism for ammonia synthesis on Mn₆N_{5+x} (x = 1)-(111) surfaces. *Phys Chem Chem Phys* **2018**, *20* (27), 18729-18736.
20. Hoffman, D. M.; Singh, B.; Thomas, J. H., *Handbook of Vacuum Science and Technology*. Academic Press: 1998.
21. Levine, I. N., *Physical chemistry*. McGraw-Hill: 2008.
22. Jennings, S. G., The mean free path in air. *Journal of Aerosol Science* **1988**, *19* (2), 159-166.
23. Briggs, D.; Grant, J. T.; Limited, S., *Surface Analysis by Auger and X-ray Photoelectron Spectroscopy*. SurfaceSpectra: 2003.
24. Carlson, T., *Photoelectron and Auger Spectroscopy*. Springer US: 2013.
25. Settle, F. A., *Handbook of Instrumental Techniques for Analytical Chemistry*. Prentice Hall PTR: 1997.
26. Palmberg, P. W.; Industries, P. E., *Handbook of Auger Electron Spectroscopy: A Reference Book of Standard Data for Identification and Interpretation of Auger Electron Spectroscopy Data*. Physical Electronics Industries: 1972.
27. Tarnag, M. L.; Wehner, G. K., Escape length of Auger electrons. *Journal of Applied Physics* **1973**, *44* (4), 1534-1540.
28. Division, P.-E. P. E., PHI Model 15-255G Precision Electron Energy analyzer **1997**.
29. Van Hove, M. A.; Weinberg, W. H.; Chan, C. M., *Low-energy electron diffraction: experiment, theory, and surface structure determination*. Springer-Verlag: 1986.
30. Davisson, C.; Germer, L. H., The Scattering of Electrons by a Single Crystal of Nickel. *Nature* **1927**, *119*, 558.
31. Thomson, G. P.; Reid, A., Diffraction of Cathode Rays by a Thin Film. *Nature* **1927**, *119*, 890.
32. McRae, E., Surface crystallography: an introduction to low energy electron diffraction by LJ Clarke. *Acta Crystallographica Section A* **1986**, *42* (2), 135-136.
33. Attard, G.; Barnes, C., *SURFACES. Edition en anglais*. Oxford University Press: 1998.
34. Jona, F.; J. A. Strozier, J.; Yang, W. S., Low-energy electron diffraction for surface structure analysis. *Reports on Progress in Physics* **1982**, *45* (5), 527.
35. GmbH, S., ErLEED User Manual. **2003**.
36. Schroeder, S. L.; Gottfried, M., Temperature-Programmed Desorption (TPD) Thermal Desorption Spectroscopy (TDS). *Adv. Phys. Chem. Lab, FU Berlin, June 2002* **2002**.
37. Chakradhar, A.; Sivapragasam, N.; Nayakasinghe, M. T.; Burghaus, U., Support effects in the adsorption of water on CVD graphene: an ultra-high vacuum adsorption study. *Chem Commun (Camb)* **2015**, *51* (57), 11463-6.

38. Nayakasinghe, M. T.; Sivapragasam, N.; Burghaus, U., Desulfurization-Related Surface Chemistry on Two-Dimensional Silica Films: Adsorption of Thiophene and Short-Chain Alkanes on Silicatene. *The Journal of Physical Chemistry C* **2018**, *122* (15), 8244-8253.
39. Funk, S.; Goering, J.; Burghaus, U., Adsorption kinetics and dynamics of small organic molecules on a silica wafer: Butane, pentane, nonane, thiophene, and methanol adsorption on SiO₂/Si(111). *Applied Surface Science* **2008**, *254* (16), 5271-5275.
40. Kadossov, E. B.; Burghaus, U., Unexpected bond activation of small organic molecules on a metal oxide-butane/CaO(100). *Chem Commun (Camb)* **2008**, (34), 4073-5.
41. Marcinkowski, M. D.; Jewell, A. D.; Stamatakis, M.; Boucher, M. B.; Lewis, E. A.; Murphy, C. J.; Kyriakou, G.; Sykes, E. C. H., Controlling a spillover pathway with the molecular cork effect. *Nature materials* **2013**, *12* (6), 523.
42. Burghaus, U.; Conrad, H., The influence of surface reconstructions on the CO oxidation reaction rate for the O Ag(110) surface. *Surface Science* **1996**, *352*, 201-205.
43. Systems, S. R., Models RGA100, RGA200 and RGA300 Residual Gas Analyzer **2009**.
44. Ranke, W. In *Modern methods in heterogeneous catalysis research: Theory and experiment. Thermal analysis-TDS*, Modern methods in heterogeneous catalysis research: Theory and experiment, 2002.
45. Redhead, P. A., *Thermal Desorption of Gases*. 1962; Vol. 12, p 203-211.
46. Falconer, J. L.; Madix, R. J., Flash desorption activation energies: DCOOH decomposition and CO desorption from Ni (110). *Surface Science* **1975**, *48* (2), 393-405.
47. King, D. A., Thermal desorption from metal surfaces: A review. *Surface Science* **1975**, *47* (1), 384-402.
48. Dohnálek, Z.; Kimmel, G. A.; Joyce, S. A.; Ayotte, P.; Smith, R. S.; Kay, B. D., Physisorption of CO on the MgO(100) Surface. *The Journal of Physical Chemistry B* **2001**, *105* (18), 3747-3751.
49. Tait, S. L.; Dohnálek, Z.; Campbell, C. T.; Kay, B. D., n-alkanes on MgO (100). I. Coverage-dependent desorption kinetics of n-butane. *The Journal of chemical physics* **2005**, *122* (16), 164707.
50. Neumark, D. M.; Wodtke, A. M.; Robinson, G. N.; Hayden, C. C.; Lee, Y. T., Molecular beam studies of the F+H₂ reaction. *The Journal of Chemical Physics* **1985**, *82* (7), 3045-3066.
51. Cross, J. B., Molecular beam kinetics: D + ClF₃. *The Journal of Chemical Physics* **1973**, *59* (2), 966-967.
52. Hou; Huang; Gulding; Rettner; Auerbach; Wodtke, Enhanced reactivity of highly vibrationally excited molecules on metal surfaces. *Science (New York, N.Y.)* **1999**, *284* (5420), 1647.

53. Smith, R. R.; Killelea, D. R.; Delsesto, D. F.; Utz, A. L., Preference for vibrational over translational energy in a gas-surface reaction. *Science (New York, N.Y.)* **2004**, *304* (5673), 992.
54. Crim, F., Bond-selected chemistry: Vibrational state control of photodissociation and bimolecular reaction. In *J. Phys. Chem.*, 1996; Vol. 100, pp 12725-12734.
55. Blythe, A. R.; Fluendy, M. A. D.; Lawley, K. P., Molecular beam scattering. *Quarterly Reviews, Chemical Society* **1966**, *20* (3), 465-483.
56. Cushing, G. W.; Navin, J. K.; Valadez, L.; Johánek, V.; Harrison, I., An effusive molecular beam technique for studies of polyatomic gas-surface reactivity and energy transfer. *Review of Scientific Instruments* **2011**, *82* (4).
57. Wheeler, M. C.; Seets, D. C.; Mullins, C. B., Kinetics and dynamics of the initial dissociative chemisorption of oxygen on Ru(001). *The Journal of Chemical Physics* **1996**, *105* (4), 1572-1583.
58. Wang, J.; Burghaus, U., Adsorption of CO on the copper-precovered ZnO(0001) surface: a molecular-beam scattering study. *J Chem Phys* **2005**, *123* (18), 184716.
59. Wang, J.; Burghaus, U., Adsorption dynamics of CO₂ on Zn-ZnO(0001): a molecular beam study. *J Chem Phys* **2005**, *122* (4), 44705.
60. Atkins, P.; de Paula, J., *Atkins' Physical Chemistry*. OUP Oxford: 2010.
61. Haberland, H.; Buck, U.; Tolle, M., Velocity distribution of supersonic nozzle beams. *Review of Scientific Instruments* **1985**, *56* (9), 1712-1716.
62. Anderson, J. B., Molecular beams from nozzle sources. In: *Molecular beams and low density gasdynamics.*(A75-28372 12-72) New York, Marcel Dekker, Inc., 1974, p. 1-91. **1974**, 1-91.
63. Anderson, J.; Fenn, J., Velocity distributions in molecular beams from nozzle sources. *The physics of fluids* **1965**, *8* (5), 780-787.
64. Arumainayagam, C. R.; Madix, R. J., Molecular beam studies of gas-surface collision dynamics. *Progress in Surface science* **1991**, *38* (1), 1-102.
65. Beutl, M.; Riedler, M.; Rendulic, K. D., Strong rotational effects in the adsorption dynamics of H₂/Pd (111): evidence for dynamical steering. *Chemical physics letters* **1995**, *247* (3), 249-252.
66. King, D. A.; Wells, M. G., Molecular beam investigation of adsorption kinetics on bulk metal targets: Nitrogen on tungsten. *Surface Science* **1972**, *29* (2), 454-482.
67. Hirscher, M.; Panella, B., Nanostructures with high surface area for hydrogen storage. *Journal of Alloys and Compounds* **2005**, *404-406*, 399-401.
68. Masel, R. I.; Masel, R. I., *Principles of adsorption and reaction on solid surfaces*. John Wiley & Sons: 1996; Vol. 3.

69. Kunat, M.; Boas, C.; Becker, T.; Burghaus, U.; Woll, C., Adsorption dynamics of CO on Cu(110): a molecular beam study. *Surface Science (Netherlands)* **2001**, *474* (1-3), 114-128.
70. Gross, A.; Wilke, S.; Scheffler, M., Six-dimensional quantum dynamics of adsorption and desorption of H₂ at Pd(100): no need for a molecular precursor adsorption state. *Surface Science* **1996**, *357-358*, 614-618.
71. Poon, G.; Grassman, T.; Gumy, J.; Kummel, A., Direct and precursor-mediated hyperthermal abstractive chemisorption of Cl₂/Al (111). *The Journal of chemical physics* **2003**, *119* (18), 9818-9828.
72. Moulder, J. F.; Chastain, J., *Handbook of X-ray Photoelectron Spectroscopy: A Reference Book of Standard Spectra for Identification and Interpretation of XPS Data*. Physical Electronics Division, Perkin-Elmer Corporation: 1992.
73. Siegbahn, K., Electron spectroscopy for atoms, molecules, and condensed matter. *Reviews of Modern Physics* **1982**, *54* (3), 709-728.
74. Devision, P.-E. P. E., PHI Model 04-500/04-548 X-ray Sources- Technical Manual. **1984**.
75. Bertrand, M. J., Handbook of Instrumental Techniques for Analytical Chemistry Edited by Frank A. Settle. Prentice Hall: Upper Saddle River. 1997. xxi + 995 pp. ISBN 0-13-177338-0. *Journal of the American Chemical Society* **1998**, *120* (26), 6633-6633.
76. Bernath, P. F., *Spectra of Atoms and Molecules*. Oxford University Press: 2005.
77. Skoog, D. A.; West, D. M.; Holler, F. J.; Crouch, S. R., *Fundamentals of Analytical Chemistry*. Cengage Learning: 2013.
78. ESCOBEDO MORALES, A.; SANCHEZ MORA, E.; PAL, U., Use of diffuse reflectance spectroscopy for optical characterization of un-supported nanostructures. *Revista mexicana de física* **2007**, *53* (5), 18-22.
79. VARIAN, Cary 50 Hardware Operation manual. **1999**.
80. Technologies, A., Cary 100/300/4000/5000/6000i/7000 Spectrophotometers. **2016**, *Tenth edition*.
81. Goldstein, J.; Goldstein, J. I.; Goldshtain, Y.; Newbury, D. E.; Joy, D. C.; Echlin, P.; Lyman, C. E.; Lifshin, E.; Sawyer, L.; Joy, O. R. N. L. D. S. D. E. M. F. D. C., *Scanning Electron Microscopy and X-Ray Microanalysis: Third Edition*. Springer US: 2003.
82. Massa, W.; Gould, R. O., *Crystal Structure Determination*. Springer Berlin Heidelberg: 2010.
83. Scott, J.; Guang, D.; Naeramitmarnsuk, K.; Thabuot, M.; Amal, R., Zeolite synthesis from coal fly ash for the removal of lead ions from aqueous solution. *Journal of Chemical Technology and Biotechnology* **2002**, *77* (1), 63-69.
84. Roth, W. J.; Nachtigall, P.; Morris, R. E.; Cejka, J., Two-dimensional zeolites: current status and perspectives. *Chemical reviews* **2014**, *114* (9), 4807-4837.

85. Shaikhutdinov, S.; Freund, H. J., Ultrathin silica films on metals: the long and winding road to understanding the atomic structure. *Adv Mater* **2013**, *25* (1), 49-67.
86. Schroeder, T.; Adelt, M.; Richter, B.; Naschitzki, M.; Bäumer, M.; Freund, H.-J., Epitaxial growth of SiO₂ on Mo (112). *Surface Review and Letters* **2000**, *7* (01n02), 7-14.
87. Chen, M.; Santra, A.; Goodman, D., Structure of thin SiO₂ films grown on Mo (112). *Physical Review B* **2004**, *69* (15), 155404.
88. Nayakasinghe, M. T.; Chakradhar, A.; Sivapragasam, N.; Burghaus, U., Water adsorption on two-dimensional silica films. *Applied Surface Science* **2016**, *364*, 822-828.
89. Gründling, C.; Lercher, J. A.; Goodman, D. W., Preparation of mixed Al₂O₃/SiO₂ thin films supported on Mo(100). *Surface Science* **1994**, *318* (1), 97-103.
90. Stacchiola, D.; Kaya, S.; Weissenrieder, J.; Kuhlenbeck, H.; Shaikhutdinov, S.; Freund, H. J.; Sierka, M.; Todorova, T. K.; Sauer, J., Synthesis and structure of ultrathin aluminosilicate films. *Angewandte Chemie International Edition* **2006**, *45* (45), 7636-7639.
91. Wendt, S.; Frerichs, M.; Wei, T.; Chen, M. S.; Kempter, V.; Goodman, D. W., The interaction of water with silica thin films grown on Mo(1 1 2). *Surface Science* **2004**, *565* (2-3), 107-120.
92. Todorova, T. K.; Sierka, M.; Sauer, J.; Kaya, S.; Weissenrieder, J.; Lu, J. L.; Gao, H. J.; Shaikhutdinov, S.; Freund, H. J., Atomic structure of a thin silica film on a Mo(112) substrate: A combined experimental and theoretical study. *Physical Review B* **2006**, *73* (16), 165414.
93. Chianelli, R. R.; Berhault, G.; Torres, B., Unsupported transition metal sulfide catalysts: 100 years of science and application. *Catalysis Today* **2009**, *147* (3), 275-286.
94. Ali, S. A., Development of improved catalysts for deep HDS of diesel fuels. *Applied Petrochemical Research* **2014**, *4* (4), 409-415.
95. Liu, C.; Liu, H.; Yin, C.; Zhao, X.; Liu, B.; Li, X.; Li, Y.; Liu, Y., Preparation, characterization, and hydrodesulfurization properties of binary transition-metal sulfide catalysts. *Fuel* **2015**, *154*, 88-94.
96. Moses, P.; Hinnemann, B.; Topsoe, H.; Norskov, J., The hydrogenation and direct desulfurization reaction pathway in thiophene hydrodesulfurization over MoS₂ catalysts at realistic conditions: A density functional study. *Journal of Catalysis* **2007**, *248* (2), 188-203.
97. Salnikov, O. G.; Burueva, D. B.; Barskiy, D. A.; Bukhtiyarova, G. A.; Kovtunov, K. V.; Koptyug, I. V., A Mechanistic Study of Thiophene Hydrodesulfurization by the Parahydrogen-Induced Polarization Technique. *ChemCatChem* **2015**, *7* (21), 3508-3512.
98. Sullivan, D. L.; Ekerdt, J. G., Mechanisms of thiophene hydrodesulfurization on model molybdenum catalysts. *J. Catal.* **1998**, *178* (1), 226-233.

99. Zhao, R.-y.; Zeng, L.-y.; Liang, J.; Liu, C.-g., Interaction between Ni promoter and Al₂O₃ support and its effect on the performance of NiMo/ γ -Al₂O₃ catalyst in hydrodesulfurization. *Journal of Fuel Chemistry and Technology* **2016**, *44* (5), 564-569.
100. Zonneville, M. C.; Hoffmann, R.; Harris, S., Thiophene hydrodesulfurization on molybdenum disulfide theoretical aspects. *Surf. Sci.* **1988**, *199* (1-2), 320-60.
101. Singhal, G. H.; Espino, R. L.; Sobel, J. E., Hydrodesulfurization of sulfur heterocyclic compounds. Reaction mechanisms. *J. Catal.* **1981**, *67* (2), 446-56.
102. Borgna, A.; Hensen, E. J. M.; van Veen, J. A. R.; Niemantsverdriet, J. W., Intrinsic kinetics of thiophene hydrodesulfurization on a sulfided NiMo/SiO₂ planar model catalyst. *Journal of Catalysis* **2004**, *221* (2), 541-548.
103. Bataille, F.; Lemberon, J.-L.; Michaud, P.; Pérot, G.; Vrinat, M.; Lemaire, M.; Schulz, E.; Breyse, M.; Kasztelan, S., Alkyldibenzothiophenes Hydrodesulfurization-Promoter Effect, Reactivity, and Reaction Mechanism. *Journal of Catalysis* **2000**, *191* (2), 409-422.
104. Lipsch, J. M. J. G.; Schuit, G. C. A., The CoO · MoO₃ · Al₂O₃ catalyst: III. Catalytic properties. *Journal of Catalysis* **1969**, *15* (2), 179-189.
105. Hensen, E. J. M.; Vissenberg, M. J.; de Beer, V. H. J.; van Veen, J. A. R.; van Santen, R. A., Kinetics and Mechanism of Thiophene Hydrodesulfurization over Carbon-Supported Transition Metal Sulfides. *Journal of Catalysis* **1996**, *163* (2), 429-435.
106. Kim, Y.; Wei, T.; Goodman, D., Identification of defect sites on SiO₂ thin films grown on Mo (112). *Langmuir* **2003**, *19* (2), 354-357.
107. Cabrera, N.; Mott, N. F., Theory of the oxidation of metals. *Reports on Progress in Physics* **1949**, *12* (1), 163.
108. Derrien, J.; Ringeisen, F.; Commandre, M., Structure and growth kinetics of SiO₂ ultra thin film on Si(111) surface **Work supported by “Groupement du Circuit Intégré au Silicium”. In *Passivity of Metals and Semiconductors*, Froment, M., Ed. Elsevier: 1983; pp 457-462.
109. Xu, X.; Goodman, D. W., New approach to the preparation of ultrathin silicon dioxide films at low temperatures. *Applied Physics Letters* **1992**, *61* (7), 774-776.
110. Xu, X.; Goodman, D. W., The preparation and characterization of ultra-thin silicon dioxide films on a molybdenum(110) surface. *Surf. Sci.* **1993**, *282* (3), 323-32.
111. He, J. W.; Xu, X.; Corneille, J. S.; Goodman, D. W., X-ray photoelectron spectroscopic characterization of ultra-thin silicon oxide films on a molybdenum (100) surface. *Surf. Sci.* **1992**, *279* (1-2), 119-26.
112. Weissenrieder, J.; Kaya, S.; Lu, J. L.; Gao, H. J.; Shaikhutdinov, S.; Freund, H. J.; Sierka, M.; Todorova, T. K.; Sauer, J., Atomic structure of a thin silica film on a Mo(112) substrate: a two-dimensional network of SiO₄ tetrahedra. *Phys Rev Lett* **2005**, *95* (7), 076103.

113. Bianconi, A.; Bauer, R. S., Evidence of SiO at the Si-oxide interface by surface soft X-ray absorption near edge spectroscopy. *Surface Science* **1980**, *99* (1), 76-86.
114. Braun, W.; Kuhlbeck, H., Chemical structure of ultrathin thermally grown oxides on a Si(100)-wafer using core level photoemission. *Surface Science* **1987**, *180* (1), 279-288.
115. Ko, C. S.; Gorte, R. J., Characterization of oxide impurities on Pt and their effect on the adsorption of CO and H₂. *Surface Science* **1985**, *155* (1), 296-312.
116. McClure, S. M.; Goodman, D. W., Simulating the Complexities of Heterogeneous Catalysis with Model Systems: Case studies of SiO₂ Supported Pt-Group Metals. *Topics in Catalysis* **2011**, *54* (5-7), 349-362.
117. Somorjai, G. A.; Editor, *The Structure and Chemistry of Solid Surfaces*. Wiley: 1969; p Unpaged.
118. Santra, A. K.; Min, B. K.; Goodman, D. W., Oxygen-induced p(1×3)-O reconstruction on Mo(112): a precursor to the epitaxial formation of MoO₂(100). *Surface Science* **2002**, *513* (3), L441-L444.
119. Santra, A. K.; Goodman, D. W., Oxide-supported metal clusters: Models for heterogeneous catalysts. *J. Phys.: Condens. Matter* **2003**, *15* (2), R31-R62.
120. Kaya, S.; Baron, M.; Stacchiola, D.; Weissenrieder, J.; Shaikhutdinov, S.; Todorova, T. K.; Sierka, M.; Sauer, J.; Freund, H. J., On the geometrical and electronic structure of an ultra-thin crystalline silica film grown on Mo(112). *Surface Science* **2007**, *601* (21), 4849-4861.
121. Shih, C.-J.; Wang, Q. H.; Lin, S.; Park, K.-C.; Jin, Z.; Strano, M. S.; Blankschtein, D., Breakdown in the Wetting Transparency of Graphene. *Physical Review Letters* **2012**, *109* (17), 176101.
122. Raj, R.; Maroo, S. C.; Wang, E. N., Wettability of Graphene. *Nano Letters* **2013**, *13* (4), 1509-1515.
123. Chakradhar, A.; Burghaus, U., Adsorption of water on graphene/Ru(0001)-an experimental ultra-high vacuum study. *Chem Commun (Camb)* **2014**, *50* (57), 7698-701.
124. Chakarov, D. V.; Oesterlund, L.; Kasemo, B., Water Adsorption and Coadsorption with Potassium on Graphite(0001). *Langmuir* **1995**, *11* (4), 1201-1214.
125. Henderson, M. A., The interaction of water with solid surfaces: fundamental aspects revisited. *Surface Science Reports* **2002**, *46* (1), 1-308.
126. Bolina, A. S.; Wolff, A. J.; Brown, W. A., Reflection Absorption Infrared Spectroscopy and Temperature-Programmed Desorption Studies of the Adsorption and Desorption of Amorphous and Crystalline Water on a Graphite Surface. *The Journal of Physical Chemistry B* **2005**, *109* (35), 16836-16845.
127. Souda, R., Nanoconfinement Effects of Water on Hydrophilic and Hydrophobic Substrates at Cryogenic Temperatures. *The Journal of Physical Chemistry C* **2012**, *116* (39), 20895-20901.

128. Kay, B. D.; Lykke, K. R.; Creighton, J. R.; Ward, S. J., The influence of adsorbate–absorbate hydrogen bonding in molecular chemisorption: NH₃, HF, and H₂O on Au (111). *The Journal of chemical physics* **1989**, *91* (8), 5120-5121.
129. Quiller, R. G.; Baker, T. A.; Deng, X.; Colling, M. E.; Min, B. K.; Friend, C. M., Transient hydroxyl formation from water on oxygen-covered Au(111). *J Chem Phys* **2008**, *129* (6), 064702.
130. Shan, J.; Aarts, J. F. M.; Kleyn, A. W.; Juurlink, L. B. F., Co-adsorption of water and hydrogen on Ni(111). *Physical Chemistry Chemical Physics* **2008**, *10* (32), 4994-5003.
131. van der Niet, M. J. T. C.; den Dunnen, A.; Juurlink, L. B. F.; Koper, M. T. M., A detailed TPD study of H₂O and pre-adsorbed O on the stepped Pt(553) surface. *Physical Chemistry Chemical Physics* **2011**, *13* (4), 1629-1638.
132. Linderoth, T. R.; Zhdanov, V. P.; Kasemo, B., Water Condensation Kinetics on a Hydrophobic Surface. *Physical Review Letters* **2003**, *90* (15), 156103.
133. Kimmel, G. A.; Petrik, N. G.; Dohnálek, Z.; Kay, B. D., Crystalline Ice Growth on Pt(111): Observation of a Hydrophobic Water Monolayer. *Physical Review Letters* **2005**, *95* (16), 166102.
134. Shan, J.; Chakradhar, A.; Yu, Z.; Burghaus, U., Adsorption of water on a hydrophobic surface – The case of antimony(111). *Chemical Physics Letters* **2011**, *517* (1), 46-50.
135. Hinch, B. J.; Dubois, L. H., Stable and metastable phases of water adsorbed on Cu(111). *The Journal of Chemical Physics* **1992**, *96* (4), 3262-3268.
136. Wu, K. J.; Peterson, L. D.; Elliott, G. S.; Kevan, S. D., Time-resolved electron energy loss spectroscopy study of water desorption from Ag(011). *The Journal of Chemical Physics* **1989**, *91* (12), 7964-7971.
137. Cao, P.; Xu, K.; Varghese, J. O.; Heath, J. R., The Microscopic Structure of Adsorbed Water on Hydrophobic Surfaces under Ambient Conditions. *Nano Letters* **2011**, *11* (12), 5581-5586.
138. Noritake, F.; Kawamura, K., The Nature of Si-O-Si Bonding via Molecular Orbital Calculations. *Journal of Computer Chemistry, Japan* **2015**, *14* (4), 124-130.
139. Ulrich, S.; Nilius, N.; Freund, H. J.; Martinez, U.; Giordano, L.; Pacchioni, G., Modifying the adsorption characteristic of inert silica films by inserting anchoring sites. *Phys Rev Lett* **2009**, *102* (1), 016102.
140. Zhang, Y.; Xu, Z., Atomic radii of noble gas elements in condensed phases. *Am. Mineral.* **1995**, *80* (7-8), 670-5.
141. Dubois, S. M. M.; Zanolli, Z.; Declerck, X.; Charlier, J. C., Electronic properties and quantum transport in Graphene-based nanostructures. *The European Physical Journal B* **2009**, *72* (1), 1-24.
142. Bakaev, V. A.; Steele, W. A., On the computer simulation of a hydrophobic vitreous silica surface. *The Journal of Chemical Physics* **1999**, *111* (21), 9803-9812.

143. Zhou, H.; Chen, Q.; Li, G.; Luo, S.; Song, T.-b.; Duan, H.-S.; Hong, Z.; You, J.; Liu, Y.; Yang, Y., Interface engineering of highly efficient perovskite solar cells. *Science* **2014**, *345* (6196), 542-546.
144. Thiel, P. A.; Madey, T. E., The interaction of water with solid surfaces: Fundamental aspects. *Surface Science Reports* **1987**, *7* (6), 211-385.
145. Funk, S.; Burghaus, U.; White, B.; O'Brien, S.; Turro, N. J., Adsorption Dynamics of Alkanes on Single-Wall Carbon Nanotubes: A Molecular Beam Scattering Study. *The Journal of Physical Chemistry C* **2007**, *111* (22), 8043-8049.
146. Whitten, J. E., Adsorption of thiophene and pyridine on W(110). *Surface Science* **2003**, *546* (2), 107-116.
147. Taguchi, Y.; Fujisawa, M.; Takaoka, T.; Okada, T.; Nishijima, M., Adsorbed state of benzene on the Si(100) surface: Thermal desorption and electron energy loss spectroscopy studies. *The Journal of Chemical Physics* **1991**, *95* (9), 6870-6876.
148. Goering, J.; Burghaus, U., Adsorption kinetics of thiophene on single-walled carbon nanotubes (CNTs). *Chemical Physics Letters* **2007**, *447* (1), 121-126.
149. Komarneni, M.; Kadossov, E.; Justin, J.; Lu, M.; Burghaus, U., Adsorption of thiophene on silica-supported Mo clusters. *Surface Science* **2010**, *604* (13), 1221-1229.
150. Tsverin, Y.; Popovitz-Biro, R.; Feldman, Y.; Tenne, R.; Komarneni, M. R.; Yu, Z.; Chakradhar, A.; Sand, A.; Burghaus, U., Synthesis and characterization of WS₂ nanotube supported cobalt catalyst for hydrodesulfurization. *Materials Research Bulletin* **2012**, *47* (7), 1653-1660.
151. Buzea, C.; Pacheco, I. I.; Robbie, K., Nanomaterials and nanoparticles: Sources and toxicity. *Biointerphases* **2007**, *2* (4), MR17-MR71.
152. Dreyer, D. R.; Park, S.; Bielawski, C. W.; Ruoff, R. S., The chemistry of graphene oxide. *Chem Soc Rev* **2010**, *39* (1), 228-40.
153. Eng, J.; Chen, J. G., Reaction pathways of cis- and trans-2-butene on Mo(110) and C/Mo(110):: selective activation of α and β C-H bonds. *Surface Science* **1998**, *414* (3), 374-388.
154. Childs, K. D.; Hedberg, C. L., *Handbook of Auger Electron Spectroscopy: A Book of Reference Data for Identification and Interpretation in Auger Electron Spectroscopy*. Physical Electronics: 1995.
155. Chakradhar, A.; Liu, Y.; Schmidt, J.; Kadossov, E.; Burghaus, U., Adsorption and dissociation kinetics of alkanes on CaO(100). *Surface Science* **2011**, *605* (15-16), 1537-1543.
156. Vericat, C.; Vela, M. E.; Benitez, G.; Carro, P.; Salvarezza, R. C., Self-assembled monolayers of thiols and dithiols on gold: new challenges for a well-known system. *Chemical Society Reviews* **2010**, *39* (5), 1805-1834.

157. Chakradhar, A.; Sivapragasam, N.; Nayakasinghe, M. T.; Burghaus, U., Adsorption kinetics of benzene on graphene: An ultrahigh vacuum study. *Journal of Vacuum Science & Technology A: Vacuum, Surfaces, and Films* **2016**, *34* (2).
158. Sivapragasam, N.; Nayakasinghe, M. T.; Chakradhar, A.; Burghaus, U., Effects of the support on the desorption kinetics of n-pentane from graphene: An ultrahigh vacuum adsorption study. *Journal of Vacuum Science & Technology A: Vacuum, Surfaces, and Films* **2017**, *35* (6).
159. Varghese, S. S.; Lonkar, S.; Singh, K. K.; Swaminathan, S.; Abdala, A., Recent advances in graphene based gas sensors. *Sensors and Actuators B: Chemical* **2015**, *218*, 160-183.
160. Londero, E.; Karlson, E. K.; Landahl, M.; Ostrovskii, D.; Rydberg, J. D.; Schroder, E., Desorption of n-alkanes from graphene: a van der Waals density functional study. *J Phys Condens Matter* **2012**, *24* (42), 424212.
161. Zaera, F., The surface chemistry of hydrocarbon partial oxidation catalysis. *Catalysis Today* **2003**, *81* (2), 149-157.
162. Bandosz, T. J., Analysis of silica surface heterogeneity using butane and butene adsorption data. *J. Colloid Interface Sci.* **1997**, *193* (1), 127-131.
163. Carrott, P. J. M.; Sing, K. S. W., Multilayer adsorption of nitrogen and alkanes by non-porous carbons and silicas. *Pure Appl. Chem.* **1989**, *61* (11), 1835-40.
164. Hokkanen, B.; Funk, S.; Burghaus, U.; Ghicov, A.; Schmuki, P., Adsorption kinetics of alkanes on TiO₂ nanotubesarray – structure–activity relationship. *Surface Science* **2007**, *601* (19), 4620-4628.
165. Tait, S. L.; Dohnalek, Z.; Campbell, C. T.; Kay, B. D., n-alkanes on MgO(100). II. Chain length dependence of kinetic desorption parameters for small n-alkanes. *J Chem Phys* **2005**, *122* (16), 164708.
166. Goering, J.; Burghaus, U.; Arey, B. W.; Eidelman, O.; Zak, A.; Tenne, R., Reactive and Non-reactive Interactions of Thiophene with WS₂ Fullerene-like Nanoparticles: An Ultra-high Vacuum Surface Chemistry Study. *Catalysis Letters* **2008**, *125* (3-4), 236-242.
167. Eng, J.; Bent, B. E.; Frühberger, B.; Chen, J. G., Studies of the Adsorption Geometry and Decomposition Mechanisms of Benzene on Clean and Carbide-Modified Mo(110) Surfaces Using Vibrational Spectroscopy. *The Journal of Physical Chemistry B* **1997**, *101* (20), 4044-4054.
168. Günster, J.; Liu, G.; Kempster, V.; Goodman, D. W., Adsorption of benzene on Mo(100) and MgO(100)/Mo(100) studied by ultraviolet photoelectron and metastable impact electron spectroscopies. *Surface Science* **1998**, *415* (3), 303-311.
169. Chen, M. S.; Santra, A. K.; Goodman, D. W., Adsorption of Benzene on a Mo(112)-c(2 × 2)-[SiO₄] Surface. *The Journal of Physical Chemistry B* **2004**, *108* (46), 17940-17945.
170. Rocha, A. S.; Rocha, A. B.; da Silva, V. T., Benzene adsorption on Mo₂C: A theoretical and experimental study. *Applied Catalysis A: General* **2010**, *379* (1-2), 54-60.

171. Fisher, A.; Blöchl, P., Adsorption and scanning-tunneling-microscope imaging of benzene on graphite and MoS₂. *Physical review letters* **1993**, *70* (21), 3263.
172. Garrett, S. J.; Holbert, V. P.; Stair, P. C.; Weitz, E., The adsorption and photochemistry of CD₃I on TiO₂ (110). *J. Chem. Phys.* **1994**, *100* (6), 4615-25.
173. Street, S. C.; Guo, Q.; Xu, C.; Goodman, D. W., Adsorption and Electronic States of Benzene on Ordered MgO and Al₂O₃ Thin Films. *The Journal of Physical Chemistry* **1996**, *100* (44), 17599-17605.
174. Ning, W.; Ya, B. L.; Zhaoxian, Y.; Sabirianov, R. F.; Mei, W. N.; Lozova, N.; Santana, J. A. C.; Dowben, P. A., The surface relaxation and band structure of Mo(112). *Journal of Physics: Condensed Matter* **2009**, *21* (47), 474222.
175. A. Shvekhgeimer, M.-G., Aliphatic nitro alcohols. Synthesis, chemical transformations and applications. *Russian Chemical Reviews* **1998**, *67* (1), 35-68.
176. Mavrikakis, M.; Barteau, M. A., Oxygenate reaction pathways on transition metal surfaces. *Journal of Molecular Catalysis A: Chemical* **1998**, *131* (1), 135-147.
177. Panja, C.; Saliba, N.; Koel, B. E., Adsorption of methanol, ethanol and water on well-characterized Pt • Sn surface alloys. *Surface Science* **1998**, *395* (2), 248-259.
178. Ulbricht, H.; Zacharia, R.; Cindir, N.; Hertel, T., Thermal desorption of gases and solvents from graphite and carbon nanotube surfaces. *Carbon* **2006**, *44* (14), 2931-2942.
179. Wiehn, M.; Levario, T. J.; Staggs, K.; Linneen, N.; Wang, Y.; Pfeffer, R.; Lin, Y. S.; Nielsen, D. R., Adsorption of Short-Chain Alcohols by Hydrophobic Silica Aerogels. *Industrial & Engineering Chemistry Research* **2013**, *52* (51), 18379-18385.
180. Wu, M. C.; Truong, C. M.; Goodman, D. W., Interactions of alcohols with a nickel oxide(100) surface studied by high-resolution electron energy loss spectroscopy and temperature-programmed desorption spectroscopy. *The Journal of Physical Chemistry* **1993**, *97* (37), 9425-9433.
181. Zhang, R.; Sun, Y.; Peng, S., In situ FTIR studies of methanol adsorption and dehydrogenation over Cu/SiO₂ catalyst. *Fuel* **2002**, *81* (11), 1619-1624.
182. Zhang, L.; Carman, A. J.; Casey, S. M., Adsorption and Thermal Decomposition Chemistry of 1-Propanol and Other Primary Alcohols on the Si(100) Surface. *The Journal of Physical Chemistry B* **2003**, *107* (33), 8424-8432.
183. Franceschini, E. A.; Bruno, M. M.; Williams, F. J.; Viva, F. A.; Corti, H. R., High-activity mesoporous Pt/Ru catalysts for methanol oxidation. *ACS Appl Mater Interfaces* **2013**, *5* (21), 10437-44.
184. Huang, W.; Wang, H.; Zhou, J.; Wang, J.; Duchesne, P. N.; Muir, D.; Zhang, P.; Han, N.; Zhao, F.; Zeng, M.; Zhong, J.; Jin, C.; Li, Y.; Lee, S. T.; Dai, H., Highly active and durable methanol oxidation electrocatalyst based on the synergy of platinum-nickel hydroxide-graphene. *Nat Commun* **2015**, *6*, 10035.

185. Wiegand, B. C.; Uvdal, P.; Serafin, J. G.; Friend, C. M., Competition between carbon-oxygen and 1-carbon-hydrogen bond scission during deoxygenation: the reactions of 1-propanol on molybdenum(110). *The Journal of Physical Chemistry* **1992**, *96* (12), 5063-5069.
186. Goering, J.; Kadossov, E.; Burghaus, U., Adsorption Kinetics of Alcohols on Single-Wall Carbon Nanotubes: An Ultrahigh Vacuum Surface Chemistry Study. *The Journal of Physical Chemistry C* **2008**, *112* (27), 10114-10124.
187. Kosinov, N.; Gascon, J.; Kapteijn, F.; Hensen, E. J., Recent developments in zeolite membranes for gas separation. *Journal of Membrane Science* **2016**, *499*, 65-79.
188. Moshoeshe, M.; Nadiye-Tabbiruka, M. S.; Obuseng, V., A Review of the Chemistry, Structure, Properties and Applications of Zeolites. *American Journal of Materials Science* **2017**, *7* (5), 196-221.
189. Roth, W. J.; Nachtigall, P.; Morris, R. E.; Cejka, J., Two-dimensional zeolites: current status and perspectives. *Chem Rev* **2014**, *114* (9), 4807-37.
190. Lepore, A. W.; Li, Z.; Davison, B. H.; Foo, G. S.; Wu, Z.; Narula, C. K., Catalytic Dehydration of Biomass Derived 1-Propanol to Propene over M-ZSM-5 (M = H, V, Cu, or Zn). *Industrial & Engineering Chemistry Research* **2017**, *56* (15), 4302-4308.
191. Li, Z.; Lepore, A.; Davison, B. H.; Narula, C. K., Catalytic Conversion of Biomass-Derived Ethanol to Liquid Hydrocarbon Blendstock: Effect of Light Gas Recirculation. *Energy & Fuels* **2016**, *30* (12), 10611-10617.
192. Stacchiola, D.; Kaya, S.; Weissenrieder, J.; Kuhlenbeck, H.; Shaikhutdinov, S.; Freund, H. J.; Sierka, M.; Todorova, T. K.; Sauer, J., Synthesis and structure of ultrathin aluminosilicate films. *Angew Chem Int Ed Engl* **2006**, *45* (45), 7636-9.
193. Bhatt, M. D.; Lee, J. S., Current progress and scientific challenges in the advancement of organic-inorganic lead halide perovskite solar cells. *New Journal of Chemistry* **2017**, *41* (19), 10508-10527.
194. Green, M. A.; Ho-Baillie, A., Perovskite Solar Cells: The Birth of a New Era in Photovoltaics. *ACS Energy Letters* **2017**, *2* (4), 822-830.
195. Kojima, A.; Teshima, K.; Shirai, Y.; Miyasaka, T., Organometal Halide Perovskites as Visible-Light Sensitizers for Photovoltaic Cells. *Journal of the American Chemical Society* **2009**, *131* (17), 6050-6051.
196. Nie, W.; Tsai, H.; Asadpour, R.; Blancon, J.-C.; Neukirch, A. J.; Gupta, G.; Crochet, J. J.; Chhowalla, M.; Tretiak, S.; Alam, M. A.; Wang, H.-L.; Mohite, A. D., High-efficiency solution-processed perovskite solar cells with millimeter-scale grains. *Science* **2015**, *347* (6221), 522-525.
197. Ono, L. K.; Leyden, M. R.; Wang, S.; Qi, Y., Organometal halide perovskite thin films and solar cells by vapor deposition. *Journal of Materials Chemistry A* **2016**, *4* (18), 6693-6713.

198. Sahli, F.; Werner, J.; Kamino, B. A.; Bräuningner, M.; Monnard, R.; Paviet-Salomon, B.; Barraud, L.; Ding, L.; Diaz Leon, J. J.; Sacchetto, D.; Cattaneo, G.; Despeisse, M.; Boccard, M.; Nicolay, S.; Jeangros, Q.; Niesen, B.; Ballif, C., Fully textured monolithic perovskite/silicon tandem solar cells with 25.2% power conversion efficiency. *Nature Materials* **2018**, *17* (9), 820-826.
199. Zhang, W.; Saliba, M.; Moore, D. T.; Pathak, S. K.; Horantner, M. T.; Stergiopoulos, T.; Stranks, S. D.; Eperon, G. E.; Alexander-Webber, J. A.; Abate, A.; Sadhanala, A.; Yao, S.; Chen, Y.; Friend, R. H.; Estroff, L. A.; Wiesner, U.; Snaith, H. J., Ultrasoft organic-inorganic perovskite thin-film formation and crystallization for efficient planar heterojunction solar cells. *Nat Commun* **2015**, *6*, 6142.
200. Yue, L.; Yan, B.; Attridge, M.; Wang, Z., Light absorption in perovskite solar cell: Fundamentals and plasmonic enhancement of infrared band absorption. *Solar Energy* **2016**, *124*, 143-152.
201. Park, N.-G., Perovskite solar cells: an emerging photovoltaic technology. *Materials Today* **2015**, *18* (2), 65-72.
202. Zeman, M., Thin-Film Silicon PV Technology. *Journal of Electrical Engineering* **2010**, *61* (5), 271.
203. Hodes, G.; Kamat, P. V., Understanding the Implication of Carrier Diffusion Length in Photovoltaic Cells. *J Phys Chem Lett* **2015**, *6* (20), 4090-2.
204. Shi, D.; Adinolfi, V.; Comin, R.; Yuan, M.; Alarousu, E.; Buin, A.; Chen, Y.; Hoogland, S.; Rothenberger, A.; Katsiev, K.; Losovyj, Y.; Zhang, X.; Dowben, P. A.; Mohammed, O. F.; Sargent, E. H.; Bakr, O. M., Low trap-state density and long carrier diffusion in organolead trihalide perovskite single crystals. *Science* **2015**, *347* (6221), 519-522.
205. Deretzi, I.; Alberti, A.; Pellegrino, G.; Smecca, E.; Giannazzo, F.; Sakai, N.; Miyasaka, T.; La Magna, A., Atomistic origins of CH₃NH₃PbI₃ degradation to PbI₂ in vacuum. *Applied Physics Letters* **2015**, *106* (13).
206. Niu, G.; Li, W.; Meng, F.; Wang, L.; Dong, H.; Qiu, Y., Study on the stability of CH₃NH₃PbI₃ films and the effect of post-modification by aluminum oxide in all-solid-state hybrid solar cells. *J. Mater. Chem. A* **2014**, *2* (3), 705-710.
207. Juarez-Perez, E. J.; Hawash, Z.; Raga, S. R.; Ono, L. K.; Qi, Y., Thermal degradation of CH₃NH₃PbI₃ perovskite into NH₃ and CH₃I gases observed by coupled thermogravimetry–mass spectrometry analysis. *Energy & Environmental Science* **2016**, *9* (11), 3406-3410.
208. Yuan, Y.; Wang, Q.; Shao, Y.; Lu, H.; Li, T.; Gruverman, A.; Huang, J., Electric-Field-Driven Reversible Conversion Between Methylammonium Lead Triiodide Perovskites and Lead Iodide at Elevated Temperatures. *Advanced Energy Materials* **2016**, *6* (2).
209. Matteocci, F.; Cinà, L.; Lamanna, E.; Cacovich, S.; Divitini, G.; Midgley, P. A.; Ducati, C.; Di Carlo, A., Encapsulation for long-term stability enhancement of perovskite solar cells. *Nano Energy* **2016**, *30*, 162-172.
210. Hodes, G.; Cahen, D., Perovskite cells roll forward. *Nature Photonics* **2014**, *8*, 87.

211. Kumar, M. H.; Dharani, S.; Leong, W. L.; Boix, P. P.; Prabhakar, R. R.; Baikie, T.; Shi, C.; Ding, H.; Ramesh, R.; Asta, M., Lead-free halide perovskite solar cells with high photocurrents realized through vacancy modulation. *Advanced Materials* **2014**, *26* (41), 7122-7127.
212. Yang, J.; Siempelkamp, B. D.; Liu, D.; Kelly, T. L., Investigation of CH₃NH₃PbI₃ Degradation Rates and Mechanisms in Controlled Humidity Environments Using in Situ Techniques. *ACS Nano* **2015**, *9* (2), 1955-1963.
213. Li, W.; Li, J.; Wang, L.; Niu, G.; Gao, R.; Qiu, Y., Post modification of perovskite sensitized solar cells by aluminum oxide for enhanced performance. *Journal of Materials Chemistry A* **2013**, *1* (38), 11735-11740.
214. Zheng, L.; Chung, Y.-H.; Ma, Y.; Zhang, L.; Xiao, L.; Chen, Z.; Wang, S.; Qu, B.; Gong, Q., A hydrophobic hole transporting oligothiophene for planar perovskite solar cells with improved stability. *Chemical Communications* **2014**, *50* (76), 11196-11199.
215. Mei, A.; Li, X.; Liu, L.; Ku, Z.; Liu, T.; Rong, Y.; Xu, M.; Hu, M.; Chen, J.; Yang, Y.; Grätzel, M.; Han, H., A hole-conductor-free, fully printable mesoscopic perovskite solar cell with high stability. *Science* **2014**, *345* (6194), 295-298.
216. Back, H.; Kim, G.; Kim, J.; Kong, J.; Kim, T. K.; Kang, H.; Kim, H.; Lee, J.; Lee, S.; Lee, K., Achieving long-term stable perovskite solar cells via ion neutralization. *Energy & Environmental Science* **2016**, *9* (4), 1258-1263.
217. Berhe, T. A.; Su, W.-N.; Chen, C.-H.; Pan, C.-J.; Cheng, J.-H.; Chen, H.-M.; Tsai, M.-C.; Chen, L.-Y.; Dubale, A. A.; Hwang, B.-J., Organometal halide perovskite solar cells: degradation and stability. *Energy & Environmental Science* **2016**, *9* (2), 323-356.
218. Liu, Y.; Page, Z. A.; Zhou, D.; Duzhko, V. V.; Kittilstved, K. R.; Emrick, T.; Russell, T. P., Chemical Stabilization of Perovskite Solar Cells with Functional Fullero-pyrrolidines. *ACS Cent Sci* **2018**, *4* (2), 216-222.
219. Guerrero, A.; You, J.; Aranda, C.; Kang, Y. S.; Garcia-Belmonte, G.; Zhou, H.; Bisquert, J.; Yang, Y., Interfacial Degradation of Planar Lead Halide Perovskite Solar Cells. *ACS nano* **2016**, *10* (1), 218.
220. Salim, M.; Chowdhury, M. S. H.; Hossain, M.; Islam, M., A micro-review on prospects and challenges of perovskite materials in organic-inorganic hybrid solar cell applications. *Digest journal of nanomaterials and biostructures* **2015**, *10* (4), 1289-1302.
221. Johnsson, M.; Lemmens, P., Crystallography and chemistry of perovskites. *arXiv preprint cond-mat/0506606* **2005**.
222. Bhalla, A.; Guo, R.; Roy, R., The perovskite structure—a review of its role in ceramic science and technology. *Materials Research Innovations* **2000**, *4* (1), 3-26.
223. Smith, J. V., : Minerals: Their Constitution and Origin. *Journal of Geology* **2005**, *113*, 373-373.

224. Mitchell, R. H.; Welch, M. D.; Chakhmouradian, A. R., Nomenclature of the perovskite supergroup: A hierarchical system of classification based on crystal structure and composition. *Mineralogical Magazine* **2018**, *81* (03), 411-461.
225. Kawamura, Y.; Mashiyama, H.; Hasebe, K., Structural study on cubic-tetragonal transition of $\text{CH}_3\text{NH}_3\text{PbI}_3$. *Journal of the Physical Society of Japan* **2002**, *71* (7), 1694-1697.
226. Baikie, T.; Fang, Y.; Kadro, J. M.; Schreyer, M.; Wei, F.; Mhaisalkar, S. G.; Graetzel, M.; White, T. J., Synthesis and crystal chemistry of the hybrid perovskite $(\text{CH}_3\text{NH}_3)\text{PbI}_3$ for solid-state sensitised solar cell applications. *Journal of Materials Chemistry A* **2013**, *1* (18), 5628-5641.
227. Zhao, Q.; Li, G. R.; Song, J.; Zhao, Y.; Qiang, Y.; Gao, X. P., Improving the photovoltaic performance of perovskite solar cells with acetate. *Sci Rep* **2016**, *6*, 38670.
228. Noel, N.; Abate, A.; Stranks, S.; Parrott, E.; Burlakov, V.; Goriely, A.; Snaith, H., Enhanced Photoluminescence and Solar Cell Performance via Lewis Base Passivation of Organic-Inorganic Lead Halide Perovskites. *ACS Nano* **2014**, *8* (10), 9815-9821.
229. Pan, A.; He, B.; Fan, X.; Liu, Z.; Urban, J. J.; Alivisatos, A. P.; He, L.; Liu, Y., Insight into the Ligand-Mediated Synthesis of Colloidal CsPbBr_3 Perovskite Nanocrystals: The Role of Organic Acid, Base, and Cesium Precursors. *ACS Nano* **2016**, *10* (8), 7943-54.
230. Chang, C. Y.; Huang, Y. C.; Tsao, C. S.; Su, W. F., Formation Mechanism and Control of Perovskite Films from Solution to Crystalline Phase Studied by in Situ Synchrotron Scattering. *ACS Appl Mater Interfaces* **2016**, *8* (40), 26712-26721.
231. Conings, B.; Baeten, L.; De Dobbelaere, C.; D'Haen, J.; Manca, J.; Boyen, H. G., Perovskite-based hybrid solar cells exceeding 10% efficiency with high reproducibility using a thin film sandwich approach. *Advanced Materials* **2014**, *26* (13), 2041-2046.
232. Kim, H.-B.; Choi, H.; Jeong, J.; Kim, S.; Walker, B.; Song, S.; Kim, J. Y., Mixed solvents for the optimization of morphology in solution-processed, inverted-type perovskite/fullerene hybrid solar cells. *Nanoscale* **2014**, *6* (12), 6679-6683.
233. Zhang, W.; Saliba, M.; Moore, D. T.; Pathak, S. K.; Hörlantner, M. T.; Stergiopoulos, T.; Stranks, S. D.; Eperon, G. E.; Alexander-Webber, J. A.; Abate, A., Ultrasoft organic-inorganic perovskite thin-film formation and crystallization for efficient planar heterojunction solar cells. *Nature communications* **2015**, *6*, 6142.
234. Forgács, D.; Sessolo, M.; Bolink, H. J., Lead acetate precursor based pin perovskite solar cells with enhanced reproducibility and low hysteresis. *Journal of Materials Chemistry A* **2015**, *3* (27), 14121-14125.
235. Fu, Y.; Meng, F.; Rowley, M. B.; Thompson, B. J.; Shearer, M. J.; Ma, D.; Hamers, R. J.; Wright, J. C.; Jin, S., Solution growth of single crystal methylammonium lead halide perovskite nanostructures for optoelectronic and photovoltaic applications. *Journal of the American Chemical Society* **2015**, *137* (17), 5810-5818.

236. Bhachu, D. S.; Scanlon, D. O.; Saban, E. J.; Bronstein, H.; Parkin, I. P.; Carmalt, C. J.; Palgrave, R. G., Scalable route to CH₃NH₃PbI₃ perovskite thin films by aerosol assisted chemical vapour deposition. *Journal of Materials Chemistry A* **2015**, *3* (17), 9071-9073.
237. Liu, M.; Johnston, M. B.; Snaith, H. J., Efficient planar heterojunction perovskite solar cells by vapour deposition. *Nature* **2013**, *501* (7467), 395-8.
238. Burghaus, U., Surface chemistry of CO₂ – Adsorption of carbon dioxide on clean surfaces at ultrahigh vacuum. *Progress in Surface Science* **2014**, *89* (2), 161-217.
239. Freund, H.-J.; Roberts, M. W., Surface chemistry of carbon dioxide. *Surface Science Reports* **1996**, *25* (8), 225-273.
240. Taifan, W.; Boily, J.-F.; Baltrusaitis, J., Surface chemistry of carbon dioxide revisited. *Surface Science Reports* **2016**, *71* (4), 595-671.
241. Toda, Y.; Hirayama, H.; Kuganathan, N.; Torrisi, A.; Sushko, P. V.; Hosono, H., Activation and splitting of carbon dioxide on the surface of an inorganic electride material. *Nat Commun* **2013**, *4*, 2378.
242. Wang, J.; Funk, S.; Burghaus, U., Adsorption dynamics of CO₂ on copper-precovered ZnO(0001)-Zn: a molecular-beam scattering and thermal-desorption spectroscopy study. *J Chem Phys* **2005**, *123* (20), 204710.
243. Askgaard, T.; Norskov, J.; Ovesen, C.; Stoltze, P., A kinetic model of methanol synthesis. *Journal of Catalysis* **1995**, *156* (2), 229-242.
244. Suib, S. L., *New and future developments in catalysis: activation of carbon dioxide*. Newnes: 2013.
245. Wang, S.-G.; Liao, X.-Y.; Hu, J.; Cao, D.-B.; Li, Y.-W.; Wang, J.; Jiao, H., Kinetic aspect of CO₂ reforming of CH₄ on Ni (1 1 1): a density functional theory calculation. *Surface science* **2007**, *601* (5), 1271-1284.
246. Walsh, A. D., 467. The electronic orbitals, shapes, and spectra of polyatomic molecules. Part II. Non-hydride AB₂ and BAC molecules. *Journal of the Chemical Society (Resumed)* **1953**, (0), 2266-2288.
247. Wang, G.-C.; Jiang, L.; Morikawa, Y.; Nakamura, J.; Cai, Z.-S.; Pan, Y.-M.; Zhao, X.-Z., Cluster and periodic DFT calculations of adsorption and activation of CO₂ on the Cu (hkl) surfaces. *Surface science* **2004**, *570* (3), 205-217.
248. Ernst, K.-H.; Schlatterbeck, D.; Christmann, K., Adsorption of carbon dioxide on Cu (110) and on hydrogen and oxygen covered Cu (110) surfaces. *Physical Chemistry Chemical Physics* **1999**, *1* (17), 4105-4112.
249. Funk, S.; Hokkanen, B.; Wang, J.; Burghaus, U.; Bozzolo, G.; Garcés, J., Adsorption dynamics of CO₂ on Cu (1 1 0): A molecular beam study. *Surface science* **2006**, *600* (3), 583-590.
250. Fu, S. S.; Somorjai, G. A., Interactions of O₂, CO, CO₂, and D₂ with the stepped Cu (311) crystal face: Comparison to Cu (110). *Surface science* **1992**, *262* (1-2), 68-76.

251. Kuhlenbeck, H.; Xu, C.; Dillmann, B.; Häfel, M.; Adam, B.; Ehrlich, D.; Wohlrab, S.; Freund, H. J.; Ditzinger, U.; Neddermeyer, H., Adsorption and reaction on oxide surfaces: CO and CO₂ on Cr₂O₃ (111). *Berichte der Bunsengesellschaft für physikalische Chemie* **1992**, *96* (1), 15-27.
252. Nakamura, J.; Rodriguez, J. A.; Campbell, C. T., Does CO₂ dissociatively adsorb on Cu surfaces? *Journal of Physics: Condensed Matter* **1989**, *1* (SB), SB149.
253. Bebensee, F.; Voigts, F.; Maus-Friedrichs, W., The adsorption of oxygen and water on Ca and CaO films studied with MIES, UPS and XPS. *Surface Science* **2008**, *602* (9), 1622-1630.
254. Rakotoveloa, G.; Moussounda, P.; Haroun, M.; Legare, P.; Rakotomahevitra, A.; Rakotomalala, M.; Parlebas, J., Adsorption of CO, CO₂ and NO molecules on a BaTiO₃ (0 0 1) surface. *Surface Science* **2009**, *603* (9), 1221-1228.
255. Azad, S.; Engelhard, M. H.; Wang, L.-Q., Adsorption and Reaction of CO and CO₂ on Oxidized and Reduced SrTiO₃(100) Surfaces. *The Journal of Physical Chemistry B* **2005**, *109* (20), 10327-10331.
256. Wei, T.; Jia, L.; Zheng, H.; Chi, B.; Pu, J.; Li, J., LaMnO₃-based perovskite with in-situ exsolved Ni nanoparticles: a highly active, performance stable and coking resistant catalyst for CO₂ dry reforming of CH₄. *Applied Catalysis A: General* **2018**, *564*, 199-207.
257. Lu, X.; Zhang, Q.; Lin, M. C., Adsorption of methanol, formaldehyde and formic acid on the Si(100)-2 × 1 surface: A computational study. *Physical Chemistry Chemical Physics* **2001**, *3* (11), 2156-2161.
258. Sadvovskaya, E. M.; Chesalov, Y. A.; Goncharov, V. B.; Sobolev, V. I.; Andrushkevich, T. V., Formic acid decomposition over V-Ti oxide catalyst: Mechanism and kinetics. *Molecular Catalysis* **2017**, *430*, 54-62.
259. Wang, S.; Zhang, F.; Cai, Q.; Li, X.; Zhu, L.; Wang, Q.; Luo, Z., Catalytic steam reforming of bio-oil model compounds for hydrogen production over coal ash supported Ni catalyst. *International Journal of Hydrogen Energy* **2014**, *39* (5), 2018-2025.
260. Yoshimoto, M.; Takagi, S.; Umemura, Y.; Hada, M.; Nakatsuji, H., Theoretical Study on the Decomposition of HCOOH on a ZnO(1010) Surface. *Journal of Catalysis* **1998**, *173* (1), 53-63.
261. Youngs, T. G. A.; Haq, S.; Bowker, M., Formic acid adsorption and oxidation on Cu(110). *Surface Science* **2008**, *602* (10), 1775-1782.
262. Liu, Y.; Li, Z. H., Adsorption and decomposition mechanism of formic acid on the Ga₂O₃ surface by first principle studies. *Surface Science* **2017**, *656*, 86-95.
263. Jiang, Z.; Qin, P.; Fang, T., Decomposition mechanism of formic acid on Cu (111) surface: A theoretical study. *Applied Surface Science* **2017**, *396*, 857-864.
264. Forgács, D.; Sessolo, M.; Bolink, H. J., Lead acetate precursor based p-i-n perovskite solar cells with enhanced reproducibility and low hysteresis. *Journal of Materials Chemistry A* **2015**, *3* (27), 14121-14125.

265. Devi, S.; Kaur, A.; Sarkar, S.; Vohra, S.; Tyagi, S., Synthesis and characterization of highly luminescent N-doped carbon quantum dots for metal ion sensing. *Integrated Ferroelectrics* **2018**, *186* (1), 32-39.
266. Khanra, P.; Kuila, T.; Kim, N. H.; Bae, S. H.; Yu, D.-s.; Lee, J. H., Simultaneous bio-functionalization and reduction of graphene oxide by baker's yeast. *Chemical Engineering Journal* **2012**, *183*, 526-533.
267. Wu, Z.; Gao, H.; Yan, S.; Zou, Z., Synthesis of carbon black/carbon nitride intercalation compound composite for efficient hydrogen production. *Dalton Trans* **2014**, *43* (31), 12013-7.
268. In, S.-I.; Almqvist, K. P.; Lee, H.-S.; Andersen, I. H.; Qin, D.; Bao, N.; Grimes, C., Low temperature synthesis of transparent, vertically aligned anatase TiO₂ nanowire arrays: application to dye sensitized solar cells. *Bulletin of the Korean Chemical Society* **2012**, *33* (6), 1989-1992.
269. Stojilovic, N., Why Can't We See Hydrogen in X-ray Photoelectron Spectroscopy? *Journal of Chemical Education* **2012**, *89* (10), 1331-1332.
270. Kumar, C. V.; Sfyri, G.; Raptis, D.; Stathatos, E.; Lianos, P., Perovskite solar cell with low cost Cu-phthalocyanine as hole transporting material. *RSC Advances* **2015**, *5* (5), 3786-3791.
271. Hariprakash, B.; Mane, A. U.; Martha, S. K.; Gaffoor, S. A.; Shivashankar, S. A.; Shukla, A. K., A Low-Cost, High Energy-Density Lead/Acid Battery. *Electrochemical and Solid-State Letters* **2004**, *7* (3).
272. O. Ayieko, C.; J. Musembi, R.; M. Waita, S.; O. Aduda, B.; K. Jain, P., Structural and Optical Characterization of Nitrogen-doped TiO₂ Thin Films Deposited by Spray Pyrolysis on Fluorine Doped Tin Oxide (FTO) Coated Glass Slides. *International Journal of Energy and Engineering* **2012**, *2* (3), 67-72.
273. Abdelmageed, G.; Mackeen, C.; Hellier, K.; Jewell, L.; Seymour, L.; Tingwald, M.; Bridges, F.; Zhang, J. Z.; Carter, S., Effect of temperature on light induced degradation in methylammonium lead iodide perovskite thin films and solar cells. *Solar Energy Materials and Solar Cells* **2018**, *174*, 566-571.
274. Henderson, M. A., Evidence for bicarbonate formation on vacuum annealed TiO₂ (110) resulting from a precursor-mediated interaction between CO₂ and H₂O. *Surface Science* **1998**, *400* (1-3), 203-219.
275. Brosseau, R.; Ellis, T. H.; Wang, H., The influence of water on the chemisorption of CO₂ onto Pd(110). *Chemical Physics Letters* **1991**, *177* (2), 118-122.
276. Krieg, F.; Ochsenbein, S. T.; Yakunin, S.; Ten Brinck, S.; Aellen, P.; Suess, A.; Clerc, B.; Guggisberg, D.; Nazarenko, O.; Shynkarenko, Y.; Kumar, S.; Shih, C. J.; Infante, I.; Kovalenko, M. V., Colloidal CsPbX₃ (X = Cl, Br, I) Nanocrystals 2.0: Zwitterionic Capping Ligands for Improved Durability and Stability. *ACS Energy Lett* **2018**, *3* (3), 641-646.

277. Nayakasinghe, M. T.; Han, Y.; Sivapragasam, N.; Kilin, D. S.; Burghaus, U., Unexpected high binding energy of CO₂ on CH₃NH₃PbI₃ lead-halide organic-inorganic perovskites via bicarbonate formation. *Chem Commun (Camb)* **2018**, 54 (71), 9949-9952.